Final
Report

Electric Island H_2OPPER

DSE Group 19

Delft University of Technology

TU Delft

[This page intentionally left blank]

DSE

Final report

by

Group 19

AE3200 Design Synthesis

at the Delft University of Technology,

Authors:

Cummins, Anthony
4436253

Dolman, Casper
4848209

Gehlen, Tjeu
4682858

Koning, Timo
4884418

Mathoera, Winand
4775848

Spaan, Henri
4854330

Timmermans, Daniël
4670671

Vlot, Dick Daniel
4381742

van Voorst, Olav
4668367

Wulffraat, Stijn
4653572

Tutor:	Dr. ir. John-Alan Pascoe
Coaches:	Juseong Lee, Msc.
	Bieke von den Hoff, Msc.
Project duration:	19-04-2021 - 01-07-2021

TU Delft

Summary

Aviation is a vital lifeline for island communities. However, air travel is also a significant source of air pollution and therefore contributes to global warming. The rising sea levels, caused by global warming, heavily affect the livability of pacific islands, causing drink water shortages and crop failure. Sustainable aviation has to be a part of the climate change solution. It is the goal of Group 19 to design a fully electrically propelled net-zero emissions aircraft suitable for island-hopping operations. This was done by a team of 10 students within 10 weeks. In the previous stage of the preliminary design, a trade-off was performed, resulting in the final concept: the H_2OPPER, a hydrogen powered electrical aircraft. In this final report, the further design of this final concept is documented and both the technical and the financial analysis of the H_2OPPER are presented.

The main aircraft parameters can be seen in Table 1 - 3 and the payload range diagram in Figure 1. Figure 2 shows the final design for the H_2OPPER. As can be seen from the drawing, the aircraft has a high-wing configuration with two engines placed at the tip.

Table 1: Aircraft technical specifications

Weight	
Maximum take-off weight [kg]	8618
Maximum zero fuel weight [kg]	6804
Maximum payload weight [kg]	1814
Occupancy	
Crew members [-]	1 - 2
Passengers [-]	19
Powerplant	
Number of engines [-]	2
Take-off power per engine [kWh]	730

Table 2: Aircraft dimensions

Exterior	
Exterior height [m]	7.9
Exterior length [m]	14.4
Wing span [m]	20.0
Interior	
Cabin height [m]	1.91
Cabin width [m]	1.95
Cabin length [m]	6.8
Seat pitch [m]	0.35

Table 3: Performance specification

Performance	
Cruise speed [kts]	175
Service ceiling [km]	4.57
Take-off distance [m]	750
Landing distance [m]	675
Maximum range [NM]	1177
Range at max. payload [NM]	321
Rate of climb [m/s]	5.8

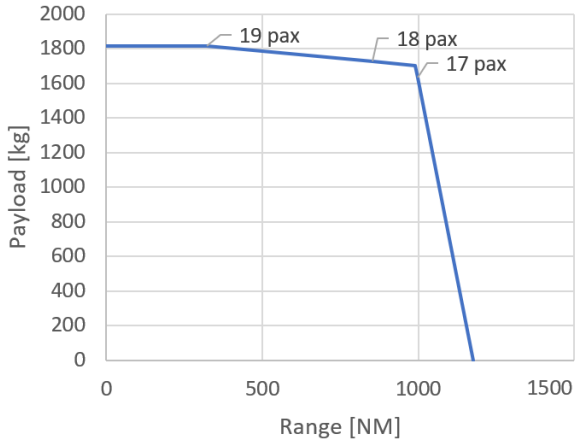

Figure 1: H_2OPPER payload-range diagram

Figure 2: H_2OPPER isometric view

In order to bring enough liquid hydrogen for the H_2OPPER to meet its range requirements, it is stored in a unique container. This multi-spherical composite tank, with a very high storage efficiency, allows for weight savings and flexibility in placement. This flexibility allowed for the tanks to be placed in the bottom of the fuselage underneath the cabin.

This hydrogen is converted to electrical power using state of the art Proton Exchange Membrane fuel cells. The fuel cells have an efficiency of at least 0.53, the remaining energy is converted to heat. Part of this heat is used to heat up the liquid hydrogen to the desired temperature. The remaining heat has to be dissipated. This is done with the use of radiators, placed underneath the engines. The acceleration of the air by the propeller increases the effectiveness of the radiator.

During the design it was found that placing these engines at the wing tips has a positive effect on the drag and the oswald efficiency of the aircraft. This decision also had an effect on other subsystems. For the wingbox a structural weight reduction was achieved, because the placement of the engine on the tip relieved some bending moment caused by the lift force. For the sizing of the vertical tail, the one engine inoperative scenario became most critical. This resulted in an increased tail and rudder surface area, increasing the structural weight of the empennage. From these combined effects it was concluded that the engines on the wing tip were more favourable than the conventional engines near the root.

Due to these innovative solution, the H_2OPPER has a range of 300 [NM] with maximum payload, meeting the set requirement. By exchanging two passengers for extra hydrogen, a range of 1000 [NM] can be reached with 17 passengers. This can be done with the available tank capacity, thus no adjustments have to be made. This makes the H_2OPPER a versatile aircraft, which can be used to serve more remote islands. It also means that not every smaller airport needs a hydrogen refueling system, reducing the cost of ground operations.

Even more important than the range requirements, were sustainability requirements. During this design phase the Green Policy, composed during the baseline phase, was used to ensure the sustainability of the design. This was done with the use of qualitative and quantitative green indicators. Since the final design was hydrogen powered, emission indicators were already met. The main focus was on the efficiency and recyclability of the design. The recyclability indicator was a deciding factor in the material choices and resulted in a structure which is 98% recyclable.

With these performance characteristics known, a revised market analysis was performed to identify the competitors and the competitiveness of the H_2OPPER. The unique selling point was found to be the sustainability with a superior range with respect to other sustainable designs, such as the ES-19. To further investigate the financial feasibility, a financial evaluation was performed. The total manufacturing cost was estimated to be 6.2 million dollars, allowing for a 30% profit margin with the required list price of 10 million dollars. The operational cost was estimated to be 10% more than current aircraft by the year 2030. Depending on how the hydrogen market evolves over the coming years, this could be reduced to 5% by 2040.

However, the H_2OPPER can only be successful on the market if the design is valid. In order to prove the validity of the design tools, extensive verification and validation was performed. The focus was put on validation and was mainly done by comparison with reference aircraft. Some discrepancies were found, but they could be justified with differences between the H_2OPPER and the reference aircraft. In addition the robustness of the design was tested, using a sensitivity analysis. This analysis focused on the effect of assumptions made in the subsystem design on a system level. This mainly showed that the uncertainty of the performance of batteries and fuel cells in the near future, could be detrimental for the design. However, there is still a margin in the operational empty weight of 70 [kg], for the H_2OPPER to meet its requirements.

This is the final report in the preliminary design phase. However, a lot of work still has to be done before the H_2OPPER can become operational. The next step will be the detailed design phase, where the subsystems are worked out in full detail and tested. The focus for this should be on the newer technology with more uncertainties, such as the hydrogen tank and fuel cell. After this, a prototype will be created before the production phase starts. Lastly, in the support phase, inspection maintenance needs to be performed during the aircraft's entire operational lifetime.

Nomenclature

Abbreviations

A/C	Aircraft
AFC	Alkaline Fuel Cell
ATLA	Air Transport Vehicle Life Cycle Analysis
BOR	Boil-Off Rate
BWB	Blended Wing Body
CFD	Computational Fluid Dynamics
CFRP	Carbon-Fibre-Reinforced Polymers
EASA	European Aviation Safety Agency
EoL	End of Life
FBD	Free Body Diagram
FBS	Functional Breakdown Structure
FFD	Functional Flow Diagram
FL	Flight Level
GHG	Greenhouse Gasses
HLD	High-Lift Device
LH2	Liquid Hydrogen
MAC	Mean Aerodynamic chord
MCFC	Molten Carbonate Fuel Cell
MST	Multi-Sphere Tank
MTOW	Maximum Take-Off Weight
MZFW	Maximum Zero Fuel Weight
NFPA	National Fire Protection Association
OEM	Operational Empty Mass
OEW	Operational Empty Weight
PAFC	Phosphoric Acid Fuel Cell
Pax.	Passengers
PEM	Proton Exchange Membrane
RAMS	Reliability, Availability, Maintainability, and Safety
RDTE	Research, Development, Testing and Evaluation
ROC	Rate Of Climb
S&C	Stability & Controllability
SIDS	Small Developing Island States
SOFC	Solide Oxide Fuel cell
TOP	Take Off Parameter
VeDSC	Vertical tail Design Stability and Control
WBS	Work Breakdown Structure
WFD	Work Flow Diagram

Symbols

α	Angle of attack	[deg]
β	Side-slip angle	[rad]
ΔH_{vap}	Heat of vaporization	[J/kg]
ΔT	Temperature difference	[K]
δ_r	Rudder deflection	[rad]
ϵ	Downwash angle	[deg]
η_r	Energy recovery efficiency	[-]
η_{fc}	Efficiency of the fuel cell	[-]
η_m	Material scarcity index	[-]
η_{pt}	Total propulsive efficiency	[-]
η_{re}	Recyclability energy efficiency	[-]
γ_{cyl}	Angle between intersection and liner	[rad]
Λ	Wing sweep angle	[rad]
λ	Taper ratio	[-]
λ_v	Taper ratio of the vertical tail	[-]
$\Lambda_{c/2}$	Half cord sweep	[rad]
μ_g	Aircraft mass ratio	[-]
ν	Material poisson ratio	[-]

ρ	Air density	[kg/m^3]
ρ_{comp}	Composite density	[kg/m^3]
ρ_{ins}	Density of the insulation	[kg/m^3]
ρ_{liner}	Liner density	[kg/m^3]
ρ_{ins}	Insulation density	[kg/m^3]
σ_{cc}	Critical crippling stress	[N/m^2]
σ_{vm}	Von Mises stress	[N/m^2]
σ_x	Bending stress in x-direction	[N/m^2]
σ_{yy}	Total bending stress in y-direction	[N/m^2]
σ_y	Yield stress	[N/m^2]
σ_z	Bending stress in z-direction	[N/m^2]
τ	Rudder effectiveness	[-]
τ_{cr}	Critical skin bucking shear stress	[N/m^2]
τ_T	Shear stress due to torsion	[N/m^2]
τ_{xz}	Shear stress in the xz-plane	[N/m^2]
τ_x	Shear stress in x-direction	[N/m^2]
τ_z	Shear stress in z-direction	[N/m^2]
θ_1	Fillet angle	[rad]
φ	Bank angle	[rad]
A	Wing aspect ratio	[-]
a	Speed of sound	[m/s]
A_v	Aspect ratio of the vertical tail	[-]
A_{cap}	Area formed by fillet radius at intersection	[m^2]
A_{prop}	Area of propeller	[m^2]
A_{triangle}	Area of triangle formed at intersection	[m^2]
A_d	Door area	[m^2]
A_{inlet}	Inlet area	[m^2]
A_i	Element area	[m^2]
A_m	Cross sectional area	[m^2]
A_{sk}	Skin area	[m^2]
B	Compressibility parameter	[-]
B	Number of blades per propeller	[-]
b_f	Outer fuselage width at the wing intersection	[m]
C	Compression buckling coefficient	[-]
c	chord length	[m]
C_D	Drag coefficient	[-]
c_g	mean geometric chord	[m]
C_L	Lift coefficient	[-]
C_T	Thrust coefficient	[-]
C_{D_0}	Zero-lift drag coefficient	[-]
$C_{D_{misc}}$	Drag increment for interference, roughness and excrescence	[-]
C_{dst}	Development support and testing cost	[$]
C_{ed}	Engineering and design cost	[$]
C_{fin}	Cost of financing	[$]
C_{L_α}	Change of aircraft lift coefficient due to a change in angle of attack	[-]
C_{l_β}	Non dimensional rolling moment due to change in side-slip angle	[-]
$C_{L_{\alpha_V}}$	Isolated vertical tail lift curve slope	[-]
$C_{L_{\alpha_{A-h}}}$	Change of aircraft minus tail lift coefficient due to a change in angle of attack	[-]
$C_{L_{\alpha_h}}$	Change of tail lift coefficient due to a change in angle of attack	[-]
$C_{L_{loiter}}$	Lift coefficient during loitering	[-]
C_{n_β}	Yawing moment coefficient due to a change in side-slip angle	[-]
C_{n_e}	Non dimensional moment due to asymmetric thrust	[-]
$C_{n_{\beta_f}}$	Fuselage contribution to the yawing moment coefficient	[-]
$C_{n_{\beta_p}}$	Propeller contribution to the yawing coefficient	[-]
$C_{n_{\beta_v}}$	Vertical tail contribution to the yawing moment coefficient	[-]
$C_{n_{\beta_w}}$	Wing contribution to the yawing moment coefficient	[-]
$C_{n_{\delta_r}}$	Yawing moment due to a change in rudder deflection	[-]
C_{pro}	Cost of outsourced RDTE	[$]
C_{ta}	Testing aircraft(s) cost	[$]
C_{to}	Aircraft testing operations cost	[$]

C_{tsf}	Test and simulation facillities cost	[$]
C_{Y_β}	Lateral force coefficient due to a change in side-slip angle	[-]
$C_{Y_{\beta_V}}$	Lateral force coefficient of the vertical tail due to a change in side-slip angle	[-]
$C_{Y_{\delta_r}}$	Lateral force coefficient of the vertical tail due to a change in rudder deflection	[-]
$C_{Y_{A-h}}$	Lateral force coefficient of tailless aircraft	[-]
$C_{Y_{v_\alpha}}$	Lateral force coefficient of the vertical tail due to a change in angle of attack	[-]
CEF	Cost escalation factor	[-]
d	Centroid distance	[m]
D_p	Propeller diameter	[m]
D_{hor}	Horizontal tail drag distribution	[N/m]
D_{ver}	Vertical tail drag distribution	[N/m]
D_{wing}	Wing drag distribution	[N/m]
d_x	x-distance to centroid	[m]
d_z	z-distance to centroid	[m]
$dimension_{m,n,p}$	Dimension m, n or p	[-]
E	Material elastic modulus	[N/m^2]
e	Oswald efficiency	[-]
E_d	Total energy density	[J/kg]
E_{rc_i}	Energy required to recycle material i	[J]
E_{vir_i}	Required energy for virgin production of material	[J]
F_{cad}	Judgement factor which accounts for the effect of computer aided design capability	[-]
F_{diff}	Judgement factor which accounts for the difficulty of a new airplane program	[-]
F_h	Horizontal tail force	[N]
$F_{x_{el}}$	Elevator force in x-direction	[N]
$F_{x_{hld}}$	High-lift device force in x-direction	[N]
$F_{y_{emp}}$	Empennage force in z-direction	[N]
F_{z_ail}	Aileron force in z-direction	[N]
$F_{z_{el}}$	Elevator force in z-direction	[N]
$F_{z_{emp}}$	Empennage force in y-direction	[N]
$F_{z_{hld}}$	High-lift device force in z-direction	[N]
G	Mass growth factor	[-]
G	Material shear modulus	[N/m^2]
g	Acceleration due to gravity	[m/s^2]
h	Convective heat transfer coefficient	[W/(m^{2}K)]
h	Height of base	[m]
$h.c.$	Hourly cost of the engineers working on the RDTE	[$]
h_f	Outer fuselage height at the wing intersection	[m]
h_{cap}	Height of the spherical cap at intersection	[m]
h_{center}	Cap height at center	[m]
h_{inter}	Height at intersection	[m]
h_{inter}	Intersection spherical cap height	[m]
h_{sk}	Skin height	[m]
I_{xx}	Area moment of inertia around the x-axis	[m^4]
I_{zz}	Area moment of inertia around the z-axis	[m^4]
K_F	Fuselage correctional factor	[-]
K_g	Gust allevation factor	[-]
K_H	Horizontal stabilizer correctional factor	[-]
K_W	Wing correctional factor	[-]
K_{δ_r}	Rudder correctional factor	[-]
k_{overlap}	Hoop ring overlap ratio	[-]
k_{air}	Thermal conductivity of the air	[W/(mK)]
k_{comp}	Composite thermal conductivity	[W/(mK)]
k_{ins}	Insulation thermal conductivity	[W/(mK)]
K_s	Shear buckling constant	[-]
l	Length of base	[m]
l_h	Moment arm between the wing and the tail	[m]
l_p	Longitudinal distance between the propeller and the centre of gravity of the aircraft	[m]
l_v	Vertical tail length	[m]
l_{cyl}	Hollow tube length	[m]
l_{fn}	Length from the nose to the leading edge of the wing	[m]
L_{fus}	Fuselage lift distribution	[N/m]
L_{hor}	Horizontal tail lift distribution	[N/m]
L_m	Circumferential length	[m]

L_{ver}	Vertical tail lift distribution	[N/m]
L_{wing}	Wing lift distribution	[N/m]
$\dot{m}$	Mass flow	[kg/s]
$M_{\text{insulation}}$	Insulation mass	[kg]
M_{liner}	Liner mass	[kg]
M_{LH2}	Mass of the liquid hydrogen	[kg]
m_d	Door mass	[kg]
M_h	Horizontal tail moment	[Nm]
M_{ins}	Mass of the insulation	[kg]
M_r	Reaction moment	[Nm]
M_x	Bending moment around the x-axis	[Nm]
M_z	Bending moment around the z-axis	[Nm]
$multi_{\text{cells}}$	Number of spheres	[-]
$multi_{\text{junctions}}$	Number of junctions in the MST	[-]
n	Load factor	[-]
$N\overline{u}$	Nusselt number	[-]
N_z	Ultimate load factor	[-]
N_{rdte}	Number of aircraft built for RDTE	[-]
n_{rpm}	Propeller revolutions per minute	[rev/min]
N_{st}	Number of aircraft that will be used for static tests	[-]
P	Power	[W]
P_{br}	Engine shaft power	[W]
Pr	Prandtl number	[-]
Q	Heat transfer	[J]
$\dot{Q}$	Heat transfer rate	[J/s]
$q_{m,n,p}$	m, n or p	[-]
R	Radius	[m]
r	Distance from noise source	[m]
r_{cyl}	Hollow tube radius	[m]
R_{cryo}	Radius of the tank insulation	[m]
R_{fillet}	Radius of the fillet	[m]
R_{liner}	Liner radius	[m]
R_{ring}	Intersection radius	[m]
$R_{\text{ringfinal}}$	Intersection radius, corrected with fillet	[m]
R_x	Reaction force in x-direction	[N]
R_y	Reaction force in y-direction	[N]
R_z	Reaction force in z-direction	[N]
RC	Recyclability percentage	[-]
RC_i	Fraction of material i that can be recycled	[-]
$RECD_i$	Fraction of material i that is already recycled	[-]
s	Width of hoop ring	[m]
S_V	Vertical tail area	[m^2]
S_w	Wetted surface area	[-]
S_{cryo}	Insulation surface area	[m^2]
S_{csw}	Control surface area	[m^2]
$S_{\text{spheresfillets}}$	Surface subtracted due to filleting	[m^2]
S_{torus}	Surface area of single intersection	[m^2]
S_{w}	Wing surface area	[m^2]
S_{ref}	Wing surface area	[-]
SPL_{max}	Maximum sound pressure level	[dB]
T	Thrust	[N]
t/c_{root}	Thickness to chord ratio at the root	[-]
T_∞	Temperature of upstream air	[K]
T_f	Total thrust energy per flight	[J]
T_s	Surface Temperature	[K]
t_{junction}	Junction thickness	[m]
t_{ins}	Thickness of the tank insulation	[m]
t_{liner}	Liner thickness	[m]
T_{emp}	Empennage torque	[Nm]
T_{engine}	Engine thrust	[N]
T_h	Horizontal tail torque	[Nm]
T_r	Reaction torque	[Nm]
t_{sk}	Skin thickness	[m]

T_{static}	Static thrust	[N]
T_y	Torsional moment around the y-axis	[Nm]
U	Cell voltage	[V]
U	Tank coefficient of heat transfer	[W/K]
U_{de}	Gust velocity	[m/s]
V	Velocity	[m/s]
V	Volume	[m^3]
V_0	Air speed in front of propeller	[m/s]
V_e	Air speed after propeller	[m/s]
$V_{\text{centerlens}}$	Volume of single lens at meeting point	[m^3]
V_{centers}	Volume of all the lenses at meeting points	[m^3]
V_{cylinder}	Volume of single central hollow tube	[m^3]
$V_{\text{cylinders}}$	Volume of central hollow tubes	[m^3]
V_{fillet}	Follet volume of single sphere	[m^3]
V_{fillets}	Volume of the sphere fillets	[m^3]
V_{lenses}	Volume of all the intersected lenses	[m^3]
$V_{\text{lensjunction}}$	Volume of intersected sphere lenses	[m^3]
V_{spheres}	Complete sphere volume	[m^3]
$V_{climb_{1engine}}$	Climb speed one engine inoperative	[-]
V_h/V	Airflow velocity ratio of the tail over the wing	[-]
V_{max}	Maximum design speed	[kts]
V_{MC}	Minimum control speed	[m/s]
V_{S1}	Stall speed without flaps	[m/s^2]
V_x	Shear force in x-direction	[N]
v_x	Displacement in x-direction	[m]
V_z	Shear force in z-direction	[N]
v_z	Displacement in z-direction	[m]
VB	Design max gust intensity speed	[m/s^2]
VC	Design cruise speed	[m/s^2]
VD	Design dive speed	[m/s^2]
w	Width of base	[m]
W_{dg}	Design gross weight	[kg]
W_{ampr}	Aeronautical manufacturers planning report weight	[lbs]
W_{engine}	Engine weight	[N]
w_e	Effected skin width	[m]
W_{fus}	Fuselage weight distribution	[N/m]
$W_{s,i}$	Subsystem weight	[N]
w_{sk}	Skin width	[m]
W_{wing}	Wing weight distribution	[N/m]
$\bar{x_{ac}}$	The x-coordinate of the aerodynamic center	[-]
$\bar{x_{cg}}$	The x-coordinate of the center of gravity	[-]
x_c	Centroid x-coordinate	[m]
x_{el}	Elevator x-location	[m]
x_e	Engine x-location	[m]
x_{hld}	High-lift device x-location	[m]
x_i	Element x-coordinate	[m]
x_m	Step function activation value	[m]
y	Dimensionless centroid distance	[-]
y_e	Moment arm of the asymmetric thrust vector	[m]
y_{ail}	Aileron y location	[m]
y_{el}	Elevator y-location	[m]
y_e	Engine y-location	[m]
y_{hld}	High-lift device y-location	[m]
$y_{s,i}$	Subsystem y-location	[m]
z_c	Centroid z-coordinate	[m]
z_{el}	Elevator z-location	[m]
z_e	Engine z-location	[m]
z_{hld}	High-lift device z-location	[m]
z_h	Horizontal tail location	[m]
z_i	Element z-coordinate	[m]

Contents

1 Introduction

Aviation is a vital lifeline for island communities. In addition, many island nations have a great dependence on tourism. For some islands, over 50% of the GDP comes from tourism [1]. These tourists mostly arrive by plane; 90% of the visitors use air-travel to reach these islands. [2] However, air travel is a significant contributor to global warming and a source of air pollutants, such as nitrogen oxides and carbon dioxide; Aviation has a contribution of around 5 % to the global-warming effect [1, p.3528].

While aviation is vital for island communities, the rising sea levels caused by global warming heavily affect the livability of pacific islands, causing drink water shortages and crop failure [2]. For some islands it is already too late, they are deemed to disappear in the upcoming years. [3] The leaders of island nations luckily realize the severity of this problem and are currently forming coalitions to have a bigger voice in the global scene [3, p.206]. One of these coalitions is the Coalition of Low Lying Atoll Nations, consisting of countries such as the Maldives and Tuvalu. This coalition sees itself as an early warning system for the world; what happens to them now, will later on happen to the rest of the world. This coalition has ambitious targets for the world; they try to get the world to match the rate of solutions with the climate change impacts felt at their nations[4].

Sustainable aviation could be of big importance in the coming years to reduce the effects of climate change, while still keeping aviation unharmed. It was the objective of group 19 to design a fully electrically propelled climate neutral aircraft suitable for island-hopping operations: the H_2OPPER. This was done by a team of ten students within ten weeks.

This project consisted of multiple phases; the first phase consisted of defining the project structure, setting project objectives and defining the user needs. In the second phase, several design options were devised and a preliminary trade-off was performed to find the most promising designs. These designs have been worked out partially in the third phase to perform a more thorough trade-off. The winner of the trade-off was the hydrogen propelled aircraft with concentrated propulsion. This design was worked out in the best attainable level of detail in the given time frame.

The aim of the report is to show the results found during the final phase of the project; the conceptual design of the H_2OPPER with its expected performance, risks, and compliance to regulations. In addition, the ground operations, finances and future activities for the aircraft have been investigated.

The report first elaborates on the functions and requirements of the H_2OPPER in Chapter 2. After this, the sustainability approach of the project is restated. The devised green indicators are updated and their implementation in the design is discussed in Chapter 3. The expected market performance and unique selling point of the H_2OPPER are re-evaluated in Chapter 4.

The following chapters discuss various parts of the aircraft, the first of which is the structure. This entails sizing the structure for the loads acting on the aircraft and making sure that all the components and payload can be accommodated. An important part is the selection of the structure materials, as it has a great

[1] URL: https://www.statista.com/statistics/789517/caribbean-direct-contribution-travel-tourism-gdp-country/#:~:text=Caribbean. [Accessed on: 16-6-2021]

[2] URL:https://unitingaviation.com/news/economic-development/aviation-benefits-for-a-better-future [Accessed on: 16-6-2021]

[3] URL: https://www.theguardian.com/global-development/2019/may/16/one-day-disappear-tuvalu-sinking-islands-rising-seas-climate-change [Accessed on: 16-6-2021]

[4] URL: https://www.sprep.org/news/coalition-low-lying-atoll-nations-climate-change-cancc-known-global-early-warning-system [Accessed on: 16-6-2021]

influence on the weight, strength and recyclability of the H_2OPPER. The structure is discussed in Chapter 5.

Next, the wing design is discussed in Chapter 6. This part involves the sizing of the high lift devices and the aileron. After this, in Chapter 7 the stability and controllability of the aircraft and the resulting sizing of the empennage, including the control surfaces are discussed. The resulting aerodynamic characteristics of the aircraft are discussed in Chapter 8.

The design of the energy and power subsystems is detailed in Chapter 9 - 12 . First, the power needs for a flight mission are calculated. Next, the fuel cell system is given with the corresponding accessory subsystems. In Chapter 11, the other systems of the aircraft are examined. Hardware and software diagrams are shown and a power budget is given. At last, the hydrogen fuel tank is investigated.

The verification and validation of all the design tools is discussed in Chapter 13. The ground operations, focusing on the hydrogen challenges, are outlined in Chapter 14. After this, the financial performance, including a breakdown of the cost and return of investment, is discussed in Chapter 15. The final design is presented in Chapter 16. In this chapter also the sensitivity of the design and the compliance to the requirements are evaluated. The risk and RAMS characteristics are described in Chapter 17 and 18, respectively. The next steps in the design process are discussed and summarized in a workflow diagram and a Gantt chart in Chapter 19. Lastly, this project is concluded in Chapter 20.

2
Aircraft Functions and Requirements

This chapter describes the functional requirements of the designed aircraft. A functional analysis was performed to identify all the required functions. This was displayed in functional breakdown structure and functional flow diagram.

2.1. Functions

With the use of a functional breakdown structure in combination with a functional flow diagram, presented on page 4 and page 5 respectively, the required functions were assessed. The life cycle consist of five main phases namely: design, certification, production, operation and retirement. To identify requirements, the operation phase was worked out in more detail then the other phases. This is the reason why the other phases are not labeled, since these are not part of the functional breakdown structure.

"The operational part is divided in three main categories, which are: normal flight, abnormal flight and support. Normal flight is the normal sequence of flight operations the aircraft will have to do repetitively throughout. Abnormal flight on the other hand are unexpected events that can occur that the aircraft will still have to be able to perform, like for example fire emergency procedures or flying in bad weather. Lastly, support is focused on the maintenance of the aircraft and other logistics that will have to be done in order to keep the aircraft perform its mission."[4].

2.2. Requirements

The user requirements of the H_2OPPER, also referred to as the top-level requirements, are as follows:

HOPPER-U-P.1	The maximum range shall be 300 [NM], with regulatory reserves
HOPPER-U-P.2	The maximum payload shall be 19 passengers
HOPPER-U-P.3	The aircraft shall be able to operate out of a 400 [m] runway
HOPPER-U-P.4	The cruise speed shall be 175 [kts]
HOPPER-U-SR.1	The aircraft shall comply with CS-23 regulations
HOPPER-U-S.1	The aircraft structure shall be 90% recyclable
HOPPER-U-S.2	The propulsion system shall be climate neutral
HOPPER-U-EB.1	The MTOW shall be no greater than 19,000 [lbs]
HOPPER-U-EB.2	The aircraft shall be able to perform 3 maximum range flights a day, with a maximum 1 [hr] turnaround time between flights
HOPPER-U-EB.3	The aircraft shall have a range of 200 [NM], with maximum payload
HOPPER-U-C.1	The list price shall be no more than 10 million [USD]
HOPPER-U-C.2	The operating cost shall be no more than 10% higher than current aircraft

From these requirements, a stakeholder analysis, an functional analysis of the aircraft and CS-23, system and subsystem level requirements were derived. These are stated at the start of each section.

Concerning the identifiers of the requirements, most requirements either contain an U (user requirement), a T (technical requirement), or a C (constraint). Furthermore, the terms in Table 2.1 indicate the subsystem of the requirements. Finally, the term CS indicates the requirement follows from CS-23.

Table 2.1: Subsystem suffixes

Pr	Propulsion	Cm	Communications	Sr	Structures
Lg	Landing gear	Av	Avionics	Cf	Comfortability
Fc	Flight control	Fs	Fuel system		

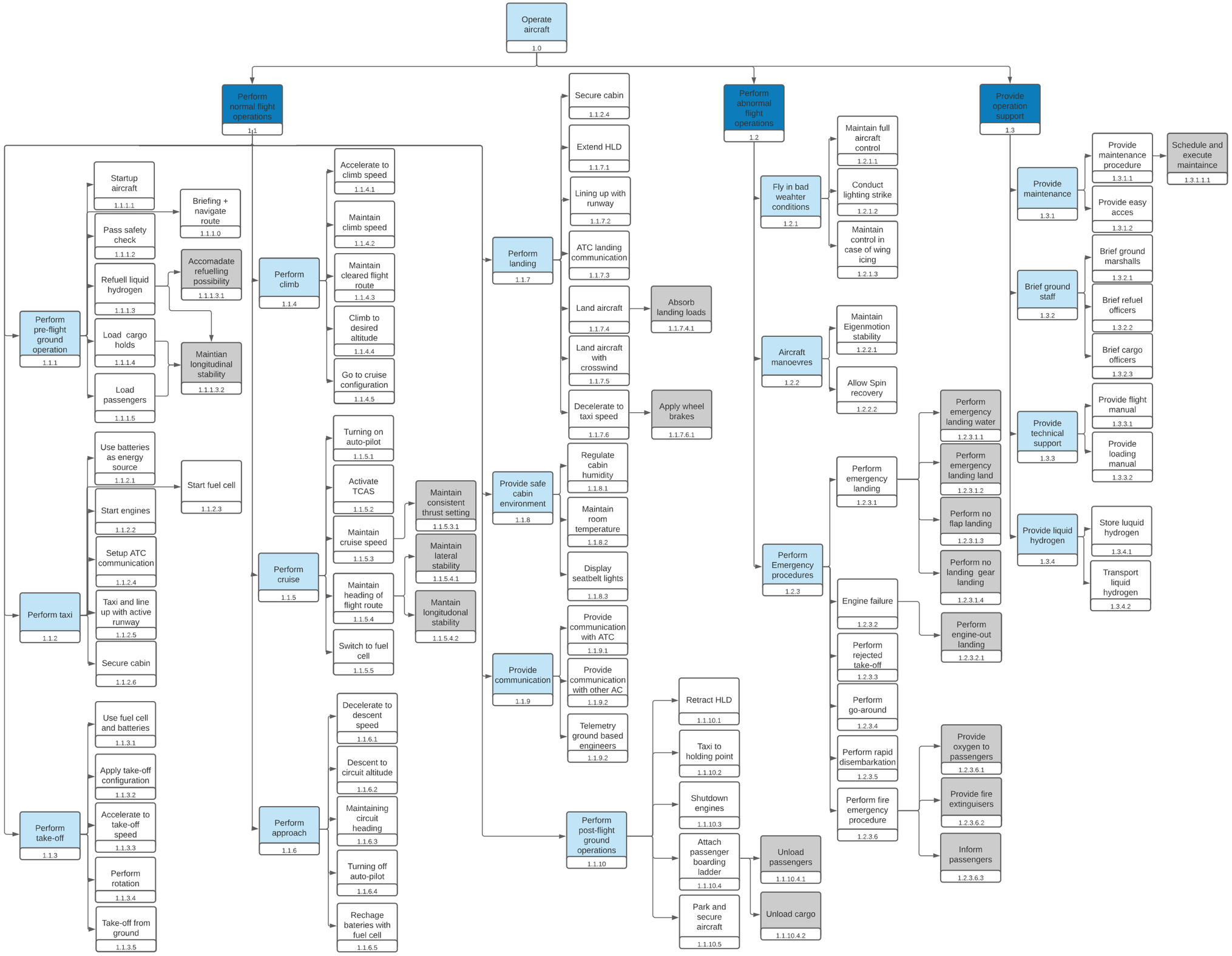
Operate aircraft
1.0
Perform normal flight operations
1.1
Perform abnormal flight operations
1.2
Provide operation support
1.3
Perform pre-flight ground operation
1.1.1
Startup aircraft
1.1.1.1
Briefing + navigate route
1.1.1.0
Pass safety check
1.1.1.2
Refuell liquid hydrogen
1.1.1.3
Accomadate refuelling possibility
1.1.1.3.1
Load cargo holds
1.1.1.4
Maintian longitudinal stability
1.1.1.3.2
Load passengers
1.1.1.5
Perform taxi
1.1.2
Use batteries as energy source
1.1.2.1
Start fuel cell
1.1.2.3
Start engines
1.1.2.2
Setup ATC communication
1.1.2.4
Taxi and line up with active runway
1.1.2.5
Secure cabin
1.1.2.6
Perform take-off
1.1.3
Use fuel cell and batteries
1.1.3.1
Apply take-off configuration
1.1.3.2
Accelerate to take-off speed
1.1.3.3
Perform rotation
1.1.3.4
Take-off from ground
1.1.3.5
Perform climb
1.1.4
Accelerate to climb speed
1.1.4.1
Maintain climb speed
1.1.4.2
Maintain cleared flight route
1.1.4.3
Climb to desired altitude
1.1.4.4
Go to cruise configuration
1.1.4.5
Perform cruise
1.1.5
Turning on auto-pilot
1.1.5.1
Activate TCAS
1.1.5.2
Maintain cruise speed
1.1.5.3
Maintain consistent thrust setting
1.1.5.3.1
Maintain heading of flight route
1.1.5.4
Maintain lateral stability
1.1.5.4.1
Mantain longitudonal stability
1.1.5.4.2
Switch to fuel cell
1.1.5.5
Perform approach
1.1.6
Decelerate to descent speed
1.1.6.1
Descent to circuit altitude
1.1.6.2
Maintaining circuit heading
1.1.6.3
Turning off auto-pilot
1.1.6.4
Rechage bateries with fuel cell
1.1.6.5
Perform landing
1.1.7
Secure cabin
1.1.2.4
Extend HLD
1.1.7.1
Lining up with runway
1.1.7.2
ATC landing communication
1.1.7.3
Land aircraft
1.1.7.4
Absorb landing loads
1.1.7.4.1
Land aircraft with crosswind
1.1.7.5
Decelerate to taxi speed
1.1.7.6
Apply wheel brakes
1.1.7.6.1
Regulate
Provide safe cabin environment
1.1.8
Regulate cabin humidity
1.1.8.1
Maintain room temperature
1.1.8.2
Display seatbelt lights
1.1.8.3
Provide communication
1.1.9
Provide communication with ATC
1.1.9.1
Provide communication with other AC
1.1.9.2
Telemetry ground based engineers
1.1.9.2
Perform post-flight ground operations
1.1.10
Retract HLD
1.1.10.1
Taxi to holding point
1.1.10.2
Shutdown engines
1.1.10.3
Attach passenger boarding ladder
1.1.10.4
Park and secure aircraft
1.1.10.5
Unload passengers
1.1.10.4.1
Unload cargo
1.1.10.4.2
Fly in bad weahter conditions
1.2.1
Maintain full aircraft control
1.2.1.1
Conduct lighting strike
1.2.1.2
Maintain control in case of wing icing
1.2.1.3
Aircraft manoevres
1.2.2
Maintain Eigenmotion stability
1.2.2.1
Allow Spin recovery
1.2.2.2
Perform Emergency procedures
1.2.3
Perform emergency landing
1.2.3.1
Perform emergency landing water
1.2.3.1.1
Perform emergency landing land
1.2.3.1.2
Perform no flap landing
1.2.3.1.3
Perform no landing gear landing
1.2.3.1.4
Engine failure
1.2.3.2
Perform engine-out landing
1.2.3.2.1
Perform rejected take-off
1.2.3.3
Perform go-around
1.2.3.4
Perform rapid disembarkation
1.2.3.5
Perform fire emergency procedure
1.2.3.6
Provide oxygen to passengers
1.2.3.6.1
Provide fire extinguisers
1.2.3.6.2
Inform passengers
1.2.3.6.3
Provide maintenance
1.3.1
Provide maintenance procedure
1.3.1.1
Schedule and execute maintaince
1.3.1.1.1
Provide easy acces
1.3.1.2
Brief ground staff
1.3.2
Brief ground marshalls
1.3.2.1
Brief refuel officers
1.3.2.2
Brief cargo officers
1.3.2.3
Provide technical support
1.3.3
Provide flight manual
1.3.3.1
Provide loading manual
1.3.3.2
Provide liquid hydrogen
1.3.4
Store luquid hydrogen
1.3.4.1
Transport liquid hydrogen
1.3.4.2

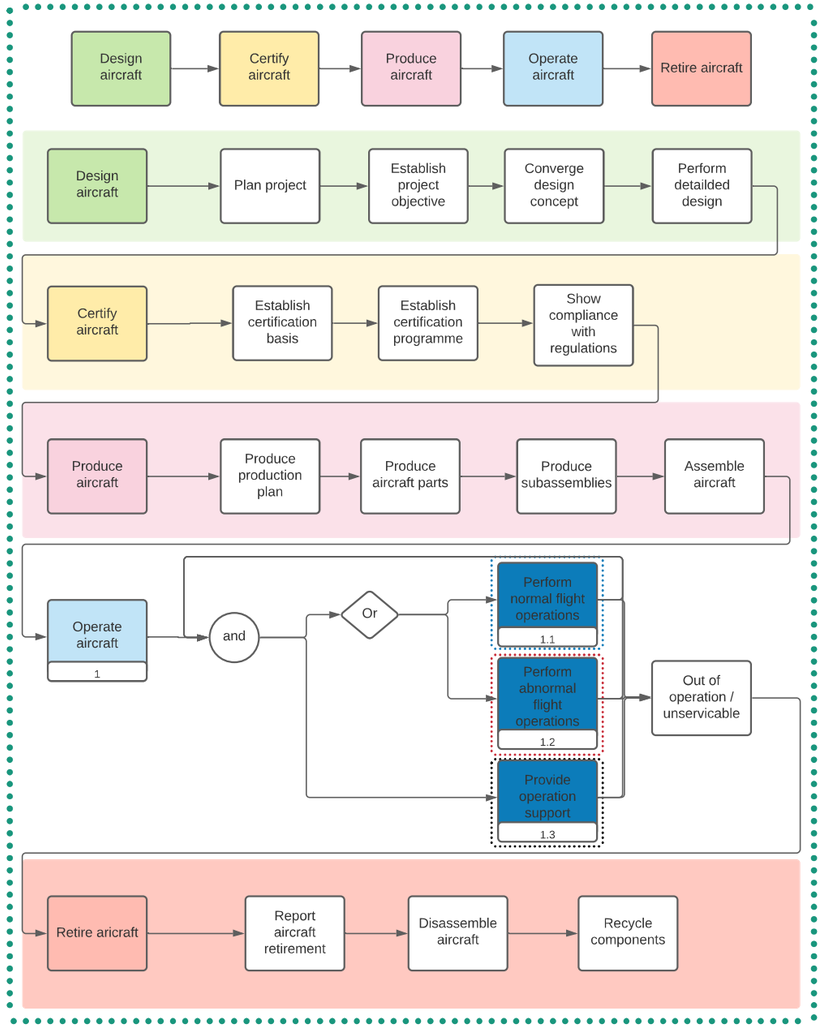
Design aircraft
Certify aircraft
Produce aircraft
Operate aircraft
Retire aircraft
Design aircraft
Plan project
Establish project objective
Converge design concept
Perform detailded design
Certify aircraft
Establish certification basis
Establish certification programme
Show compliance with regulations
Produce aircraft
Produce production plan
Produce aircraft parts
Produce subassemblies
Assemble aircraft
Operate aircraft
1
and
Or
Perform normal flight operations
1.1
Perform abnormal flight operations
1.2
Provide operation support
1.3
Out of operation / unservicable
Retire aricraft
Report aircraft retirement
Disassemble aircraft
Recycle components

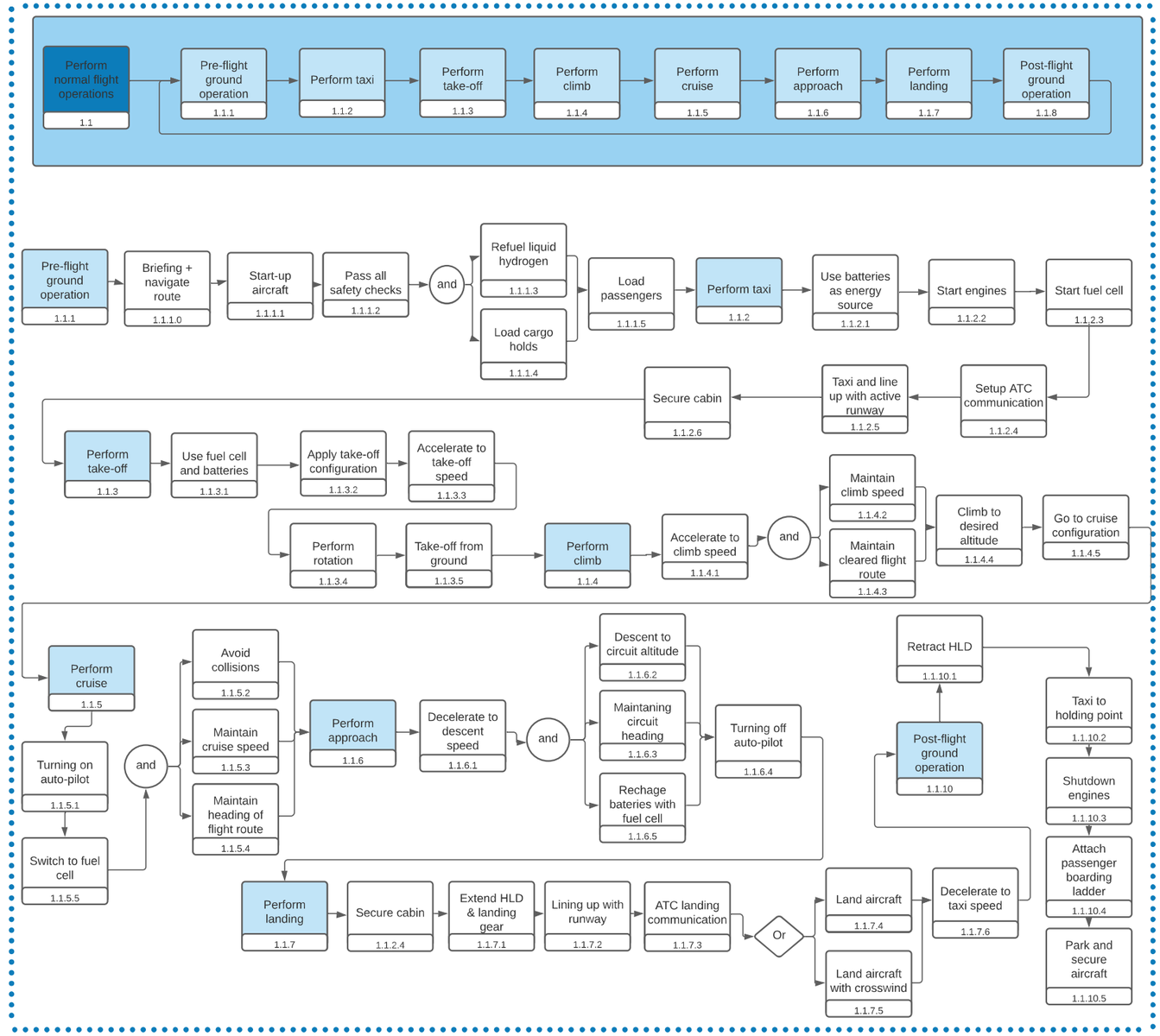
Perform normal flight operations
1.1
Pre-flight ground operation
1.1.1
Perform taxi
1.1.2
Perform take-off
1.1.3
Perform climb
1.1.4
Perform cruise
1.1.5
Perform approach
1.1.6
Perform landing
1.1.7
Post-flight ground operation
1.1.8
Briefing + navigate route
1.1.1.0
Start-up aircraft
1.1.1.1
Pass all safety checks
1.1.1.2
and
Refuel liquid hydrogen
1.1.1.3
Load cargo holds
1.1.1.4
Load passengers
1.1.1.5
Use batteries as energy source
1.1.2.1
Start engines
1.1.2.2
Start fuel cell
1.1.2.3
Setup ATC communication
1.1.2.4
Taxi and line up with active runway
1.1.2.5
Secure cabin
1.1.2.6
Use fuel cell and batteries
1.1.3.1
Apply take-off configuration
1.1.3.2
Accelerate to take-off speed
1.1.3.3
Perform rotation
1.1.3.4
Take-off from ground
1.1.3.5
Accelerate to climb speed
1.1.4.1
Maintain climb speed
1.1.4.2
Maintain cleared flight route
1.1.4.3
Climb to desired altitude
1.1.4.4
Go to cruise configuration
1.1.4.5
Avoid collisions
1.1.5.2
Maintain cruise speed
1.1.5.3
Maintain heading of flight route
1.1.5.4
Turning on auto-pilot
1.1.5.1
Switch to fuel cell
1.1.5.5
Descent to circuit altitude
1.1.6.2
Maintaning circuit heading
1.1.6.3
Rechage bateries with fuel cell
1.1.6.5
Decelerate to descent speed
1.1.6.1
Turning off auto-pilot
1.1.6.4
Retract HLD
1.1.10.1
Post-flight ground operation
1.1.10
Taxi to holding point
1.1.10.2
Shutdown engines
1.1.10.3
Attach passenger boarding ladder
1.1.10.4
Park and secure aircraft
1.1.10.5
Extend HLD & landing gear
1.1.7.1
Lining up with runway
1.1.7.2
ATC landing communication
1.1.7.3
Land aircraft
1.1.7.4
Land aircraft with crosswind
1.1.7.5
Decelerate to taxi speed
1.1.7.6

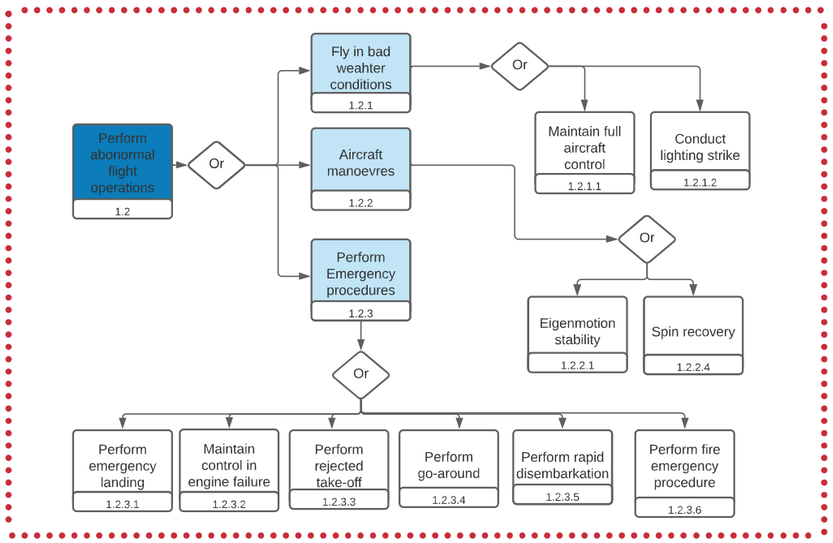
Perform abonormal flight operations
1.2
Or
Fly in bad weahter conditions
1.2.1
Aircraft manoevres
1.2.2
Perform Emergency procedures
1.2.3
Maintain full aircraft control
1.2.1.1
Conduct lighting strike
1.2.1.2
Eigenmotion stability
1.2.2.1
Spin recovery
1.2.2.4
Perform emergency landing
1.2.3.1
Maintain control in engine failure
1.2.3.2
Perform rejected take-off
1.2.3.3
Perform go-around
1.2.3.4
Perform rapid disembarkation
1.2.3.5
Perform fire emergency procedure
1.2.3.6

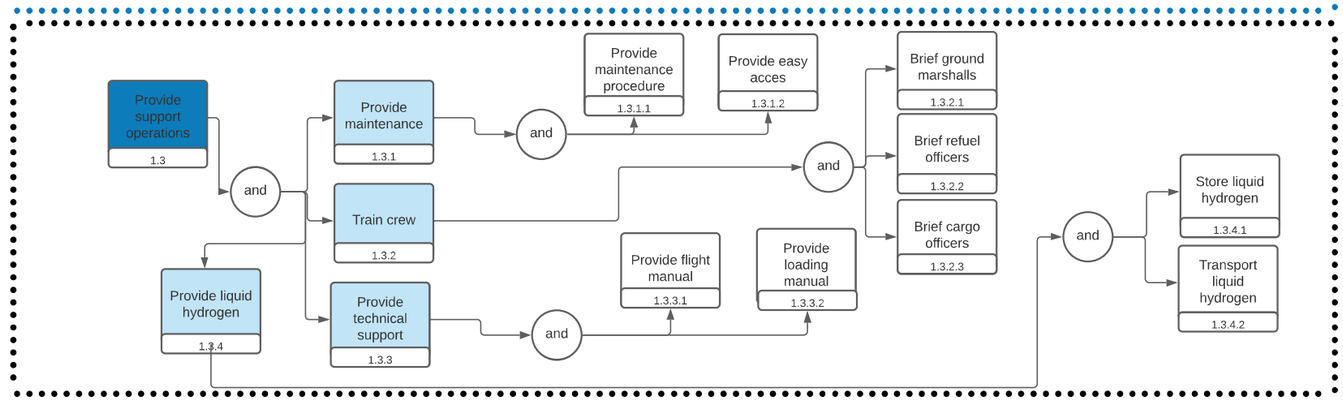
Provide support operations
1.3
and
Provide maintenance
1.3.1
Train crew
1.3.2
Provide technical support
1.3.3
Provide liquid hydrogen
1.3.4
Provide maintenance procedure
1.3.1.1
Provide easy acces
1.3.1.2
Provide flight manual
1.3.3.1
Provide loading manual
1.3.3.2
Brief ground marshalls
1.3.2.1
Brief refuel officers
1.3.2.2
Brief cargo officers
1.3.2.3
Store liquid hydrogen
1.3.4.1
Transport liquid hydrogen
1.3.4.2

3
Green Policy

In this chapter, the sustainability approach of the H_2OPPER is handled. First, in Section 3.1, the past endeavors are summarized, where the original indicators are addressed. Then, in Section 3.2, the indicators are refined to make them fit the current conceptual design phase, such that they could be applied in an optimal way. Section 3.3 focuses on the implementation of the indicators and overall green policy. Finally, Section 3.4 gives an evaluation of the green policy.

3.1. Policy Synopsis

With sustainability being of such paramount importance in this project, the need for a sustainable development strategy arose. In the starting phase of this project, such a strategy was formulated in the form of a Green policy. This policy aimed at ensuring that the final design was going to meet the HOPPER-U-S.1 and HOPPER-U-S.2 requirements concerning sustainability.

Due to the deep-rooted aspect of sustainability, it was necessary to set a domain for the policy. A choice was made that for the preliminary design phase, the Green policy was limited to the aircraft operating phase only. As the relatively long aircraft operating phase was considered to have a far larger environmental impact than any other life cycle phase. This argument was supported by the preliminary results from the "Air Transport Vehicle Life Cycle Analysis (ATLA)" [5] [6]. To account for the recyclability requirement, the End of Life (EoL) phase was also included in the policy domain but was limited to just the recyclability aspect.

In this domain, the objective of the policy was to design for climate-neutral flight. Where climate-neutrality is achieved when all aircraft activities result in no net effect on the climate system [7]. This was considered to be achievable since the expected flight altitude of 10,000 [ft] is low enough that no contrail formation would occur [8] and due to electric propulsion sources not having direct greenhouse gas (GHG) emissions.

When the domain and objective were set, four Green indicators were created to either quantitatively or qualitatively judge the performance of certain aspects of the concept with respect to the relevant sustainability requirements. These indicators will be briefly discussed below but can be found in more detail in [4].

- *IND-GP-01: Efficiency*, a quantitative indicator that evaluates the system level efficiency of the design.
- *IND-GP-02: Total greenhouse gas emissions*, a qualitative indicator concerning the emission of greenhouse gasses of the design.
- IND-GP-03: *NO_x emission in landing and take-off*, a qualitative indicator regarding the overall production of NO_x during the landing and take-off phases.
- *IND-GP-04: Material recyclability*, a quantitative indicator that assesses the total recylability of a material by comparing energy consumption of virgin production and recycling.

To ensure that the final design would actually end up meeting the policy objective, extensive monitoring on the proper adaption of the indicators was performed by the sustainability managers. This was achieved by assessing the correctness of the indicator calculations and checking whether these indicators have been sufficiently used as guideline during design choices. When a design failed to comply with any of the minimum set values of the indicators, the design was not approved and appropriate measures were taken to make sure that the design complied with those minimum values. This consisted of changing the design and re-iterating it until the requirements were met.

3.2. Indicator Refinement

During the conceptual design process, some complications concerning the Green policy and its indicators were discovered. While the indicators themselves were not inherently incorrect, it was found that the recyclability indicator could not be used as originally intended as the formula was not yet usable due to the materials being still largely unknown. Furthermore, the NO_x emission in landing and take-off could not be estimated in the preliminary design phase. Even though the indicators were still relevant as guidelines, they fell more towards the background instead of actively being used in the design process.

The selection of a concept allows for more refined and specific indicators with respect to the concept characteristics. To make the indicators more relevant and applicable, the upcoming design tasks and their corresponding design parameters were inventoried. Using these parameters, the indicators were adjusted to match the design process.

- *IND-GP-01: Energy efficiency*
  As can be seen in Equation 3.1, the efficiency indicator is re-evaluated and re-determined completely. The indicator now displays the trade-off between C_L over C_D, the added/removed weight, and total efficiency. This trade-off is relevant for every subsystem and part imaginable. For example take the cooling system; if a certain cooling system has an increased efficiency which comes with a disadvantage of added weight, a choice must be made whether the increased efficiency justifies the added weight and decreases total energy usage. This choice can be evaluated using the indicator. The same question can be asked for a wing: does a certain increased C_L over C_D compensate for possible added wing weight?

  $$GI_1 = \frac{C_L}{C_D} \cdot \frac{1}{W + \Delta W \cdot G} \cdot \eta_{total} \tag{3.1}$$

  Where Δ W is the initial weight saving and G is the mass growth factor. η_{total} is the total efficiency, which is the product of propeller efficiency, Power management and distribution efficiency, fuel cell efficiency and electrical system efficiency. In order to make a quick estimation of this weight gain factor, a tool from JS Cheema [9] was adopted. This tool relies on the operational empty weight fraction and the fuel weight fraction staying constant for a change in mass, allowing for a quick iteration. It must be noted that this tool is more suited for conventional kerosene aircraft since a hydrogen aircraft would have a significantly lower fuel weight fraction, with a possible excessive growth factor. However, when more accurate estimations of the weights are unavailable in the earlier phases of the preliminary design phase, this tool would function as an acceptable estimate.

  The drag coefficient in Equation 3.1 can be calculated using:

  $$C_D = C_{D_0} + \frac{C_{L_{cruise}}^2}{\pi \cdot A \cdot e} \tag{3.2}$$

  Where C_{D_0} is the zero lift drag, A the aspect ratio and e the Oswald efficiency.

  The tool uses wing, tail, fuselage and landing gear as drag-producing subsystems. Wing, tail and fuselage are the only lift-producing elements. For induced drag, only the wing and tail are considered as the influence of the fuselage is negligible [10, p.12]. Preliminary coefficient estimates are taken from literature [11, p.418], and surfaces are sized using the L 410 NG as reference aircraft [1] [2].

  It should be noted that using this approach calculations are simplified, but it is deemed acceptable since it is used in a trade-off and it is not the final analysis.

- *IND-GP-02: GHG for H_2 production and logistics*
  As a hydrogen-powered concept was chosen, the GHG indicator is no longer relevant for the entire domain of the policy. Instead, the indicator was now focused on the production of hydrogen and the logistics that came with the use of liquid hydrogen. The production and storage of hydrogen is as of yet still not without GHG emissions in most cases [12]. For the operations and logistics of this project,

[1] URL: `http://www.let.cz/documents/L410NG.pdf` [Accessed on: 01-06-2021]
[2] URL: `https://web.archive.org/web/20190423024417/http://www.let.cz/files/file/KeStazeni/2016/EN_Brochure_L410_UVP-E20.pdf` [Accessed on: 01-06-2021]

the methods of producing green hydrogen and consequently its storage and transportation are investigated thoroughly. Where GHG emissions are inevitable, an additional GHG emission recapture method should be researched and implemented.

- *IND-GP-03: NO_x emission in landing and take-off*
  While NO_x is not officially a GHG, it plays an important role in the destruction of ozone in the atmosphere [13]. Hence, a net emission of NO_x will make the concept fail to meet the climate neutral requirement. As it is known that hydrogen will be used as a fuel, NO_x emissions are not expected. However, since the hydrogen will react with air and not pure oxygen, NO_x theoretically could still occur in the case of incomplete combustion [3]. Therefore, this is an important indicator that should be investigated during the design of the fuel cells.

- *IND-GP-04 Recyclability*
  Equation 3.3 shows the improved recyclability indicator. It was chosen to exclude the scarcity index from the equation as, except for metals of batteries, there are no common aerospace materials on the element risk list [4]. Next to that, the operative empty weight was omitted from the equation as it is already included in the weight part of the energy efficiency indicator.

  To let the indicator calculate the actual energy needed to reproduce a certain design option, the non-recyclable material part is multiplied by the embodied energy for primary production, and the recyclable material part is multiplied by the embodied energy for recycling. Additionally, it was decided to include the recycle fraction from current supply, i.e. the fraction of the material that is already recycled in the current supply, which is included as a factor that is multiplied by the entire equation. This factor is the total embodied energy including the percentage of recycled materials and its embodied energy divided by total embodied energy for virgin material. The indicator is, therefore, a direct indication of the energy required for producing a particular part or subsystem.

$$GI_4 = \sum_{i=1}^{i=n} m_i \cdot (RC_i \cdot E_{rc_i} + (1 - RC_i) \cdot E_{vir_i}) \cdot \left(1 + \left(\frac{E_{rc_i}}{E_{vir_i}} - 1\right) \cdot RECD_i\right) \tag{3.3}$$

  In the formula above, RC_i is the fraction of material i that can be recycled, E_{rc_i} is the energy required to recycle material i and E_{vir_i} is the required energy for virgin production of material i, both in Joule. Lastly, $RECD_i$ is the fraction of material i that is already recycled. The value of the parameters above was taken from literature such as Ashby [14].

- *IND-GP-05: Noise level*
  Now, a new indicator is added regarding noise levels. In the Baseline Report and Midterm Report, there were already calculations done regarding noise levels of the aircraft. However, it was noted that the noise should be a sustainability matter as noise pollution has an enormous environmental impact [15]. Therefore, it is chosen to make the noise level an indicator in the Green policy. The noise level is computed using Equation 3.4 [16].

$$SPL_{max} = 83.4 + 15.3 \log_{10} P_{br}/1000 - 20 \log_{10} D_p + 38.5 M_t - 3(B-2) + 10 \log_{10} N - 20 \log_{10} r \tag{3.4}$$

  In the equation above, D_p is the propeller diameter, N is the number of propellers, B is the number of blades per propeller and P_{br} is the engine shaft power. The distance from propeller noise source r is assumed to be 75 [m], which is the distance from the ground after flying 2500 [m] at the minimum climb gradient as depicted by CS-23. This is the same method as the ICAO regulations use. Finally, M_t is the rotational tip Mach number, which is determined using Equation 3.5; where n_{rpm} is the revolutions per minute of the propeller and c is the speed of sound [16].

$$M_t = \frac{n_{rpm} \cdot \pi \cdot D_p}{60 \cdot c} \tag{3.5}$$

[3] URL: https://www.thechemicalengineer.com/features/hydrogen-the-burning-question/ [Accessed on: 29-06-2021]
[4] URL: https://www2.bgs.ac.uk/mineralsuk/download/statistics/risk_list_2015.pdf [Accessed on: 01-06-2021]

3.3. Implementation

To support the more active role of these new parameters, a more structured approach concerning their implementation was needed. Hence a tool was created that would calculate the efficiency, recyclability and noise indicators instantaneously. Each department could fill in the parameters of two corresponding design options. The tool would then present the performance of the three quantitative indicators for both design options and how they compare to each other. This allowed the indicators to support different departments in making design choices. For example, the tool was key in the decisions regarding the material choice for the fuselage using the IND-GP-04 indicator and the wingtip mounted engine placement was based on the IND-GP-01 indicator.

To ensure consistent use of the latest design parameters, a dedicated place in the design N2 chart was made. This would function as a central place for the most recent values for all different design aspects. In this N2 chart all parameters related to the Green indicators were displayed in green to clarify dependencies and further encourage departments to make use of the tool.

Furthermore, this tool added consistency concerning the indicator formula usage, meaning that the sustainability managers had to do less monitoring on the calculation correctness and were able to spend more time working in their own technical department. However, the sustainability managers still needed to verify that the departments did indeed use the tool for decisions and major design choices still needed to be agreed upon by the sustainability managers.

Finally, the qualitative indicators that were not suited for the tool functioned more as boundaries for certain design choices and limited the designer to stay within the climate neutral domain. The responsible departments contacted the sustainability managers about whether they experienced any trouble in meeting these requirements and possible mitigation options were discussed.

3.4. Evaluation

Now, onto the actual results and evaluation of the green policy. Perhaps the greatest success of the quantifiable indicators is the fact that engineers from each department were actively working on the sustainability aspects of their specific department and design parts. It was seen throughout the design that all the departments were actively working on the green indicators and were overall using the green policy. Because of that, the goal of realizing climate neutral flight is achieved. Next to that, the Hopper surpassed the 90% recyclability requirement. Thanks to the efforts of the structures department in combination with the recyclability indicator, a structural recyclability percentage of 98% percent was reached. It can therefore be said that the green indicators had a significant positive influence in correctly implementing sustainability into the H_2OPPER, and that the green policy was an overall success.

4
Market Analysis

This chapter gives a quick recap about the current market and competitors in Section 4.1. Then in Section 4.2, the performance of the H_2OPPER is updated and revised. Finally, in Section 4.3, the unique selling point of the H_2OPPER is revised to fit to the updated aircraft performance.

The current study adds to this literature by showing that more reductions in greenhouse gases increase willingness to pay an additional ticket price. This was somewhat limited in the 15% ticket price increase condition, particularly for long-haul flights.

4.1. Current Market and Competitors

Currently, despite growing efforts in reducing the climate impact of flight, there is no existent market segment for climate neutral aircraft. This results in a loss in customers as more people decide to avoid air travel due to a significant contribution to global warming. This problem would be tackled when the contribution to global warming would be reduced significantly. Research shows that air travelers are even willing to pay a 15% increase in price for a 50% reduction of greenhouse gas emission [17]. Therefore, the loss in customers is non-existent when no GHG are emitted; moreover, customers are willing to pay more for reduced GHG emissions, increasing revenue for airlines. An aircraft that does not have any climate impact is thus desired to increase the customer base and could even increase the ticket price. This is exactly what the aim of the H_2OPPER is: to bring a competitive climate neutral aircraft on the market and thereby increasing the climate neutral market share in the aviation industry.

In the already executed market analysis, several competitor aircraft were compared to the expected performance of the H_2OPPER [4]. In this analysis, the H_2OPPER was compared to both conventional kerosene burning aircraft (DHC-6 Twin Otter-400 and the Beechcraft 1900D), as well as to a climate neutral aircraft, the battery-powered ES-19. The analysis showed that the overall performance of the H_2OPPER is comparable to that of the two conventional aircraft. When compared to the ES-19, it came forward that the H_2OPPER excelled in range performance and was able to cope with a similar runway length.

Table 4.1: Competition analysis

	H_2OPPER	**Beech 1900D**	**DHC-6 Twin**	**L 410 NG**	**ES-19**
Passengers [-]	19	19	19	19	19
Payload [lbs]	4000	4210	4061	5071	-
Ferry range [NM]	1177	1356	989	1387	216
Min. runway length [m]	750	1058	366	600	750
List price [$]	$10M	$7.5M	$5.9M	$7.8M	-
MTOW [lbs]	19,000	17120	12500	15432	-
Cruise speed [knots]	175	250	175	225	180
Operational cost per hour [€]	1250	1158	837	-	-

4.2. Performance Re-evaluation

The performance parameters in the Baseline Report were determined in a very preliminary design phase. Therefore, to make a more relevant performance comparison possible, the parameters were updated according to final performance results. The ultimate performance of the H_2OPPER is shown in Table 4.1. Note

that since the Baseline Report, the Aircraft Industries L 410 NG was added to the competing kerosene aircraft, as after the Baseline it was added as reference aircraft. The values of all the aircraft can be found in Table 4.1[1][2][3][4].

As can be noted from Table 4.1, the final performance of the H_2OPPER aircraft is comparable to the conventional kerosene aircraft. It is even more interesting to compare the H_2OPPER to the other climate neutral aircraft, the ES-19.

As there is limited data known about the ES-19, only four parameters can be compared: passengers, minimum runway length, cruise speed and range. The minimum required runway length and the number of passengers is equal for both aircraft. Regarding the cruise speed, the ES-19 has a slightly higher cruise speed then the H_2OPPER. This is a minor competitive advantage for the ES-19. The range of the H_2OPPER is far superior to that of the ES-19. The range of 1177 [NM] can be achieved without payload, while with max payload a range of over 321 [NM] can be realized. The benefit of liquid hydrogen is visible when a small reduction in the payload is replaced with liquid hydrogen. Reducing the boarded passengers from 19 to 17 results in a range increase of 679 [NM] adding up to a total of 1000 [NM]. This increases the flight routes in which the H_2OPPER can operate, and thus a larger competitive advantage is realized.

For the operational cost, the H_2OPPER will be compared with conventional aircraft as no direct comparison could be made with the ES-19. It was found that there will be a small increase of 5 to 10 % in operational cost for the H_2OPPER, mainly determined by the fuel cost and maintenance.

4.3. Unique Selling Point

In the baseline report, the unique selling point of the H_2OPPER is to be a "climate neutral aircraft with superior range compared to another climate neutral aircraft, in addition, it should be able to cope with a shorter runway to take-off and land" [4, p.11]. As presented in Table 4.1, the designed H_2opper has a ferry range of 1177 [NM] and range of 321 [NM] with maximum payload. This outscores the range of the ES-19 by a good amount and in combination with being climate neutral and has a short take-off distance, the H_2opper will therefore obtain a competitive position in the current market.

[1] http://www.aero-news.net/index.cfm?do=main.textpost&id=732cbc6e-a18e-4523-b985-cedc2277d071 [Accessed: 23-04-2021]

[2] https://heartaerospace.com/ [Accessed: 23-04-2021]

[3] https://www.vikingair.com/sites/default/files/Viking-Twin-Otter-Series-400-Technical-Specifications-R-01-2018.pdf [Accessed: 23-04-2021]

[4] https://let.cz/documents/L410NG.pdf [Accessed: 23-04-2021]

5
Structures

This chapter discusses the structural design of the aircraft, focusing on the preliminary sizing of the wingbox, empennage and fuselage for manoeuvre and gust loading conditions. In Section 5.1 the functions and requirements of the aircraft structure are given. After this, the layout of the fuselage is shown in Section 5.3. The structural layout of the wingbox, empennage and fuselage are given in Section 5.4. An analysis of the design loads is given in Section 5.2. The design tool, used to optimize the structure, is elaborated in Section 5.5. The landing gear design is discussed in Section 5.6. Lastly, the material selection is motivated in Section 5.7.

5.1. Subsystem Overview

The subsystem overview shows the functions and requirement of the main structural components of the aircraft, namely the fuselage, wingbox, empennage and landing gear.

5.1.1. Functions

The function of the aircraft structure is to transfer all the aerodynamic and weight forces of the aircraft. Additionally, enough space needs to be provided for all the aircraft subsystems and the payload. The main objective of the structural design is to achieve the lowest possible weight, and at the same time handle the most extreme load cases.

5.1.2. Requirements

HOPPER-C-R-SR-4	The aircraft shall be able to withstand positive loads up to the ultimate load factor of 5.1
HOPPER-C-R-SR-5	The aircraft shall be able to withstand negative loads up to the ultimate load factor of -1.52
HOPPER-C-R-SR-6	The aircraft shall not tip during normal loading conditions when resting on its landing gear
HOPPER-C-R-SR-11:	The aircraft wings shall not bend upwards by more than 1 [m] during the entire mission
HOPPER-C-R-SR-12:	The aircraft wings shall not bend downwards by more than 0.5 [m] during the entire mission
HOPPER-C-CF-1:	The passenger seat shall be at least 0.41 [m] wide
HOPPER-C-CF-2:	The passenger seat shall have armrests of at least 0.04 [m]
HOPPER-C-CF-5:	The passenger seats shall have a pitch of 0.762 [m]
HOPPER-C-CF-6:	The aisle shall have a height of at least 1.66 [m] and width of 0.38 [m]
HOPPER-C-CF-7:	The aircraft shall provide space under each passenger seat for hand luggage with maximal dimensions of 40 x 30 x 20 [cm]
HOPPER-C-CF-8:	The aircraft shall provide the possibility to bring a minimum of 15 [kg] of cargo luggage
HOPPER-C-CF-11:	The aircraft shall have a window on each side of the fuselage within 0.5 meter of each row of seats
HOPPER-C-CF-14:	The aircraft shall have 1 lavatory
HOPPER-C-CF-15:	The aircraft shall have at least 1 passenger door
HOPPER-C-CF-16:	The aircraft shall have 3 emergency doors
HOPPER-C-R-CS-5:	The aircraft shall be able to withstand a gust speed of 20.12 [m/s] at VB for 0-4572 [m] altitude

HOPPER-C-R-CS-6:	The aircraft shall be able to withstand a gust speed of 15.24 [m/s] at VC for 0-4572 [m] altitude
HOPPER-C-R-CS-7:	The aircraft shall be able to withstand a gust speed of 7.62 [m/s] at VD for 0-4572 [m] altitude
HOPPER-C-R-CS-16:	Each passenger entry door shall qualify as a floor level emergency exit. This exit shall have a rectangular opening of not less than 0.61 [m] wide by 1.22 [m] high
HOPPER-C-R-CS-17:	The aircraft shall have an emergency on the side of the cabin opposite the passenger entry door that has a rectangular opening measuring not less than 0.51 [m] by 0.91 [m] high
HOPPER-C-R-CS-23:	For each pilot compartment, where the flight crew are separated from the passengers by a partition, there shall be a means to facilitate two-way communication between flight crew and cabin occupants, such as an opening or openable window or door or other means.
HOPPER-C-R-CS-12:	There must be a clearance between each propeller and the ground of at least 18 [cm].

5.2. Load Analysis

During the aircraft's lifespan, it will go through a lot of different flight situations. In order to be able to design the aircraft to withstand all possible loads encountered during flight, a load analysis was performed. The goal of this load analysis was to come up with critical load cases for the aircraft structure design.

A critical load case is combination of flight loads which will be designed for, since at no other point in the flight profile higher loads will be achieved. Multiple critical load cases can be identified, which are all limiting for different parts of the wing box. These load cases follow from the CS-23 requirements and are either associated with performing a manoeuvre or encountering a gust.

5.2.1. Manoeuvre and gust loads

The maximum positive limit load factor encountered during manoeuvres is stated in CS-23 as Equation 5.1.

$$n = 2.1 + \frac{24,000}{W + 10,000} \tag{5.1}$$

Where W is the MTOW in [lbs]. Since the H_2OPPER has a MTOW of 19,000 [lbs], the corresponding positive limit load factor is 2.93 . The load factor is a measure of the load to which the aircraft is subjected a equal to the lift over the drag. Following CS-23, the associated negative limit load factor was calculated by multiplying the maximum positive load factor by -0.4, resulting in a negative limit load factor of -1.17. [18]

The gust loads that are encountered during flight are calculated using a gust loading diagram. Following CS-23, the aircraft needs to be able to withstand gusts of a certain velocity at three different design speeds, as shown in Table 5.1. It should be noted that the design cruise speed (VC) is higher than the actual cruise speed of the aircraft, since the design cruise speed is prescribed by CS-23.

Table 5.1: Gust velocity the aircraft needs to withstand at a certain design speed

Design speed	Aircraft EAS [m/s]	Gust velocity [m/s]
Maximum gust intensity speed (VB)	95.02	20.12
Cruise speed (VC)	105.28	15.24
Dive speed (VD)	125	7.62

The load factor the aircraft experiences due to gusts was calculated using Equation 5.2, as depicted by CS-23.

$$n = 1 + \frac{K_g U_{de} V C_{L_\alpha}}{498\left(\frac{W}{S}\right)} \tag{5.2}$$

Here n is the load factor, U_{de} the gust velocities [ft/s], V the aircraft EAS [knots], C_{L_α} the wing lift curve slope per radian and K_g the gust allevation factor as depicted by Equation 5.3.

$$K_g = \frac{0.88\mu_g}{5.3 + \mu_g} \tag{5.3}$$

Where μ_g is the aircraft mass ratio as described in Equation 5.4.

$$\mu_g = \frac{2(W/S)}{\rho(MAC)C_{L_\alpha} g} \tag{5.4}$$

Where ρ is the density of air [slugs/ft^3], MAC the mean aerodynamic chord [ft] and g the acceleration due to gravity [ft/s^2].

The calculated manoeuvre and gust loads were combined and plotted in a manoeuvre and gust loading diagram, which is shown in Figure 5.1. The red line depicts the gust loads and the black line the manoeuvre loads at different aircraft velocities.

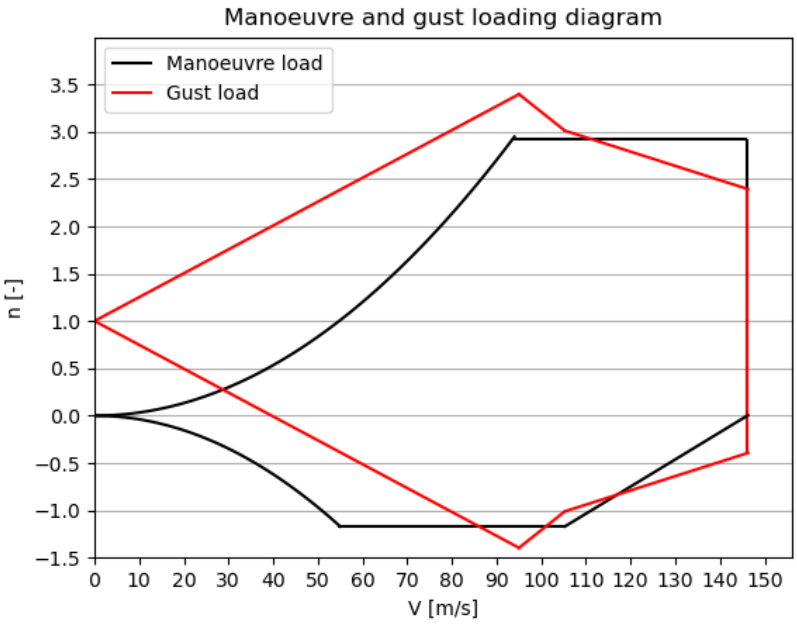

Figure 5.1: Manoeuvre and gust loading diagram of the H_2OPPER.

As can be seen in Figure 5.1, the maximum positive and negative limit load factor follow from gust loads which happen at VB and respectively are 3.40 and -1.40. These are the load factors that the aircraft was designed for.

5.2.2. High-lift device and control surface loads

Not only the positive and negative maximum loads are critical load cases encountered during flight. The wing of the aircraft contains high-lift devices and ailerons. Furthermore, the horizontal and vertical tail contain elevators and the rudder, respectively. These surfaces introduce loads inside the aircraft for which the structure should be designed.

From CS-23, the VF design speed gives the maximum speeds at which flaps can be deflected. The aircraft needs to be able to withstand a gust velocity of 7.62 [m/s] at this design speed. Therefore, the high-lift device

load case is a combination of the load factor due to the gust and the loads due to flap deflection.

For the load case with ailerons deflected, CS-23 specifies that the load case consist of a combination of 2/3 of the maximum positive limit load factor and the loads due to aileron deflection combined.

For the loads on the horizontal tail, the load cases considered were the maximum positive and negative load factors from the loading diagram, combined with the load introduced by deflection of the elevator.

The critical load case for the vertical tail follows from the one-engine inoperative requirement from engine failure and is a combination of the load on the tail surface and the load on the rudder.

During all loading cases, full thrust from the engine(s) was considered.

5.2.3. Critical load cases

From the manoeuvre and gust loading diagram, and the high-lift device and control surface loads, four critical load cases were distinguished for the wing structure:

- Maximum positive n
- Maximum negative n
- Maximum positive n with flaps deflected
- 2/3 of maximum positive n with ailerons deflected

For the structural design of the fuselage and horizontal tail, only the first two load cases were considered. Furthermore, it should be noted that during calculations for all load cases, not the limit load factor, but the ultimate load factor was used. This ultimate load includes a safety factor of 1.5 over the limit load.

5.3. Fuselage Internal Layout

Using the requirements from Subsection 5.1.2, a fuselage layout was designed. The cross-sectional layout of the fuselage is shown in Figure 5.2 and the top view of the fuselage is shown in Figure 5.3. For passenger comfort, each seat row has a window on either side, adding up to a total of fourteen. The main entrance is located at the back of the fuselage and three more emergency exits are present for fast disembarking.

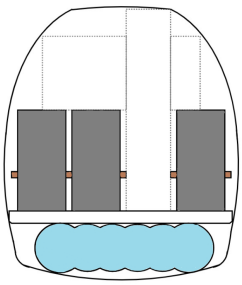

Figure 5.2: Cabin cross-sectionial layout

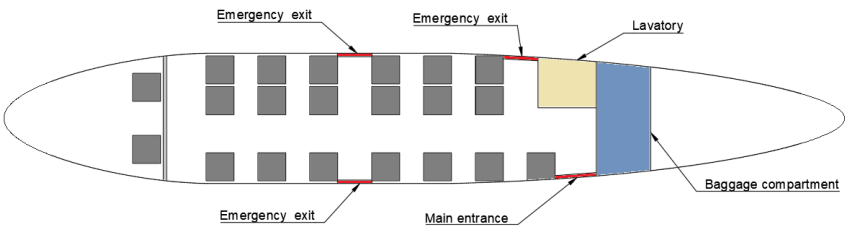

Figure 5.3: Cabin layout top view

Due to the placement of the hydrogen tanks on the bottom side, a relatively high fuselage height was required, combined with a wide fuselage bottom. Furthermore, due to the hydrogen tank, there was no space for luggage in the bottom of the fuselage. Therefore, a baggage compartment of 1.62 [m^3] was added behind the cabin, which is loaded through the main entrance door. This way, in addition to the small bag of 40x30x20 [cm] below the chair in front, all passengers can bring a large suitcase of 65x42x24 [cm]. The parameters of the fuselage layout are displayed in Table 5.2 and Table 5.3.

Table 5.2: Fuselage cross-sectional layout parameters

Parameter	Value [m]
Seat width	0.41
Seat height	0.95
Armrest width	0.04
Aisle height	1.66
Aisle width	0.38
Hydrogen tank width	1.65
Hydrogen tank height	0.44
Fuselage width	2.11
Fuselage height	2.50

Table 5.3: Fuselage top view layout parameters

Parameter	Value [m]
Seat pitch	0.762
Emergency exit width	0.51
Main entrance width	0.61
Extra seat pitch emergency exit	0.15
Lavatory width	0.862
Baggage compartment length	0.90
Nosecone length	3.0
Tailcone length	5.78
Fuselage length	13.24

5.4. Structural Layout

In this section the layout of the main structural components is discussed, namely the main wingbox, empennage and fuselage. The design tool, used to obtain these designs, is discussed later in Section 5.5.

5.4.1. Main Wingbox

Figure 5.4 shows the cross section of the wingbox at the root. The front spar of the main wingbox is located at 25 % of the chord length and the aft spar at 75 %. The wingbox has the same taper ratio as the wing and is symmetric around the x and z-axes. The wingbox has a constant skin thickness, along the cross section and the span, of 2 [mm]. For the stringer a simple L type stringer is chosen, with a height and width of 30 [mm]. The stringers are evenly spaced along the top and bottom skin and the number of stringer decrease from the root to the tip. For the rib spacing a value of 0.8 [m] is chosen [19]. The amount of stringers decreases linearly in five steps from 15 at the root to only 3 at the tip. Similarly the bottom stringers decrease from 8 at the root to 4 at the tip. The stringers follow the taper of the wingbox, so that the spacing stays equal.

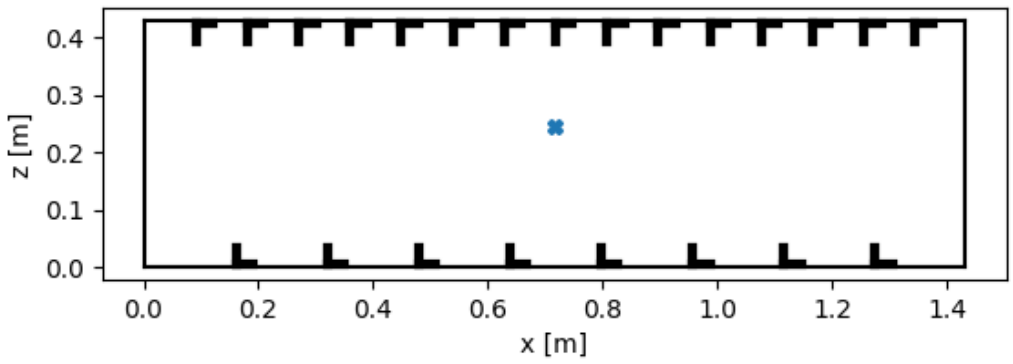

Figure 5.4: Main wing wingbox cross section at the root, with the blue cross marking the centroid of the wingbox

5.4.2. Empennage

The final design for the horizontal tail wingbox can be seen in Figure 5.5. This design has a constant skin thickness of 2 [mm], 2 top stringers and 10 bottom stringers with a width and height of 30 [mm]. In contrary to the main wingbox, the horizontal tail has more stringers on the bottom side. The horizontal tail provides negative lift for longitudinal stability, causing the most critical compression in the bottom side of the wingbox.

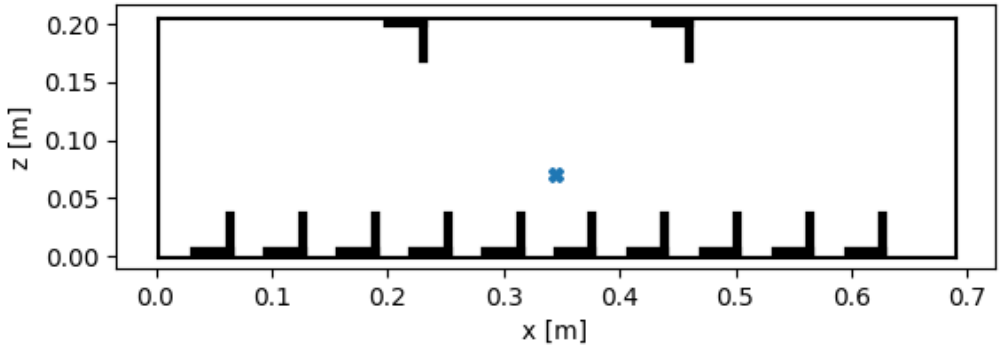

Figure 5.5: Horizontal tail wingbox cross section at the root

The final design for the vertical tail wingbox can be seen in Figure 5.6. The front spar is located at 25 % of the chord length and the aft spar at 50 %, due the large size of the rudder. This design has a constant skin thickness of 2 [mm], 10 top stringers and 10 bottom stringers with a width and height of 30 [mm], decreasing linearly. The number of stringers on the top and bottom are equal due the symmetric load case of the vertical tail.

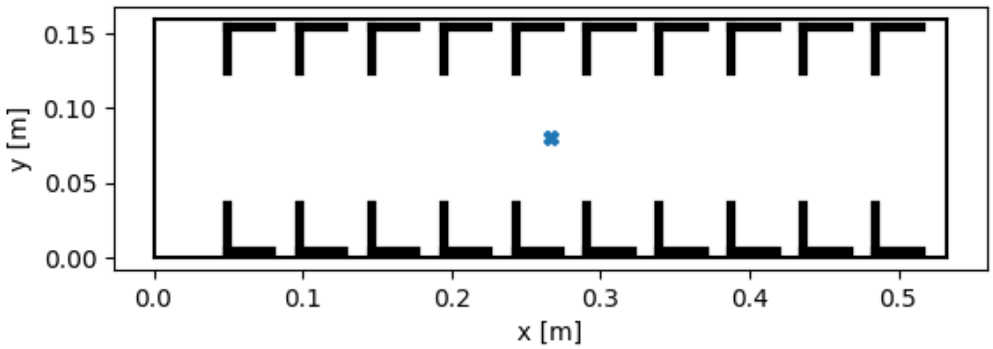

Figure 5.6: Vertical tail wingbox cross section at the root

5.4.3. Fuselage

The final design for the fuselage has a skin thickness of 2 [mm], with 32 stringers, with a width and height of 40 [mm], equally spaced along the circumference. The frames of the fuselage have a thickness of 2 [mm], a height of 100 [mm], and have a spacing of 800 [mm].

5.5. Design Tool

In order to optimize the weight and performance of the structural components, an iteration tool is created. The purpose of this tool is to iterate over the possible structural configurations and selects the lightest design for which no failure modes occur. The design tool for the wingbox is elaborated in more detail and for the fuselage and empennage the adaptations are discussed.

5.5.1. Assumptions

When designing the tools limited time was available, so multiple assumptions have been made to simplify the problems. In this subsection these assumptions will be addressed as well as the errors it introduces. The magnitude of these errors is difficult to determine since this would require a more in depth analysis of the problem. Therefore, most of the effects are qualitatively assessed.

Main wing

- One of the most noticeable simplifications of the problem is the load case. For the lift of the main wing and horizontal stabiliser a constant distributed load is assumed. The impact of this simplifications is that the wingbox will be overdesigned. The actual lift distribution is not known during this design phase. The realistic lift distributed will lead to a more concentrated load near the root which reduces

the overall moment if the same lift force is applied. If a linear decreasing lift distribution was chosen, an under designed wing box will be the result. Therefore the decision was made for the constant distributed load. This constant distributed load however acts as point load on the center line of the wingbox when looking at the cross section. This will neglect the torsional load introduced by the lift loading which can be off center in reality and will therefore result in an underdesigned wingbox.

- A second assumption was to simplify the wingbox to a rectangular shaped cross section. A more optimal wing box shape is one which follows the shape of the airfoil. Combining the aerodynamic and structural functions of the skin. The leading edge skin is assumed to not carry any loads, but its weight is considered in the wing weight. This assumption does lead to an overdesigned wing box since all the loads have to be transferred through the wingbox itself. In reality the leading edge skin could carry part of the torsional load, reducing the load carried by the wingbox. Thus, this assumption mitigates the assumption of neglecting the torsional load caused by the lift.
- For the torsion introduced by the control surfaces, the simplification was made that these act as point loads while in reality these are distributed over multiple hinges. This assumption will result in overdesign before the point of application and underdesign after. These combined do not result in a significant weight difference. The torsion caused by the drag of the control surfaces was also neglected. This is justified due to the lower magnitude of the force and up to five times smaller moment arm, compared to the lift.
- The wingbox model does not take cut-outs for inspection and system maintenance into account. Cut-outs result in stress concentrations around it. Therefore, more material has to be added around the cut-outs, than what is removed. This results in a net increase of the structural weight.
- The stringers are modelled as point areas, meaning that only the area distance of the stringers is taken into account for the moment of inertia. This is valid because the moment of inertia of the stringers is an order of magnitude lower than the area distance. Therefore, the influence on the sizing is negligible.
- When calculating the von Mises stress, only the stress in the spanwise direction and shear stress in the xz-plane are taken into account. This assumption is valid, when considering the skin as thin walled. With a skin thickness of 2 [mm] the stresses in lateral direction will be negligible.

Empennage

- The assumptions made for the main wing, also apply to empennage. In addition there are some assumptions specific to the empennage.
- Both horizontal tail surfaces produce a reaction moment around the x-axis on the vertical tail. For the vertical tail it is assumed that these reaction moments are equal and opposite and thus cancel out. This is justified because a symmetric loading case is considered for the horizontal tail. This results in two moments with equal size in opposite directions. Thus, having no effect on the sizing.
- The sweep of the vertical tail is not taken into account. Doing so would result in a slightly higher torsional moment due to the lift force. With the low angle of sweep of the vertical, this torsion should be a magnitude lower than the torsion caused by the rudder. Thus, having no significant effect on the sizing.

Fuselage

- The cross section of the fuselage is modelled as circular, instead of the actual oval shape. The diameter is taken to be the coverage of the width and the height of the fuselage. This underestimates the moment of inertia around the y-axis, and overestimates the moment of inertia around the z-axis. With the largest moment being around the y-axis, this causes a slight overdesign.
- The drag of the empennage and the aerodynamic moment of the horizontal tail are neglected. This force and moment are a magnitude lower than the lift generated by the horizontal and torsional moment caused by the vertical tail force. This causes a slight underdesign.

- The weight of the aircraft minus the wing is constantly distributed over the fuselage. This is not far from the actual loading and will have no significant impact on the design.
- The floor is not considered in the load calculations, doing so would increase the moment of inertia of the structure and thus lower the maximum stress. This causes an overdesign, because an estimate of the floor weight is included in the total fuselage weight.

5.5.2. Wingbox Loading

One of the critical structural components in an aircraft is the wingbox, which absorbs and transfers the loads experienced by the wing to the fuselage. A free body diagram (FBD) is created to show the forces acting on the wing and the resulting reactions moments at the wing root. Figure 5.7 shows the forces in z-direction acting on the wingbox. L_{wing} is the lift distribution over the wing, taken to be constantly distributed. W_{wing} is the weight distribution of the wing, also taken to be constantly distributed. W_{engine} is the weight of the engine, with a distance y_e to the root. The weight of the other subsystems in the wing is also taken into account, $W_{s,i}$ is the weight of the system and $y_{s,i}$ is the distance to the root. R_z and M_r are respectively the reaction force in z-direction and the reaction moment at the root.

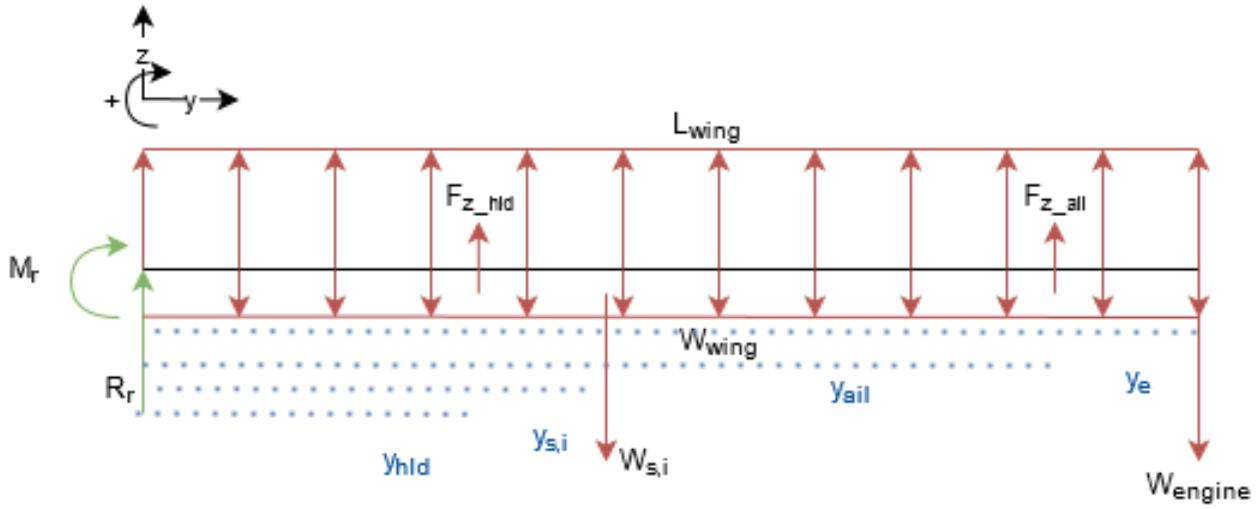

Figure 5.7: Free body diagram of the wingbox span in the yz-plane

Figure 5.8 shows the cross section of the wingbox, with the forces and torsional moment acting on it. T_{engine} is the thrust force of the engine, with distances e_x and z_e from the centre of the wingbox. F_{hld} is the force created by the high-lift devices, acting a distance of x_{hld} from the centre of the wingbox. Similarly for the aileron, which is not show in the FBD.

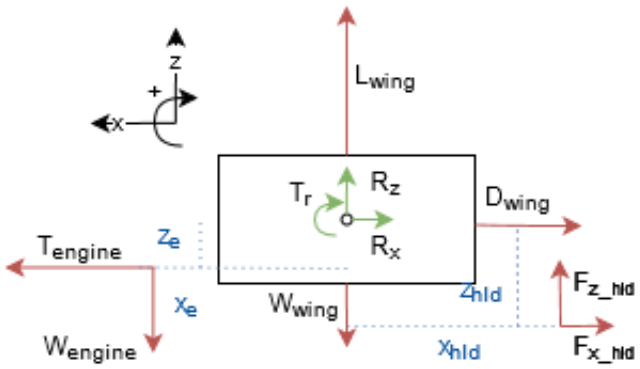

Figure 5.8: Free body diagram of the wingbox cross section in the xz-plane

5.5.3. Empennage Loading

The empennage wingbox design mainly follows the same design approach as that of the main wingbox. The only difference is the load cases that need to be considered for the vertical and horizontal tail. Similar to the wing, the horizontal tail also has a constant distributed lift force acting on it. Instead of torsion caused by the high-lift devices and the aileron, the horizontal tail experiences torsion by deflection of the elevator. Figure 5.9 shows the FBD of the horizontal tail in the xz-plane, this is similar to the FBD of the main wingbox, with the elevator replacing the HLD and aileron forces. The FBD in the xz-plane, as shown in Figure 5.10 is also similar to the main wing, with the main difference being the absence of the engine.

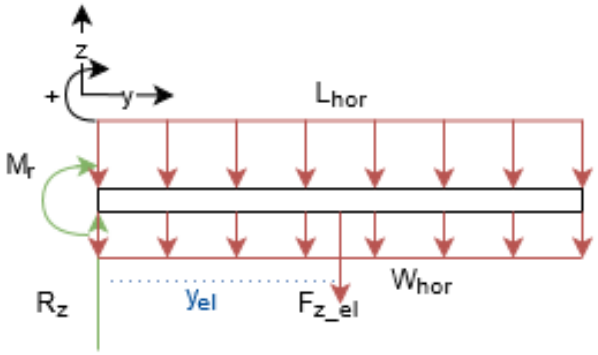

Figure 5.9: Free body diagram of the horizontal tail in the yz-plane

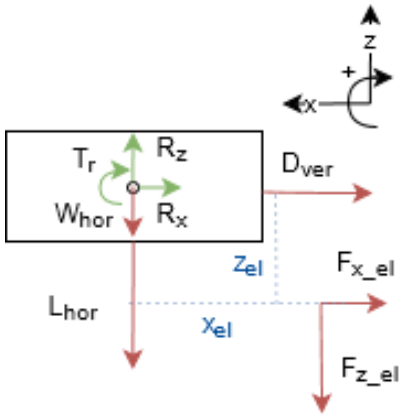

Figure 5.10: Free body diagram of the horizontal tail in the xz-plane

The vertical tail has a slight different loading case. The horizontal tail is integrated with the vertical tail, so it also has to carry these loads to the fuselage. This means that the reaction forces of the horizontal tail also act on the vertical tail. Figure 5.11 shows the free body diagram of the vertical tail, the vertical constantly distributed lift L_v, the rudder force F_r, and force F_h moment M_h and torsion T_h caused by the horizontal tail.

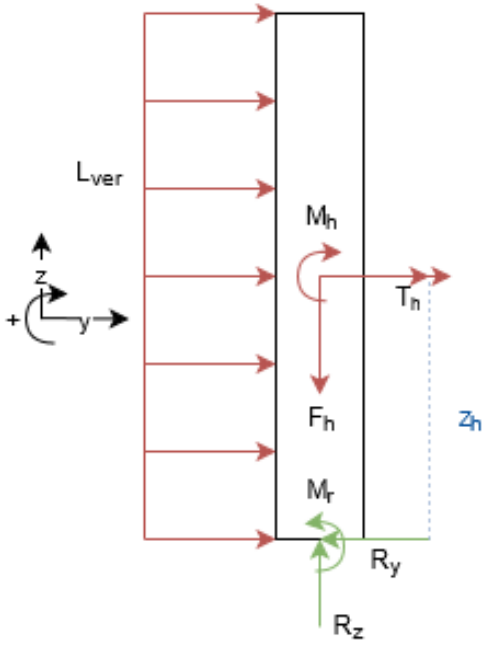

Figure 5.11: Free body diagram of the vertical tail in the yz-plane

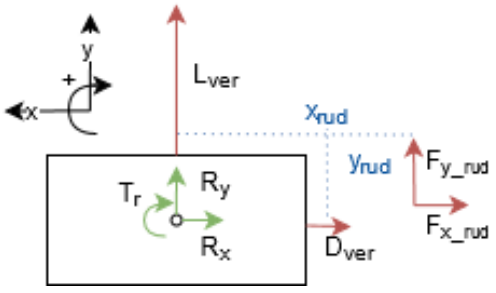

Figure 5.12: Free body diagram of the vertical tail in the xy-plane

5.5.4. Fuselage Loading

Figure 5.13 shows the free body diagram of the fuselage in the xz-plane. It is assumed that the fuselage is clamped at the wing, this results in reaction forces R_x and R_z and moment M_r, acting at the location of the wing x_{wing}. The empennage forces F_{x_emp} and F_{z_emp}, and moment M_{emp} act at the end of the fuselage. The weight of the aircraft minus the weight of the wing is taken as a constantly distributed load W_{fus}. The lift produced by the fuselage is also taken as a constantly distributed load L_{fus}.

Figure 5.14 shows the FBD of the fuselage in the yz-plane. This FBD also shows the force tail F_{y_emp} and the torsional moment T_{emp} generated by the vertical tail. In addition, the resulting reaction force R_y and torsional moment T_r.

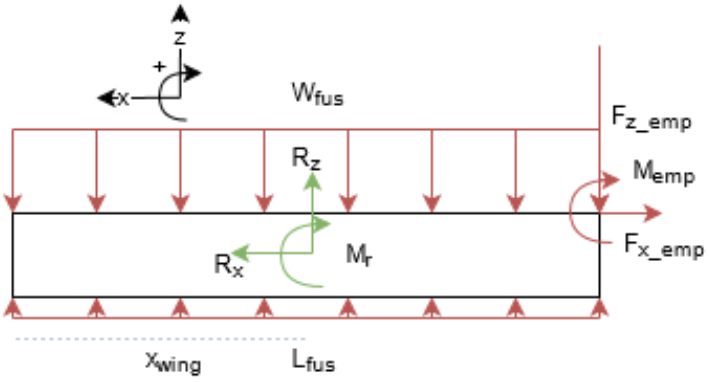

Figure 5.13: Free body diagram of the fuselage in the xz-plane

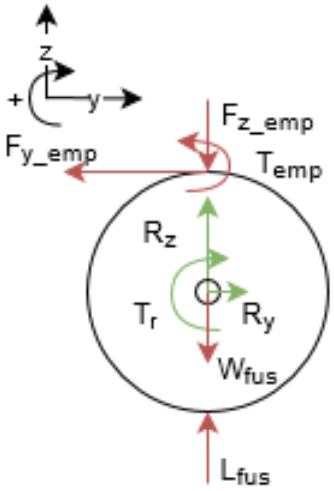

Figure 5.14: Free body diagram of the fuselage in the yz-plane

5.5.5. Analytical Model

In order to analyze the stresses and deformations in the structure, analytical model is created. This model is based on the theory and equations from the Aircraft Structures for Engineering Students book by T.H.G. Megson [20].

The first step is to calculate the geometric properties of the cross section. In order to calculate the moments of inertia of the wingbox, the coordinates of the centroid are calculated. Equation 5.5 and Equation 5.6 are used to calculate the x-coordinate x_{xc} and z-coordinate z_c of the centroid. In this equation, x_i and z_i are the distances of element i to the centre of the wingbox. A_i is the area of the stringer or skin element.

$$x_c = \frac{\sum_{i=0}^{n} x_i A_i}{\sum_{i=0}^{n} A_i} \tag{5.5}$$

$$z_c = \frac{\sum_{i=0}^{n} z_i A_i}{\sum_{i=0}^{n} A_i} \tag{5.6}$$

Both the skin and the stringers contribute to the moment of inertia of the wingbox. The stringers are seen as point areas, so only the area distance to the centroid is taken into account. For the skins higher power terms of t are neglected.

The contribution of the skin to the area moment of inertia around the x-axis I_{xx}, is calculated with Equation 5.7. This equation uses the thickness of the skin t_{sk}, the height of the skin h_{sk}, the area of the skin A_{sk} and the z-distance to the centroid d_z.

The contribution of the skin to the area moment of inertia around the z-axis I_{zz}, is calculated with Equation 5.8. This equation uses the width of the skin w_{sk} and the x-distance to the centroid d_x.

$$I_{xx} = \frac{t_{sk} \cdot h_{sk}^3}{12} + A_{sk} \cdot d_z^2 \tag{5.7}$$

$$I_{zz} = \frac{t_{sk} \cdot w_{sk}^3}{12} + A_{sk} \cdot d_x^2 \tag{5.8}$$

The internal forces and moments are described using Macaulay's step functions. This step function is given in Equation 5.9, here x_m is the activation value of the function. This makes it possible to describe the forces

as a function of y.

$$[x-x_m]^0 \begin{cases} 0 & x < x_m \\ x-x_m & x > x_m \end{cases} \tag{5.9}$$

The internal shear force in x-direction V_x is calculated with Equation 5.10. The main contributions to this are the thrust of the engine and the drag of the wing.

$$V_x(y) = R_x - \frac{L_{wing}}{L/D} \cdot y + T_{engine} * [y-y_e]^0 \tag{5.10}$$

The internal shear force in z-direction V_z is calculated with Equation 5.11. The main contributions to this are the lift of the wing, and the weight of the wing and the engine.

$$V_z(y) = R_z + (L_{wing} - W_{wing}) \cdot y - W_{engine} * [y-y_e]^0 - W_{s,i} * [y-y_{s,i}]^0 \tag{5.11}$$

The internal bending moment around the x-axis can be found by integrating Equation 5.11. The resulting integration constant equals the reaction moment at the root $M_{r,x}$.

$$M_x(y) = M_{r_x} + R_z \cdot y + (L_{wing} - W_{wing}) \cdot \frac{y^2}{2} - W_{engine} * [y-y_e]^1 - W_{s,i} * [y-y_{s,i}]^1 \tag{5.12}$$

The internal bending moment around the x-axis can be found by integrating Equation 5.10. The resulting integration constant equals the reaction moment at the root $M_{r,x}$.

$$M_z(y) = M_{r_x} + R_x \cdot y - \frac{L_{wing}}{L/D} \cdot \frac{y^2}{2} + T_{engine} * [y-y_e]^1 \tag{5.13}$$

The torsional moment, T, around y-axis is calculated with Equation 5.14. The main contributions to this are the moments generated by the high-lift devices and the aileron.

$$T_y(y) = T_r + F_{hld} \cdot x_{hld} \cdot [y-y_{hld}]^0 - T_{engine} \cdot z_e \cdot [y-y_e]^0 + F_{ail} \cdot x_{ail} \cdot [y-y_{ail}]^0 \tag{5.14}$$

The T calculated with Equation 5.14 is then used to calculate the twist of the wingbox. In this equation A_m is the cross sectional area, G is the shear modulus of the material and L_m is the total length of the skins in the cross section.

$$\theta = \frac{T}{4 \cdot A_m^2 \cdot G} \oint_{L_m} \frac{1}{t_{sk}} ds \tag{5.15}$$

The displacement of the wing is calculated with the moment curvature relationship. The deflection in x-direction v_x is found by integrating Equation 5.16 twice and the same for the deflection in z-direction v_z with Equation 5.17. These equations use the respective M and I, and the elastic modulus of the material, E. The integration constants resulting from the integration drop out, when considering the boundary condition of no deflection at the root.

$$\frac{d^2 v_x}{dy^2} = -\frac{1}{EI_{zz}} M_z \tag{5.16}$$

$$\frac{d^2 v_z}{dy^2} = -\frac{1}{EI_{xx}} M_x \tag{5.17}$$

The stresses caused by the bending moments acting on the wingbox, σ_x and σ_z, are calculated with Equation 5.18 and Equation 5.19 respectively. Where x and z are the distances to the centroid of the cross section. Both stresses act in the y-direction and can be added up to obtain the stress in y-direction σ_{yy}.

$$\sigma_x = \frac{M_x \cdot z}{I_{xx}} \tag{5.18}$$

$$\sigma_z = \frac{M_z \cdot x}{I_{zz}} \tag{5.19}$$

The shear stresses caused by the shear forces acting on the wingbox, τ_x and τ_z, are calculated with Equation 5.20 and Equation 5.21 respectively. It is assumed that the shear forces act through the shear centre of the cross section. In this case the shear centre coincides with the centre of the cross section, because of the symmetry around the x and z-axis. Here x and z are the distances to the shear center and are integrated over a skin distances.

$$\tau_x = -\frac{V_x}{I_{zz}} \int_s t x \, ds \tag{5.20}$$

$$\tau_z = -\frac{V_z}{I_{xx}} \int_s z \, ds \tag{5.21}$$

Figure 5.15 shows the two distances, s_1 and s_2, over which is integrated. Due to symmetry of the cross section, the resulting equations for these distances can also be used for the other sides.

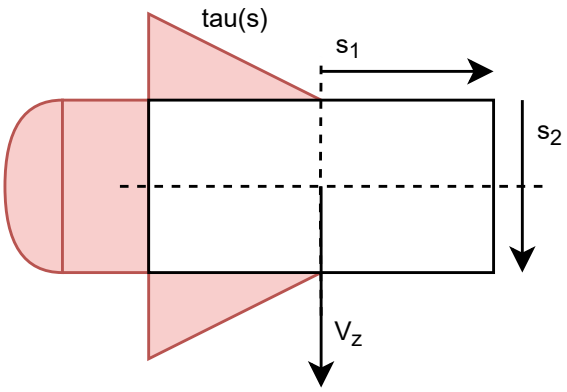

Figure 5.15: Shear flow due to a shear force in z-direction

Besides the shear stress due to shear forces, there is also shear stress due to torsion around the shear centre. This shear stress is calculated with Equation 5.22. Where T is the torsion calculated with Equation 5.14, t the skin thickness and A_m the cross sectional area. To obtain the total shear stress in the xz-plane τ_{xz}, all shear stresses are added together as shown in Equation 5.23.

$$\tau_T = \frac{T}{2 \cdot t_{sk} \cdot A_m} \tag{5.22}$$

$$\tau_{xz} = \tau_{xz} + \tau_z + \tau_T \tag{5.23}$$

5.5.6. Failure Modes

There are multiple ways in which the wingbox can fail, either the material can fail or the structure as a whole. For the material the yield stress σ_y is considered, this is the stress at which deformation of the material is irreversible. Therefore, the maximum stress in the wingbox may not exceed the yield stress of the material. The maximum stress is calculated using the von Mises theory of elastic failure. The simplified equation for the von Mises stress σ_{vm} is given in Equation 5.24. This equation only takes into account the bending stress in y-direction σ_{yy} and the shear stress in the xz-plane τ_{xz}.

$$\sigma_{vm} = \sqrt{\sigma_{yy}^2 + 3\tau_{xz}^2} \tag{5.24}$$

For the failure of the structure, three failure modes are considered: buckling of the skin, crippling of the stiffeners and crippling of the top and bottom panels. The first failure mode, buckling of the skin, is caused by shear stress. The shear stress at which buckling will occur is estimated with Equation 5.25 [21]. In this equation K_s is the shear buckling coefficient of the skin, b the width of the skin section, and E the elastic modulus of the material.

$$\tau_{cr} = K_s \cdot E \cdot (\frac{t}{b})^2 \tag{5.25}$$

From Niu [460, Fig. 11.3.5][21] an estimate of K_s can be found, depending on the aspect ratio of the panel a/b and the edge conditions. In reality the edge conditions are in between those of hinged and clamped conditions. However, it is assumed that the connections with the ribs and the stringers are in hinged conditions, as this is the most critical case. This results in panel layout 3. Assuming that the rib spacing is much larger than the stringer spacing, results in an a/b of larger than 5 . This results in the most critical condition with a K_s of 5.

The second structural failure mode, crippling, is caused by the compression stress. Crippling can occur in both the skin and the stringers. However, the stress is divided over both the stringers and the skin. If

crippling in the skin occurs earlier, the stress is transferred to the stringers instead of crippling. Therefore, the combined crippling stress of the stringers and the skin is considered, the crippling stress of the panel. This is calculated with Equation 5.26, where the individual crippling stresses of the components σ_i are weighted with their area A_i and summed. $(\sigma_{cc})_{\text{panel}}$ is then found by dividing by the sum of all the areas. This and the following equations are obtained from course AE2135-II "Structural Analysis and Design". [1]

$$(\sigma_{cc})_{panel} = \frac{\sum \sigma_{cc}^{i} \cdot A_i}{\sum A_i} \tag{5.26}$$

The crippling stress of the skin $(\sigma_{cc})_{\text{skin}}$ is calculated with Equation 5.27. In this equation C is the compression buckling coefficient of the skin, b the width of the skin section, and E and μ the elastic modulus and the poisson ratio of the material.

$$\sigma_{cc} = C \cdot \frac{\pi^2 \cdot E}{12(1-\nu)} (\frac{t}{b})^2 \tag{5.27}$$

From AE2135-II lecture 7 [49, fig 12.8.3] an estimate for C can be found, depending on the aspect ratio of the skin a/b and the edge conditions. For the skin simply supported conditions and an a/b larger than 5 are again considered. This results in the most critical condition, with a C of 4.

The crippling stress of the stringers can be calculated in a similar way. The L shaped stringer can be seen as two connected skin sections. The individual σ_{cc} of the skins is calculated with Equation 5.27 and Equation 5.26 is then used to calculate $(\sigma_{cc})_{\text{stringer}}$. The stringer skin does have a different C, because of the free edge on one side. This results in a C of 0.425 for the stringer skin.

The smaller width of the stringer with respect to the skin, means that the stringers usually have a larger σ_{cc}. The stiffeners not only provide stiffness by taking part of the compression stress, they also stiffen a part of the attached skin. This skin section has the σ_{cc} of the stringer instead of that of the skin. The width of the skin that is effected w_e is calculated with Equation 5.28. In this equation C is the compression buckling coefficient of the skin, $(\sigma_{cc})_{\text{stif}}$ the crippling stress of the skin, t_{sk} the skin thickness, and E and μ the elastic modulus and the poisson ratio of the skin material.

$$w_e = \frac{t_{sk}}{2} \cdot \sqrt{\frac{C \cdot \pi^2}{12(1-\nu^2)}} \cdot \sqrt{\frac{E}{(\sigma_{cc})_{stif}}} \tag{5.28}$$

The skin area that is effected by the stiffener, $2w_e * t_{sk}$, is then subtracted from the skin area and added to the stiffener area. With these new areas, $(\sigma_{cc})_{\text{skin}}$ and $(\sigma_{cc})_{\text{stringer}}$, $(\sigma_{cc})_{\text{panel}}$ is calculated with Equation 5.26.

In addition to these failure modes there are also restrictions set to the displacement and twist of the wing tip. The maximum allowed deflections follow from the requirements, 0.5 [m] downwards and 1 [m] upwards. No requirement was set for twist, for now the maximum allowed twist at the tip is limited to 1 [°]. In a later design stage the effect of this twist on the aerodynamic performance of the wing should be further investigated, and the allowable twist might need to be adjusted.

5.5.7. Fuselage Model

The fuselage design mainly follows the same design approach as that for the wingbox. However, the loading case is different and a different cross section needs to be considered. The fuselage will be modeled as a circular cross section with L stringers evenly distributed over the skin. The critical loading case is identified, and based on this, the fuselage is sized with a constant cross section over the length of the fuselage. This ensures that the entire fuselage can handle the loads, but will result in a heavier structure.

The equations used in the fuselage tool are almost the same as those for the wingbox in Subsection 5.5.5. An exception to this is the calculation of the area moment of inertia of the skin. For this the equation for a

[1] Obtained from course AE2135-II Structural Analysis and Design, lecture 7

thin walled circular cross section is used as shown in Equation 5.29.

$$I_{xx} = \frac{\pi \cdot t \cdot d^3}{8} \tag{5.29}$$

The fuselage tool computes the weight for the fuselage with a constant cross sections. So this does not take into account the presence of: windows, doors and the cabin floor. To account these parts in the estimation, a semi-empirical method described by Torenbeek is used [22]. The doors and windows are accounted for by subtracting the weight of the material of the cut-out and adding the weight of the reinforcement and the weight of the filling. For small openings it can be assumed that the reinforcing material equals the removed material [22]. The windows are made out of plexiglass, with a density of 1180 [kg/m^3]. A thickness of 1 [cm] is assumed, which should be an overestimation because the cabin is not pressurized. With a size of 20 by 30 [cm] an area of 0.06 [m^2] is calculated, resulting in a weight of 0.7 [kg] per window. For the doors an estimation by Torenbeek is used for unpressurized aircraft, as shown in Equation 5.30. With a door width of 0.8 [m] and a height of 1.5 [m] the area of the door A_d is calculated to be 1.2 [m^2]. This results in a mass per door m_d of 18 [kg]. For the weight of the cabin floor an estimation by Torenbeek for passenger aircraft is taken, namely 5 [kg/m_2].

$$m_d = 14.9\sqrt{A_d} \tag{5.30}$$

5.5.8. Iteration tool

The main objective of the structural design is to obtain the lightest design that can carry all the loads without any failure modes occurring. In order to obtain this optimal design, an iteration tool is created. This tool generates different designs by varying the skin thickness, number of stringers and stringer size. For every design it analyses if any failure mode occurs and the weight is calculated. The lightest successful design is then selected. The tool can also be used to find the most optimal material for a certain component. By iterating over different materials, the lightest design combination is selected.

The design obtained with this tool is the most optimal with the assumptions stated in Subsection 5.5.1 and the simplified layout. This tool is thus used to give a preliminary weight estimation of the structural components and to quantify the effect of design decisions on the operational empty weight of the aircraft. In the detailed design phase a better optimized layout can be obtained by varying the skin thickness over the cross section or a more complex stringer distribution.

5.6. Landing Gear

The landing gear placement plays an important role in the ground stability of the aircraft. Multiple requirements dictate the placement of the landing gear and are described in this section. A tri-strut with a single nose wheel was chosen as configuration due to the visibility advantage during ground operations, the added stability during braking and the prevention of ground-looping [23]. The longitudinal positions, with the nose of the aircraft as datum, were designed to be 1.5 and 6.5 [m] for the nose and main gear respectively. The lateral separation of the main landing gear was selected to be 1.19 [m].

The longitudinal placement is dictated by three criteria namely: the tip back angle, scrape angle and the nose wheel loading for adequate steering capacity. The tip back angle should be greater than the scrape angle to ensure stability. The tip back angle was determined to be 18 [deg] and the scrape angle 15 [deg] to ensure enough clearance between the tail and the runway during take-off (see Figure 5.17 for visual representation). For the nose wheel, a minimum loading of 8% of the total weight is required [24]. This combined with c.g. location which will be later discussed in Subsection 7.2.2 resulted in the longitudinal placement described at the beginning of this subsection. The longitudinal positioning of the nose landing gear is selected to be 1.5 [m] from the nose of the aircraft to be able to fit the landing gear in the fuselage when retracted.

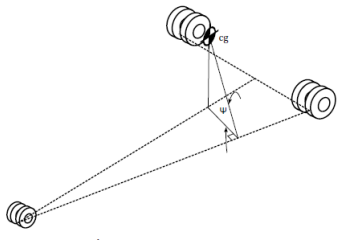

Figure 5.16: Visual representation of the tip over angle

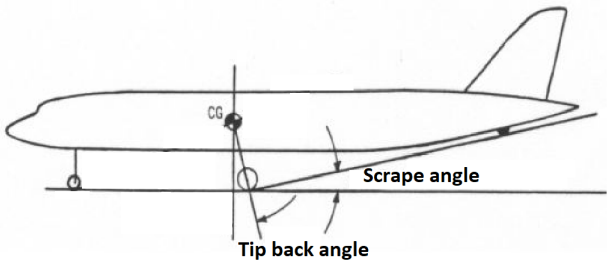

Figure 5.17: Visual representation of tip back and scrape angle

The lateral placement is also determined by three criteria namely: tip over angle, tip clearance and prop clearance. The tip over angle is a requirement to prevent tipping over under asymmetric loading or sidewinds. The tip over angle is determined to be 55 [deg] [2] and is visualised in Figure 5.16. The tip and prop clearance criteria maintain clearance to the runway if a landing with crosswind is not performed correctly. These angles are both taken as 8 [deg] and are measured from the outer landing gear to the tip or prop. For the engine clearance, another 6 inches is added [24]. Due to the high wing configuration, the tip over criteria was found to be limiting, even with tip mounted engines.

5.7. Material Selection

Material selection is an import step in the design phase. To make this selection multiple materials which are common in aerospace design were chosen to be analysed. These are aluminium, titanium, GLARE and composite fibre reinforced polymers (CFRP). Since sustainability is the driving factor of the H_2OPPER, this is a key factor for the materials. At least 90% of the materials used have to be recyclable. Moreover, the used materials have to be as sustainable as possible. These two criteria were investigated by analyzing the production energy as well as the recycling energy costs, which are used in the recyclability indicator as discussed in Subsection 5.7.1. From the material selection it was clear that an overall recyclability of 98 % is achieved for the main structural components of the aircraft.

5.7.1. Material sustainability

For the four considered materials the sustainability has been investigated by using the recyclability indicator presented in Section 3.1. This indicator uses several properties such as embodied energy for primary production and recycling, as well as the percentage of material that is already recycled. The recyclability percentage is also a key factor in the indicator. The results for the different materials are shown in Table 5.4. It should be noted that the recyclability indicator does not include the weight of the different components yet which is the explanation for the unit [MJ/kg]. This indicator is used in Subsection 5.7.3 where a material is selected for different parts of the aircraft.

Table 5.4: Recyclability indicator and raw material costs for the four considered materials [14]

	Embodied energy, primary production [MJ/kg]	Embodied energy, recycling [MJ/kg]	Recyclability percentage [%]	Recycled percentage [%]	Recyclability indicator [MJ/kg]	Normalized indicator [-]	Cost [USD/kg]
Aluminium	220	30	100	45	18.3	1	2.7
Titanium	720	96	100	24	76.0	4.15	63
GLARE	300	43	85	38	54.8	2.99	20.25
CFRP	500	500	0	0	500	27.3	44

CFRP is not recyclable with current technology. This would limit the use of this material in order to still meet the 90% recyclability of the entire aircraft, especially considering the fact that the hydrogen tank is

[2] Obtained from course AE1222-II, lecture 7

also made of carbon material. From literature it was found that the use of CFRP provides a 20% percent weight saving over conventional aircraft [25]. It was decided that these weight savings do not outweigh the huge increase in the recyclability indicator. Therefore the decision was made to discard CFRP as potential material for the structural design. Aluminium, titanium and GLARE however do show promising results in terms of recyclability and costs and therefore were analysed in more detail.

5.7.2. Material properties

Beside the sustainability of the materials, the properties have been analysed to design for specific load cases and applications. This section will first elaborate on the strengths and weaknesses of the main chosen material groups: aluminium alloys, titanium alloys and GLARE. Secondly, the properties of different aluminium alloy series will be discussed to achieve a more optimal design. Four different alloy series were investigated: 2000, 6000, 7000 and the aluminium- lithium (Al-Li) series.

Remarks on material types

Aluminium overall has properties that perform well in many areas. Thermo-mechanical processing allows for a high level of property control which ensures further optimisation of the material. The biggest downside of aluminium is that it has poor corrosion resistance. It is especially susceptible to stress corrosion. Furthermore, it is hard to weld without non-fusion techniques.[26]

Titanium has two main advantages over other metals. Firstly, it has the highest weight-to-strength ratio of any metal. This allows for lighter and smaller structures. Secondly, titanium makes an oxide film that prevents from oxidizing mineral acids, chemicals, water and salt solutions. This makes it really corrosion resistant, it can withstand long periods of exposure to salt water in marine atmospheres, which is useful in island regions. On the other side, the costs of titanium are more than competitor metals due to extraction and melting complexities. [27]

GLARE has two main advantageous properties over other materials. The tensile strength is significantly higher then the common 1.5 times the yield stress [28]. This is due to the added fibres. Secondly, GLARE has a high damage tolerance and impact resistance. This is mainly because of slow fatigue crack growth due to the glass fibres. The main downsides of GLARE are the high material costs, it is 5-10 times more expensive per kilogram than conventional aluminium alloys, and the low buckling resistance which limits the use in compression loaded structures [26][28].

Specific aluminium alloy series:

The Al-2000 series is an alloy with copper and once was the most common aerospace alloy. The 2000 series is susceptible to stress corrosion cracking and therefore is later replaced mainly by the Al-7000 series. [29]

The Al-6000 series is alloyed with magnesium and silicon. This series has a good formability and weldability but does not provide the same strength as the 2000 and 7000 series. It does however have good damage tolerance properties and corrosion resistance. [29]

The Al-7000 series is alloyed with zinc and can be hardened with thermo-mechanical processing to the highest strengths of any aluminium alloy. This series provides good machinability and high thoughness as well [29].

The Al-Li series is alloyed with lithium and is increasingly popular in aicraft design [29]. This alloy provides 8-15% higher specific stiffness than conventional aluminium alloys. The added lithium reduces the density and increases the elastic modulus. The Al-Li series provides good fatigue and cryogenic properties and has excellent corrosion and stress corrosion resistance which is especially helpful in humid and salty environments like island regions. However, the disadvantages compared to conventional aluminium alloys are the higher material cost, more complex recyclability and multi-stage thermo-mechanical treatments.

For the selection of material, a literature study was performed to analyze the different materials used in modern aircraft [27][29][30]. Multiple materials from different series were analysed and further investigated.

The properties of these materials are displayed in Table 5.5[3] .

Table 5.5: Material properties of the considered materials [31].

	Yield strength [MPa]	Young's modulus [GPa]	Density [g/cm^3]
Al-2000 (2024-T361)	462	73.1	2.78
Al-6000 (6061-T914)	455	69	2.70
Al-7000 (7050-T74)	386	71	2.83
Al-7000 (7055-T77511)	614	75	2.86
AL-Li (2055-T8)	538	76.5	2.71
AL-Li (2099-T83)	525	78	2.63
Titanium (Ti-5Al-5Mo-5V-3Cr)	1055	110	4.64
GLARE (3-4/3-0.4)	284	58.1	2.50

The combination of Table 5.4 and Table 5.5 show that, in terms of recyclability and cost, aluminium outscores the other materials. This can be seen from the properties of all the aluminium alloys. This is an important finding for the material selection, which will be discussed in Subsection 5.7.3.

5.7.3. Material selection for aircraft parts

In this subsection the materials selected for the different aircraft parts are presented. The selection is based on the following criteria: weight, recyclability indicator, recyclability percentage and cost. Table 5.6 gives an overview of the different aircraft components and their respective weight, recyclability indicator value, recyclability percentage and cost. The selected aircraft parts are the main wing, empennage, fuselage and landing gear. It should be noted that the costs presented in Table 5.6 are the costs for the raw materials. It is expected that the added manufacturing cost for aluminium processing is smaller compared to that of titanium and GLARE due to the ease in machinability [32].

Table 5.6: Material selection per structural component.

	Material	Weight [kg]	Recyclability indicator [GJ]	Recyclability percentage [%]	Cost [USD]
Main wing					
Wing skin	Al-Li 2099-T83	470	8.6	100	1270
Wingbox upper stringers	Al-7055-T77511	140	2.6	100	380
Wingbox lower stringers	Al-Li 2099-T83	115	2.1	100	310
Leading edge wing	GLARE	68	3.7	85	1380
Empennage					
Skin	Al-Li 2099-T83	95	1.7	100	260
Horizontal upper stringers	Al-7055-T77511	30	0.6	100	80
Horizontal lower stringers	Al-Li 2099-T83	7	0.1	100	20
Vertical stringers	Al-7055-T77511	42	0.8	100	110
Leading edge	GLARE	15	0.8	85	310
Fuselage					
Fuselage top skin	GLARE	235	12.9	85	4760
Fuselage bottom skin	Al-6061-T914	263	4.8	100	710
Fuselage stringers	Al-Li 2099-T83	425	7.8	100	1150
Landing gear	Ti-5Al-5Mo-5V-3Cr	135	10.3	100	8600
Total		2040	57	98	19340

[3]URL: `http://www.matweb.com/` [Accessed on: 6-11-2021]

Wing materials

For the wing materials the distinction is made between the wing skin, wing leading edge and wingbox. The wingbox is further divided in the top and bottom stringers and the wingbox skin.

For the selection of the materials used in the wingbox, the tool described in Section 5.5 was used to optimize the weight and material used for the stringers and the wingbox skin. From literature study it was clear that most conventional aircraft use different materials for the upper and lower stringers, due to the difference in compression and tension loading. Therefore, it was decided to use two vastly different aluminium alloys to see the effect of different parameters. From Table 5.5, it can be seen that the materials Al-7055-T77511 and Al-Li 2099-T83 differ a lot in terms of yield strength, Young's modulus and density. Other aluminum alloys were not considered due to the favourable characteristics of these alloys. It must also be noted that GLARE is not considered due to the compression loading and titanium is discarded due to the high costs. From the tool it was clear that Al-7055-T77511 is optimal for the top stringers and Al-Li 2099-T83 for the skin and bottom stringers of the wingbox. For the top stringers the increase in yield stress outweighed the increased density of the material, resulting in Al-7055-T77511. For the skin and the bottom stringers this is not the case and the lighter material is optimal, resulting in Al-Li 2099-T83.

For the leading edges of the empennage and main wing it was decided to use GLARE due to its favourable impact resistance property. The weight is also calculated by the tool mentioned above. The total recyclability of the aircraft will become lower when GLARE is used, however the 90% recyclability will not be compromised with the current selected materials.

For the skin of the wing the same material will be used as that for the wingbox, namely Al-Li 2099-T83. High impact resistance for the wing skin is not needed, since it expected that the high wing configuration reduces the possibility of impacts from debris on the runway during take-off and landing. Recommendations will be made to further analyse the possible weight decrease if other materials were chosen for the outer wing skin. The used tool was not designed for the complex shape of the outer wing, therefore no complete analysis of weight savings could be performed.

Empenage materials

The material selection procedure of the empennage was performed in the same manner as that of the main wing. The same distinction in structural components was made and the results are presented in Table 5.6. The vertical stabiliser does not use different materials for the stringers since it is designed for equal side loading. GLARE is again used for the leading edges due to its favourable impact resistance.

Fuselage materials

The selected materials for the fuselage are shown Table 5.6, where the distinction was made the top and bottom side for the stringers and skin. The same two aluminium alloys, Al-7055-T77511 and Al-Li 2099-T83, were considered as well as GLARE and Al-6061-T914.

For the top of the fuselage GLARE is chosen as structural material. Since this component is mainly loaded in tension, the use of GLARE was a possibility. Using the tool this resulted in a weight reduction. The overall recyclability percentage will be lower if GLARE is used. However, GLARE is only used for the fuselage top part and leading edges of wing and stabilizers. Therefore, the overall recyclability percentage of 90% will not be compromised.

The lower part of the fuselage is loaded in compression, which eliminates the possibility to use GLARE. Furthermore, the lower side of the fuselage experiences small impacts of for example small rocks that are present on the runway during take-off and landing. Moreover, the fuselage bottom gets in contact with splashing water and salt. Therefore, strength is not the only parameter to be considered. The Al-6000 series does have good damage tolerance properties and corrosion resistance compared to other aluminium alloys. It remains resistant to corrosion even when the surface is abraded. For this reason in combination with the strength properties, the alloy Al-6061-T914 is chosen for the lower side of the fuselage.

The material selection for the stringers in the fuselage was also based on weight savings and resulted in the seleciton of material Al-Li 2099-T83 for the top and bottom side stringers based on the outcome of the

tool.

Landing gear:

When choosing a material for the landing gear, multiple criteria have an impact on the selection. Corrosion is a big factor due to it being subjective to a rough environment when landing. The available volume for retractable landing gear is limited which results in the need for a compact design. The selected material is therefore the titanium alloy Ti-5Al-5Mo-5V-3Cr, which is conventional in modern aircraft. This alloy has been chosen because it has more hardenability and ultimate strength compared to its competitors Ti-10V-2Fe-3Al alloy and Ti-5Al-5V-5Mo1Cr-1Fe alloy [27]. Ti-5Al-5Mo-5V-3Cr fulfills the requirements of having a high yield stress, which is required for a compact design. Furthermore, the corrosion resistance of Ti-5Al-5Mo-5V-3Cr lowers the need for landing gear maintenance. The weight of the landing gear is estimated with the use of a class 2 weight estimation, since no tools were designed for these loads.

This weight computed is the total system weight and not only the structural components. Therefore, the ratio between the structural part and total weight, obtained from literature, of 0.36 is used to identify the amount of structural material that is used in the landing gear [33].

5.8. Recommendations

This design phase focused on the preliminary sizing of the main structural components. For this a tool was created to quickly obtain a new design based on new inputs from the other subsystems. This way, it was possible to quantify the effect of design on the structural weight. The first step in the next design phase, is to perform a detailed stress analysis. By analyzing the stress distribution over the span of the wing, is is possible to further optimize the design. This can be done by obtaining a close to constant stress distribution over the skins. This way, overdesigned parts of the structure can be downsized, by either removing stringers or reducing the skin thickness. It is also beneficial for efficiency of the design, that all failure modes are close to occurring at the ultimate load. For the current design buckling and crippling happened before the other failure modes, making the design less efficient. In the next design phase, the structure has to be optimized for all failure modes.

For now only a static load cases were considered, it is thus recommended to also perform a dynamic one. Flutter, the dynamic instability of the wing, can cause failure of the wing system. Flutter occurs at certain velocities and can be excited by a high angle of attack of the ailerons [20]. Flutter conditions are highly dependent on the c.g. location of the wing. In further study, the placement of the engine and other systems in the wing can be optimized to counteract flutter. This can be done by obtaining a cg position of the wing in front of and as close as possible to the flexural axis. In addition to this, the effect of the wing tip placed engines needs to be investigated. As this might also introduce an oscillating motion in wing.

Another failure mode that is not analyzed is fatigue. Both the material choice and the design of the structure influence the fatigue performance. The fatigue behaviour was considered in the material trade-off, but the fatigue and crack free life should be established in further design. This can be done by extensive coupon testing of the different materials. The assembled structure should also be tested at least once, to validate the expected fatigue behaviour. Based on the outcome of these tests a maintenance schedule should be set up. Fatigue can cause the failure of individual components such as skins or fasteners. Thus, it is important that failure of one of these components does not result in a failure of the entire system, giving a fail safe design. The system must still be strong enough to function until the next inspection. The structure must be redundant and accessible for inspections by providing inspections holes or removable panels. Since many fuel systems are located in the wing and also need inspection, the accessibility of the wingbox is particularly important.

The aircraft structure has been designed to withstand manoeuvre and gust loading. In the next stage of the design it should be analyzed if the design can also withstand all other loading conditions, such as normal and emergency landing. From this, critical loading conditions might arise for the landing gear and its forces on the fuselage.

6
Wing Design

In this chapter, the aerodynamic design of the wing, and the mobile surfaces on it, will be presented. The general wing parameters, such as the aspect ratio, are calculated based on the design methodology of Raymer [34] in Section 6.2. The airfoil selection is elaborated in Section 6.3, followed by the sizing of the High Lift Devices in Section 6.4. Lastly, the sizing of the ailerons was done in Section 6.5.

6.1. Subsystem Overview

The subsystem overview shows the functions and assumptions used in the design of the wing and mobile surfaces.

6.1.1. Functions

The wing is there to provide lift in order to keep the aircraft airborne. Furthermore, the High Lift devices are needed for take-off and landing, in order to increase the overall lift coefficient. The ailerons are used to manoeuvre the aircraft in roll direction.

6.1.2. Assumptions

- **Panel method for airfoil characteristics:** This is a simplification to determine lift characteristics of the airfoil, since it uses points distributed over the airfoil. If the method overestimates the lift coefficient this would result in bigger high lift devices needed. However, combined with DATCOM methods which account for statistical relations this is deemed accurate.
- **Airfoil:** Only one airfoil was considered in the wing design. Further optimization might improve aircraft characteristics.

6.2. General Wing Parameters

In this section, the general parameters of the aircraft wing are determined. Overall, the method from Raymer for wing geometry was used [35].

Surface area and aspect ratio

In the Midterm Report [36], it was decided that an aspect ratio of 9 would be chosen for the wing. This was based on multiple reference aircraft like the L 410 NG and the Beechcraft 1900D. A surface area, S, of 45 [m^2] was also chosen, based on the wing and power loading diagrams from the Midterm Report [36]. These were used as starting values. Later they were varied in the sensitivity analysis and iteration phase to optimize the design. In the final design S is 43 [m^2] and A is 9.302.

Wing sweep

Sweeping of an aircraft wing is usually done to reduce lift loss due to supersonic flow [35]. This is due to the speed of the wind perpendicular to the leading edge being lower than the actual velocity of the aircraft. In Figure 6.1, the effect of Mach number on theoretical and historical wing sweep is shown.

As can be seen in the figure, for a Mach of 0.3, which is the speed the H_2OPPER will fly at, both the historical trend as well as the theoretical ideal sweep are (almost) zero. It was therefore decided that the quarter-chord would be

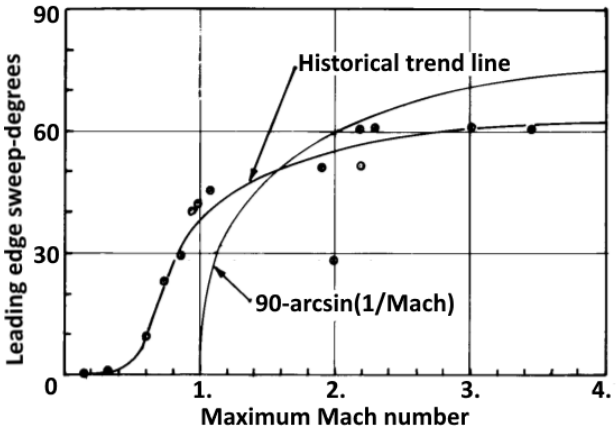

Figure 6.1: Historical and theoretical wing sweep as a function of Mach [34]

unswept, since the Mach number of about 0.3 is low enough so that transonic effects can be ignored, and it makes the structural design and packaging of wing components easier.

Taper ratio

Tapering of the wing is used to achieve a more elliptical lift distribution. Since the sweep also has an effect on this, an optimal taper ratio can be found as a function of sweep. The graph shown in Figure 6.2 shows this variation of taper ratio with quarter-chord sweep angle [35] for untwisted wings. This was valid to use since the wing of the H_2OPPER will also be untwisted.

As can be seen in the Figure, for unswept wings, a taper ratio of about 0.45-0.5 is common. For the H_2OPPER a taper ratio of 0.5 was chosen, as the aerodynamic characteristics did not vary much and more volume inside the wing box was usable.

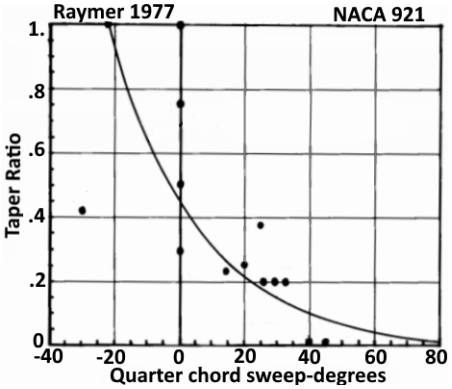

Figure 6.2: Historical taper ratio as function of sweep[34]

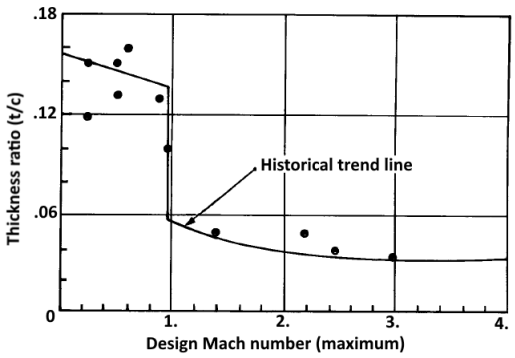

Figure 6.3: Thickness to chord for different Mach numbers[34]

Thickness to chord

Thickness ratio has a big effect on multiple parameters. First of all, the drag increases with increased thickness due to more flow separation. However, the maximum lift coefficient increases, as well as the stall angle. This is due to the bigger nose radius. Furthermore, increasing thickness has a considerable effect on wing weight, due to the larger moment of inertia, the wing can become significantly lighter. The historical trend for thickness-to-chord ratio also demonstrates this. As can be seen in Figure 6.3, for low speed aircraft, the thickness to chord tends to be higher. A value of 0.16 was chosen for the design Mach number of 0.3. This is on the high side of the statistical relation in Figure 6.3, which was done to accommodate more space for systems in the wing box.

6.3. Airfoil Selection

The NACA34016 airfoil was chosen for the wing of the H_2OPPER.

With the general wing topology established, the airfoil to be used was selected. It was decided that the airfoil would be a NACA 5-digit airfoil. This allowed for more customisation than the basic 4-digit airfoils, but would not require the complex and time-consuming mathematics and optimization of the 6-digit airfoils. For 5 digit NACA airfoil the following quote holds:

"The first digit, when multiplied by 3/2, yields the design lift coefficient (cl) in tenths. The next two digits, when divided by 2, give the position of the maximum camber (p) in percentage of chord. The final two digits again indicate the maximum thickness (t) in percentage of chord. For example, the NACA 23012 has a maximum thickness of 12%, a design lift coefficient of 0.3, and a maximum camber located 15% back from the leading edge." [1]

The thickness to chord was derived earlier. The design lift coefficient of the airfoil was determined by Equation 6.1. [2]

[1] URL: https://web.stanford.edu/~cantwell/AA200_Course_Material/The%20NACA%20airfoil%20series.pdf [Accessed on: 31-5-2021]

[2] Obtained from course AE2111-II Lecture 2 [Accessed on: 20-6-2021].

$$C_L = 1.1 \frac{1}{\frac{1}{2}\rho V_\infty^2} \left(\frac{W}{S} \right) \tag{6.1}$$

These desired cruise lift coefficient and thickness were converted to this NACA digits. This yields the NACA34016 airfoil.

To perform analysis on the aerodynamic characteristics of the airfoil in Xfoil, it is important to know the Reynolds number during flight. The Reynolds operating number, Re, at cruise is found using Equation 6.2.

$$Re = \frac{\rho V x}{\mu} \tag{6.2}$$

Where ρ is the air density, V is the velocity and x is the characteristic linear dimension, in this case the chord length. This mean chord length was found from $c = \frac{S}{b}$, where the wingspan was found from $b = \sqrt{SA}$.

6.4. High-Lift Device Sizing

Equations used in this section and next section all originate from AE2111-II Systems Design lecture 3. [3]

High lift devices are used during flight phases in which more lift is required. These are mainly take-off and landing. Therefore, to size the high lift devices, the required value for the maximum lift coefficient is needed, as well as the maximum lift coefficient without HLDs.

The first is used as one of the design parameters. Increasing the required $C_{L_{max}}$ will increase the weight and complexity of the high lift devices, but will result in better take-off and landing characteristics, reducing for example the maximum required power.

To determine the wing lift coefficient first the maximum lift coefficient of the NACA34016 airfoil was obtained from Xfoil using panel code to be 1.89 . The maximum lift coefficient of the wing is then approximated using the DATCOM method. For this method it first needs to be established whether the wing classifies as high or low aspect ratio, with Equation 6.3.

$$A > \frac{4}{(C_1 + 1)\cos \Lambda_{LE}} \tag{6.3}$$

Where C1 is a constant dependent on taper ratio as shown in Figure 6.4[4].

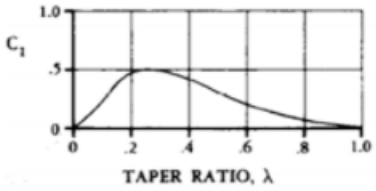

Figure 6.4: C1 as function of taper ratio

The wing maximum lift coefficient was then found using the semi-empirical DATCOM Equation 6.4.

$$C_{L_{\max}} = \left[\frac{C_{L_{\max}}}{C_{l_{\max}}} \right] C_{l_{\max}} + \Delta C_{L_{\max}} \tag{6.4}$$

In this equation, the ratio between the lift coefficient of the airfoil and the wing, $\left[\frac{C_{L_{\max}}}{C_{l_{\max}}} \right]$, can be obtained from Figure 6.5. As it is a function of leading edge sweep, this sweep was found with Equation 6.5, as it is a geometrical relation between the sweep at quarter chord and the taper ratio of the wing. $\Delta C_{L_{\max}}$ is a term

[3] Obtained from course AE2111-II Lecture 3 [Accessed on: 20-6-2021].
[4] Obtained from course AE2111-II Lecture 3 [Accessed on: 20-6-2021].

to account for Mach numbers above 0.2 . However, since this is for take-off and landing, this is irrelevant to the H_2OPPER, as take-off and landing speeds are far below Mach 0.2.

$$\tan \Lambda_{LE} = \tan \Lambda_{C/4} + [(1-\lambda)/\mathbf{A}(1+\lambda)] \tag{6.5}$$

The resulting leading edge sweep was 2.5 [°], which is still extremely small when looking at Figure 6.5[5], resulting in the ratio of wing to airfoil maximum lift coefficient assumed to be 0.9 .

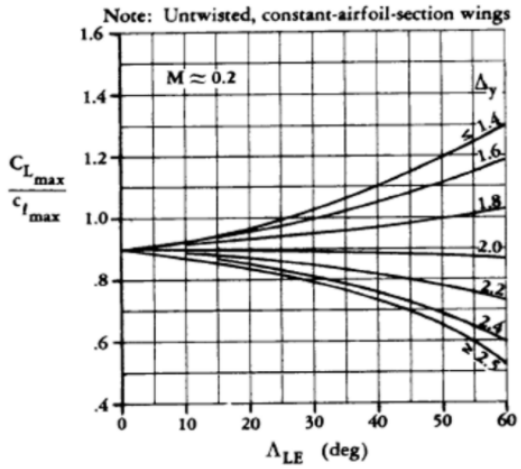

Figure 6.5: Wing to airfoil $C_{L_{max}}$ as function of sweep

Now that the wing lift coefficient and the required maximum lift coefficient are known, the required change in lift coefficient due to the HLDs is found. To calculate this $\Delta C_{L\max}$ based on high lift device parameters, Equation 6.6 is used.

$$\Delta C_{L\max} = 0.9 \Delta C_{l\max} \frac{Swf}{S} \cos \Lambda_{\text{hinge,line}} \tag{6.6}$$

Two parameters in this equation can be varied by the designer, namely the flapped area fraction, $\frac{Swf}{S}$, and $\Delta C_{l\max}$, a constant depending on the type of HLD chosen.

The flapped area is the ratio between the wing surface area influenced by the flap and the total wing area. This fraction can be different for leading edge and trailing edge high lift devices. In that case, Equation 6.6 is used twice, with different values for $\frac{Swf}{S}$ and $\Delta C_{l\max}$, and the $\Delta C_{L\max}$ is found by adding the two. The flapped area is visualised in Figure 6.6[6]. $\Delta C_{l\max}$ is dependent on flap type chosen, as mentioned earlier. The different values are listed in Figure 6.7 [7].

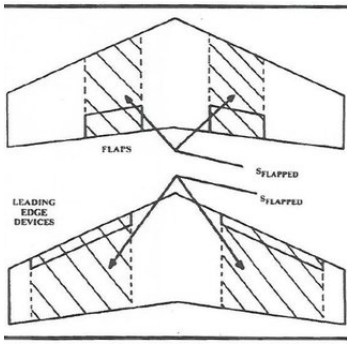

Figure 6.6: Flapped area

High lift device	$\Delta C_{l_{max}}$ when *fully deployed*
TE devices (flaps)	
Plain and split	0.9
Slotted	1.3
Fowler	$1.3 \cdot c'/c$
Double slotted	$1.6 \cdot c'/c$
Triple slotted	$1.9 \cdot c'/c$
LE devices	
Fixed slot	0.2
Leading edge flap	0.3
Kruger flap	0.3
Slat	$0.4 \cdot c'/c$

Figure 6.7: $\Delta C_{l\max}$ for different flaps

Then, multiple flap combinations and their required flapped area were investigated. For some of the flap types the change in lift coefficient is dependent on the ratio c'/c. Which is the chord with flap deployed over the chord. To find this, it was assumed c_f is a quarter of the chord. Then, since $c' = c + \Delta c$:

$$\frac{c'}{c} = 0.25 \frac{\Delta c}{c_f} + 1 \tag{6.7}$$

[5]Obtained from course AE2111-II Lecture 3 [Accessed on: 20-6-2021].
[6]Obtained from course AE2111-II Lecture 3 [Accessed on: 20-6-2021].
[7]Obtained from course AE2111-II Lecture 3 [Accessed on: 20-6-2021].

Where $\Delta c/c_f$ is taken from Figure 6.8. This Figure shows for different types of flaps, the relation between deflection angle and $\Delta c/c_f$, which is how much the flap extends in comparison to the original flap cord.

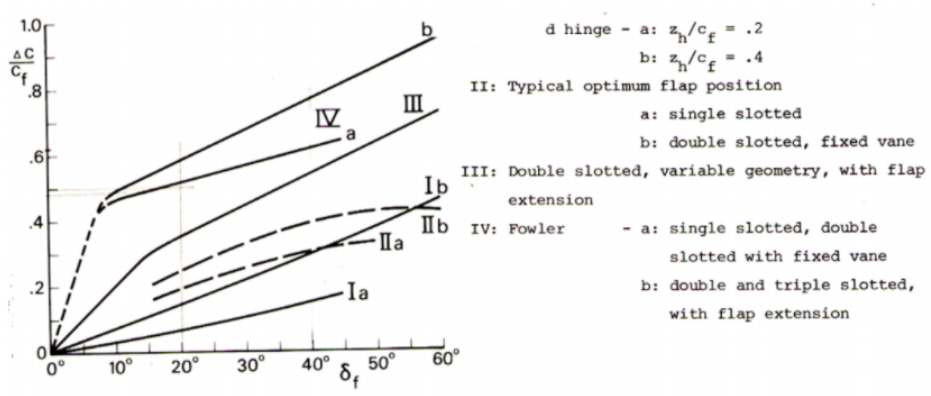

Figure 6.8: Chord extension for different flap types[8]

Chosen configuration

In the design of the H_2OPPER, the required take-off power has a big effect on the OEW. The mass of the propulsion group becomes significantly more when a higher maximum power is needed. Therefore, the relatively large value of 2.8 was chosen as a maximum lift coefficient. This value was a compromise between weight reduction in the propulsion group, while still maintaining an achievable maximum lift coefficient. A higher maximum lift also results in a higher take-off lift coefficient, which in turn ensures a slower take-off speed and thus a lower take-off power. From Equation 6.4 and the Xfoil analysis, a wing lift coefficient of 1.7 was found. This means the high lift devices have to add another 1.1 .

It was chosen to use Fowler flaps over a flapped area of 65% of the wing area. Taking into account a deflection of 40 [°] in Figure 6.8, the required ΔC_L can be obtained. It should be noted that these are rather unusual and complicated flaps for this aircraft type due to the many moving parts. However, a reduction of take-off power had such an impact on the design that this configuration was preferred. The (extra) weight for this complicated flap was taken into account in Subsection 7.2.1.

6.5. Aileron Sizing

Ailerons are used in order to control the roll of the aircraft. The required roll rate of the aircraft is determined by the CS-23 requirements. The H_2OPPER is a class-II aircraft, so it is expected to roll 45 degrees in 1.4 seconds, or 32 degrees per second, following from the CS-23 requirement. This roll rate was calculated using Equation 6.8.

$$P = -\frac{C_{l_{\delta_a}}}{C_{l_p}} \delta_a \left(\frac{2V}{b}\right) \tag{6.8}$$

In this equation, $C_{l_{\delta_a}}$, is the change in rolling moment coefficient due to the aileron deflection, it is calculated with Equation 6.9. C_{l_p} is the change in rolling moment coefficient due to the rolling of the aircraft itself, called roll damping coefficient, and is found with Equation 6.10. δ_a is the aileron deflection angle. For this aircraft, a deflection angle of 15°is used, as this is a typical value for this size aircraft. V and b are the flight velocity and span, respectively. The landing speed was used in this case, as this is the lowest velocity the aircraft will fly at and thus the limiting scenario.

$$C_{l_{\delta_a}} = \frac{2c_{l_\alpha}\tau}{S_{ref}b} \int_{b_1}^{b_2} c(y) y dy \tag{6.9}$$

Where c_{l_α} is the lift curve slope of the airfoil, retrieved from Xfoil. $c(y)$ is the chord length as a function of y along the half-span of the wing. This is a geometric relation described in Equation 6.11. τ is the aileron

effectiveness and is dependent on the aileron chord. The value of tau can be found in Figure 6.9.

The change in the rolling moment coefficient is called the roll moment coefficient:

$$C_{l_p} = -\frac{4\left(c_{l_\alpha} + c_{d_0}\right)}{S_{ref} b} \int_0^{b/2} y^2 c(y) dy \tag{6.10}$$

In this equation c_{d_0} is the airfoil zero lift drag, not from the wing. The other parameters have been mentioned before.

$$c(y) = \frac{2S_w}{(1+\lambda)b}\left[1 - \frac{1-\lambda}{b}|2y|\right]. \tag{6.11}$$

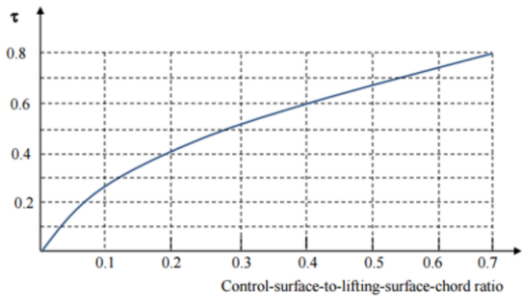

Figure 6.9: Aileron effective vs chord ratio[9]

Chosen configuration

Using the method described above, the aileron was sized. The parameters that can be varied are b1, b2 and τ, which means the start and stop location of the aileron on the wing, and the chord of the aileron (influencing τ). The ailerons are placed all the way to the end. This generates a bigger moment arm, increasing effectiveness. Furthermore, the speed over the wing behind the propeller is also higher, further improving the aileron control. The aileron chord was chosen to be a quarter of the aircraft chord, resulting in a τ of 0.48 . The span starting and ending point were then 80 and 95 % of the half-wing span, respectively. This was enough to reach a roll rate of 43 [deg/s].

7
Empennage Design

In this chapter, the process of the empennage design is described. Section 7.1 shows the functions and assumptions of the empennage design. Section 7.2 handles the longitudinal stability and control requirements and Section 7.3 focuses on satisfying the lateral stability and controllability requirements.

7.1. Subsystem Overview

The subsystem overview shows the functions and assumptions of the empennage design.

7.1.1. Functions

The function of the empennage is to provide stability and control in both longitudinal and lateral directions. Where the horizontal tail is responsible for stability and control in the longitudinal direction and the vertical tail is responsible for the lateral direction. The main objective of the empennage design is to achieve the smallest possible vertical and horizontal tail surfaces while maintaining sufficient stability and controllability.

7.1.2. Assumptions

- **Class-II weight estimation method is applicable to a hydrogen aircraft:** The class-II weight estimation method is developed for conventional kerosene aircraft. The weights estimated by this method are deemed accurate enough for application to a kerosene aircraft as most systems are not changed a lot by using hydrogen as fuel. It must be noted that fuel-specific systems, and other systems that heavily rely on the fuel used, were not estimated through class-II estimation but rather by self-made estimations.
- **Aircraft flies in steady, straight flight:** Basic flight mechanics formulas can be used. For overall energy and power calculations, this is reasonably accurate for this stage of design.
- **The contribution of $C_{Y_{A-h}}$ is neglected for vertical tail sizing:** due to their relatively small contribution and difficult predictability, their contribution was neglected. This allowed for more a simplified calculation that marginally overestimates C_{Y_β}.

7.2. Longitudinal Stability & Controllability

Empennage design has a large influence on the stability & controllability (S&C) of the aircraft. The horizontal tail must be sized such that the aircraft is both longitudinally stable and controllable for each loading configuration. Furthermore, to be longitudinally stable, the center of gravity of the entire aircraft must remain in front of the neutral point of the aircraft.

This section focuses on the longitudinal stability and controllability requirements, which are used for designing the horizontal tailplane. Furthermore, Subsection 7.2.1 and Subsection 7.2.2 show the process of determining the mass and c.g. estimations, which are inputted in the loading diagram of Subsection 7.2.3. Afterwards, a scissor plot is shown in Subsection 7.2.4, which is used to size the horizontal tailplane. When the tail is finalized, the elevators are sized in Subsection 7.2.5.

7.2.1. Class-II Weight Estimation

Whether the aircraft meets controllability and stability requirements largely depends on the aircraft's center of gravity range, which is influenced by the allocation and mass of all the different subsystems. Therefore, an estimate of each subsystem's mass must be calculated first. These masses are computed using a class-II weight estimation for cargo/transport of Raymer. This method uses empirical formulae, such as Equation 7.1 [35, p.395-409], to compute the mass of almost all the subsystems. In the Raymer formula below; W_{dg} is the design gross weight, N_z is the ultimate load factor, S_w is the wing surface area, A is the aspect

ratio, $(t/c)_{root}$ is the thickness to chord ratio at the root, λ is the taper ratio, Λ is the wing sweep and S_{csw} the control surface area.

$$W_{wing} = 0.0051 \cdot (W_{dg} \cdot N_z)^{0.577} \cdot (S_w)^{0.649} \cdot A^{0.5} \cdot (t/c)_{root}^{-0.4} \cdot (1+\lambda)^{0.1} \cdot (cos\Lambda)^{-1.0} \cdot S_{csw}^{0.1} \tag{7.1}$$

The class-II weight estimation method uses reference aircraft with conventional system configurations and does not take into account the combination of liquid hydrogen and fuel cells. This method is therefore not directly applicable to calculate the operating empty weight. A few changes have been made to make the method applicable to a hydrogen aircraft: firstly, kerosene-specific systems are not used in the weight estimation. Secondly, when a subsystem weight could not be estimated using a class-II weight estimation formula or a self-made estimation could already be made, the weight of the subsystem was added manually. This was, amongst others, the case for the fuel cells, hydrogen tanks and other hydrogen-specific aircraft weights.

Considering the results: the resulting OEW of the class-II weight estimation is higher than reference aircraft that have similar MTOW, as is shown in Subsection 13.2.7. This is expected due to the fact that hydrogen aircraft carry significantly lower fuel mass than kerosene aircraft. Whereas hydrogen aircraft carry a lot of weight due to hydrogen-specific subsystems such as the fuel cells and large radiators required to cool the liquid hydrogen, increasing OEW compared to kerosene aircraft.

Regarding the class-II weight estimation itself; it must be noted that this method can be rather inaccurate when looking at individual subsystem mass, especially since not all used parameters are accurately known. However, when summing up the individual elements, the accuracy of this method is increased. This is because component mass differs a lot between different aircraft of the same class, but the total mass differs significantly less. To avoid errors and inconsistencies, the computed subsystem weights were compared and verified with subsystem weights of similar reference aircraft [22, p.279-280], which is documented in Chapter 13. Therefore, the accuracy reached for the method applied on the entire aircraft is deemed accurate as the first estimate. Nevertheless, when more accurate estimates of the subsystems masses were developed, they were used to update/replace the class-II weight estimations. In all cases, it was found that the self estimated mass of the subsystems matched the order of magnitude of the class-II weight estimations, which validated both the self-made estimations and the class-II weight estimation.

It must be noted that the self-made estimations were preferred over the class-II weight estimations. However, it was not possible to design/determine the weights of each subsystem or part with the limited time at hand. Therefore, it was not achievable to substitute all the class-II weight estimations by self-made estimates, which constrained the weight estimation to partially self estimated and partially class-II weight estimation.

7.2.2. Center of Gravity Estimation

Now that the mass of each subsystem is determined, the corresponding center of gravity of each subsystem must be found to compute the centre of gravity of the operative empty weight. The c.g. of each subsystem is determined using preliminary design sketches that estimate and show the the allocation of each subsystem. Using these estimates and the weights computed earlier, the c.g. of the OEW is computed using Equation 7.2. In this equation, W_i and x_{cg_i} respectively are the weight and the x coordinate of center of gravity of part/subsystem i, which are documented in Table 16.8.

$$x_{cg} = \frac{\sum_{i=1}^{i=n} W_i \cdot x_{cg_i}}{\sum_{i=1}^{i=n} W_i} \tag{7.2}$$

7.2.3. Aircraft Loading Diagram

Having determined the c.g. of the aircraft at OEW for an assumed tail size and longitudinal wing position, the aircraft loading diagram could be made. One of the design choices to achieve balance of the aircraft is the distribution and location of systems and payload in the fuselage. This is incorporated in the aircraft loading diagram, which shows the change in c.g. location and aircraft mass during loading opera-

tions.

The aircraft carries 19 passengers in a three seats per row configuration, with one extra seat behind the sixth row. Furthermore, there is a luggage compartment located at the back of the fuselage. The aircraft loading diagram of the H_2OPPER is shown in Figure 7.1. As can be seen in the diagram, the loading operation starts by first loading the luggage in the luggage compartment, which results in the c.g. shifting backwards slightly. The aircraft is designed according to the window-aisle rule, which is common in aircraft design to keep the center of gravity shift to a minimum. However, this will not present the most extreme case. When only the aft or only the front seats are filled, the c.g. moves even more. To avoid this extreme case, cabin personal should ensure that the aircraft is boarded according the window to aisle rule.

Therefore, for the first extreme case the window seats are loaded from the front to the back, after which the aisle seats are loaded from the front to the back as well. For the other extreme case the same procedure is followed, but then from the back to the front. In Figure 7.1, the shift in c.g. because of the loading of passengers is shown by the round-shaped figures, which end up in the maximum zero fuel weight (MZFW) when fully loaded. Finally, the hydrogen is loaded into the fuel tank. This can only be done in one way, so the operation results in a straight line to the final filling point, which is at the maximum take-off weight (MTOW).

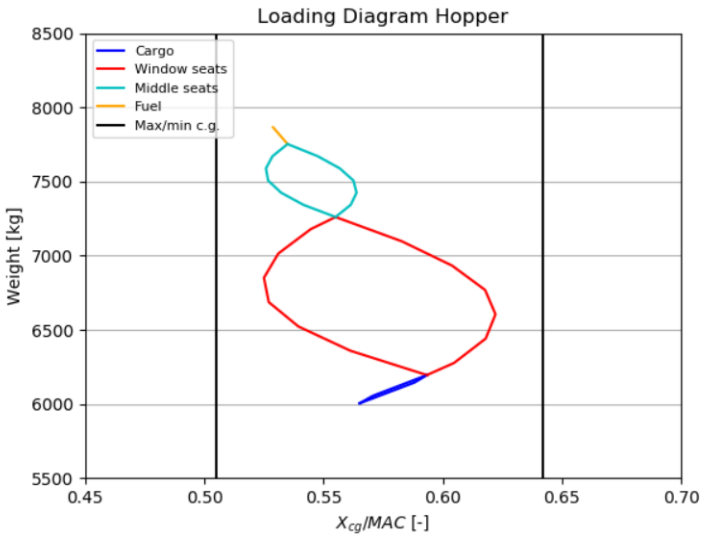

Figure 7.1: H_2opper loading diagram

The output of the diagram is the maximum range of the c.g. during loading operations, which can be used to determine if the aircraft is stable and controllable in Subsection 7.2.4. There has been taken a margin of 2% for the c.g. variations caused by passengers and attendants moving, since these movements are significantly present, but do not cause large c.g. changes. The resulting c.g. range ranges from 50.49% to 64.21% as percentage of the MAC.

7.2.4. Scissor Plot

Equations used in this section all originate from AE3211-I Systems Engineering & Aerospace Design lecture 4 & 5. [1], [2]

With the c.g. range determined, the scissor plot of the aircraft could be made. This scissor plot determines if the aircraft is both stable and controllable and can be used to size the horizontal tail surface.

For an aircraft to be stable, the c.g. must always stay in front of the neutral point of the aircraft. This neutral

[1] AE3211-I Lecture 4, URL: `https://brightspace.tudelft.nl/d2l/le/content/293146/viewContent/1909573/View` [Accessed on: 15-11-2021].

[2] AE3211-I Lecture 5, URL: `https://brightspace.tudelft.nl/d2l/le/content/293146/viewContent/1909574/View` [Accessed on: 15-11-2021].

point is the point through which the resultant change in lift acts when the angle of attack is changed. Using moment equations, the most aft CG location can be calculated. To be able to size the horizontal tail, this equation is written with S_h/S on the left hand side, as shown in Equation 7.3. In this equation, $C_{L_{\alpha_h}}$ is the change of tail lift coefficient due to a change in angle of attack, $C_{L_{\alpha_{A-h}}}$ is the change of aircraft minus tail lift coefficient due to a change of α. $\frac{d\epsilon}{d\alpha}$ is the change in downwash due to delta α. l_h is the moment arm between the wing and the tail, c is the chord and $\frac{V_h}{V}$ is the tail over wing airflow velocity ratio, which equals 0.95 for fin-mounted stabilizers. Finally, $\bar{x}_{cg}$ and $\bar{x}_{ac}$ are the x coordinates of the center of gravity and aerodynamic center respectively.

$$\frac{S_h}{S} = \frac{1}{\frac{C_{L_{\alpha_h}}}{C_{L_{\alpha_{A-h}}}}\left(1-\frac{d\epsilon}{d\alpha}\right)\frac{l_h}{\bar{c}}\left(\frac{V_h}{V}\right)^2}\bar{x}_{\text{c.g.}} - \frac{\bar{x}_{ac}-0.05}{\frac{C_{L_{\alpha_h}}}{C_{L_{\alpha-h}}}\left(1-\frac{d\epsilon}{d\alpha}\right)\frac{l_h}{\bar{c}}\left(\frac{V_h}{V}\right)^2} \tag{7.3}$$

Equation 7.3 is the stability curve of the aircraft. It represents a S_h/S curve where the c.g. range of the aircraft must be to the left of, which is achieved by having the most aft c.g. in front of the neutral point. A stability margin of 5% of the MAC was taken into account for the stability curve, which means that an additional 5% margin between $\bar{x}_{cg}$ and $\bar{x}_{np}$ is required. Furthermore, there should always be a minimum control force for the pilot, which would not be the case if the most aft c.g. would be directly on the stability curve.

For an aircraft to be controllable the pilot needs to be able to change the parameter C_{L_h} by deflecting the elevator. Again, using moment equations, the most forward c.g. location can be calculated, as shown in Equation 7.4. As with the stability curve, this equation is also written with S_h/S on the left hand side.

$$\frac{S_h}{S} = \frac{1}{\frac{C_{L_h}}{C_{L_{A-h}}}\frac{l_h}{\bar{c}}\left(\frac{V_h}{V}\right)^2}\bar{x}_{cg} + \frac{\frac{C_{m_{ac}}}{C_{L_{A-h}}} - \bar{x}_{ac}}{\frac{C_{L_h}}{C_{L_{A-h}}}\frac{l_h}{\bar{c}}\left(\frac{V_h}{V}\right)^2} \tag{7.4}$$

To compute the stability and controllability curves, first $\bar{x}_{ac}$ must be computed. The aerodynamic center of the aircraft without the tail was calculated using Equation 7.5, where the first term is the aerodynamic center of the wing and is located at 0.25 times the MAC, the second and third terms are the contributions by the fuselage. In this equation, b_f and h_f are the outer fuselage width and height at the wing intersection respectively, l_{fn} is the length from the nose to the leading edge of the wing and c_g is the mean geometric chord.

$$\bar{x}_{ac} = \bar{x}_{ac_w} - \frac{1.8}{C_{L_{\alpha_{A-h}}}}\frac{b_f h_f l_{fn}}{S\bar{c}} + \frac{0.273}{1+\lambda}\frac{b_f c_g (b-b_f)}{\bar{c}^2(b+2.15b_f)}tan(\Lambda_{1/4}) \tag{7.5}$$

The theoretical lift curve slope of a planar lifting surface, be it the wing or the horizontal stabilizer, can be calculated with:

$$C_{L\alpha} = \frac{2\pi A_h}{2+\sqrt{4+\left(\frac{A\beta}{\eta}\right)^2\left(1+\frac{\tan^2\Lambda_{0.5C}}{\beta^2}\right)}} \tag{7.6}$$

where A is the aspect ratio, η is the airfoil efficiency, $\Lambda_{0.5C}$ is the sweep at the half-chord, and β is the Mach compressibility correction, given by $\sqrt{1-M^2}$.

The lift curve slope of the aircraft-minus-tail is given by Equation 7.7. Where $\frac{S_{net}}{S}$ is the ratio of wing area outside the fuselage to the total wing area.

$$C_{L_{\alpha_{A-h}}} = C_{L_{\alpha_w}}\left(1+2.15\frac{b_f}{b}\right)\frac{S_{net}}{S} + \frac{\pi}{2}\frac{b_f^2}{S} \tag{7.7}$$

The moment coefficient at the aerodynamic center, which is needed for the controllability curve, is computed using Equation 7.8. The first term in this equation is the wing contribution. The second term is the

change in zero-lift wing pitching moment due to flap deflection which follows from wind tunnel tests, this value is taken from an empirical data set which was matched with the Hopper's $\Delta C_{L_{max}}$ and equals -0.33 [3]. Lastly, the third term is the contribution by the fuselage, where $C_{L_{\alpha_{A-h}}}$ is now computed at 1.1 times the stalling velocity. Here, $C_{m_{0_{airfoil}}}$ and C_{L_0} are airfoil characteristics that are taken from XFOIL for the NACA34016 airfoil.

$$C_{m_{ac}} = C_{m_{0_{airfoil}}} \left(\frac{A cos^2 \Lambda}{A + 2cos\Lambda} \right) + \Delta_{flap} C_{m_{ac}} - 1.8 \left(1 - \frac{2.5 b_f}{l_f} \right) \frac{\pi b_f h_f l_f}{4 S \bar{c}} \frac{C_{L_0}}{C_{L_{\alpha_{A-h}}}} \tag{7.8}$$

Finally, the wing downwash gradient is calculated with Equation 7.9. In this equation $\frac{K_{\epsilon_\Lambda}}{K_{\epsilon_{\Lambda=0}}}$, is the term that accounts for wing sweep angle which equals to 1 for zero wing sweep. Furthermore, r is two times the distance between the aerodynamic center of the wing and tail divided by the wing span. Lastly, m_{tv} is the distance between the horizontal tail and the vortex shed plane divided by half of the wing span, which equals 0.22 .

$$\frac{d\epsilon}{d\alpha} = \frac{K_{\epsilon_\Lambda}}{K_{\epsilon_{\Lambda=0}}} \cdot \left(\frac{r}{r^2 + m_{tv}^2} \frac{0.4876}{\sqrt{r^2 + 0.6319 + m_{tv}^2}} + \left[1 + \left(\frac{r^2}{r^2 + 0.7915 + 5.0734 m_{tv}^2} \right)^{0.3113} \right] \left\{ 1 - \sqrt{\frac{m_{tv}^2}{1 + m_{tv}^2}} \right\} \right) \frac{C_{L_{\alpha_w}}}{\pi A} \tag{7.9}$$

Putting the stability and controllability curves together results in the scissor plot as shown in Figure 7.2. As explained before, the c.g. of the aircraft has to be in between the stability and controllability curve. The c.g. range calculated with the aircraft loading diagram in Subsection 7.2.3 was implemented in the scissor plot to determine the minimum required tail surface. Furthermore, the c.g. range was optimized by changing the seating, luggage compartment and fuel tank locations. Note that a safety margin is added to stability but not to controllability, this is to account for required "control feel", which is only limiting the backwards cg position and is therefore abundant for the controllability limit [4].

Figure 7.2: Scissor plot of the H_2opper

Using the scissor plot, the horizontal tail is sized by an iteration procedure. This iteration had the center of gravity of the wing and surface area of the horizontal tail as inputs, and consisted of selecting a c.g. for

[3] AE3211-I Lecture 5, URL: https://brightspace.tudelft.nl/d2l/le/content/293146/viewContent/1909574/View [Accessed on: 15-11-2021].

[4] AE3211-I Lecture 5, URL: https://brightspace.tudelft.nl/d2l/le/content/293146/viewContent/1909574/View [Accessed on: 15-11-2021].

the wing where the c.g. range of the aircraft could be moved as much to the bottom as possible. Then, the inputted tail surface area was altered until the c.g. range in the graph did not coincide with one of the stability and control (S&C) graphs while keeping the S_h minimised. This process was repeated until a minimal surface area that met the S&C requirements was reached. This led to a final horizontal tail surface area of 9.0 [m^2], where 10% contingency is included to make the surface area of the horizontal tail to wing ratio more consistent to reference aircraft, as can be read in Subsection 13.2.11. This contingency also accounts for the weight uncertainties of the subsystems that could not be estimated from designing operations but had to be estimated from class-II procedures.

7.2.5. Elevator Sizing

The elevator is the only control surface used for longitudinal stability. To size the elevator, multiple things need to be kept in mind. First, the stick force needed to control the elevator should be within an allowable range. However, as the aircraft will be controlled by a fly-by-wire system, the stick forces can be determined by the controller. This is therefore no issue. Next to the stick force, the elevator should be able to keep the aircraft stable by producing a counteracting moment with respect to the lift from the wing.

For the sizing of the elevator, an assumption was used based on a ratio between loads on the horizontal tail and the elevator. From Raymer [34, p.347], it is obtained that a typical horizontal tail loading condition leads to an elevator carrying 40 [%] of the load with respect to the horizontal tail, but in opposite direction. In addition, the ratio between the elevator and the tail have been determined for two reference aircraft; the L 410 NG and the DHC-6. The ratios of these aircraft are 0.463 and 0.35 respectively [37]. These aircraft were chosen as they have both a high-wing configuration and carry the same amount of passengers. From these numbers, a guess can be made that the surface ratio will be around 0.4 .

By using this method, the effects on stability are not taken into account. It is recommended to use a more detailed method of sizing of the elevator in later phases. This method should include the aerodynamic forces and moments around the aircraft, and follow set requirements, such as minimum rotational acceleration.

This method can be justified for this phase, as the elevator currently has little influence on other design parts of the H_2OPPER. Only the weight of the empennage, used to determine the structure of the aircraft, includes a parameter based on the elevator. The weight of the elevator however is expected to change only moderately and therefore this method can be adopted in this phase.

7.3. Lateral Stability and Controllability

The lateral stability and controllability of an aircraft is largely dependant on its vertical tail. For its sizing there exist two critical conditions [38]. The first one being the requirement of the aircraft being able to land in 30 knots crosswind. Secondly, the aircraft must be able to maintain straight flight at the minimum control speed V_{MC} when the critical engine becomes inoperative, without exceeding a bank angle φ of more than 5°as required per CS-23 regulations. In this section a first conceptual design of the vertical tail was made to function as an initial estimate with low accuracy. Afterwards, the lateral stability was investigated in more detail allowing for a more detailed design iteration. Finally, the three conditions were investigated, where the tail was sized for the driving critical condition.

7.3.1. Initial Statistical Volumetric Ratio Sizing

The first step in the vertical tail design process was the rough sizing of the tail volume. This is a conceptual design approach described by D. Ciliberti [39]. It is a purely statistical method that relies on the fact that aircraft with similar volume coefficients also generally have comparable stability characteristics.

The non dimensional vertical tail volumes ($\frac{S_v l_v}{Sb}$) of four high wing, T-tail aircraft (EMB-120, ATR-42, ATR-72, Q400) were plotted with respect to their wing surface area. As shown in Figure 7.3 linear trend-line was then constructed and, in combination with the known wing surface area, was used to determine a initial reference tail volume. This method was continuously used throughout the sensitivity analysis and iteration procedures to function as a sanity check.

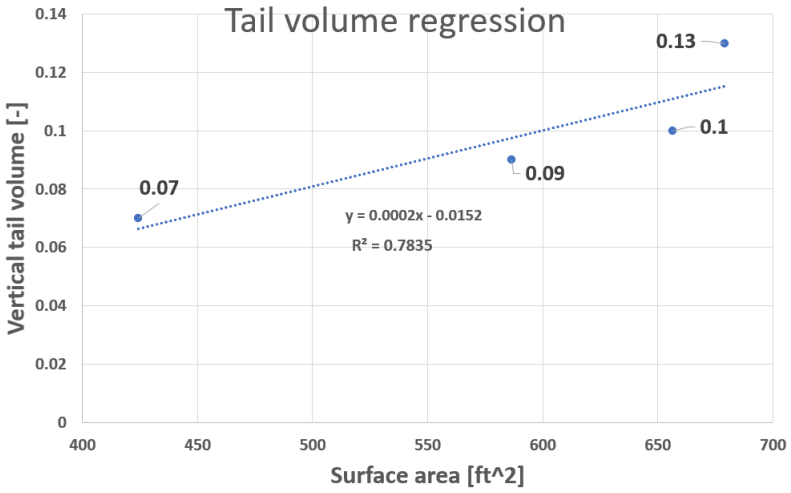

Figure 7.3: Linear regression of vertical tail volume coefficients

Following the tail aspect ratio A_v and taper ratio λ_v guidelines created by D.P. Raymer [34] a A_v of 1.2 and a λ_v of 0.8 were chosen as a first estimate.

7.3.2. Stability and Control Derivatives

This section first focuses on finding the rough sizing of the tail volume in Subsection 7.3.1. After which, the stability and control derivatives are worked out in Subsection 7.3.2, to make a more accurate sizing possible. In Subsection 7.3.3, the equations of motion for one engine inoperative are applied to the sizing procedure of the vertical tail. The method discussed in the past subsections are then used to create a tool to make the actual sizing and iteration possible, and following the sizing and iteration is executed in Subsection 7.3.4. Finally, Section 7.4 shows recommendations for future vertical tail sizing procedures.

In order to make a more accurate estimation that corresponds to the chosen design configuration, the lateral stability/control derivatives and the corresponding non dimensional equations of motion were used. Stability derivatives are constants that describe the aircraft's natural reaction towards external forces or moments. Control derivatives are constants that indicate how the forces on the aircraft change by changing the respective control service deflection. Each relevant derivative and the corresponding estimation method is further elaborated below.

Stability derivative C_{Y_V}:
This stability derivative represents the non dimensional force in the lateral direction on the vertical tail. This force is dependant on both the aircraft natural reaction to a change in side-slip angle β, which is defined as $C_{Y_{\beta_V}}$ and on the lateral force that arises from a change in rudder deflection δ_r, which is defined as $C_{Y_{\delta_r}}$. C_{Y_V} is then calculated through:

$$C_{Y_V} = C_{Y_{\beta_V}} \beta + C_{Y_{\delta_r}} \delta_r \tag{7.10}$$

The $C_{Y_{\delta_r}}$ and $C_{Y_{\beta_V}}$ are heavily dependant on the disturbances caused by the rest of the aircraft configuration. These disturbances are generally difficult to estimate and are usually only known with relative accuracy after wind-tunnel testing. Hence the Vertical tail Design Stability and Control (VeDSC) method from [40] and [39] was used. This method was investigated to be suitable for regional turboprop and commuter airplanes and is thus considered as a viable method for calculating the stability and control derivatives, however, the sizing method is not applicable since the one engine inoperative condition is not used as a critical condition. VeDSC provides a way to estimate these force derivatives using a combination of configuration dependant correction factors, the isolated vertical tail lift curve slope $C_{L_{\alpha_V}}$, the vertical tail to wing ratio $\frac{S_V}{S}$ and the rudder effectiveness τ. $C_{L_{\alpha_V}}$ could be estimated using the Helmbold-Diederich [41] formula:

$$C_{L_{\alpha_v}} = \frac{2\pi A_v}{2 + \sqrt{\frac{B^2 A_v^2}{\kappa^2}\left(1 + \frac{\tan^2 \Lambda_{c/2}}{B^2}\right) + 4}} \tag{7.11}$$

Where A_v is the vertical tail aspect ratio, $\Lambda_{c/2}$ is the half cord sweep of the vertical tail, B is the compressibility parameter: $\sqrt{1-M^2}$ where M is the mach number. κ is the ratio of section lift-curve slope and is assumed to be equal to $1/B$ [42].

The stability derivative $C_{Y_{\beta_V}}$ was estimated using:

$$C_{Y_{\beta_V}} = -K_F K_W K_H C_{L_{\alpha_V}} \frac{S_V}{S} \tag{7.12}$$

Where K_F is the fuselage correctional factor, K_W the wing correctional factor and K_H the horizontal stabilizer correctional factor. These factors could readily be obtained from figures 4.49, 4.51 and 4.53 in [40]. Note that the sign of this derivative should be negative since a positive β leads to a lateral force in negative Y-direction.

In similar fashion the control derivative $C_{Y_{\delta_r}}$ could be estimated using:

$$C_{Y_{\delta_r}} = K_{\delta_r} \tau C_{L_{\alpha_V}} \frac{S_V}{S} \tag{7.13}$$

Where K_{δ_r} is the rudder correction factor that was estimated using equation 4.18 from [40]. The rudder effectiveness was more difficult to estimate. The Roskam estimator, used in the VeDSC method, was not obtainable through the resources available. Hence initially the semi-empirical formula for τ from [43] was used as an estimate. However, results from [44] showed that the rudder effectiveness is heavily dependant on its shape and dimensions. Where CFD and wind-tunnel tests revealed that a much higher effectiveness could be achieved than initially estimated by the semi-empirical formula. The sign of $C_{Y_{\delta_r}}$ is positive since a positive deflection leads to a force in positive Y direction.

Stability derivative C_{n_β}:
This stability derivative represents the non dimensional moment that acts around the vertical axis of the aircraft caused by a change in β. A positive C_{n_β} means that the aircraft will naturally create a counteracting stabilizing moment for increasing moment, which is highly desirable for stability. This derivative generally has negative contributions from the fuselage, wing and engines; and a strong positive contribution from the vertical tail. Meaning C_{n_β} can be described as:

$$C_{n_\beta} = C_{n_{\beta_f}} + C_{n_{\beta_p}} + C_{n_{\beta_w}} + C_{n_{\beta_v}} \tag{7.14}$$

To estimate the contributions $C_{n_{\beta_f}}$, $C_{n_{\beta_p}}$ and $C_{n_{\beta_w}}$ from the fuselage, propeller and wing respectively, a semi-empirical method presented by Torenbeek [38] was used. This method was preferred over the improved VeDSC method due to its relative simplicity allowing for quicker iteration later in the design phase.

For $C_{n_{\beta_f}}$, the following equations Equation 7.15 and Equation 7.16 and corresponding inputs from Figure 7.4 were used:

$$C_{n_{\beta_f}} = -k_\beta \frac{S_{fs} l_f}{Sb} \left(\frac{h_{f_1}}{h_{f_2}}\right)^{\frac{1}{2}} \left(\frac{b_{f_2}}{b_{f_1}}\right)^{\frac{1}{3}} \tag{7.15}$$

$$k_\beta = 0.3\frac{l_{cg}}{l_f} + 0.75\frac{h_{f_{max}}}{l_f} - 0.105 \tag{7.16}$$

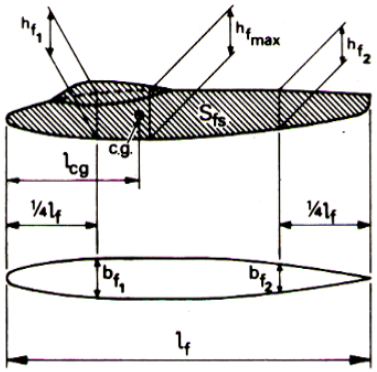

Figure 7.4: Fuselage geometry in relation to the yawing moment due to sideslip [38]

The wing contribution $C_{n_{\beta_w}}$ was taken to be a set value of -0.017 for all high wing configurations according to the Torenbeek method. It was recognized that this value should most likely vary for different high wing designs, as was accounted for in the VeDSC method. However, since the wing contribution to C_{n_β} in total is generally only around 10-15%, the absolute discrepancy caused by this assumption was considered to be small enough to prefer the faster estimation method from Torenbeek.

The contribution of the propeller was estimated using:

$$C_{n_{\beta_p}} = -0.053 B_p \sum \frac{l_p D_p^2}{Sb} \tag{7.17}$$

Where l_p was the longitudinal distance between the propeller and the centre of gravity of the aircraft, B_p the number of propeller blades and D_p the propeller diameter.

Finally $C_{n_{\beta_v}}$ was again estimated using the improved VeDSC method since the Torenbeek method for this derivative required the still unknown values for the flow disturbance at the vertical tail again. Meaning that $C_{n_{\beta_v}}$ is estimated by:

$$C_{n_{\beta_v}} = K_F K_W K_H C_{L_{a_v}} \frac{l_v}{b} \frac{S_v}{S} \tag{7.18}$$

Where the K-factors represent the same correction factors from the different parts of the configuration as in Equation 7.12 again. It is essentially C_{Y_V} multiplied with the non dimensional arm: the vertical tail length l_v divided by the span b.

Control derivative $C_{n_{\delta_r}}$:
Although this derivative was not explicitly mentioned or calculated, it was reasoned that it could be derived in similar fashion as for $C_{n_{\beta_v}}$. Hence $C_{n_{\delta_r}}$ was defined as:

$$C_{n_{\delta_r}} = K_{\delta_r} \tau C_{L_{\alpha_V}} \frac{l_v}{b} \frac{S_V}{S} \tag{7.19}$$

Note, however, that the sign of this derivative should be negative. Since for a positive rudder deflection a moment is created to further increase β.

7.3.3. One Engine Inoperative Equations of Motion

For a two engine aircraft the critical load case for the vertical tail is generally the one engine inoperative case. The vertical tail then has to compensate for the moment created by the asymmetric thrust vector, as can be seen in the left sketch of Figure 7.5.

However, to compensate for this lateral force created by the vertical tail a bank angle φ needs to be introduced so that the weight vector also gets a balancing lateral component in opposite direction as is depicted in the right sketch of Figure 7.5.

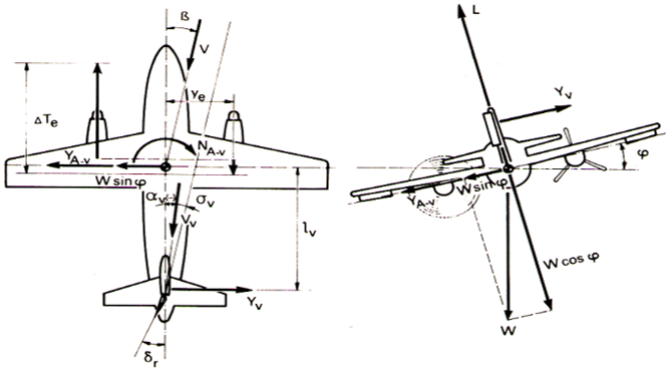

Figure 7.5: Flight on asymmetric power [38]

Torenbeek presented a formula to do an initial calculation of the required $\frac{S_v}{S}$ for this critical case:

$$\frac{S_v}{S} = \frac{C_L \frac{y_e}{l_v} \frac{\Delta T_e}{W} + \beta \left(C_{n_\beta}\right)_{\text{A-h}} \frac{b}{l_v}}{\tau_r \delta_r - \left(\beta - \sigma_v\right)} \cdot \frac{1}{\left(\frac{V_v}{V}\right)^2 C_{Y_{v_\alpha}}} \tag{7.20}$$

However, as mentioned earlier in this section, the disturbance factors σ and $\frac{V_v}{V}$ are generally very difficult to estimate. Furthermore, that also meant that it was also not possible to verify the $\varphi < 5°$ condition. Hence a different approach was taken. Using the simplified equations of motion from [45], the one engine inoperative case could be described in matrix form by:

$$\begin{bmatrix} C_L & C_{Y_\beta} & 0 & C_{Y_{\delta_r}} \\ 0 & C_{l_\beta} & C_{l_{\delta_a}} & 0 \\ 0 & C_{n_\beta} & 0 & C_{n_{\delta_r}} \end{bmatrix} \begin{bmatrix} \varphi \\ \beta \\ \delta_a \\ \delta_r \end{bmatrix} = - \begin{bmatrix} 0 \\ 0 \\ C_{n_e} \end{bmatrix} \tag{7.21}$$

Since the second row of this equation is independent of $\frac{S_v}{S}$, and δ_a has no influence on the other two equations in this simplified form, this row was neglected. Meaning that the only non dimensional coefficient that has not been described yet is C_{n_e}. This is the non dimensional moment created by the asymmetric thrust, that is defined as:

$$C_{n_e} = \frac{\Delta T \cdot y_e}{\frac{1}{2}\rho V^2 S b} \tag{7.22}$$

It is important to note that the magnitude of C_{n_e} varies inversely to the square of the airspeed V. The minimal speed at which an aircraft is able to maintain straight flight with $\varphi < 5°$ is defined as the the minimum control speed V_{MC}. To eliminate this free variable, the maximum allowed control speed of $1.2 \cdot V_{stall}$ as per CS-23 regulations was used as a constraint.

The thrust force ΔT was then estimated by first calculating C_L with:

$$C_L = \frac{W}{\frac{1}{2}\rho V^2 S} \tag{7.23}$$

This was then followed by assuming constant airspeed, meaning that the thrust equalled drag:

$$\Delta T = D = \left(C_{D_0} + \frac{C_L^2}{Ae\pi} \right) \frac{1}{2} \rho V^2 S \tag{7.24}$$

Finally, to be able to derive the required $\frac{S_v}{S}$, the last row from Equation 7.21 representing the non dimensional moments around n was used. Where the $\frac{S_v}{S}$ was separated from its respective control/stability derivatives leading to:

$$\frac{S_v}{S} = \frac{-C_{n_e} - \left(C_{n_\beta}\right)_{A-h} \cdot \beta}{K_F K_W K_H C_{L_{a_v}} \frac{l_v}{b} \cdot \beta + K_{\delta_r} \tau C_{L_{\alpha_V}} \frac{l_v}{b} \cdot \delta_r} \tag{7.25}$$

Where $\left(C_{n_\beta}\right)_{A-h}$ is the summation of $C_{n_{\beta_f}}$, $C_{n_{\beta_p}}$ and $C_{n_{\beta_w}}$, which are all independent of $\frac{S_v}{S}$. Furthermore, δ_r was set to be the maximum rudder deflection of 30° based on reference aircraft from [38]. Finally β was initially set to be the angle a 30 knts crosswind would cause as per CS-23 regulation.

To check whether for this calculated $\frac{S_v}{S}$ the bank angle would be below 5°, the first row of Equation 7.21 was rewritten to:

$$\varphi = -\frac{C_{Y_\beta} \beta + C_{Y_{\delta_r}} \delta_r}{C_L} \tag{7.26}$$

If φ exceeded the 5° condition, due to the inverse relation with β, the side-slip could be increased to reduce the bank angle below 5° again.

7.3.4. Design Tool

The method discussed in the previous subsections was recreated in the form of a tool, allowing for quick iterations later in the design phase. The initial values for A_v and λ_v from Subsection 7.3.1 were used to calculate first estimates.

When the possibility of wingtip-mounted engines was investigated, initially a very large surface area was found. However, by increasing the rudder size and dimension the rudder effectiveness could be significantly increased. Using roughly the same design as in [44], similar effectiveness of 0.8 was deemed reasonable. Furthermore, the horizontal tail surfaces were able to be sized small enough to be fitted in front of the large rudder at half the span of the vertical tail by also increasing the taper ratio of the vertical tail. Hereby reducing the loads on the vertical tail and allowing for a higher aspect ratio, which in turn improved the isolated vertical tail lift curve slope and thus reduced the vertical tail size in total. Lastly, also the fuselage was made longer to increase the tail length l_v. Ultimately the vertical tail was sized to have a S_v of 9.8 [m^2], an A_v of 2.2 and a λ_v of 0.5 [rad].

7.4. Recommendations

In Section 7.2, the sizing of the horizontal tail was presented. A result of the sizing was that the ratio between the surface area of the horizontal tail over the wing is a bit lower than that of the reference aircraft. Because of this, a 10% contingency was added to the surface area of the horizontal tail. It is recommended that all the subsystems and parts that are not yet designed, are designed such that a self-made weight estimation can be performed to overrule class-II weight estimation. When all subsystems masses are self-made estimations the 10% contingency could be decreased, as the uncertainty for the weight estimation is smaller for self-made estimations than for class-II weight estimations.

In Section 7.3 a preliminary vertical tail design was presented based on estimated stability and control derivatives. However, due to the high sensitivity of the derivatives, the rudder deflection on the vertical tail size and the relatively high uncertainty of these constants, further validation of this tail design needs to be done. A suitable approach would be simulating the design in CFD, followed by wind tunnel testing of a scale model of the total configuration. This would allow for more accurate estimates on the control and stability derivatives and further iteration of the shape and size of the vertical tail. Furthermore, the Dutch roll characteristics, which depend on the ratio between C_{n_β} and C_{l_β} need further investigation. Although Dutch roll might not be directly related to the safety of the aircraft, it can still cause significant discomfort for both passengers and the pilots.

8
Aerodynamic Characteristics

In this chapter the main aerodynamic characteristics of the H_2OPPER aircraft will be investigated. First, the assumptions that are made are listed inSection 8.1. Then, in Section 8.2 an estimation will be made regarding the zero lift drag, C_{D_0}. Furthermore, the spanwise lift distribution, otherwise known as the Oswald efficiency factor, will be analyzed in more detail in Section 8.3. Finally, in Section 8.4 the placement of the engines and its aerodynamic effect will be discussed in-depth.

8.1. Assumptions

- **Wetted area of tail is twice its respective surface area:** Allows for more design-specific results while only slightly underestimating the wetted area by not accounting for the curvature of the wings.
- **The airflow is assumed to be isentropic:** The flow is assumed to be isentropic, i.e.: the entropy remains constant, which means that the flow a undergoes a reversible adiabatic process. This assumption is made to simplify calculations and leads to a small error in the estimation of the Reynolds number. However, the effect of this error is deemed negligible.

8.2. Zero-Lift Drag Estimation

In order to achieve a more accurate estimate for the zero-lift drag C_{D_0}, a semi-empirical method by P. M. Sforza was adopted [46]. This method relies on estimating the total wetted area of the design S_w, together with an estimate of the Reynolds number Re_l that was then inputted into a semi empirical formula to estimate C_{D_0}:

$$C_{D_0} = \left(0.00258 + 0.00102 \cdot e^{-6.28\times10^{-9}Re_l} + 0.00295 \cdot e^{-2.01\times10^{-8}Re_l}\right)\frac{S_w}{S} \tag{8.1}$$

The methods to estimate the wetted areas of the wing, fuselage and nacelles presented by Sforza were deemed to be relevant enough for this design. However, as the tail wetted area was determined through a statistical relation with the wing area, the choice was made to use a different estimate here. Instead of the statistical relation, the vertical and horizontal tail areas were doubled and then summed together to form a quick and design-specific estimate, which meant that C_{D_0} could also be iterated for the tail size.

Furthermore, the statistical correlation presented by Sforza for estimating the characteristic length $\frac{S_w}{b}$ was not used since S_w could be calculated directly from the method earlier in that paper. For the Reynolds number, the design cruise conditions were used. Making the final calculation of the C_{D_0} possible. However, due to the substantial semi-empirical nature of this estimation and the high impact of C_{D_0} on all other system and design characteristics, a larger contingency of 20 % was used. This was iterated multiple times before arriving at a final value of 0.251 .

8.3. Oswald Efficiency Estimation

The Oswald efficiency factor is of big influence in the amount of induced drag experienced by the aircraft. Getting a good approximation of this factor in the preliminary design is challenging. Usually, testing or at least CFD analysis is necessary to get a correct value. In [47], a method for preliminary estimations is established. Since existing methods based on theories often overestimate the Oswald factor, the method presented in this paper combines those with a statistical approach. This results in their method having deviations from reality of under 4% for conventional aircraft that do not have dihedral or winglets. Therefore this method is deemed accurate in the analysis of this aircraft.

First, a theoretical Oswald efficiency factor based on sweep and taper ratio is derived. This is done by first

using the polynomial curve-fitted on the work of Horner [48] in Equation 8.2.

$$f(\lambda) = 0.0524\lambda^4 - 0.15\lambda^3 + 0.1659\lambda^2 - 0.0706\lambda + 0.0119 \tag{8.2}$$

However, for the taper ratio λ in this formula, the sweep of the wing should be taken into account, which is done using Equation 8.3. Since the wing of the H_2OPPER does not have sweep, this formula reduces to a constant, which it was designed to do for unswept wings. Then, the theoretical Oswald factor is found with Equation 8.4.

$$\Delta\lambda = -0.357 + 0.45 \cdot e^{0.0375\varphi_{25}} \tag{8.3}$$

$$e_{\text{theo}} = \frac{1}{1 + f(\lambda - \Delta\lambda) \cdot A} \tag{8.4}$$

As mentioned earlier, this theoretical Oswald factor is usually overestimating the actual value. Correction factors for the fuselage influence, Mach number and zero lift drag coefficient should be taken into account. This is done with Equation 8.5, which is based on the work of Kroo [49].

$$e = \frac{k_{e,M}}{Q + P\pi A} \tag{8.5}$$

In this formula, Q is found with Equation 8.6. $P = KC_{D_0}$, where K is a constant 0.38. A is the aspect ratio and $k_{e,M}$ is the correction for Mach number, given in Equation 8.7. Since the Mach number flown at is well below the compressibility Mach number, a value of 1 is taken here.

$$Q = \frac{1}{e_{\text{theo}} \cdot k_{e,F}} \tag{8.6}$$

$$k_{e,M} = \begin{cases} a_e \left(\frac{M}{M_{\text{comp}}} - 1\right)^{b_e} + 1, M > M_{\text{comp}} \\ 1, M \leq M_{\text{comp}} \end{cases}, \tag{8.7}$$

Q takes into account the theoretical Oswald factor as well as the correction for the fuselage influence $k_{e,F}$, which is given by Equation 8.8:

$$k_{e,F} = 1 - 2\left(\frac{d_F}{b}\right)^2 \tag{8.8}$$

8.4. Wingtip-Mounted Engines

General conventional designs use wing mounted tractor propellers. Such a configuration comes with the added benefit of having a higher dynamic pressure on the wing behind the propeller, locally increasing its lift [50]. However, due to this increase in dynamic pressure and swirl in the slipstream of the propeller the lift and drag distribution over the entire wing is affected while also causing a higher viscous drag in the propeller slipstream [51].

The use of hydrogen driven electric propellers in the H_2OPPER concept allows for added design flexibility with respect to its propulsion system and its lay-out. A wingtip-mounted propeller placement is an example of a such a unconventional configuration.

8.4.1. Potential Benefits

The benefits of this configurations were already described in the 1960s; to increase the wing's maximum lift coefficient while also reducing its induced drag and increasing its spanwise lift distribution, also known as the Oswald efficiency e [52]. These theoretical beneficial effects were achieved by attenuating the wingtip vortex when the propellers rotated in opposite direction to that of the wingtip vortex, which in turn also reduces the downstream swirl.

More recent studies made an effort to explore the aerodynamic effects of this configuration in more depth [53], [54]. Sinnege et al tested smaller scale models of both the conventional and wingtip-mounted configuration in a low speed wind tunnel. They confirmed the expected benefits as described in the previous paragraph. It should be noted that these effects were most pronounced at higher power settings (C_T) and higher lift coefficients (C_L). Where the drag reduction could reach up to ~50% for $C_L = 0.9$ and $C_T = 0.17$. At relative low C_T and C_L, the wingtip-mounted configuration actually had a *higher* drag than the conventional configuration. For the lowest tested C_L of 0.3, the crossover point was roughly at $C_T = 0.09$. While the

tests performed by Hooker et al were also in low speed wind tunnels on somewhat larger scale models, no comparison was presented with a conventional configuration, making it more difficult to draw conclusions from the results. However, it remained abundantly clear that the thrust settings have a large impact on the wing lift and drag reduction.

8.4.2. Implementation

The use of this wingtip-mounted configuration has so far been limited due to additional reversing gearbox required for kerosene-based counter rotating propellers and insufficient control power to overcome a one-engine inoperative condition [53]. However, the use of electric engines allow for counter rotating propellers without the need for an additional gearbox. Together with decrease in wing mass by causing a larger bending relief during flight, they have the potential to outweigh the disadvantage of a larger and heavier tail required for sufficient control power.

In order to make a first estimate regarding the possible integration of wing-tip mounted propellers, the GP-IND-06 was used. Before making an assumption regarding the potential benefits of this configurations, an estimation was made of the additional weight that would result from this design change. Mainly the vertical tail would get larger due to the one-engine inoperative condition where the moment arm of one engine is significantly larger. However, by increasing the rudder size and its effectiveness the total estimated additional weight was estimated around just 40 [kg]. Furthermore, due to the higher bending relief caused by placing the engines at the tips resulted in a estimated total of around 24 [kg] *lighter* wingbox. The effect on the x_{cg} of this added weight at the tail was also investigated, however, the effect of this potential shift in x_{cg} was negligible. Even in the case of a significant shift, the result would be a more forwardly placed wing, meaning a increased arm to the vertical tail and ultimately decreasing the size of the vertical tail again. Hence this did not result in any other additional weight and thus also no further 'snowball' effects. Which meant a initial total of just 16 [kg] of total added weight. Due to the the early design stage where not all 'snowball' effects were clear, using the mass gain factor tool from Section 3.2, an additional heavy weight gain factor of 3.7 was applied. Using GP-IND-01 meant that the total configuration would become less than 1% heavier. Hence a drag reduction of over 1% would have already led to a higher total efficiency . Following the research presented in Subsection 8.4.1, it was more than reasonable to expect that such a reduction was possible and thus the decision was made to implement this configuration and examine its effects in more detail.

Later in the design phase, more accurate estimations could be performed regarding the extra added weight. For the latest and final design, the wingtip-mounted engine caused an extra 22 [kg] for the vertical tail, an extra 20 [kg] for the longer fuselage and total of 23 [kg] reduction in the wingbox. Leading to a total weight increase of 19 [kg]. However, due to the still relative uncertainty regarding the weight of the large rudder and any other at that time still unknown 'snowball effects', a weight gain factor was again applied. This lead to a total weight increase that was again below 1%.

At this stage also the potential benefits specifically for the H_2OPPER concept were looked at more closely. The C_T in cruise was calculated to be 0.20 at a corresponding C_L of 0.54. If the results from Sinnege et al were to be extrapolated directly to this design, a drag reduction of at least ~30% would be expected. However, the results from that experiment were very specific to that tested configuration. Some important differences are for example that those specific tests were performed for a very different propeller diameter to span ratio, at a much lower Reynolds number, with a less efficient propeller blade and at relatively low values for C_T. Making this test configuration more representative of smaller vehicles and the question was raised of how applicable these results really were.

In the end, it was decided that since the weight gain was only marginal for already quite heavy safety margins and the required drag reduction for making this the more efficient design being significantly lower than what theoretically could be expected, the wingtip-mounted engines had a high enough probability of being more efficient in this design. Meaning, they were thus implemented in the final design. This high expected probability was supported by the fact that the beneficial effects were also observed in the works of Hooker, where a the tested conditions were already more representative of this design. Since efficiency is so closely related to its energy consumption and thus to the sustainability of the design while also leading to an increased range meant that this configuration was ultimately more desirable.

8.4.3. Recommendations

Due to the still relative high uncertainty regarding the magnitude of drag reduction and increase in lift and e, it is highly recommended that a low speed wind tunnel test is performed in the next phase of this design. It can be a similar test as performed by Sinnege et al, however, the conditions and model design should match that of the H_2OPPER. Once the aerodynamic benefits are validated another design iteration should be performed where the more accurate effects are implemented. Furthermore, the higher inertia loads due to the wing-tip mounted engines and the aerolastic effects should investigated in more depth to examine their effect on the wing mass.

9
Required Power and Energy

During the different phases of the flight, the aircraft needs different power levels. First an overview of the requirements and assumptions is given in Section 9.1. In Section 9.2, a method description is given for finding the power for each flight phase. The power profile has a significant impact on the overall design, for example on the sizing of the battery. Furthermore, the time needed for each phase was obtained, and with this, the total needed energy and thus hydrogen was calculated. Then, in Section 9.3, the resulting budgets are presented.

9.1. Subsystem Overview

In this section the requirements and assumptions for the power and energy of the H_2OPPER are shown.

9.1.1. Requirements

HOPPER-T-F-TO-1	The aircraft shall be able to accelerate to 61 [kts] for take-off
HOPPER-T-F-TO-4	The aircraft shall be able to take-off and land within 750 [m]
HOPPER-T-F-CL-1	The aircraft shall be able to climb to cruise altitude (10,000 [ft]) within 600 [s]
HOPPER-T-F-CL-2	The aircraft shall be able to climb to 10,000 [ft]
HOPPER-T-F-CL-3	The aircraft shall be able to climb at least 4 [m/s]
HOPPER-T-F-CL-4	The aircraft shall be able to reach a climb gradient of 3%
HOPPER-T-F-CL-5	The aircraft shall be able to climb with a 1.2 % gradient with 1 engine operative
HOPPER-T-F-CR-1	The aircraft shall be able to maintain 175 [kts] during cruise
HOPPER-T-F-CR-4	The aircraft shall have a maximum range of at least 300 [NM] with regulatory reserves
HOPPER-T-F-CR-5	The aircraft shall have a range of 200 [NM] at maximum payload with regulatory reserves
HOPPER-T-F-AP-4	In case of missed approach the aircraft shall be able to follow a 3% climb gradient
HOPPER-T-F-AP-5	In case of missed approach with 1 engine the aircraft shall be able to follow a 2% climb gradient

9.1.2. Assumptions

- **Aircraft flies in steady, symmetric, straight flight:** Basic flight mechanics formulas can be used. For overall energy and power calculations this is reasonably accurate for this stage of design.
- **The wind does not influence energy consumption:** Energy consumed could fluctuate a bit due to the wind, however on average this has no significant influence.
- **The lift/drag polar is constant:** Simplifies calculations. The inaccuracy here is in the zero lift drag estimation, which was done for the aircraft in cruise. Since in the other flight phases like take-off and climb the lift coefficient is a lot higher and therefore the induced drag is dominant, this error is no significant issue.
- **The time span for startup and taxi are 15 and 7 minutes respectively:** If the startup and taxi times are significantly higher, this might cause problems for the battery energy levels. However since the aircraft is small and operating on smaller airports the maximum times are expected to be correct.

9.2. Method Description

First the method to calculate all needed powers and times for every flight phase is described. Then, the total needed energy and resulting hydrogen is found. Lastly, the inputs and outputs are shown, so the end results of the described method.

9.2.1. Power for each phase

First, the power during cruise is obtained, as the other powers are calculated in a similar way.

Cruise

During cruise, there is an optimal value of the lift coefficient (C_L) to fly at in order to achieve maximum range. For a propeller aircraft this is the lift coefficient that results in minimum drag. This optimal value of the lift coefficient was found using Equation 9.1[1]:

$$C_{L_{opt}} = \sqrt{C_{D_0} \pi A e} \tag{9.1}$$

In this equation, A is the aspect ratio, e is the Oswald efficiency factor and C_{D_0} is the zero lift drag coefficient. Then, using this lift coefficient, the flight velocity is found using Equation 9.2.

$$V_{cruise} = \sqrt{\frac{2W}{C_{L_{opt}} \rho S}} \tag{9.2}$$

Where W is the aircraft weight, ρ is the air density and S the surface area. It has to be noted that for certain values of the aerodynamic parameters (a high aspect ratio, Oswald factor or zero lift drag, resulting in a high optimal C_L), the resulting cruise velocity will be lower than the required 175 [kts]. In that case, a cruise speed of 175 [kts] was used and the corresponding value for C_L was calculated backwards using Equation 9.3.

$$C_L = \frac{2W}{\rho V^2 S} \tag{9.3}$$

To obtain the required power for steady flight, the drag force still had to be calculated. The drag coefficient was found using the drag polar:

$$C_D = C_{D_0} + \frac{C_L^2}{\pi A e} \tag{9.4}$$

Then, since lift has to equal weight during cruise, and $P_r = DV$, the required power could be found using:

$$P_r = \frac{C_D}{C_L} W * V \tag{9.5}$$

To determine the time for the cruise phase of the flight, the inputted range was divided by the flight velocity.

Climb

During climb, a number of variables can be tuned. First of all, the Rate Of Climb (ROC) is something that can be chosen by the designer. This is the amount of meters the aircraft climbs every second. Furthermore, the speed at which the aircraft climbs is a variable as well. By changing these, the power profile and also energy used will vary. Having a higher climb speed and ROC will result in a higher required power. The climb speed was chosen by looking at reference aircraft and then varying the speed to reach an optimal ratio between power and energy needed for our system.

With a chosen climb velocity, the lift coefficient for climb can be found with Equation 9.3. The drag coefficient and required power to overcome drag can then be calculated using Equation 9.4 and Equation 9.5, respectively.

[1] AE2230-I Lecture 4, URL: `https://brightspace.tudelft.nl/d2l/le/content/293140/Home` [Accessed on: 24-06-2021].

To calculate the climb power the engines have to deliver, Equation 9.6 was used. The second term results from the potential energy needed to climb.

$$P_{climb} = P_r + ROC * W \tag{9.6}$$

The time to climb results from the rate of climb. It is obtained by dividing the aimed cruise altitude by the rate of climb.

Climb One Engine Inoperative

For the HOPPER-T-F-CL-5 requirement from Subsection 9.1.1, the one engine operative climb angle γ was calculated using:

$$\gamma = arctan(a/100) \tag{9.7}$$

Where a is the climb rate percentage. The climb speed was calculated by:

$$V_{climb_{1engine}} = 1.2 \cdot VS1 \tag{9.8}$$

Where VS1 is the stall speed without flaps, resulting from CS-23. The rate of climb is then computed from simple geometry.

Then using the Equation 9.6 the power needed during one engine inoperative climb was calculated.

Loiter

During loiter, the aircraft no longer aims to achieve maximum range. Instead, it is most efficient to fly for maximum endurance, since the loiter time is a set parameter. Achieving maximum endurance means flying at minimum power required. This resulted in the lift coefficient for this phase as:

$$C_{L_{loiter}} = \sqrt{3C_{D_0}\pi Ae} \tag{9.9}$$

Then, the same procedure as for climb was executed, calculating flight velocity, drag and required power, using Equation 9.2, Equation 9.4 and Equation 9.5, respectively. The time for loiter is set by CS-23 to be 45 minutes.

Descent

Descent is quite similar to climb, however, in this case the engine power will actually be lower than the power needed to overcome drag. Therefore, Equation 9.6 could still be used with a negative rate of climb. The speed during decent is lower then during cruise, and was chosen similarly as reference aircraft.

Take-off

The take-off is a more involved flight phase. During take-off, the maximum power of the aircraft will be utilized. Since there are many factors involved, for example runway length, rolling resistance, air resistance, torque limitations by the engine, it was decided to rely on statistics in determining this power instead of calculating it. This was done using the TOP as was done in the Midterm Report.[36] A statistical relation between take-off distance and take-off parameter is found. Then, by taking the take-off lift coefficient into account, this TOP parameter is linked to wing and power loading.

The time for take-off power setting, was also found using statistics. It was found that take-off can be divided in 2 phases: maximum power setting, which is maintained for 42s, followed by the climb-out, which is at 85% of maximum power for 132s. [55] These are statistical averages for all aircraft. Since the H_2OPPER is a relatively small aircraft these values are expected to be slightly overestimated. However, these numbers were still used to rather overestimate then underestimate the duration of these phases. It should be noted

that the aircraft has already climbed a few hundred metres during climb-out, however this is ignored in the climb phase, so it is left as a contingency.

9.2.2. Energy and Hydrogen calculations

With the power and time for each flight phase obtained, the required hydrogen for flight could be calculated. This power is the output power however, so to obtain the input power the output power had to be divided by the efficiencies of the system. The efficiencies are listed in Subsection 11.4.1, and the fuel cell efficiency is given in Subsection 10.2.2.

With the input powers obtained, the total energy was found by multiplying the time of the phase with this power, and summing the different phases. The total hydrogen mass was then obtained by dividing the total energy with the specific energy of hydrogen (120 MJ/kg).

9.2.3. Program Inputs and Outputs

All equations explained in previous subsections were used in a tool to calculate the power needs. The inputs and most important outputs of the program are listed in Table 9.1. Note that the hydrogen mass and cruise time is for a full payload flight. Furthermore it can be seen that power is reserved for a compressor and low power systems and a startup heater, these systems are discussed in more detail in Subsection 10.4.3 and Section 11.3 respectively.

Table 9.1: Input and output of power script

Input	Value	Unit	Output	Value	Unit
Cruise speed	90	[m/s]	Hydrogen	118	[kg]
Climb speed	60	[m/s]	Max engine input power	1570	[kW]
Descent speed	70	[m/s]	Fuel cell power/cruise power	823	[kW]
Descent angle	1.5	[°]	Battery power	840	[kW]
Cruise charging power	20	[kW]	Battery mass	420	[kg]
Descent charging power	280	[kW]	Climb power	1030	[kW]
Startup heater power	12	[kW]	Descent power (including charging)	701	[kW]
Compressor power	64	[kW]	Cruise time	1.7	[h]
Low voltage power	14	[kW]			
Startup time	15	[min]			
Taxi time	7	[min]			
Climb time	10	[min]			
Loiter time	45	[min]			
S	43	[m^2]			
C_{D_0}	0.0251	[-]			
e	0.785	[-]			
A	9.302	[-]			

9.3. Power and Energy Results

9.3.1. Maximum power

In Figure 9.1, the wing and power loading diagram is shown, with the chosen design point. As can be seen the chosen point is not completely to the right, at minimum surface area. Instead, a slightly larger wing is chosen, which reduced the take-off power.

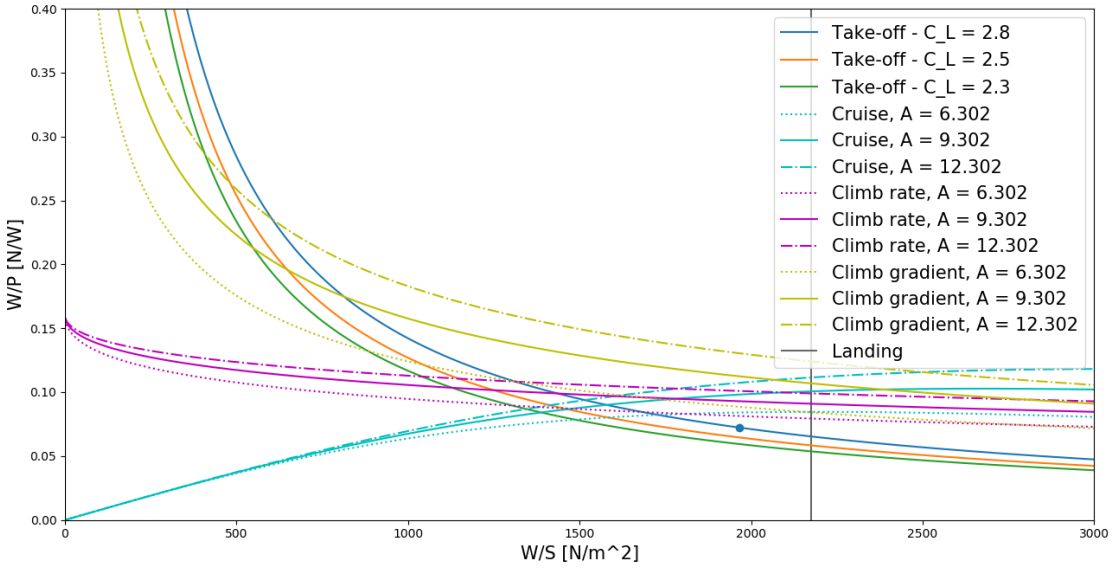

Figure 9.1: Wing loading and power loading diagram

9.3.2. Hybrid

As can be seen in Table 9.1 there is a big difference in power needed during take-off and during cruise. Since the maximum power during take-off must only be provided for a short amount of time it was chosen to overcome this gap in cruise power and take-off power by using batteries. The big gap in power means that the batteries are required to have a high power density. Therefore, it was chosen to make use of Lithium metal batteries. These batteries have an energy density of up to 369 Wh/kg, a specific power of 2000 W/kg and a cycle life of more than 1000 cycles [56]. The fuel cell is sized for cruise conditions. However, during climb the required power is higher than during cruise. Thus the batteries will also be used during climb, to provide the extra necessary power.

The batteries are sized to achieve max power during take-off, together with the fuel cell power, which is sized for cruise. Therefore, to calculate the required battery mass, the cruise power was subtracted by the take-off power to find the needed battery power. After this, the power difference was divided by the power density of the batteries to arrive at the battery weight. Then, the energy the batteries have to provide during take-off and climb was summed to check if the battery contained enough energy. A 10% margin was taken here, since the batteries can not be charged to 100%. It was shown that the energy was not limiting, which means there is excess energy available.

Before take-off two phases which consume energy have to be performed: start-up and taxiing. Since the velocity is zero or low during these phases, the fuel cell can not lose its heat with the help of the radiator. However, the battery weight was power limited, which means that not all energy of the batteries will be used for take-off , climb-out and climb. This extra battery energy will be used for startup and taxiing of the aircraft. This will mean that the fuel cell does not have to be used for these stages of the mission and thus no large amounts of heat have to be removed.

In the end it was calculated with the help of Table 9.1 that a total of 420 [kg] of batteries is needed. With this battery weight the battery is still limited by power. Therefore, if the assumption of taxi and startup times is not true, the battery is still able to provide power for a taxi that is twice as long.

9.3.3. Power charts

From the equations in Section 9.2 the power needed during the different flight phases could be calculated. It was decided to plot the power needs during the different flight phases to get a better understanding of the performance of the aircraft. In Figure 9.2 the required power is shown. It is also displayed that power is delivered by the battery, fuel cell or both.

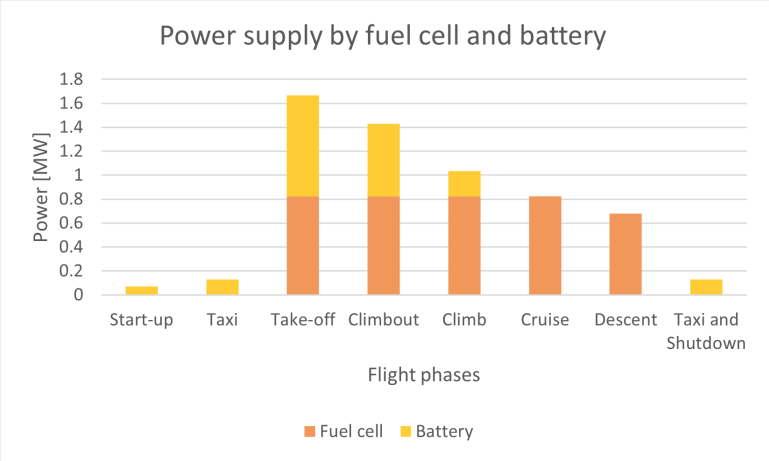

Figure 9.2: Power supply by the fuel cell and battery during different flight phases

It is also interesting to see where the delivered power is used. For this, pie charts were constructed for the different flight phases. The pie charts for take-off, cruise and descent can be seen in Figure 9.3. During take-off it can be seen that the largest part of the power is required for the engines. This is still the case during cruise but now also the batteries are charged at a slow rate. It was decided to charge the batteries during cruise to enable the use of batteries for performing manoeuvres and overall better dynamic response. Then, during descent the batteries are charged at a high rate so that they will be fully charged at landing.

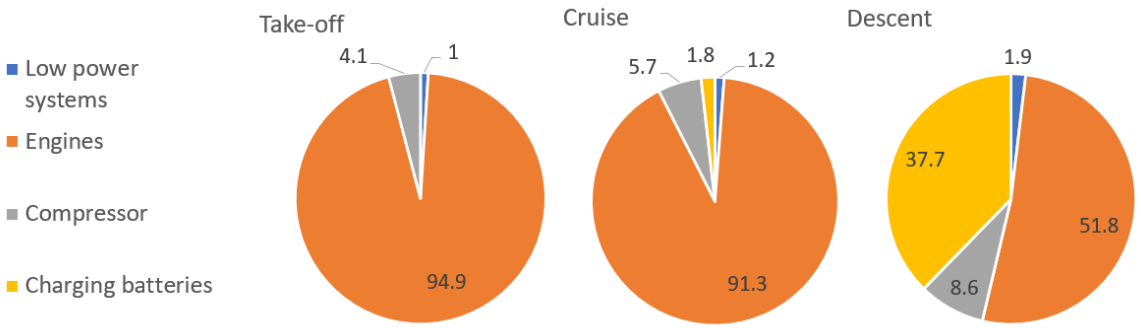

Figure 9.3: Power distribution in percentage

In Figure 9.3 it can be seen that power is reserved for a compressor and low power systems, these systems are discussed in more detail in Subsection 10.4.3 and Section 11.3 respectively.

9.3.4. Energy charts

It also interesting to take a look at the energy that is needed during the different flight phases. The high power that is used during take-off is only need for a very short time. This means that the energy that is used during this phase is lower than in for example cruise and descent. In Figure 9.4 the total energy per flight phase can be seen. Logically cruise and loiter take up most energy since they require power during a long time.

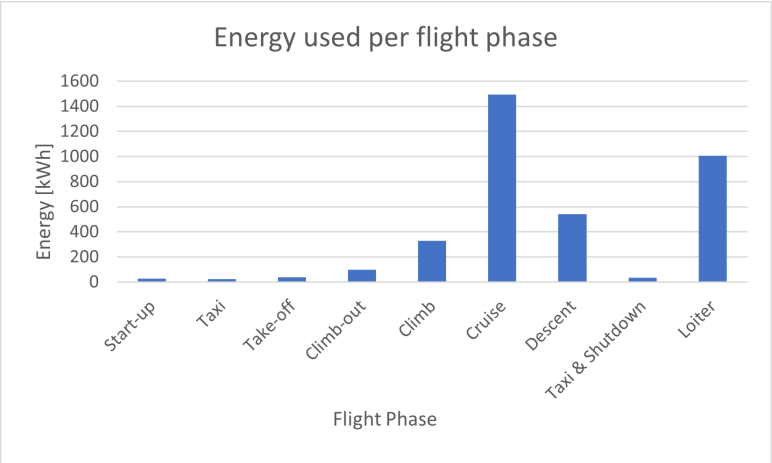

Figure 9.4: Energy distribution per flight phase for maximum payload and a range of 200 NM

Finally, it is interesting to see the charging levels of the battery during the different flight phases. Start-up and taxi are phases which rely completely on energy from the battery. During take-off, climb-out and climb the battery assists the fuel cell to reach the required power output. Then during cruise and descent the batteries are charged again. In Figure 9.5 the energy in the batteries can be seen for a maximum payload flight with a range of 200 [NM]. It is important to note that there is a limit to how fast batteries can be charged. Tesla claims that it can charge its lithium ion batteries at a rate of 4C [2]. For the lithium-metal batteries it is assumed that a rate of 2C can be realised. If the batteries are charged at a rate of 2C, they can be fully charged in 30 minutes [3]. Therefore it was chosen, that if possible, a descent of 30 minutes is flown . This then means that it is not necessary to charge the battery on the ground. The taxi and shutdown of the previous flight can be performed within the same cycle as the next flight. This can also be seen in the figure, the starting energy level is the energy at which the aircraft was shut down. However, it must still be possible to charge the battery on the ground in case of emergencies or very short flights. This is shortly highlighted in Chapter 14.

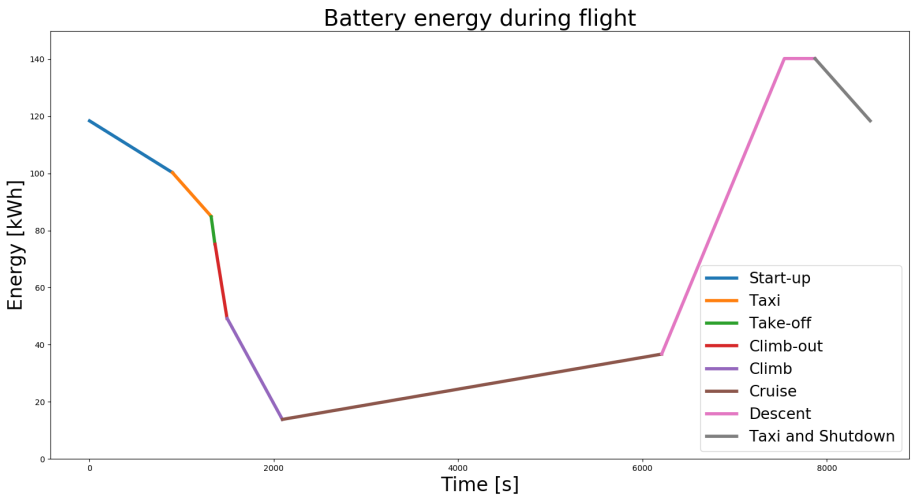

Figure 9.5: Battery energy during maximum payload flight of 200 NM

[2] URL: https://energsoft.com/blog/f/c-rate-of-batteries-and-fast-charging#:~:text=Tesla%2C%20the%20electric%20car%20company,be%20around%20100%20cm%5E3. [Accessed on: 24-06-2021]
[3] URL: https://www.bluesky-energy.eu/en/2020/04/24/what-is-c-rate/ [Accessed on: 28-06-2021]

10
Fuel Cell

To convert the energy stored inside the hydrogen tank to usable electrical energy a fuel cell is used. First, in Section 10.1 the functions, requirements and assumptions for the fuel cell subsystem are discussed. Then, in Section 10.2 the Proton Exchange Membrane (PEM) fuel cell is discussed in more detail. After this, in Section 10.3 an initial sizing for the fuel cell is given. Then, in Section 10.4 all the subsystems of the fuel cell are discussed. After this, the system overview and wing planform are given in Section 10.5. Then, the sustainability of the fuel cell is discussed in Section 10.6. Finally, in Section 10.7 recommendations are given for the fuel cell when the design of the H_2OPPER will be continued.

10.1. Subsystem Overview

The subsystem overview shows the functions, requirement and important assumptions of the fuel cell.

10.1.1. Functions

The function of the fuel cell is to convert the stored energy in the liquid Hydrogen to usable electric energy. It should provide the necessary power for cruise and charge the batteries.

10.1.2. Requirements

HOPPER-T-F-CR-Pr.1	The fuel cell system shall be able to deliver a maximum of 825 [kW] of power during flight
HOPPER-T-F-CR-Pr.2	The fuel cell hybrid system shall be able to deliver a maximum of 1590 [kW] of power during flight.
HOPPER-C-R-NC-2	NO_x emissions shall be 0 [g/kN] of thrust

10.1.3. Assumptions

- **Components of fuel cell can be placed as desired:** Enables to divide components over the wing instead of needing one large block in the aircraft. Except for the humidifier and anode re-circulation pump which must be placed close to the fuel cell[1].
- **Lithium metal batteries will be available in the coming 5 years:** Used energy and power densities are valid. If this assumption is not met, the battery mass would become larger.
- **Linear mass increase fuel cell stack:** The mass of purely the fuel cell stack can be extrapolated in a linear way. This is valid since they can be put in parallel or series to reach higher powers.

10.2. Fuel Cell Types

Fuel cells exist in all shapes and sizes and therefore choosing the proper fuel cell is very important. The fuel cell that is needed for the H_2OPPER had to conform to requirements that enabled its usage in aviation. First of all, some fuel cells have very high operating temperatures ranging up to 1000 [°C]. This can be dangerous if it is not handled with care. Jet engines do operate at these high temperatures as they can get rid of the heat with the exhaust flow. The mass flow out of the fuel cell is very small compared to this and thus almost all the heat should be removed with the help of a cooling system. Therefore it is more desirable to have lower operating temperatures for the fuel cell. Secondly, as a result of the very high operating temperatures these fuel cells also have a very long start-up time. This is of course not desired when using a fuel cell in an aircraft. Finally, for the design concept, the fuel cell needed to be able to run on pure hydrogen. This would ensure the climate neutrality aspect of the aircraft.

In Table 10.1 a trade-off can be seen for different types of fuel cells. What can be observed is that both

[1] Personal communication: Matthew Dekkers - AeroDelft

the Molten Carbonate Fuel Cell (MCFC) and the Solide Oxide Fuel cell (SOFC) have too high operating temperatures and very long start-up times and can therefore not be used as fuel cell for the H_2OPPER. Furthermore, the Phosphoric Acid Fuel Cell (PAFC) and Direct Methanol fuel cell (DMFC) both have a low efficiency and will therefore be eliminated as well. Finally, the Proton Exchange Membrane Fuel Cell (PEM) and Alkaline Fuel Cell (AFC) both score similar. The biggest disadvantage of the AFC fuel cell is that it is easily poisoned by CO_2. This means that the air needs to be purified or pure oxygen needs to be used. Furthermore, most strong fuel cell systems used in for example the automotive industry are mostly PEM fuel cells[2] . Therefore, the PEMFC fuel cell was selected as most suitable for the H_2OPPER.

Table 10.1: Fuel cell type trade-off including (score) [57, p.276].

Parameter	**PAFC**	**AFC**	**PEMFC**	**DMFC**	**MCFC**	**SOFC**
Temperature Range [°C]	150-220 (++)	50-150 (++)	80-90 (++)	60-90 (++)	600-700 (–)	700-1000 (–)
Start-up Time [h]	1-4 (–)	<0.1 (++)	<0.1 (++)	<0.1 (++)	5-10 (–)	1-5 (–)
Efficiency [%]	35-45 (-)	45-60 (+)	40-60 (+)	35-40 (-)	45-60 (+)	45-55 (+)

10.2.1. PEM Fuel Cell

The PEM fuel cell is a fuel cell in which hydrogen and oxygen react together to form an electric current, water and heat. To increase the power output of a fuel cell, multiple cells are connected in series to form a so-called fuel cell stack. Each individual cell consists of a cathode and an anode. Inside the PEM fuel cell, the following half-reaction takes place at the anode [58]:

$$H_2 \rightarrow 2H^+ + 2e^- \tag{10.1}$$

At the cathode the following half-reaction takes place:

$$O_2 + 4H^+ + 4e^- \rightarrow 2H_2O \tag{10.2}$$

This results in the following total reaction:

$$2H_2 + O_2 \rightarrow 2H_2O \tag{10.3}$$

The fuel cell stack itself is only a small part of the total system. In Figure 10.1[3] all the sub-systems that are part of the fuel cell system can be seen. The systems all have their own functions within the total system. The cooling system makes sure that the fuel cell stays below the maximum temperature of 80 [°C] [4]. The hydrogen subsystem makes sure that the hydrogen is taken from the tank and brought to the fuel cell stack. An important part of the hydrogen subsystem is the anode re-circulation pump. This pump makes sure that the hydrogen that is not used in the reaction as it travels through the fuel cell is reused and does not go to waste. The air subsystems provide the oxygen that is needed for the reaction. The control system controls all the flows into the fuel cell. This will make sure that the hydrogen and air are provided in the right ratios to generate the power output that is desired. Finally, there is the safety system. This system makes sure that the fuel cell shuts down in case of emergency. Furthermore, it includes fire extinguishers in case a fire might break out because of the heat generated by the fuel cell. In Section 10.4 every subsystem will be explained in more detail for the fuel cell system used in the H_2OPPER aircraft.

[2]URL: `https://www.energy.gov/eere/fuelcells/types-fuel-cells` [Accessed on: 28-06-2021]
[3]URL:`https://www.datocms-assets.com/36080/161437457-heavy-duty-system-100.pdf` [Accessed on: 2-06-2021]
[4]URL:`https://www.datocms-assets.com/36080/161437457-heavy-duty-system-100.pdf` [Accessed on: 2-06-2021]

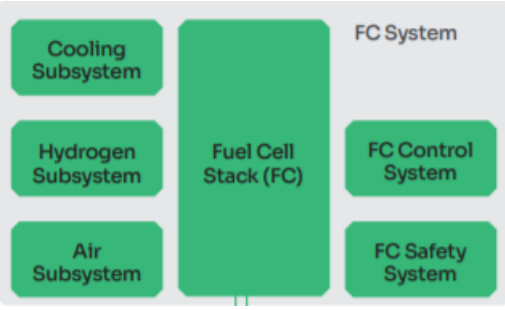

Figure 10.1: Fuel Cell System

10.2.2. Fuel cell efficiency

The efficiency of a fuel cell is not constant, it actually varies with output power. According to PowerCellution [5], the efficiency of the fuel cell can be found by:

$$\eta_{fc} = \frac{U}{1.23} \tag{10.4}$$

Where U is the cell voltage. To apply this to the used fuel cell, the voltage - current graph was consulted, as shown in Figure 10.2[6]. During take-off, climb and cruise the fuel cell is operating at almost maximum power, hence the voltage will be around 0.65 [V], meaning an efficiency of 0.53. During descent, the power is lower, and so the efficiency will be higher.

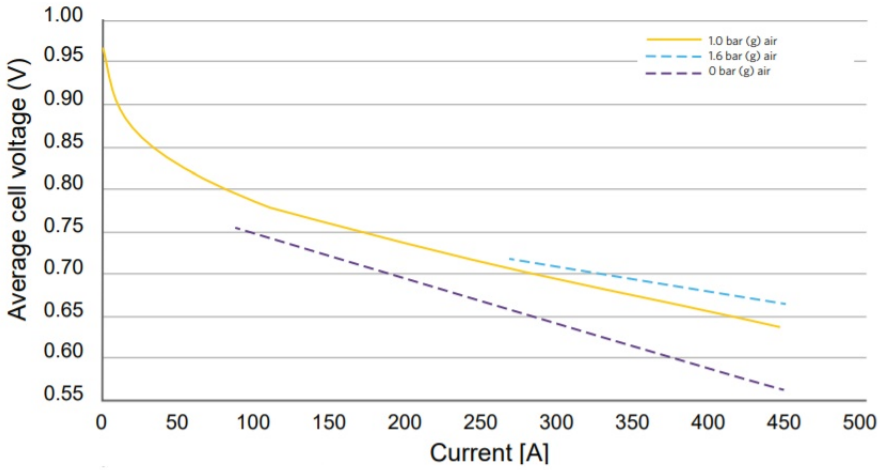

Figure 10.2: Fuel cell average cell voltage versus current

10.3. Initial Sizing

In order to obtain an estimation of the required weight and volume of the fuel cell, the current market was analyzed. It quickly became apparent that the compact, low weight and strong fuel cell that will be needed for the aircraft was not produced at the time of writing. The power output that will be needed as specified in Table 9.1 can already be performed by fuel cells that currently exist. However, this is only possible with stationary fuel cells and fuel cells on very large ships. The strongest fuel cells that are used in non-stationary vehicles can be found in big trucks. Horizon will be releasing a compact 6 [kW/l], 370 [kW] maximum power output fuel cell for use in trucks in the near future [7]. This is a big step in the right direction and shows that even stronger lightweight and compact fuel cells will be available soon.

Furthermore, it could be concluded from the market analysis that the fuel cell weight largely consists of the

[5] Personal communication: Andreas Bodén - PowerCellution
[6] URL: `https://www.datocms-assets.com/36080/1611437833-p-stack.pdf` [Accessed on: 15-06-2021]
[7] URL: `https://www.horizonfuelcell.com/mediacoverage` [Accessed on: 15-06-2021]

systems associated with the fuel cell. For example, the cooling system, hydrogen handling system, safety system and air handling system In order to size the fuel cell needed for H_2OPPER, it was decided to initially split the system up in the fuel cell stack and all other components associated with the fuel cell. To size the fuel cell stack itself, the strongest fuel cell stack that is currently produced was used. It is the so-called P-Stack from PowerCellution. The fuel cell has a power density of almost 3 [kW/kg] [8]. This power density contains the fuel cell, as well as some piping for the cooling liquid and packaging, but none of the other systems. Since, in order to output higher powers, fuel cells can simply be stacked in series or parallel, it was decided to use the power density of 3 [kW/kg] for the H_2OPPER fuel cell stack as well. The mass of the stack then resulted from dividing the total output power by this power density.

To size the associated subsystems of the hydrogen fuel cell, the trends of fuel cell volumes and masses were investigated. What was quickly noted, is that when doubling the fuel cell output power, the mass of the other subsystems was not necessarily doubled. To get a better idea of the trend, products of multiple fuel cell companies were investigated and the fuel cell powers were plotted against the system weights. The weight, in this case, is the weight of the fuel cell minus the weight of the actual fuel cell stack, since this was assumed to be linear. A trend line was created, which is shown in Figure 10.3. In this Figure the Fuel Cell types from Ballard [9] is shown. Other companies like Spectronik and Powercellution show similar results. As can be seen in the Figure, a logarithmic trend line was found to be accurate. This trend line was then used to obtain an initial weight estimation of the fuel cell.

In Section 10.5, a more detailed mass allocation will be shown.

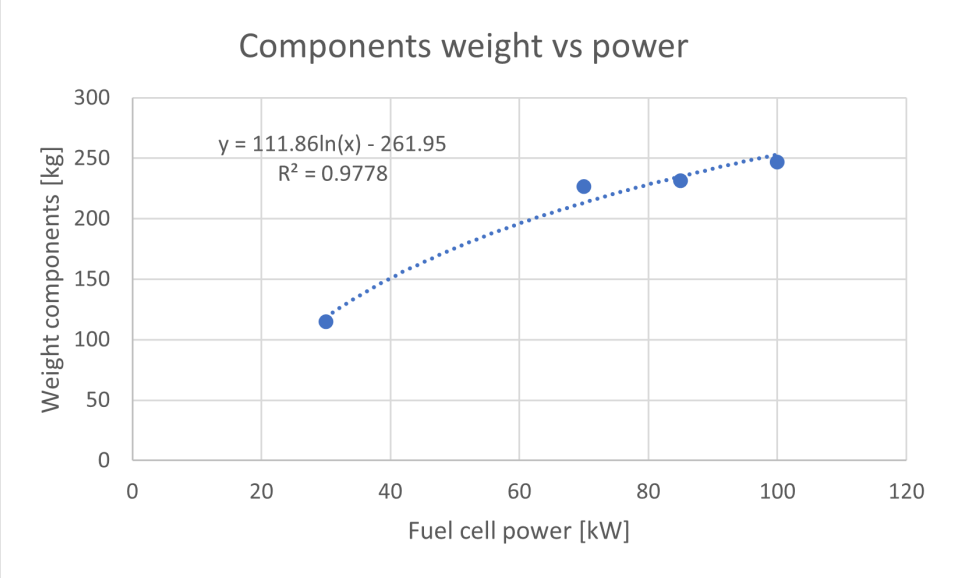

Figure 10.3: The weight of fuel cell minus stack of fuel cells currently in the market

10.4. Subsystems Fuel Cell

In this part of the chapter the subsystems of the fuel cell system will be discussed in more detail. First in Subsection 10.4.1 the cooling system will be explained in more detail. After this in Subsection 10.4.2 the anode re-circulation pump is shortly discussed. Then, in Subsection 10.4.3 the air handling system is explained. Finally in Subsection 10.4.4 the water management system is explained.

10.4.1. Cooling

Because of the fact that the fuel cell only has an efficiency of around 50 percent, the cooling subsystem is a very important part of the fuel cell system. The low efficiency means that for a 100 kW power output also 100 kW in heat is generated. Since the fuel cell has an optimal temperature range, it should not heat up to higher temperatures than that. For larger output fuel cell system there are two possibilities for liquid cooling

[8] URL: https://www.datocms-assets.com/36080/1611437833-p-stack.pdf [Accessed on: 31-5-2021]

[9] URL: https://www.ballard.com/fuel-cell-solutions/fuel-cell-power-products/motive-modules [Accessed on: 14-6-2021]

systems: regular liquid cooling and phase change cooling. For the main cooling component of the fuel cell on board the aircraft, it was chosen to make use of a liquid cooling system.

Currently, the liquid cooling system is the most used cooling technique for PEM fuel cell stacks that have a higher power output than 80 kW. Phase change cooling does have some advantages over liquid cooling. It makes use of the latent heat of a coolant instead of the sensible heat. For comparison, the latent heat of water is over 500 times larger than the sensible heat of water if its temperature is increased by 1 [K]. However, phase change cooling has not been used widely yet and therefore was not chosen to be used [59]. It will however be part of the humidifier process as explained in Subsection 10.4.3.

Since the fuel cells generate a lot of heat it is important that cooling is done from the inside. Cooling from the outside will not be able to remove enough heat from the cells. The cooling channels through which the coolant flows are therefore integrated in the fuel cells. In Figure 10.4, a cross section of a single cell is shown and it can be seen that the channels are situated between the cathode and anode channels.

For the cooling liquid often a 50/50 mixture of water with ethylene glycol is used. The ethylene glycol makes sure that the freezing point of the mixture drops below 237 [K] [10] and therefore also allows using the fuel cell and its cooling systems in lower temperatures. The coolant is used to keep the fuel cell at the optimal operating temperature of 60 to 80 degrees Celsius. To uniformly cool the fuel cell the temperature difference of the coolant at the fuel cell inlet and outlet may not be too big.

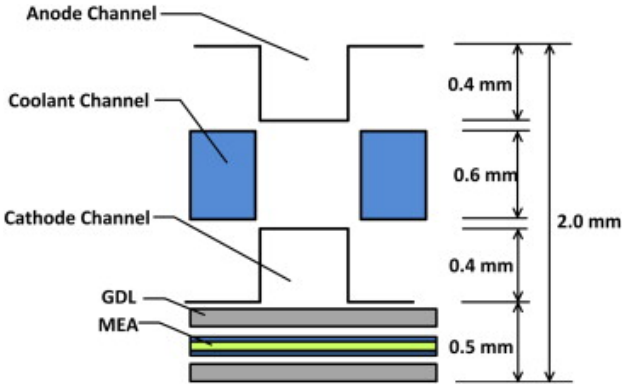

Figure 10.4: Cell with coolant channels [59, p.7]

First it was necessary to calculate how much heat needs to be removed by the cooling system. In Subsection 10.2.2 it can be found that the lowest fuel cell efficiency that will be encountered during flight is 53%. This means that 47% is generated as heat. In Figure 10.5 it can be seen that 80% of the heat needs to be removed by the cooling system, 20% will happen due to natural convection, extra reactant and internal water evaporation. This means that a total of 282 kW of heat from the fuel cell needs to be removed by the cooling system. Similarly, the engine has an efficiency of 93%. In this case the entire other 7% is assumed to be heat that needs to be removed by the cooling system. In Table 10.2, a total heat overview can be found. Furthermore, it is shown how much heat is removed by the sub-parts of the cooling system.

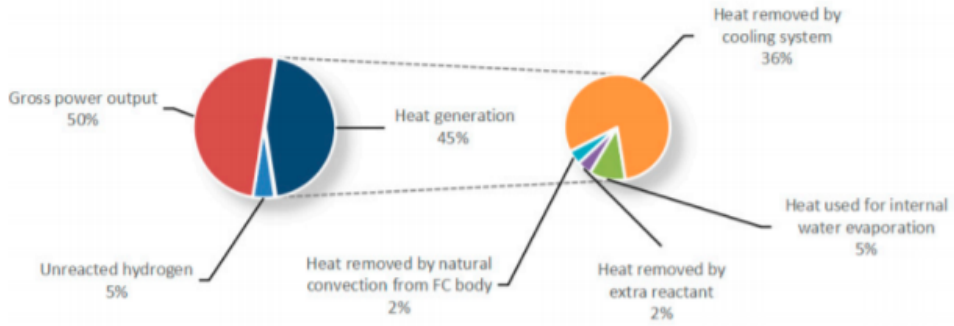

Figure 10.5: How much cooling needs to be removed by the cooling system [60, p.2]

Table 10.2: Heat generation and removal systems per wing

Component	Heat generated [kW]	Component	Heat absorbed [kW]
Fuel cell	365	Liquid hydrogen	34

[10] URL: https://www.engineeringtoolbox.com/ethylene-glycol-d_146.html [Accessed on: 4-5-2021]

Engine	55	Natural convection, extra reactant and internal water evaporation	73
		Humidifier	31
		Radiator	282
Total	420		420

Cooling with Cryogenic Hydrogen

The hydrogen that is used as fuel will be stored at 20 [K]. The hydrogen that enters the fuel cell should have a temperature of around 333 [K] [11]. By using the hydrogen to cool down the fuel cell and therefore in turn using the heat generated by the fuel cell to warm up the hydrogen, weight can be saved on the cooling system. To calculate how much heat can be removed by warming up the hydrogen knowledge about two properties was needed. Firstly, assuming that the pressure stays constant, the specific heat of hydrogen equals 14320 [J/(kg·K)][12]. Furthermore, the heat of evaporation is needed since hydrogen goes from a liquid to a gaseous phase when it is heated up from 20 [K] to 333.15 [K]. The heat of evaporation of hydrogen equals 446.1 [kJ/kg]. Then, as was calculated in Subsection 10.4.4 around 6.9 [g] of hydrogen is used by the fuel cell per second. Heating up this hydrogen will thus require around 34 [kW].

Cooling with Radiator

In the end, it was concluded that a big part of the heat has to be removed using a regular cooling system. In a PEM fuel cell this is normally done with the help of a radiator. A radiator transfers the heat from the coolant to the air that is flowing over the radiator. The radiator is built up of many so-called fins which drastically increase its surface area. Increased surface area also means increased contact area with the airflow and thus a lot more heat can be dissipated to the airflow.

Therefore, an attempt on estimating heat transfer by convection was done. By looking at the Reynolds Number and Pratzl number, an estimate could be made on the convective heat transfer coefficient h. However, since these formula are specified for specific shapes (for example a flat plate), and the Reynolds number is very hard to predict when the flow is disturbed by the radiator, the inaccuracy of the predicted heat transfer coefficient was deemed too inaccurate.

The other method used to size the radiator was by investigating the current market. AKG-group makes radiator cooling modules of up to 330 [kW] cooling capabilities[13]. However, this includes a fan, motor to drive the fan, wind tunnel etc, while this is not necessary for the aircraft system, since the ambient airflow can be used for cooling. Therefore the company was contacted, after which they clarified the radiator weight itself is 133 [kg].[14]

For an first estimate on the size of the radiator that will be needed to remove 282 [kW] of heat two experts were contacted. Kaylan Wessendorp estimated that to remove the heat a frontal surface area of 0.83 [m^2] would be necessary [15]. Luc Reinhard estimated a frontal area of 0.53 [m^2] [16]. They both scaled this area based on their own radiators. So the same amount of power per surface area is assumed as their radiator. However it must be noted that this is calculated with an expected mass flow of 12-15 [kg/s], which is higher than will be realised during take-off and climb as has been calculated with Equation 10.5. A lower mass flow means that the actual radiator frontal area needs to be bigger.

To further justify how much heat can be removed with the help of a radiator, an analysis on a car radiator was performed. The car radiator has a frontal area of 0.88 [m^2]. This radiator is thus similar in size to the radiator of the H_2OPPER. In [61] a car radiator is analysed and the effect of increasing the airflow over the radiator

[11] Personal communication: Andreas Bodén - PowerCellution

[12] URL: https://www.nuclear-power.net/hydrogen-specific-heat-latent-heat-vaporization-fusion/ [Accessed on: 14-06-2021]

[13] URL: https://www.ccs-oilcoolers.nl/en/2010.300.0000-oil-cooler-akg/2010.300.0000/ [Accessed on: 10-6-2021]

[14] Personal communication: Eric Ermers - CCS Oil Coolers

[15] Personal communication: Kalyan Wessendorp - Forze Delft

[16] Personal communication: Luc Reinhard - AKG Gruppe

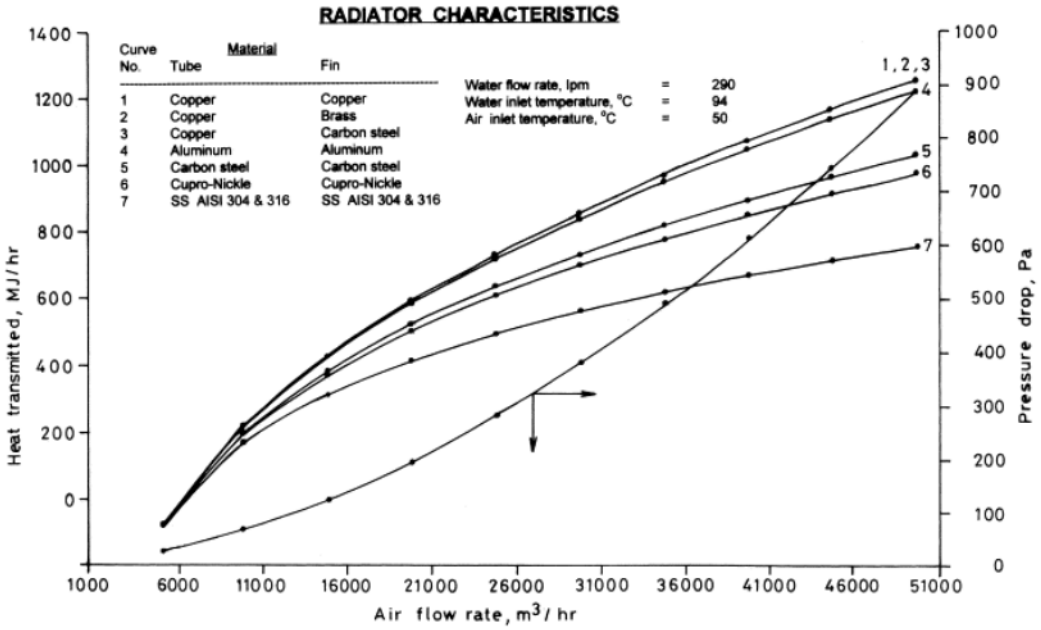

Figure 10.6: Radiator heat removal per air flow rate [61, p.11]

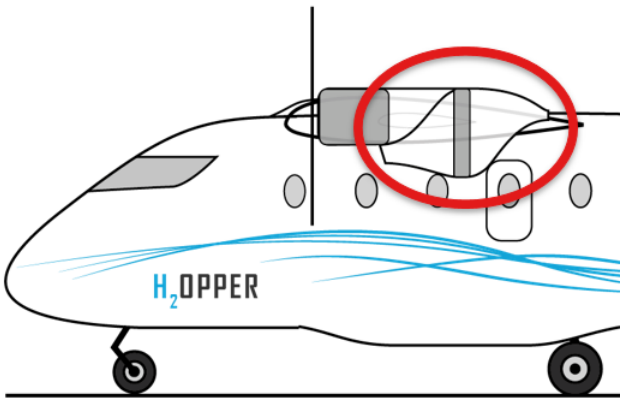

Figure 10.7: Radiator side view

is calculated. In Figure 10.6 this effect is visible. It can be easily seen that by increasing the airflow the total amount of heat that is removed increases significantly. What is important to note is that the temperature difference between the airflow and the coolant in the Figure 10.6 is only 44 degrees Celsius. The worst case scenario that might be encountered during flight is a coolant temperature of 80 degrees and an ambient air temperature of around 35 degrees, a total difference of 45 degrees Celsius. However, in most flight phases the air temperature will be much lower.

From Table 10.2 it can be calculated that the radiator needs to remove 282 [kW] of heat. Per hour this means that around 1000 [MJ] of heat needs to be removed. In Figure 10.6 it is shown that to remove this heat an airflow of 36000 [m^3/hr] is needed (mass flow of 12.25 [kg/s] at sea level). By using Equation 10.5 it can be calculated that an inlet area of 0.167 [m^2] is needed using the climb speed that is given in Table 9.1. This inlet area could be placed as a duct under the engine as can for example be seen on the reference aircraft L 410 NG. In Figure 10.7 the radiator set-up can be seen. After the inlet the area is increased so that the radiator can fit in the duct.

$$\dot{m} = \rho A_{\text{inlet}} V \tag{10.5}$$

Where $\dot{m}$ is the mass flow, ρ is the density, A the inlet area and V the velocity.
Cooling system overview The cooling subsystem can be quite complicated. To get a better overview of the

entire system, a cooling diagram is provided in Figure 10.8. In this cooling diagram it can be seen how the hot cooling fluid that flows out of the engine and fuel cell is cooled down again.

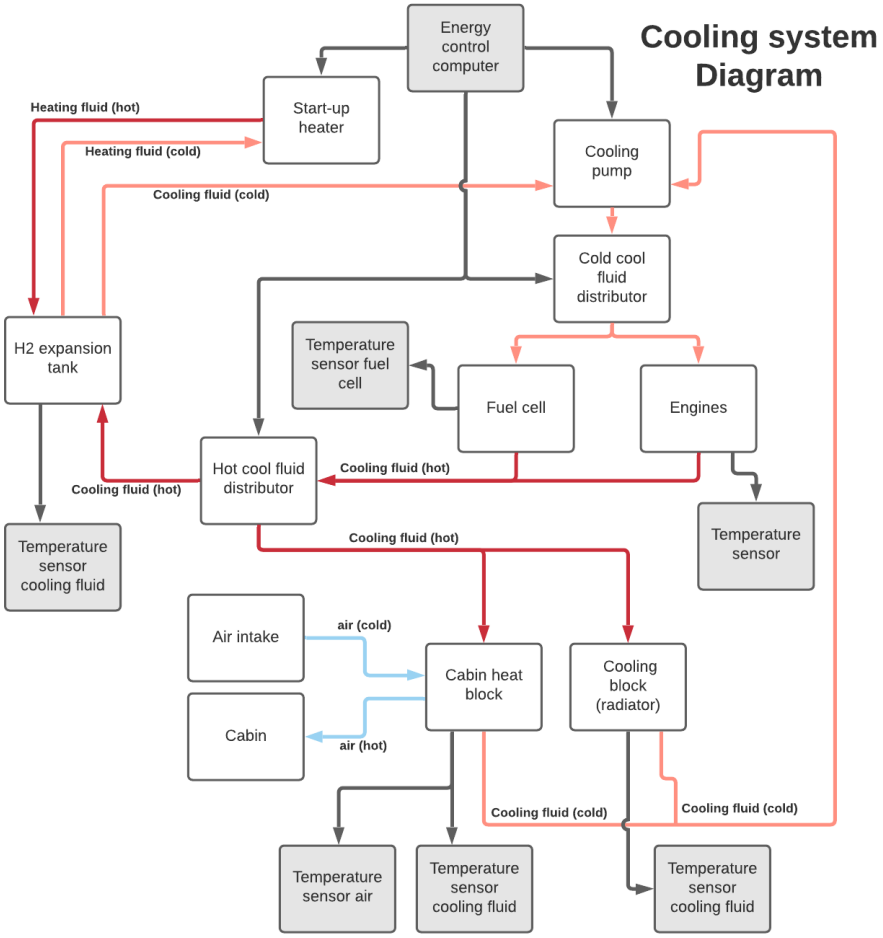

Figure 10.8: Cooling diagram

10.4.2. Anode Re-circulation Pump

Another subsystem that can be found in a fuel cell is a so-called anode re-circulation pump or blower. When a fuel cell is producing power, usually more hydrogen and air are supplied than is necessary for the reaction. This will cause no problem for the air supply, since this is just a constant flow that is taken from the surrounding air. However, since the hydrogen is taken on board in a tank there is no unlimited supply during flight. Therefore it is important that the excess supply of hydrogen through the fuel cell gets re-used. The anode re-circulation pump makes sure that no hydrogen goes to waste [62].

10.4.3. Air handling

The PEM fuel cell of course needs oxygen to react with the hydrogen. This oxygen can be obtained in two ways. Either a pure oxygen tank can be brought on board the aircraft or the oxygen can be taken from the air. Since the fuel cell system is already a very heavy system it is chosen to not bring an additional tank but to take the oxygen from the airflow around the wing. Since the airflow does not only contain oxygen, filters will be needed to get rid of the undesired substances (like for example CO). Furthermore, the cell membranes need to be in a fully hydrated state to attain the highest performance and therefore the air needs to be humidified. For the best performance of the fuel cell, the air also needs to be pressurized to around 2.5 bars, which will be achieved with the help of the compressor. This will help with providing the desired oxygen excess ratio.

Air flow rate

For a lot of the components of the air handling system, the flow rate of the air is the biggest factor regarding the size and mass of the component. Therefore it was investigated what air flow rate is necessary for the fuel cell operations. First, the hydrogen flow rate was calculated. This was done by dividing the fuel cell power by the energy density of hydrogen, being 120 [MJ/kg]. This hydrogen mass flow rate then needs to be converted to oxygen mass flow rate. Following from Equation 10.3, and the fact that an O_2 atom is 16 times as heavy as a H_2 atom, the mass flow rate of oxygen is 8 times the flow rate of hydrogen. Since oxygen is 21% of air, the air mass flow rate can then be found. This resulted in a necessary 0.27 [kg/s] flow rate.

Air intake

The first component in the air handling line is the air intake. This air intake has to accommodate the required air flow. The area can be calculated using:

$$A = \frac{\dot{m}}{\rho V} \tag{10.6}$$

Since the flow velocity is quite high during cruise, only a small air intake opening is needed (about 33 [cm^2]). However, the fuel cell will also be running at maximum power during take-off, climb-out and climb. During these flight phases, the air flow speed is significantly slower. Therefore, a variable area air intake is necessary.

During take-off, the fuel cell already needs to deliver maximum power. However, the aircraft is not moving yet. Therefore, the air intake is placed behind the propeller. When the propeller starts turning, an airflow is created that can be used to power the fuel cell. To determine the airflow produced by the propeller, the thrust produced by the propeller has to be known. With this thrust and Equation 10.7, the propeller exit speed can be calculated, as the aircraft is standing still, so V_0 is zero.

$$T = 0.5\rho A(V_e^2 - V_0^2) \tag{10.7}$$

Since propeller aircraft have constant power, and $P_a = T * V$, the theoretical thrust force when standing still would be infinite. However this is not realistic. Equation 10.8 displays a formula found for maximum theoretical static thrust [63].

$$T_{\text{static}} = P^{\frac{2}{3}} \left(2\rho A_{\text{prop}}\right)^{\frac{1}{3}} \tag{10.8}$$

Since this is a theoretical maximum, the actual value for maximum thrust will be lower. In the paper [63] the actual maximum thrust found was about 2/3 of this static maximum, which was therefore used here as well. It has to be noted that this is a very approximate estimation, it is not very accurate, however the main goal of this calculation was to check if using the propeller as mass flow generation for the fuel cell is realistic. With the thrust value found, the exit velocity was calculated, which in turn was used to calculate the required intake area, being about 45 [cm^2]. The actual propeller exit velocity definitely should be tested, however this area is easily manageable on the wing leading edge, therefore this design is deemed feasible.

If after testing it is found that the airflow is not sufficient an oxygen tank must be added. This tank can be very small and light since it only needs to provide oxygen to the fuel cell for take-off. During climb-out and climb the velocity of the airflow is already fast enough to provide the fuel cell with enough air.

Filter To size the filter, the mass flow rate was again taken into account. Looking at existing air filtering systems made by MANN+HUMMEL, an indication of the mass/volume of the filter was made. Taking the highest filtering requirements into account, which was also chosen by Ballard, a Fuel Cell producing company, the Entaron filter model was chosen as reference.[17] Using the earlier obtained flow rate a specific type was chosen, which weighs just under 10 [kg].

[17] URL: `https://www.mann-hummel.com/en/oe-products/stories-en/best-protection-for-the-fuel-cell/` [Accessed on: 18-6-2021]

Compressor To get a better understanding of the power and volume needed for a compressor the company Rotrex was contacted. Rotrex is a company that makes compressors for fuel cells. Currently, they are designing a compressor for a 400 [kW] fuel cell [18]. The specifications can be found in Table 10.3. The EK40AA compressor from Rotrex will be used as compressor for the fuel cell system in the H_2OPPER.

Humidifier As a humidifier, a direct water injection humidifier was chosen in combination with an evaporative cooling system. This system will make use of the water produced by the PEM fuel cell to humidify the air. Such a combination of systems can humidify the air and at the same time get rid of about 10% of the heat generated by the fuel cell [64].

10.4.4. Water generation and removal

The PEM fuel cell produces water from the oxygen and hydrogen, in addition to electricity and heat. This water cannot be stored on board of the aircraft because it will increase the weight of the aircraft significantly. By using the molar ratio between water and hydrogen, 18:2, it can be calculated that 100 [kg] of hydrogen will turn into 900 [kg] of water. A part of this water can be used to humidify the in-going air. The remainder will be ejected using a nozzle similar to fuel dump nozzles. Note that even though water vapour is a greenhouse gas, emission below 10,000 [ft] will not build up and reduce themselves by precipitation [19]. One consideration needed to be made when choosing to eject the water; it is preferred to not release water during take-off and climb. Since the water from the fuel cell will have a temperature of 80 [°C], which could be a hazard for people or animals below the aircraft during climb. Therefore, a holding tank needed to be sized.

The water generated per second can easily be calculated by dividing the energy generated (including heat) by the energy density of hydrogen. The power produced by one fuel cell is 413 [kW]. A 50 % efficiency of the fuel cell means that the power into the fuel cell is 825 [kW]. Dividing this value by the energy density of hydrogen, 120 [MJ/kg] , gives a hydrogen mass flow of 6.9 [g/s] [65]. Using the molar ratio, it is calculated that 61.9 [g] of water is produced each second. If the water is not released for a period of 2 [min], a mass of 7.4 [kg] needs to be stored for each fuel cell. At 80 [°C], the water has a density of 997 [kg/m^3] [20]. This means that 2 [min] of water capture has a volume of 7.4 [L]. Steel water tanks can be used to store this volume. Polymer tanks could also be an option to save weight, but considerations need to be made about the softening of the polymer at 80 [°C].

To release the water, a pump is needed to transfer the water from the holding tank to the ejection nozzle. The pump needs to be able to handle a flow rate of 7.4 / 2 [L/min]. As this is a small pump, the mass and power needs are neglected in the mass and power budget. The mass of the tanks are also neglected due to their small size. For example, metal containers of 10 [L] have a mass of only 3 [kg] [21]. The location of the ejection nozzle should be as far outboard as possible to minimize the hot water hitting the aircraft.

[18] URL: https://www.rotrex.com/fuel-cell-compressor/ [Accessed on: 7-06-2021]
[19] URL: https://climatechangeconnection.org/solutions/transportation/air-travel/ [Accessed on: 14-6-2021]
[20] URL: https://www.usgs.gov/special-topic/water-science-school/science/water-density?qt-science_center_objects=0#qt-science_center_objects [Accessed on: 15-6-2021]
[21] URL: https://docs.rs-online.com/c899/0900766b815852b0.pdf [Accessed on: 28-6-2021]

10.5. System Overview and Wing Planform

Table 10.3: Weight and volume of the subsystems of the fuel cell per wing

Subsystem	Component	Mass estimate	Volume estimate
Fuel cell stack	Cells	141.66 [kg]	84.0 by 87.5 by 15.6 [cm]
Air handling system	Air intake		
	Filter	10 [kg]	35.7x39.8x63.8 [cm]
	Compressor [22]	40 [kg]	45 by 23 by 18 [cm]
	Humidifier	20 [kg]	18 by 31 by 28 [cm] times 3
Hydrogen handling system	Anode Recirculation pump		
Battery		210 [kg]	20 by 70 by 220 [cm]
Cooling system	Cooling liquid pump	27 [kg]	18 by 33 by 60 [cm]
	Radiator	133 [kg]	frontal area 0.53-0.83 [m^2]
	Piping/cooling liquid	50 [kg]	
	Expansion tank	20 [kg]	

In Table 10.3 the weights and volumes of the different subsystems of the fuel cell can be seen. For the anode recirculation pump no mass could be found. However, since it is a very small system the weight is expected to be low. To see whether the subsystems can fit in the wing it is first important to calculate the volume of the wingbox. The wingbox starts at root with dimensions of 1.50 by 0.4 [m] and ends at the tip with dimensions of 0.75 by 0.2 [m]. The wingbox can be seen as a cut of a pyramid because of the taper ratio of the wing. The volume of a pyramid can be calculated using Equation 10.9:

$$V = \frac{l \cdot w \cdot h}{3} \tag{10.9}$$

Where V is the volume in [m^3], l is the length of the base, w is the width of the base and h is the height of the base all given in [m]. The total volume of the wingbox can be calculated by first using the root as a base and then subtract a pyramid that uses the tip as a base. This will result in a wingbox volume of 3.5 [m^3].

Now it is important to see if the entire fuel cell system can fit within the wing. For the stack itself, the volume can be easily calculated by using the Powercellution Datasheet [23]. The width and length of the fuel cell stack stay the same when the power is increased. However, the height increases by 1.033 [mm] per cell that is added. Since each of the stacks will deliver 206.25 [kW], it can be calculated that the height of the stack will become 864 [mm]. In each wing, two of these stacks need to produce the 412.5 [kW] output that is desired. This means that the fuel cell stacks will combined be 0.84 [m] by 0.887 [m] by 0.156 [m], which accounts for a total of 0.116 [m^3].

The largest components of the fuel cell are the subsystems. To make a precise estimate of whether all these systems will fit in the wing, an assumption had to be made. It was assumed that except for the humidifier and the anode re-circulation pump the subsystems do not necessarily have to be located close to the fuel cell. This assumption allows for the free placement of all the subsystems within the wing. To calculate whether all these subsystems will fit in the wing the Powercellution heavy-duty system is used as a basis. The volume of this entire system is 284 liters. From this, the volume of the stack can be removed. The volume of a 100 [kW] fuel cell stack is about 35 liters. This means that in the worst-case scenario the rest of the systems will take up 249 liters. To reach the 400 [kW] output that is going to be needed per fuel cell, 4 of these heavy-duty systems would have been needed. This would then add up to a total of 996 liters for all the subsystems. This would easily fit within 3.5 [m^3]. The only thing that must still be taken into account is the rib spacing of 80 cm. Only the fuel cell stack and the battery are too big to fit inside the ribs. Fortunately both can be divided into multiple parts to fit within the rib spacing.

[23] URL: `https://www.datocms-assets.com/36080/1611437833-p-stack.pdf` [Accessed on: 18-06-2021]

Furthermore, a large part of the cooling system will not be placed in the wingbox. As has been explained in Subsection 10.4.1, the radiator will be placed in a duct under the wing. This means that even less space is needed in the wing.

Also, it must be noted once again that the volume increase and output increase will not be a one on one relation. As could be seen in Section 10.3 the weight of a fuel cell system does not increase linearly. This will then also be seen for the volume. Therefore, it can be concluded that the wingbox will have enough space to fit all the subsystems of the fuel cell system.

From this, a layout of the fuel cell system in the wing can be made. This layout is displayed in Figure 10.9.

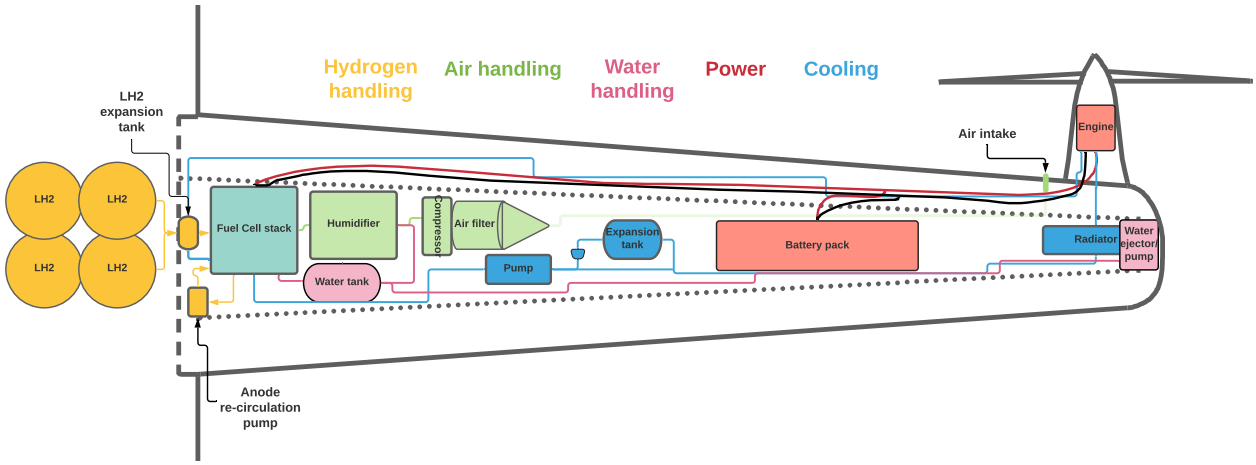

Figure 10.9: Wing plan showing the subsystems needed for the fuel cell

10.6. Fuel Cell Sustainability

As reported in Chapter 3, several green indicators are used to evaluate the greenness of the design. One of the indicators, IND-GP-07 concerns the production of NO_x during landing and take-off. Fuel cells do not emit any NO_x,[67] so the design scores excellent on this green indicator.

Furthermore, as investigated in Clean Sky, the contrails formed by fuel cells are 60-80% less in comparison to a normal aircraft. Furthermore, below 30,000 [ft], contrails and cirrus can actually not even form [66]. In addition, water vapour precipitates itself below 10,000 [ft] and therefore no build-up of water vapour is expected. [24]

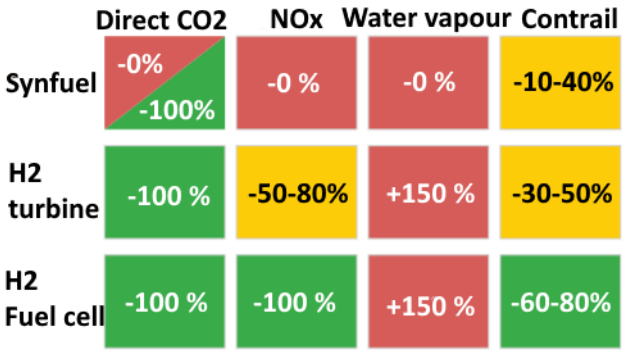

Figure 10.10: Emissions hydrogen systems [66]

These effects are summarized in Figure 10.10.

10.7. Recommendations

During the design, twos ideas were investigated to achieve a more efficient design. These are cooling using the wing, and secondly, the Meredith effect. These ideas will be elaborated here, including recommendations for future design.

10.7.1. Cooling with Wing

Over the wing, there is a big flow of air travelling at a relatively high speed. It was investigated whether by heating the skin of the aircraft (by letting the cooling liquid flow under the skin), a lot of energy could be dissipated to the air. This method is a form of forced convection heat transfer [68]. The total rate of heat transfer was calculated using:

[24] URL: https://climatechangeconnection.org/solutions/transportation/air-travel/ [Accessed on: 14-6-2021]

$$\dot{Q} = hA(T_\infty - T_s) \tag{10.10}$$

In this equation, $\dot{Q}$ is the heat transfer rate, h is the convective heat transfer coefficient, A is the area where convection occurs (in this case the wing area is used). T_∞ is the temperature of the upstream air, and T_s is the surface temperature of the object (in this case the wing skin). An upstream temperature of 20[°C] was assumed, and a skin temperature of 70[°C], which is about the temperature the fuel cell is allowed to be. No heat exchanger is used to move extra heat from the liquid into the wing.

The convective heat transfer h, follows from the Nusselt number, which in turn depends on the Reynolds number, as well as the Pratzl number, of the air [68]. Wang et al. tested the following relation to be accurate regarding this dependence for the flow over a NACA63421 airfoil:

$$\overline{Nu} = 0.0943 Re^{0.636} \mathrm{Pr}^{1/3} \quad \left(\text{for } Re \geqslant 5 \times 10^5 \right) \tag{10.11}$$

Where $\overline{Nu}$ is the average Nusselt number over the airfoil, Re is the Reynolds number and Pr is the Prandtl number. Since a different airfoil is used then in this experiment, there can of course be differences, however they are expected to be small.

Then, to find the convective heat transfer:

$$h = \overline{Nu} \frac{k_{air}}{c} \tag{10.12}$$

It was found that, with the wing surface area present, only around 30/40 [kW] of power could be dissipated over the wing.

Furthermore, heating the wing has an effect on boundary layer characteristics. Hassanalian et al [69] investigated top surface heating, inspired by the albatross. This bird has a black top surface of its wing, presumed to increase his lift. They concluded that lift can be increased by up to 70% and drag could be reduced by 60% for certain angles of attack. In another paper however, the maximum effect was only found to be 2.5% and 1.6% respectively, and this was for Reynolds numbers a lot lower then the one of the H_2OPPER [70]. Furthermore, it was elaborated that placing the heating strips on the wrong location may actually decrease performance considerably. Therefore, since the loss of heat is minimal, and there are still many uncertainties, this design feature is recommended for future design to be explored, as it might be very promising for design where lift over drag is important as well as the loss of heat.

10.7.2. Meredith Effect

Using the radiator heat to heat up the mass flow through an aircraft duct and thereby creating thrust is a phenomena already established in WWII, known as the Meredith effect. The idea is to first slow down the air by a diffuser, then let it flow through a radiator and thus speed it up again to a higher velocity, much like a ramjet engine [71]. Just as in a ramjet, the effect is more effective with increasing velocity. Marco Pellegrini and Luca Piancastelli studied the effect of the Meredith effect on the total force [71]. It was found that, for their radiator at 90 [m/s], the forward force exactly cancelled the drag force induced by the pressure difference over the radiator. In the paper, the radiator is also placed behind the propeller and has a similar dimension and shape. However, there are still many differences and uncertainties, like the temperature difference between the radiator and the air, the compression ratios etc. Therefore, it is recommended to further analyze and test the effect to find out whether it is possible that effective thrust is generated using the Meredith effect. For the design at this stage, no extra drag nor thrust is taken into account resulting from the radiator.

11
Systems

In this chapter, the systems used by the aircraft will be sized and discussed. First, a subsystem overview is given in Section 11.1. A high-level hardware diagram is given in Section 11.2, in addition to the sizing of the propulsion and cooling systems. A low-level hardware diagram is given in Section 11.3, with explanations of the different systems. In Section 11.4, an electrical diagram is given, in addition to the sizing of the cables of the aircraft. Section 11.5 gives an overview of the software systems of the aircraft. At last, Section 11.6 shows the estimated power needs of the systems and Section 11.7 discusses the masses of the systems.

11.1. Subsystem overview

The subsystem overview shows the functions and requirement of the energy storage tank.

11.1.1. Functions

The systems have multiple functions and these can be divided into the following categories:

- Provide the fuel cell with hydrogen and oxygen
- Remove the heat from the fuel cell and the engines
- Deliver power to the engines and other systems
- Support the aircraft with systems such as attitude control and cabin support.

11.1.2. Requirements

HOPPER-T-F-EP-1	The aircraft shall contain required ATC communication tools
HOPPER-T-F-EP-Av.1	The avionics of the aircraft shall be usable after a lightning strike
HOPPER-T-F-EP-Av.2	The avionics of the aircraft shall be usable with an engine out
HOPPER-C-R-CS-10	Each liquid-cooled engine shall have an independent cooling system, including coolant tank
HOPPER-C-R-CS-11	Each propeller shall be able to be controlled separately
HOPPER-C-R-CS-15	Engine shall be able to be restarted in flight
HOPPER-C-R-CS-16	During take-off and initial climb at the all engine(s) operating climb speed, the propeller must limit the engine r.p.m., at full throttle or at maximum allowable take-off manifold pressure, to a speed not greater than the maximum allowable take-off r.p.m
HOPPER-C-R-CS-17	Maximum continuous demand of the electrical power system shall not exceed 100 % of the load limits of the alternator(s) or generator(s) that are equipped with current monitoring capability

11.1.3. Assumptions

- **There is enough space for the low level hardware:** Only the volume of the high level hardware is assessed if it fits in the aircraft. Since low level hardware is generally of smaller size it was assumed that it will be able to fit in the aircraft.
- **There is enough space for wiring:** All the wiring and piping require space to run without interference. It was assumed that the wiring and piping can run freely if not inside the cabin. Moreover, it was thus assumed that all subsystems can reach other subsystems.

11.2. High Level Hardware Diagram

In Figure 11.1, the high level hardware diagram for the aircraft is shown. This diagram puts more emphasis on the fuel cell. Different flows have been given their own color: dark blue for hydrogen, blue for water,

light blue for air, yellow for electricity, red for hot coolant and pink for cold coolant. In addition, computer inputs and sensor outputs are shown in grey. These will be further explained in the software diagram, in Section 11.5. In the upcoming subsections, the sizing of the propeller, engine, and the cooling and heating system will be elaborated.

The hydrogen comes from the LH2 tank. This tank is controlled by two valves, one of which delivers the hydrogen to the fuel cell, via an expansion tank. The other valve directs the boiled-off hydrogen to the expansion tank as well to minimise losses. However, when the fuel cell is not operative the boil-off has to be directed to an aircraft outlet. The hydrogen in the tank is expanded using heat from the fuel cell, except at start-up, where it needs to be heated using an external heater. The power for this heater is provided by the power management and distribution system (PMAD) which contains the battery discussed in Subsection 9.3.2. A more detailed overview of the PMAD can be found in Figure 11.3. The electricity provided by the fuel cell is used to power the engines, as well as the low voltage systems.

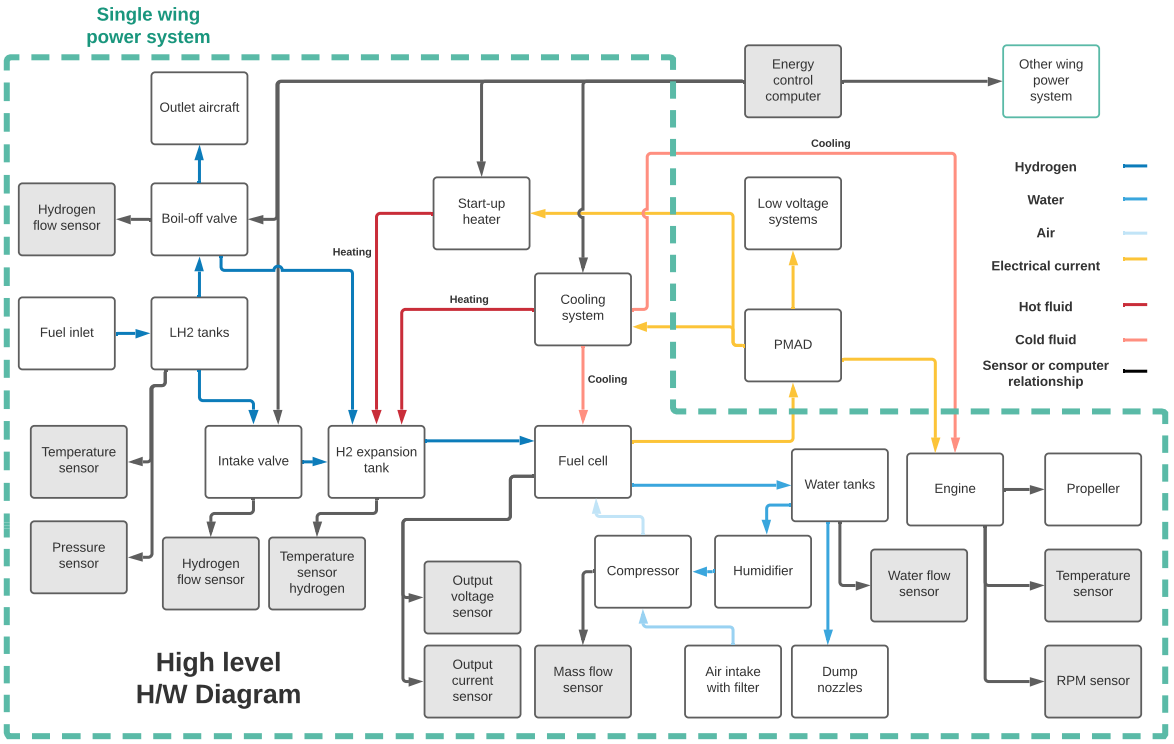

Figure 11.1: High level H/W diagram

11.2.1. Propeller

The propeller of the H_2OPPER has a diameter of 2.43 [m] and a mass of 79.7 [kg]. The sizing was based on reference aircraft and an empirical relationship between the diameter and output power. The propeller of the reference aircraft, the L 410 NG, uses the AV-725 propeller [1]. This propeller has a diameter of 2.3 [m], has a mass of 77 [kg], and has five blades. The propeller sized in the midterm report had a diameter of 2.8 [m] and four blades. The new propeller scored better in the noise level indicator, as it has a smaller diameter and more blades, the new noise level produced by the propeller is 107.66 [dB].

This propeller however is only able to handle an engine with a maximum power of 635 [kW] [2]. The power input of the propeller is found by dividing the output power by the propeller efficiency. No propeller efficiency could be found for this propeller and therefore an efficiency of 0.80 was assumed, based on the characteristic curve of the propeller efficiency for fixed pitch propellers [72, p.7]. Since the AV-725 propeller has a feathering system (variable pitch) it is assumed that the propeller efficiency is 0.80 for all flight phases.

[1] URL: `http://www.let.cz/l410ng` [Accessed on: 7-6-2021]
[2] URL: `http://www.aviapropeller.cz/av725.htm` [Accessed on: 7-6-2021]

The power input per propellers is then calculated by dividing the maximum power need per propeller, 1170 / 2 [kW], by 0.80, resulting in an input power of 730 [kW]. This is above the power that the AV-725 propeller is able to handle. From Raymer [34, p.221], it is obtained that there exists an empirical relationship between the fourth root of the power of an engine and the diameter of the propeller. Using this relationship, it can be estimated that the propeller diameter should be 1.036 times larger. This results in a new propeller with a diameter of 2.43 [m] and a mass of 79.7 [kg]. It should be noted that the aircraft will use counter-rotating engines. This means that the propellers need to be mirrored. This has no effects on the weight of the propellers, but it might increase the production cost.

11.2.2. Engine

It is calculated that each engine should deliver 730 [kW]. From a literature research, a DC brushless aircraft engine type was found, the magni500. This engine has an efficiency of 0.93, works on a voltage of 540 [V] and has a weight of 133 [kg]. This engine however is only able to deliver a maximum of 730 [kW] [3]. A twice as smaller engine in terms of power delivery from the same producer has the same engine efficiency. It is therefore assumed that a slightly more powerful engine will also be able to reach an efficiency of 0.93. To get an estimation of the weight of the engine, a linear regression is taken between the power and weight for the two engines. When sizing for 730 [kW], a weight of 160 [kg] is obtained. As this is a very basic estimation, a margin of ± 10 [kg] will be taken for the engine weight.

11.2.3. Cooling and Heating

The cooling system is sized based on the required coolant flow. In [73], it was found that a coolant flow of 190 [L/min] is needed to cool down a fuel cell of 100 [kW]. This would mean that for a fuel cell output power of 412.5 [kW] a coolant flow of almost 800 [L/min] must be necessary. However it must be noted that increasing the flow rate will only affect the cooling up to a certain point. This can be substantiated by [61]. In this paper it is shown that a cooling flow rate above 540 [L/min] will not increase the heat that can be removed substantially. Fortunately, heat removal is not only dependent on the coolant flow rate but also on the temperature difference between the coolant and the ambient air, as well as the air flow rate itself. As was shown in Subsection 10.4.1 by increasing the airflow rate is was still possible to remove the heat with only a coolant flow rate of 290 [L/min]. Therefore in the next stage of the design it must be possible to find the best combination of airflow rate and coolant flow rate to remove all the heat. However since this combination is not known yet it is decided to size for a flow rate of 800 [L/min]. A coolant pump was found that is capable of reaching this flow and is also able to handle temperatures up to 80 [°C]. Two of these pumps have a power need of 4.5 [kW] [4].

For the heating system, a heating element had to be chosen that is able to heat the hydrogen to 80 [°C]. The amount of hydrogen that goes through the fuel cell per second can be calculated by dividing the power output of the fuel cell [J/s] by the energy density of hydrogen [J/kg] : $800{,}000/(120 \cdot 10^6) = 0.0067$ [kg/s]. By assuming that the hydrogen only will need to be heated during the first minute of operations, it can be calculated that 0.4 [kg] of hydrogen needs to be heated up to 80 [°C]. The energy needed to heat up hydrogen from -253 [°C] (20 [K]) to 80 [°C] consists of two parts. The energy of vaporization and the energy of heating up. The total energy need is calculated to be 2 [MJ]. By using a 12 [kW] heater, this energy can be reached within 3 minutes, which is deemed a reasonable start-up time. It should be noted that this assumes no heat loss from the expansion tank. Start-up times may therefore be slightly longer.

11.3. Low Level Hardware Diagram

The low level hardware diagram shown in Figure 11.2 lists necessary systems to assist aircraft missions. These systems have been divided in to the 6 categories Exterior Lighting, Navigation and Communication, Cockpit Interface, Environment Sensors, Cabin Systems and Attitude and Control. Note that when designing an aircraft in full detail more low level hardware systems have to be considered. With regard to the level of detail of this design Figure 11.2 includes only the hardware systems that either require the most power or that are of critical importance.

[3] URL: `https://www.magnix.aero/products` [Accessed on: 7-6-2021]

[4] URL: `https://www.iwakipumps.jp/en/products/magnetic/520/mx/` [Accessed on: 7-6-2021]

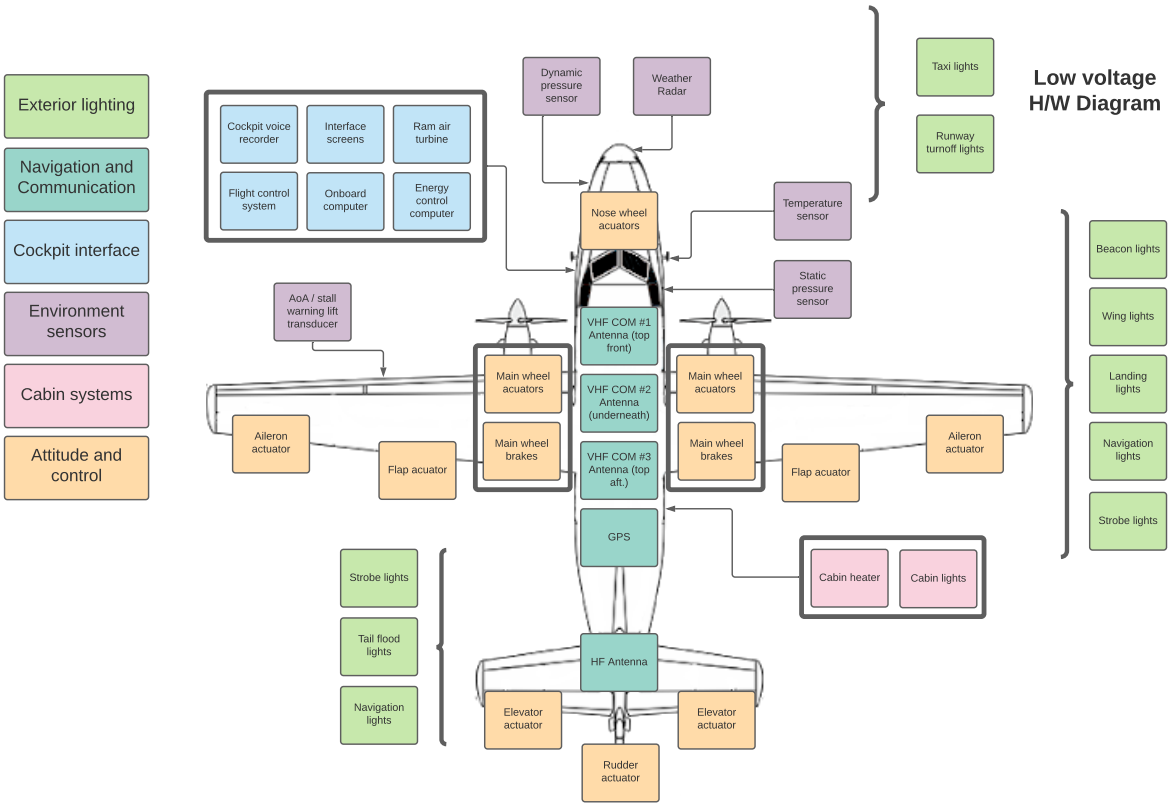

Figure 11.2: Low level H/W diagram

11.3.1. Exterior Lights

The exterior lighting of the aircraft has multiple functions. First of all, the lights have as purpose to illuminate the surroundings of the aircraft to improve the visibility of the pilot. Examples of those lights are the taxi lights as well as the runway turnoff lights and the landing lights. Second, lights are used to be seen by others. The lights used for this purpose are the beacon lights, navigation lights and strobe lights. Finally, lights are used to illuminate the aircraft. Lights with this purpose are the wing lights and the tail flood lights. The wing lights are used to illuminate the leading edge of the wing to facilitate aircraft inspection. The tail flood lights are to improve the visibility of the airline logo and the aircraft registration number. Lights can have multiple functions as well. The wing lights do make the aircraft more visible for instance.

11.3.2. Navigation and Communication

In order to determine the position of the aircraft and navigate to its destination, the aircraft is equipped with a Global Positioning System (GPS). Moreover, the aircraft is equipped with three very high frequency (VHF) antennas. The VHF aviation communication system is used for line-of-sight communication. This employs aircraft-to-aircraft and aircraft-to-ATC (Air Traffic Control) communication. The reason for the aircraft having three VHF antennas is to be able to communicate with others from any orientation. Moreover, the VHF antennas are placed apart to minimize cross-coupling. Cross-coupling occurs when two antennas operate at the same frequency and as a result absorb the power radiated by other antennas. The aircraft is equipped with an HF antenna as well. This antenna is used for long-range communications.

11.3.3. Cockpit systems

In the cockpit, the interface for the pilot and on-board computers can be found. These two systems work together to display flight information to the pilot. Particular to the H_2OPPER design is the addition of an energy control computer to regulate the energy system discussed in Figure 11.1. Furthermore, the cockpit is also provided with a flight control system to put control surfaces in motion. In case of an emergency the cockpit can be powered with a ram air turbine (RAT) that can be manually folded out of the fuselage.

Communications from the cockpit are recorded and stored in a 'black box'.

11.3.4. Cabin systems

The cabin is provided with heating and lighting. As can be seen in Figure 10.8 warm air that was used to cool the cooling fluid is led to the cabin. By regulating the hot air supply the cabin temperature can be controlled.

11.3.5. Attitude and control

All parts that are required to move such as extracting and retracting the landing gear as well as positioning the control surfaces are controlled by actuators. The actuators for the design are chosen to be electrical driven instead of hydraulic driven. The reason for this choice is that electrical actuators are more aligned with the Green policy. First of all, electric actuators have a higher efficiency compared to hydraulic actuators. Secondly, hydraulic actuators can leak hazardous fluids which are costly to clean up.[5]

11.4. Electrical Diagram

An electrical diagram is made to give an overview of the connections between the electrical systems of the aircraft. The diagram can be seen in Figure 11.3. The electricity flows are divided in two types: high voltage and low voltage flows. Most of the low voltage systems have been grouped in the 'Other low voltage systems' block to make a clearer diagram. These low voltage systems correspond to the low level H/W diagram from Section 11.3. The diagram also shows what is part of the power management and distribution (PMAD) system with a green block.

The fuel cell is the primary supplier of electricity in the system. This electricity is led through a converter to get a steady 540 [V] for the engines. This electricity is then inverted to a three-phase power for the engines. The electricity from the fuel cell is also used to charge the battery in the system. The battery also provides energy to the engine. This connection does contain a diode to prevent the battery from discharging with the electricity to the fuel cell. Both the fuel cell and the battery are also able to power the low voltage systems, but the electricity first needs to be converted down to a voltage of 28 [V]. With this electricity, the low voltage systems, such as heaters and coolers are powered. If other voltages are needed, the electricity is converted to another voltage. A few examples of the converters have been shown in the diagram as well.

It should be noted that there is a fuel cell, battery and engine in each wing of the aircraft. Both sides are able to power the other low voltage systems of the aircraft. In addition, the battery and fuel cell are connected to both sides. In case of a malfunction of one of the energy suppliers, both engines can still be powered. In the following subsections, more detail is given on the efficiencies and cables of the system.

[5] Retrieved from: https://www.tolomatic.com/de-de/blog/artmid/843/articleid/337/high-force-linear-actuators-%E2%80%93-hydraulic-vs-electric-webinar

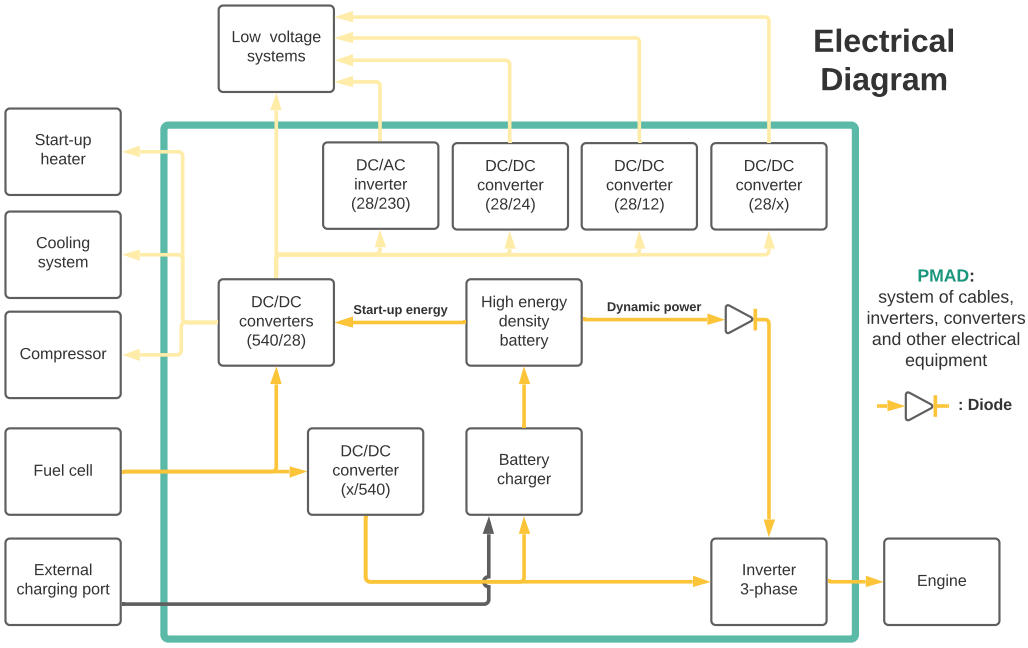

Figure 11.3: Electrical diagram of the Island Hopper.

11.4.1. Efficiencies

In the system, there are various places where energy is lost. For example, in the converters and inverters. In Table 11.1, the efficiencies of the electrical system are displayed. These efficiencies are taken into account in the power budget of the aircraft.

Table 11.1: Overview of the efficiencies of the electrical system

Part	**Efficiency** [-]
540/28 DC/DC converter	0.91 [6]
Smaller DC/DC converters	0.97 [7]
3-phase inverters	0.989 [8]
Engines	0.93 [9]
Fuel cell	0.5 [10]

11.4.2. Cables

This subsection discusses the sizing of the cables. Some considerations need to be made when sizing the cables. First, some of the cables need to able to handle higher currents than normally found in aircraft. These are the cables from the fuel cell and batteries to the engines. The maximum possible power and amperage of the cables are shown in Table 11.2. In addition, an estimate is given on the one-way distance the cable has to travel and the mass per meter for each cable. From the table, a mass of 120 [kg] can be estimated for the high current cables.

The mass per meter for each cable is determined with the cross-section and material of each cable. Copper

[6] URL: `https://www.emea.lambda.tdk.com/nl/KB/PAF450F280-PAF600F280-Datasheet.pdf` [Accessed on: 10-6-2021]
[7] URL: `https://www.victronenergy.nl/upload/documents/Datasheet-Orion-Tr-DC-DC-converters-low-power,-non-isolated-EN.pdf` [Accessed on: 10-6-2021]
[8] URL: `https://www.magnix.aero/products` [Accessed on: 10-6-2021]
[9] See 3-phase inverters source [Accessed on: 10-6-2021]
[10] See Subsection 10.2.2

is chosen for the wire as it is commonly used for wires. It has a high electrical conductivity which means less heat is produced. It also is an easy to recycle material [11]. Allowable ampacities were obtained from the National Fire Protection Association (NFPA) for varying wire cross-sections [74]. The ampacities were given for a maximum temperature of 60 [°C]. An exponential relationship was found and is used to determine the cross-sections for the cables. The mass per meter of these cables is then found by multiplying the cross-section by the density of copper, 8960 [kg/m^3] [12]. The insulation of the copper wires will most likely be a thermoset as this material will not melt at high temperatures. The sizing however is disregarded for now as the weight of the insulation is expected to be a magnitude lower compared to the copper.

Table 11.2: Overview of the power estimations per group

Cable	**Power [kW]**	**Current [A]**	**Mass per meter [kg/m]**	**One-way distance [m]**
FC - inverter	400	740	2.4	10
FC - Battery charger	400	740	2.4	1
FC - Converter	30	56	0.05	1
Battery - inverter	340	630	1.4	10
Cross-link	400 & 340	740 & 630	2.4 & 1.4	5

The second considerations is that at high altitudes, the air density is lower. This means that the free air in the aircraft is less able to dissipate the heat from the cables compared to at sea-level [75, p.2]. However, at 10,000 [ft], only a temperature rise of less than 4 [°C] needs to be accounted for. The chosen cables have been sized for 60 [°C], which would now be maximally 64 [°C].

The third consideration is on the magnetic fields that the cables produce. The maximum exposure-level to a magnetic field in public is set to 200 [μ T] [76, p.832]. The cable with the highest current, 750 [A], produces this level of magnetic field at a distance of 0.75 [m] from the cable. This could be within the distance of passengers. To prevent this, it is possible to reduce the magnetic field by placing the starting and returning cable besides each other. The cables would have the same current, but in opposite direction, and therefore creating opposite magnetic fields reducing their energy. However, the magnetic fields are still present as the two cables cannot coincide perfectly. To reduce the magnetic field even further cables could be twisted or shielded using foils. Twisting two wires results in the effective centers of the wires to be closer to each other and thus reducing the total magnetic field more. In future phases it is recommended to size the shielding regarding the maximum allowable magnetic fields for the passengers, but also the aircraft equipment. For example, the magnetic field from the cable should not interfere with the GPS systems onboard.

11.5. Software Diagrams

The software (S/W) diagram is divided into four parts; fuel cell power, hydrogen/oxygen flow, flight control and safety control. Each of these parts are discussed in the subsections below. The S/W diagram is shown in Figure 11.4. In addition, a data handling diagram is made to give a brief overview of the data flows of the system. This diagram is found in Figure 11.5.

11.5.1. Fuel cell power

This part of the S/W diagram is used to decide the output power the fuel cell has to deliver. Since the batteries are used for the dynamic response of the aircraft, they deliver small power peaks etc, the fuel cell should provide the average of the power. However, since the batteries are mainly drained during take-off, they also have to be recharged during the flight. Based on the flight distance left, the weather conditions (head/tailwind for example) and the current state of charge of the batteries, a recharge rate is chosen for the battery. Then, with this recharge rate and the predicted average power needed for flight, the required fuel cell power is determined. This required power then determines the hydrogen and oxygen flow, as will be described in the following subsection.

[11] URL: `https://edisontechcenter.org/wires.html` [Accessed on: 18-6-2021]
[12] URL: `https://www.rsc.org/periodic-table/element/29/copper` [Accessed on: 10-6-2021]

11.5.2. Hydrogen/oxygen Flow

The software diagram of this part shows the interaction in the energy control system which determines the hydrogen flow into the fuel cell. This system is based on Fuzzy logic and a fuel cell model. The fuel cell model is used to get a prediction of the output power and hydrogen flow that goes out of the system. These values are compared to the measured values from the fuel cell. The error is calculated and is put into the Fuzzy system. In addition, the power requested from the energy control computer is also given as an input to this system.

The Fuzzy logic system allows for more controlled inputs and produces less overshoot in the input hydrogen flows, without the need of complicated systems, such as controllers based on artificial intelligence [77, p.626]. The Fuzzy logic system works by fuzzifying the inputs, which means that an input is compared to a set such as: a bit warm, warm and very cold. The input is given a degree of membership for each set varying from 0 to 1; the chance that the hydrogen has a slightly low flow is 0.4 , and that it has a moderate flow is 0.6 . This sets can be defined by possibility distributions. With these fuzzy inputs, fuzzy rules are applied. Examples of these rules are: If the hydrogen has a slightly low flow, turn the flow valve slightly open. Fuzzy outputs are received from these rules; slightly open the valve. These outputs need to be defuzzyfied to get actual numbers. This defuzzyfication is based on an algorithm that finds the best output based on the the various degrees of memberships of all the inputs [78].

To implement this system, it is needed to get as many fuzzy rules in a database. These can be obtained from expert judgements or experimental data [77, p.634]. The proposed system is not completely designed; no fuzzy rule data set and membership functions have been devised. The control diagram would also need to be expanded. It is recommended to look into the implementation of this system post-DSE, as it allows for smoother operations of the fuel cell, leading to an increase of the life-span of the fuel cell [77, p.635].

11.5.3. Flight control

The flight control system puts emphasis on the sensors and actuators of the aircraft. Environment and flight sensor outputs are registered by the onboard computer and are processed to calculate various flight data, such as the velocity and heading of the aircraft. This data is displayed to the pilots on the interface screens, and is exported to the auto-pilot. The auto-pilot is able to give control inputs, as are the pilots. The control system consists of velocity and attitude control. It gives commands to the engines, and actuators for the lift devices. The control system also gives commands to the brake system. It should be noted that the pilot inputs need to be processed first however, as the inputs of the aircraft are done by a fly-by-wire system. A control system will need to be set-up when producing the aircraft.

11.5.4. Safety

The energy control computer is used to ensure all components and payload remain safe. Several parameters, such as the temperatures of the engine and the fuel cell, are analyzed. If temperatures get to high, the energy control computer is able to take appropriate actions, by for example increasing cooling fluid flows, or decreasing the power output that is requested from the main control computer. Certain rules need to be set-up to make sure that the power does not decrease below critical levels. This will need to be done in future phases of the aircraft design.

11.5.5. Data Handling

Lastly, the data handling diagram shows the data flows of the aircraft. Two computers are used; the onboard computer and the energy control computer. The onboard computer has two main tasks: provide communication, and process the flight data and inputs of the pilots. The onboard controls the pilot interfaces, as well as the actuators of the control surfaces of the aircraft. The onboard computer also gives inputs to the energy computer: the required power. The energy control computer processes all the hydrogen and oxygen flows, as well as the safety systems of the batteries and the cooling systems. This is done by giving control signals to for example the valves and pumps.

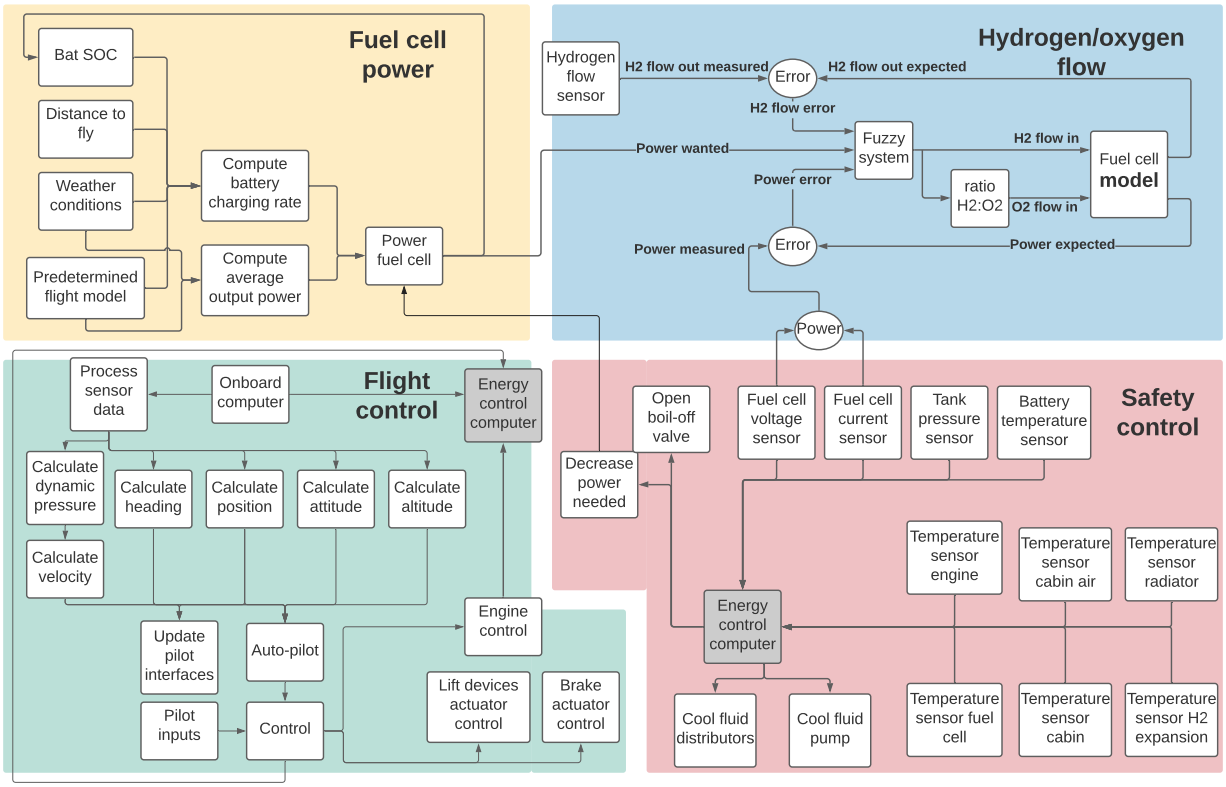

Figure 11.4: Software diagram of the H_2OPPER

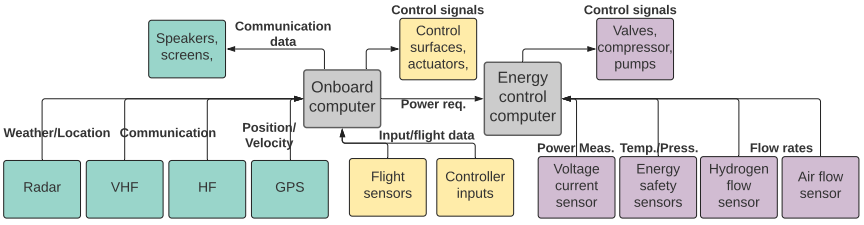

Figure 11.5: Data handling diagram of the H_2OPPER

11.6. Power Budget

A power budget was made to get an overview of the power needs of the aircraft. In Table 11.3 the required power for earlier discussed groups in Section 11.3 is shown, in addition to the power needs of the start-up heater and the cooling pumps. The powers given are not always needed during the entire flight. For example, the start-up heater only needs to be turned on on the ground for less than three minutes. The energy system of the aircraft is sized on the most critical mission segment; take-off. It needs to deliver 1586 [kW] during this period. This consists of the power needs of the low-voltage systems, 14 [kW], and of the engine, 1570 [kW]. These required powers obtained from Table 11.3 are taken into consideration together with the efficiencies in Table 11.1 in Subsection 11.4.1.

The estimations of the power of the low-voltage systems were performed by researching existing aircraft parts and studying their data sheets when provided. Note that the aircraft parts found are not necessarily the parts used for this design. In some cases only technical data was available for aircraft parts intended for slightly smaller or larger aircraft.

Table 11.3: Overview of the power estimations per group

Group	Power [W]	Group	Power [W]
Exterior lighting	1500 [13]	Cabin systems	200 [14]
Navigation and Communication	250 [15] [16]	Attitude and control	4200 [17]
Cockpit systems	3000 [18] [19]	Cooling pump	4500 [20]
Start-up heater	12000 [21]	Engines	1,570,000

11.7. System Changes to the Mass Budget

A second class mass estimation was performed using the method defined by Raymer [34, p.403] and is shown in Section 16.6. For these estimations, some alterations were made to better reflect the H_2OPPER. First, since the power system is electric instead of kerosene based, more electrical energy needs to be transported. This means that an additional 150 [kg] in wiring is needed for the powering of the engines. This weight is determined from the electric wire estimation from Table 11.2, with a margin to account for differences in cable length and insulation weight. Secondly, due to the Raymer method being published in 1989 it overestimates the weight of computer technology. In order to account for this the uninstalled avionics weight was decreased by 200 [lbs] in the Raymer method [22].

[13] URL: https://aeroleds.com [Accessed on: 4-5-2021]
[14] URL: https://www.ventilatieshop.com/buisventilatoren/blauberg-buisventilatoren/blauberg-iso-mix-160-geisoleerde-buisventilator-staal-aansluiting-160mm/ [Accessed on: 4-5-2021]
[15] URL: https://buy.garmin.com/nl-NL/NL/p/576890#specs [Accessed on: 4-5-2021]
[16] URL: https://www.aircraftspruce.com/pages/av/antenna_com/avt4.php [Accessed on: 4-5-2021]
[17] URL: https://www.linak.com/products/linear-actuators/la37/#/diagramsbrochuresmanuals
[18] URL: https://buy.garmin.com/en-US/US/p/66916,http://www.let.cz/documents/L410NG.pdf [Accessed on: 4-5-2021]
[19] URL: https://flightdata.aero/wp-content/uploads/2020/12/FDS-sentry-zine-2020-EN.pdf [Accessed on: 4-5-2021]
[20] URL: https://www.iwakipumps.jp/en/products/magnetic/520/mx/ [Accessed on: 4-5-2021]
[21] URL: https://nl.rs-online.com/web/p/heating-elements/273135/ [Accessed on: 11-6-2021]
[22] URL: https://buy.garmin.com/en-US/US/p/151198 [Accessed on: 11-6-2021]

12
Hydrogen Storage

In the previous phase it was decided to use liquid hydrogen (LH2) as the energy source of the aircraft. In Section 12.1, an overview is given of the functions, requirements and assumptions for the hydrogen storage subsystem. In Section 12.2, the reasoning for liquid hydrogen is restated. The sizing of the storage tank is shown in Section 12.3. To liquefy hydrogen, it is required to cool it to a temperature of 20 [K]. To store a liquid at such low temperatures, various considerations need to be taken into account regarding the materials of the tank. These considerations are given in Section 12.4. In Section 12.8, the limitations of the sizing method are discussed. The final design is given in Section 12.5 and recommendations for future phases are given in Section 12.9.

12.1. Subsystem Overview

The subsystem overview shows the functions and requirement of the energy storage tank. The assumptions used are given as well.

12.1.1. Functions

The energy storage subsystem stores the liquid hydrogen at cryogenic temperatures and shall allow for liquid hydrogen to be extracted for use by the fuel cell.

12.1.2. Requirements

HOPPER-T-G-RF-1	The aircraft shall be able to be refuelled with a maximum of 2 people
HOPPER-T-G-RF-2	The aircraft shall provide enough space for fuel to reach the maximum required range
HOPPER-T-HS-1	The hydrogen tank shall be able to withstand an ultimate pressure of 5.7 [bar]
HOPPER-T-HS-2	The hydrogen tank shall operate at pressure of 3.8 [bar]
HOPPER-T-HS-3	The hydrogen tank shall have a boil-off rate no more than 1.6 % per hour
HOPPER-T-HS-4	The temperature inside the tank shall be 20 [K]

12.1.3. Assumptions

- **Composite properties are isotropic:** Composites with uni-directional fibres have different properties in other directions, for example in Young's modulus. This assumption is valid when using multi-directional lay-ups to get a quasi-isotropic material.
- **The temperature inside the aircraft is constantly 40 [°C]:** This temperature is based on average high temperatures on the ground on pacific island nations + 10 [°C] margin [1]. The higher the outside temperature, the more boil-off is to be expected. This assumption is used as it takes a high margin. At 10,000 [ft] it can be expected that the temperature inside the aircraft will be lower, therefore the boil-off rate will be overestimated.
- **The pressure in the tank remains constant:** When liquid hydrogen becomes warmer than 20 [K] it boils off which rises the pressure in the tank. This pressure is needed for the flow of liquid hydrogen out of the tank. However, the ratio between the volume of the boiled off hydrogen and the volume of the withdrawn liquid hydrogen is not the same resulting in a change in pressure.

12.2. Liquid Hydrogen

Hydrogen has a very low density due to it being the lightest molecule. On the other hand, it has a specific energy of 120 [MJ] [79, p.10] which is higher than that of kerosene. Effectively hydrogen has to either be

[1] URL: `https://www.travelonline.com/maldives/weather` [Accessed on: 22-6-2021]

compressed and stored in a pressure tank or cooled down to cryogenic temperatures to obtain a density feasible for aviation. In Table 12.1 the density of hydrogen is indicated as well as an estimate for the hydrogen storage efficiency $\eta_{storage}$ and the tank volumetric efficiency η_{vol}.

Table 12.1: Fuel system parameter for liquid and compressed hydrogen storage [79, p.10]

Parameter	**300 bar H_2**	**700 bar H_2**	**Liquid H_2**
ρ_{H_2} [kg/m^3]	20	40	70
η_{storage} [-]	0.05	0.10	0.20
η_{vol} [-]	0.50	0.50	0.50

As can be seen in Table 12.1, when considering LH2, the increased density leads to an increase in the hydrogen storage efficiency. This means that more hydrogen in kilograms can be carried for the same total tank mass including its contents. In the Midterm report a preliminary analysis was performed which concluded that for this design only LH2 is feasible due to a limitation in available mass [36, p.18].

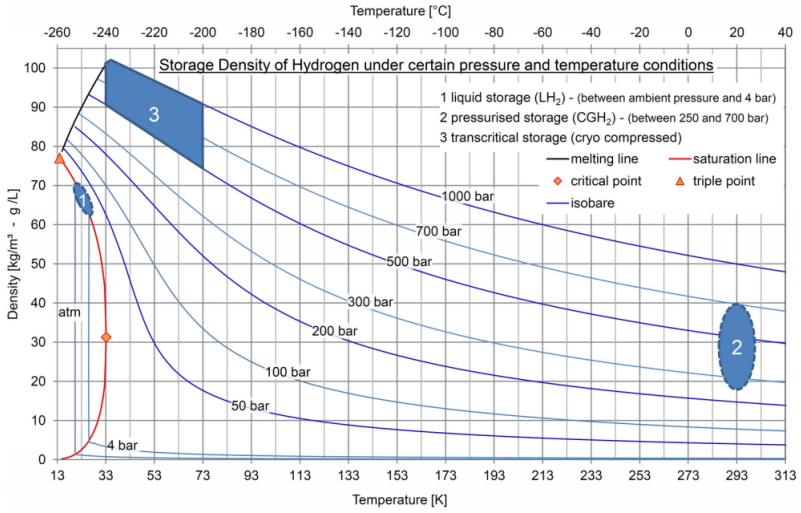

Figure 12.1: Density of hydrogen at specific temperature and pressure [79, p.6]

In Figure 12.1 the saturation line for hydrogen is indicated with a orange line. In order for the hydrogen to remain liquid the temperature should either remain below 20 [K] at atmospheric pressure or at a slightly higher temperature with a higher tank pressure. The region wherein the LH2 has a density feasible for the design is indicated in Figure 12.1 as region 1. The LH2 will be stored in the tank at a pressure of 3.8 [bar] to allow for a small temperature increase. The pressure was chosen using the LH2 orbiter tank of the SpaceLiner Reusable Launch Vehicle (RLV) as reference [80, p.30]. As the tank is pressurized, there is no need for a pumping system to keep the hydrogen flowing.

In the cryogenic tank there will be unwanted heat flowing in affecting the liquid state of the hydrogen. As a result small amounts of LH2 will turn gaseous, called boil-off, which will increase the tank pressure. For cryogenic tanks a boil-off rate of 1.6 [%] per hour of the total fuel weight is regarded as allowable considering the time span the LH2 will be in the tank [80, p.86]. This has an influence on the amount of insulation needed around the tank, and it should also be taken into account when designing the pressure valve, as the pressure in the tank will increase due to the boil-off, which must be prevented from increasing too much.

12.3. Tank Geometry

The tank geometry has effects on several parts of the aircraft. Firstly, the shape of the tank has an influence on the diameter of the fuselage. Next to that, the hydrogen tank may have a significant effect on the centre

of gravity of the aircraft. Therefore, it was aimed to design a tank that allows for flexibility in shape and placement.

A short analysis was performed to find the performance of various tank designs. Three options are discussed in this subsection. The following tanks are regarded: spherical, cylindrical and multi-spherical. From these tanks, it was decided that the multi-spherical tank would be the best for the H_2OPPER. This decision was based on a trade-off based on three criteria: flexibility (placement of tank), efficiency (use of material) and cost. The scores of each tank are summarized in Table 12.2.

Spherical tank:
A spherical tank is the easiest to size; after having determined the required volume of hydrogen, the inner radius of the tank can be calculated using $r_{\text{inner}} = \sqrt[3]{3V/4\pi}$. Spherical tanks are also the most efficient in terms of surface area compared to the volume. Having less surface area will lead to less heat being absorbed into the tank, therefore less insulation is needed for the tank. Due to the efficient use of materials, it is also expected that this tank will be the most cost effective in material cost.

This tank however has the disadvantage of being less flexible in sizing. In the last phase, it was already noticed that the fuselage diameter is very dependent on the size of the tank. In addition, the tank only has two practical placements in the aircraft: in the front, between the cabin and the cockpit, or aft of the cabin. Multiple smaller spherical could be used to be more flexible in placement, but this would increase complexity as each tank would need to have its own connections to the fuel system. In addition, the advantage of having less surface area compared to the volume is diminished.

Cylindrical tank:
The next tank that is considered is a cylindrical tank. This type of tank can be shaped in multiple ways, such as a pure cylinder with flat end-caps, to a cylinder with two hemispheres on each end. This allows for more flexibility in the design of the tank. For example, multiple long cylinders could be placed under the floor of the cabin.

These types of tanks are less efficient compared to spherical tanks, as they have more surface area compared to their volume, which increases the weight of the tank. Also, again multiple tanks need to be used, increasing complexity in the system, albeit less complex than the many spherical tanks option.

It is expected that, due to the simple shape, the tank will have a lower tooling cost compared to the spherical tank. However, more material will be required for the tank, which increases the material cost.

Multi-spherical tank:
The last option that is discussed is a multi-spherical tank (MST). This tank shape consists of multiple spheres that overlap each other. Various shapes are possible regarding the number of spheres. For example, one could stack eight spheres in a 2 x 2 x 2 configuration, or place nine spheres in a 3 x 3 x 1 configuration. This allows for great flexibility in shape. An example of the tank is given in Figure 12.2

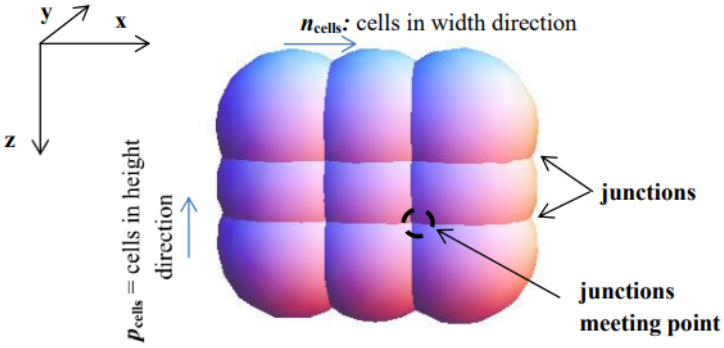

Figure 12.2: Example MST [80, p.79]

In addition, as the tank consists of spherical components, it has better characteristics than the cylindrical tank with respect to surface area. Also, as the spheres are all attached to each other, only one set of connections and boil-off valves is needed for the tank.

It is expected however that the tank will cost more than the previous options. This is due to the unusual shape which would require a more complex mold.

Trade-off

In Table 12.2 each tank is given a qualitative score for flexibility, efficiency and cost. A single positive or negative sign is awarded whenever a shape option has a better or worse performance compared to the other options. Two positive or negative signs are awarded whenever a shape option has a clear considerable advantage or disadvantage over the other options.

During the design of an aircraft, subsystems have to reckon with other subsystems. Flexibility was considered the most important criteria during the design process due to the novelty of the design. Efficiency was treated as the second most important criteria since sustainability plays a major role in this design process. Cost was considered as well since the allowable manufacturing cost of the aircraft is limited.

Table 12.2: Qualitative overview of tank shape scores

	Spherical	**Cylindrical**	**MST**
1. Flexibility	- -	+	++
2. Efficiency	++	-	+
3. Cost	+	+	-

In Table 12.2, it can be seen that either a spherical tank or a MST are favourable options. However, the spherical tank can only be placed behind the cabin while the MST can be placed under the cabin or in the wings as well. In order to remain flexible the MST was opted for. Furthermore, due to the flexibility of the MST it is able to position it close to the fuel cell and thus keeping critical piping as short as possible.

12.4. Tank Materials

Before continuing on to the sizing of the tank, a choice is made on the type of materials used in the tank. A material is selected for the tank wall and for the insulation on the inside of the tank. In addition, inner- and outer-liners were needed to protect the tank wall and insulation. A literature study was performed to get an overview of the possible materials for the tank.

Table 12.3 gives a summary of the materials that have been chosen for the tank design, in addition to the density and thermal conductivities used in the sizing equations [2] [3]. The liners were not used for the calculation of the insulation, therefore no thermal conductivity is given.

Table 12.3: Overview of the materials used for the tank sizing

Type	**Material**	**Density [kg/m^3]**	**Thermal conductivity [W/(m K)]**
Tank wall	CFRP - AS4/8552 ply	1580	7.5
Insulation	Polyurethane - B3 32	32	0.022
Inner liner	Aluminium 5052-H38	2700	-
Outer liner	Polyamide-12	1010	-

Tank Wall

When choosing a material for the tank wall, it should be kept in mind that the tank needs to function at cryogenic temperatures (20 [K]). In addition, the tank will be kept at a pressure of 3.8 [bar] due to boil-off of the LH2. Several material options were found as possible tank walls for cryogenic tanks: metals, continuous-fibre composites and reinforced metallic composites [81, p.24]. From these three, it was decided to choose either for the metals or the composites as little information was available on reinforced metallic composites in cryogenic applications.

Both metals and composites are able to be used in the tank, but composites do come with some additional complications. Firstly, due to the big temperature differences that the tank experiences, differences in ther-

[2] URL: `https://www.engineeringtoolbox.com/metal-alloys-densities-d_50.html` [Accessed on: 10-6-2021]
[3] URL: `https://designerdata.nl/materials/plastics/thermo-plastics/polyamide-12` [Accessed on: 10-6-2021]

mal expansion between the fibres and the resin of the composite could weaken the tank. In addition, the hydrogen may diffuse into the resin of the composite, leading to delamination of the tank walls [82, p.7]. However, these problems can be mitigated, by for example using materials with corresponding thermal coefficients and using liners to prevent hydrogen from diffusing. This would allow for a lighter fuel tank. It must be recognized that composites score lower compared to metals regarding the recyclability criteria. The weight savings do increases the efficiency of the aircraft, which is also a Green Indicator and as the mass budget is limited, it is decided to continue with composites as the material type for the tank wall.

From I. Tapeinos, it was found that carbon-fibre-reinforced polymers (CFRP) can be successfully used for the tank wall of MST in cryogenic operations [80, p.4]. The CFRP used in the the paper is made of the ply AS4/8552 [83, p.5]. This ply consists of a high strength and high strain aerospace grade carbon fibre, AS4, and an epoxy resin, which are combined in a one-to-one ratio [4]. This composite type is adopted for the fuel tank as it is shown to be able to work at cryogenic operations.

Tank Liner

The paper also discusses the use of a liner inside the tank. This liner is needed to protect the composite from delamination, which can occur when hydrogen diffuses into the matrix of the composite wall. The suggested material for the liner was Polyamide-12. This polymer however, was shown to produce cracks during cryogenic operations of the tank. Another possible option is to use metal coatings as a liner material. The problem with metal coatings however, is that the coating might separate from the tank wall during thermal cycling due to differences in thermal coefficients [5]. This problem is however also present when using polymer as the liner material [80, p.100]. Therefore, it is opted to design the inside liner out of a metal.

One of the possible metals is aluminium. An aluminium foil can be placed on the inside to shield the composite from hydrogen vapour. Another option is to evaporate aluminium to create an uniform aluminium film inside the tank [84, p.1], but from a literature research, the maximum thickness that was reached with this method was 500 [nm], which limits the possible usage of the method [85, p.1]. Therefore, it is decided to use an aluminium foil on the inside of the tank as this allows for more flexibility in the thickness of the liner. The alloy 5052-H38 was chosen due to its ductility at cryogenic temperatures [6]. It is however difficult to find the thickness needed for the liner as data on aluminium permeability varies significantly [86, p.2]. For now, an assumption of 1 [mm] is taken for the foil. In the future, a test should be performed to obtain a more accurate thickness. The assumption is justified as the mass of the liner only has a small influence on the total mass of the tank.

Insulation

With the tank liner sorted, the insulation can now be designed. There are several ways to insulate the tank. An option is to use aerogels, materials which are light and have low thermal conductivity. Aerogels however, are very brittle and are therefore not a viable solution for cryogenic operations [80, p.31]. The second option is to use multi-layered thermal insulation. Layers of thin sheets are placed around the tank and prevent heat loss by radiation. They do require a high vacuum to operate. The last option is to use rigid foams. Foams do not require a vacuum and can work at cryogenic temperatures [80, p.31]. The use of foams however comes with a drawback; air is able to travel through the foam and get in contact with the tank. Due to the low temperature of the tank, the air will condensate in the foam [82, p.9]. To prevent this, the foam needs to be shielded from the air. This can be done with a plastic liner around the tank and filling the foam with a non-condensable gas, such as helium. A possible foam type for the tank is polyurethane as this foam material performs well in cold temperatures [87, p.1].

There are several types of polyurethane foams. From A. Demharter it is obtained that high density foam, Polyurethane B3 32, is used for cryogenic applications [87, p.5]. This type has a density of 32 [kg/m^3] and a thermal conductivity of 0.022 [W/(m*K)]. For the liner of the foam, it is possible to use Polyamide-12. This material is chosen as it has a low density and it has a low permeability [80, p.130]. The latter is needed

[4] URL: `https://www.hexcel.com/user_area/content_media/raw/HexPly_8552_eu_DataSheet.pdf` [Accessed on: 1-6-2021]

[5] Personal communication: Prof. dr. ir. S. van der Zwaag - Aerospace materials

[6] URL: `https://www.gasparini.com/en/blog/metals-and-materials-for-low-temperatures/` [Accessed on: 14-6-2021]

to protect the foam from condensed air. The reason why Polyamide-12 can be chosen for the liner on the outside is that it will not be in contact with cryogenic temperatures, which caused the polymer to crack. For the same reason as the aluminium liner, it is difficult to determine the thickness of the polymer based on the permeability without testing. Therefore, the thickness of the polymer is set to 1 [mm]. It should be testes whether this thickness is able to hold the helium gas within the foam. This decision is justified as the mass of the liner only has a small influence on the total mass of the tank.

12.5. Final Tank

The tank for the H_2OPPER has been sized using a tool based on the equations from Section 12.7. The following layout has been chosen: seven 6 x 8 tanks will be placed in the belly of the aircraft, where each wing will be served by three separate tanks to increase reliability. An example of a single tank without insulation is shown in Figure 12.3. The seventh tank can only be used when flying with less payload, to reach an improved range. The internal radii of the sphere is 145 [mm]. The tanks take up a space of of 155 [cm] laterally, 395 [cm] longitudinally and 34 [cm] in height. This includes the insulation, the liners, and a margin of 5 [cm] on each end for valves. The thicknesses and masses of the individual layers are given in Table 12.4

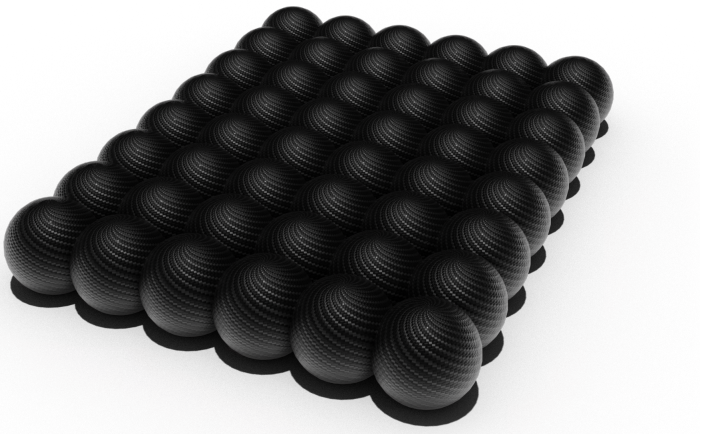

Figure 12.3: Example of a single tank

No pumping system is needed for the system. As the tank will be pressurized by the boil-off , only valves are needed to control the flow of the LH2.

The tanks together have a mass of 156 [kg] and are able to carry 234 [kg] of LH2, of which 23 [kg] is reserved for boil-off. When flying at maximum payload, only 118 [kg] of LH2 can be taken onboard, of which 10 [kg] is reserved for boil-off.

In Figure 12.4, the usage of the LH2 against the flight time is shown for a maximum range flight. For this graph a constant usage of the fuel cell is assumed and a 45 [min] reserve fuel time is considered. The boil-off during the flight is also shown. It can be seen that the boil-off only consists of a small part of the LH2 onboard.

A list of recommendations is given in Section 12.9, which need to be considered before the tank can be installed into the H_2OPPER.

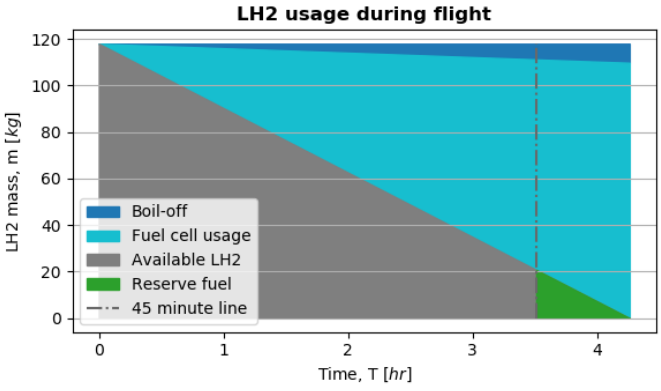

Figure 12.4: LH2 usage during flight

Table 12.4: Overview of the material thicknesses and masses

Type	Thickness [mm]	Mass [kg]
Tank wall	1.11	101.9
Insulation	50	29.4
Inner liner	1	6.1
Outer liner	1	18.6

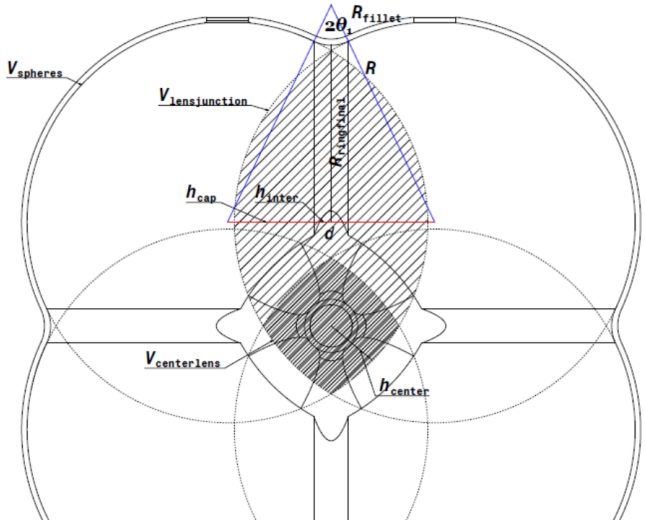

Figure 12.5: Cross section of MST tank [80, p.80]

12.6. Expected Performance

First, the tank needs to be able to perform at a pressure of 3.8 [bar]. The safety margin of 50 % gives an ultimate pressure of 5.7 [bar]. The reference tank, shaped with a 2x2 configuration, only showed bursts at a pressure of 7.2 [bar]. The tank for the H_2OPPER is sized with the same parameters, but with a different shape of 6x8. The larger tank size could have an effect on the ultimate pressure the tank can withstand. The tank thickness and junction straps however are sized accordingly to be able to withstand the desired ultimate pressure. It is still recommended to perform a burst test to determine the actual pressure the tank is able to handle.

Secondly, the tank needs to be able to perform in cryogenic temperatures of 20 [K]. At these temperatures, the inner liner of the reference tank produced some cracks. This liner however was made of a polymer. The tank of the H_2OPPER will be made with an aluminium alloy, which should lead to less cracks compared to the polymer due to the higher ductility at 20 [K]. Less cracks would also mean that delamination of the overwrap material is less likely. Therefore, the life-time of the tank is expected to be higher than the reference tank. The life-time of the reference tank is however unknown. Several fuel-cycles need to be performed to determine the actual life-time of the tank.

12.7. Tank Sizing

The sizing of the tank shell was done as suggested by Tapeinos, I[80]. This means the tank consists of a CFRP shell bounded by polymer hoops at sphere junctions. In order to size the MST, first a sphere configuration has to be determined as seen in Equation 12.1. Here, m_{cells} is the cells in length direction, n_{cells} the cells in width direction and p_{cells} the cells in height direction.

$$multi_{\text{cells}} = (m_{\text{cells}})(n_{\text{cells}})(p_{\text{cells}}) \tag{12.1}$$

Tank inner volume

Once the configuration is known, the volume of the tank can be determined. In Equation 12.2 [80, p.83] the volume of the centers refers to the volume that is found in the middle of a 2 x 2 x 2 cell tank when cells partly overlap. Furthermore, the volume of the fillets refers to the volume formed when the surface between cells is smoothened as seen in Figure 12.5. However, overlapping volume of spheres should be subtracted to avoid considering it more than once. There, overlapping volumes are referred to as V_{lenses} and are indicated in Figure 12.5 with the light shaded area. Finally, in the middle of the four cells a cylindrical structural element is placed. This volume should also be subtracted from the tank volume and is referred to as $V_{\text{cylinders}}$.

$$V = V_{\text{spheres}} + V_{\text{centers}} + V_{\text{fillets}} - V_{\text{lenses}} - V_{\text{cylinders}} \tag{12.2}$$

The volume of the spheres is computed in Equation 12.3. It is found by multiplying the number of spheres, $multi_{\text{cells}}$, with the volume of a sphere. R is the radius and is true for all spheres in the tank.

$$V_{\text{spheres}} = multi_{\text{cells}} \frac{4}{3}\pi R^3 \tag{12.3}$$

To obtain the volume of the lenses in Equation 12.6 it first necessary to know the number of lenses. In Equation 12.4 a geometrical relation has been given to compute the number of lenses with respect to the configuration of the cells.

$$\text{multi}_{\text{junctions}} = [n_{\text{cells}}\,(m_{\text{cells}}-1) + m_{\text{cells}}\,(n_{\text{cells}}-1)]\,p_{\text{cells}} + m_{\text{cells}}\,n_{\text{cells}}\left(p_{\text{cells}}-1\right) \tag{12.4}$$

In Equation 12.5 the centroid distance between spheres is defined as d. By decreasing d two adjacent spheres get closer to each other and thus $V_{lensjunction}$ increases. In Equation 12.6 the volume of all the lenses is found by multiplying the volume of a lens junction by the number of junctions.

$$V_{\text{lensjunction}} = \frac{\pi(2R-d)^2\left(d^2+4dR\right)}{12d} \tag{12.5}$$

$$V_{\text{lenses}} = multi_{\text{junctions}}\,V_{\text{lensjunction}} \tag{12.6}$$

In order to find the volume of all the centers, it is important to know how many center volumes are in the MST. Once again, this can be determined with a geometrical relationship seen in Equation 12.7.

$$multi_{\text{centers}} = [(m_{\text{cells}}-1)\,(n_{\text{cells}}-1)]\,p_{\text{cells}} + \left(p_{\text{cells}}-1\right)(n_{\text{cells}}-1) \tag{12.7}$$

Equation 12.8 is used to obtain the volume of the centers. As seen in Equation 12.9 the volume of a centerlens is dependent of d and a new variable, the final ring radius $R_{ringfinal}$. In Figure 12.5 it can be seen that $R_{ringfinal}$ is the distance between the fillet and the center of the line connecting two sphere origins d.

$$V_{\text{centers}} = multi_{\text{centers}}\,V_{\text{centerlens}} \tag{12.8}$$

$$V_{\text{centerlens}} = \frac{\pi\left(2R_{\text{ringfinal}}-d\right)^2\left(d^2+4dR_{\text{ringfinal}}\right)}{12d} \tag{12.9}$$

To obtain $R_{ringfinal}$ three other parameters are needed which are shown in Equation 12.10. These concern the fillet angle θ_1, the ring radius R_{ring} and h_{inter} is the spherical cap height. The spherical cap height is the distance between the center of d and the intersection of the fillet boundary with d. The ring radius R_{ring} is the distance between the point where two spheres would cross if there had not been a fillet and the center of d. In Equation 12.11 it can be seen how R_{ring} is derived using the Pythagorean theorem. In Figure 12.5 h_{inter} is indicated on the line d. The spherical cap height is found using Equation 12.12. h_{inter} depends on the fillet angle θ_1 and the fillet radius R_{fillet}. The fillet radius R_{fillet} is indicated in Figure 12.5. The fillet angle, θ_1, is indicated in Figure 12.5 as well and is found using Equation 12.13.

$$R_{\text{ringfinal}} = R_{\text{ring}} + \left[\left(R\cos(\theta_1) - R_{\text{ring}}\right) - \left(h_{\text{inter}}\tan\left[\frac{\theta_1}{2}\right]\right)\right] \tag{12.10}$$

$$R_{\text{ring}} = \sqrt{R^2 - \left(\frac{d}{2}\right)^2} \tag{12.11}$$

$$h_{\text{inter}} = R_{\text{fillet}}\sin(\theta_1) \tag{12.12}$$

$$\theta_1 = \arcsin\left(\frac{d/2}{R+R_{\text{fillet}}}\right) \tag{12.13}$$

Next, the volume of the cylinders has to be determined in Equation 12.14. The volume of a cylinder is found with the cylinder radius r_{cyl} and the length of a cylinder l_{cyl} as seen in Equation 12.15.

$$V_{\text{cylinders}} = multi_{\text{centers}}\,V_{\text{cylinder}} \tag{12.14}$$

$$V_{\text{cylinder}} = \pi r_{\text{cyl}}^2 l_{\text{cyl}} \tag{12.15}$$

The cylinder radius r_{cyl} is calculated in Equation 12.16 by taking the maximum of either of the three entries. In this equation s is the width of a polymer strap, $k_{overlap}$ is the strap arc length overlap parameter, $t_{junction}$ is the junction laminate thickness and h_{center} is the height of the spherical cap in the tank center as denoted in Figure 12.5 and determined in Equation 12.18.

The rationale for Equation 12.16 is that the cylinder radius r_{cyl} should first be able to accommodate the ring cross-sectional areas of the four junctions with its perimeter. It should also be at least twice the junction laminate thickness. Finally, r_{cyl} should at least be equal to h_{center} to ensure a smooth transition of the structural element.

$$r_{\text{cyl}} = \text{Max}\left[\frac{4sk_{\text{overlap}}}{2\pi}, 2t_{\text{junction}}, h_{\text{center}}\right] \quad (12.16) \qquad l_{\text{cyl}} = \sqrt{R^2_{\text{ringfinal}} - \left(\frac{d}{2} - r_{\text{cyl}}\right)^2} \quad (12.17)$$

In Equation 12.17 the length of the cylinder is determined with by applying the Pythagorean theorem with $R_{ringfinal}$, d and r_{cyl}. Note that the length of the cylinder is taken at the boundary of the fillet by $(\frac{d}{2} - r_{cyl})$ in Equation 12.17.

$$h_{\text{center}} = \frac{2R - d\sqrt{2}}{2} \quad (12.18)$$

After using the previous equation to calculate $V_{cylinders}$ the volume of the fillets $V_{fillets}$ is calculated with Equation 12.19. In order to calculate the volume of a single fillet in Equation 12.20 it is necessary to know the triangular cross-sectional area $A_{triangle}$ of the enclosed space between the fillet and the original sphere boundaries. Moreover, the cross-sectional area A_{cap} that is needed is created by the fillet radius in $A_{triangle}$. Both these areas are indicated in Figure 12.6.

$$V_{\text{fillets}} = multi_{\text{junctions}}\, V_{\text{fillet}} \quad (12.19) \qquad V_{\text{fillet}} = \left(A_{\text{triangle}} - A_{\text{cap}}\right)\left(2\pi R_{\text{ring}}\right) \quad (12.20)$$

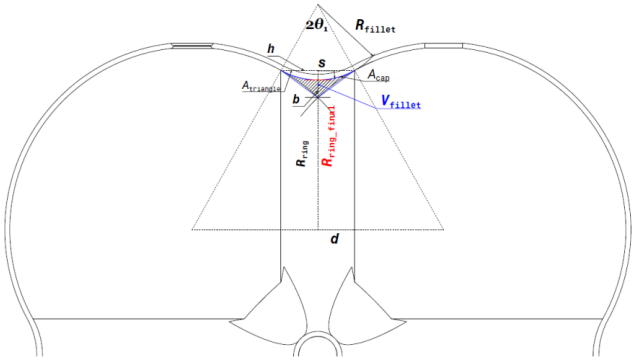

Figure 12.6: Cross section of MST tank 2 [80, p.82]

In Equation 12.21 and Equation 12.22 it can be seen that $A_{triangle}$ and A_{cap} depends on geometrical relations with as parameters R_{fillet} and θ_1.

$$A_{\text{triangle}} = \frac{bh}{2} = \frac{(2R_{\text{fillet}}\sin(\theta_1))\left(R\cos(\theta_1) - R_{\text{ring}}\right)}{2} \quad (12.21) \qquad A_{\text{cap}} = \frac{R^2_{\text{fillet}}}{2}(2\theta_1 - \sin(2\theta_1)) \quad (12.22)$$

Some of the parameters used in the volume calculations need to be determined by testing. These parameters are; the fillet radius,R_{fillet}, the polymer strap width,s, the strap overlap ratio,$K_{overlap}$ and the junction thickness $t_{junction}$. The values for these parameters could be found as a ratio of the radius of each sphere. The optimal values for these numbers were found to be: 0.1 , 0.35 , 0.75 and 0.027 respectively.

Tank surface area

The surface area of the tank is an important characteristic for determining the insulation thickness since larger surface area allows for more heat to be transferred [80, p.83]. In Equation 12.23 the surface area of the tank is determined by distinguishing different parts of the tank, as done before in Equation 12.2. The method of obtaining the parameters of this equation are given below.

$$S = S_{\text{spheres}} + S_{\text{fillets}} + S_{\text{cylinders}} + S_{\text{centers}} - S_{\text{lenses}} - S_{\text{spheresfillets}} \quad (12.23)$$

To start, S_{spheres} is calculated using Equation 12.24. The equation uses the number of spheres, $multi_{\text{cells}}$, and the radius, R, of the individual spheres. The next equation is used to calculate S_{fillets}, and can be found in Equation 12.25. It uses the number of junctions in the MST, $multi_{\text{junctions}}$, and the surface of the torus, S_{torus}. S_{torus} is found by using Equation 12.26. This equation uses the width of the hoop ring, s, the intersection radius with fillet correction, $R_{\text{ringfinal}}$, and the relative angle of the intersection, γ_{cyl}. $R_{\text{ringfinal}}$ was found earlier using Equation 12.10 and γ_{cyl} is found by using Equation 12.27. The inputs of this equation are: the length of the central hollow tube, l_{cyl}, and again $R_{\text{ringfinal}}$, both obtained earlier.

$$S_{\text{spheres}} = multi_{\text{cells}}\, 4\pi R^2 \tag{12.24}$$

$$S_{\text{fillets}} = multi_{\text{junctions}}\, S_{\text{torus}} \tag{12.25}$$

$$S_{\text{torus}} = 2\pi s R_{\text{ringfinal}} \left(\frac{2\pi - \gamma_{\text{cyl}}}{2\pi} \right) \tag{12.26}$$

$$\gamma_{\text{cyl}} = \arcsin\left(\frac{l_{\text{cyl}}}{2R_{\text{ringfinal}}} \right) \tag{12.27}$$

The next equations are used to calculate $S_{\text{cylinders}}$ with Equation 12.28. Inputs are the number of centers, $multi_{\text{centers}}$, found using Equation 12.7, and S_{cylinder}. The latter is obtained using Equation 12.29. The inputs are the radius of the central hollow tube, r_{cyl}, and length of the central hollow tube, l_{cyl}. Both are obtained earlier.

$$S_{\text{cylinders}} = multi_{\text{centers}}\, S_{\text{cylinder}} \tag{12.28}$$

$$S_{\text{cylinder}} = 2\pi \left(r_{\text{cyl}}\, l_{\text{cyl}} + r_{\text{cyl}}^2 \right) \tag{12.29}$$

Next, the S_{centers} is calculated using Equation 12.30. The inputs of this equation are the number of centers, $multi_{\text{centers}}$ and S_{center}. The latter is found using Equation 12.31. The inputs of this equation are: the radius of the spheres, R, and the height of the spherical cap in the center, h_{center}. h_{center} is already obtained using Equation 12.18.

$$S_{\text{centers}} = multi_{\text{centers}}\, S_{\text{center}} \tag{12.30}$$

$$S_{\text{center}} = 2\,[2\pi R h_{\text{center}}\,] \tag{12.31}$$

The following equation looks at S_{lenses}, which is calculated using Equation 12.32. The inputs are the number of junctions in the tank, $multi_{\text{junctions}}$, and $S_{\text{lensjunction}}$. The latter is found using Equation 12.33. The input of this equation is the height of the spherical caps at the intersections, h_{cap}, and can be found using Equation 12.34. The inputs of this equation are the radius of the spheres, R, and the intersection radius, R_{ring}. The latter is already obtained using Equation 12.11.

$$S_{\text{lenses}} = multi_{\text{junctions}}\, S_{\text{lensjunction}} \tag{12.32}$$

$$S_{\text{lensjunction}} = 2\left(2h_{\text{cap}}\right) \tag{12.33}$$

$$h_{\text{cap}} = R - \sqrt{R^2 - R_{\text{ring}}^2} \tag{12.34}$$

The last equation concerns the calculation of $S_{\text{spheresfillets}}$, which is performed using Equation 12.35. The inputs of this equation are the number of junctions in the tank, $multi_{\text{junctions}}$, and $S_{\text{spherefillet}}$, which is obtained from Equation 12.36. The inputs of this equation are the radius of the spheres, R, and the cap height at the intersections, h_{inter}. The calculation of h_{inter} is already shown in Equation 12.12.

$$S_{\text{spheresfillets}} = multi_{\text{junctions}}\, S_{\text{spherefillet}} \tag{12.35}$$

$$S_{\text{spherefillet}} = 2\,[2\pi R h_{\text{inter}}\,] \tag{12.36}$$

By combining all the parameters into Equation 12.23, it is possible to find the surface area of the tank for a certain configuration.

Tank mass

Finally, the tank mass can be calculated with Equation 12.38. This is done by multiplying the tank surface area with the respective material thickness based on the thin-walled assumption and the density of the composite, ρ_{comp}. In the equation, a clear distinction is made between the thickness of the spherical cell, t, and the thickness at the intersection of two spheres t_{junction}. The other inputs of the equation are the different surface areas: S_{spheres}, S_{centers}, S_{lenses}, $S_{\text{spheresfillets}}$, S_{fillets} and $S_{\text{cylinders}}$.

$$t = \text{Max}\left[\frac{PR}{2\sigma_{\text{allowable}}}, 6t_{\text{ply}} \right] \tag{12.37}$$

The thickness of the spherical cell is determined in Equation 12.37. It can be seen that the thickness is either a minimum of $6t_{ply}$ or dependant on the pressure P, the allowable stress of the laminate $\sigma_{allowable}$ and the radius R.

$$M_{\text{structural}} = \rho_{\text{comp}}\, t \left(S_{\text{spheres}} + S_{\text{centers}} - S_{\text{lenses}} - S_{\text{spheresfillets}}\right) + \rho_{\text{comp}}\, t_{\text{junction}} \left(S_{\text{fillets}} + S_{\text{cylinders}}\right) \quad (12.38)$$

Insulation

The sizing of the insulation layer is an iterative process. The first step is to calculate the surface area of the insulation layer on the inside of the fuel tank, S_{cryo} . This is easily done by repeating the steps for the fuel tank surface, but replacing the sphere radius , R, with the insulation radius, R_{cryo} , which is found by using Equation 12.39 and assuming an initial value for the insulation thickness, t_{ins}. In addition, the same centroid distance, d, should be used to get an insulation layer that fits around the tank.

Next, the heat transfer from the outside to the inside, Q , is calculated using Equation 12.40. This is the energy in Joules that is allowed to be absorbed by the tank. In this equation, BOR is the boil-off rate in percentages, M_{LH2} is the mass of the hydrogen and ΔH_{vap} is the heat of vaporization of the liquid hydrogen.

The next step is to find the tank coefficient of heat transfer, U. This is done by using Equation 12.41. This equation uses S_{cryo} calculated using the assumption on t_{ins}. In addition, the temperature difference between the outside and the inside of the tank, ΔT, is needed. A lower value of U means that the tank should be able to resist heat absorption more. With this overall tank coefficient, the individual components of the tank are determined, among which is the insulation.

With the tank coefficient of heat transfer, the t_{ins} can again be calculated with Equation 12.42. The inputs for this equation are: the thickness of the composite layer, t, the thermal conductivities of the composite and the insulation, k_{comp} and k_{ins}, and the heat transfer coefficient of the outside, h_{out}. This parameter is dependent on the flow of the air around the tank; the lower the value, the more insulation is needed. A value of 30 [W/(m^{2}K)] is assumed, based on ventilated air [7].

The new t_{ins} is used from the start of the insulation thickness calculation. The iteration will stop after a set margin is reached. The margin for the iteration is set to 0.0001 [m] as smaller differences lead to insignificant changes in the mass of the insulation.

When calculating the t_{ins}, it was found that no insulation was needed. This did not sound correct, but the verification of the tool showed correct behaviour; decrease in allowable boil-off rate leads to more insulation, and the units used correspond in the equations. One of the possibilities that could have lead to this result is that the allowable boil-off rate could be too lenient, therefore eliminating the need for insulation. Only by testing the boil-off on a real tank it is possible to verify that no insulation is needed. To prevent any problems in the future, a 5 [cm] layer of insulation is added as a contingency in the case that the tank does require insulation. This number was chosen as it allows for some margin in the insulation while not negatively impacting the C_{d_0} due to the bigger fuselage needed. In the sensitivity analysis, the insulation size will be increased even more to see the effects of a thicker layer.

$$R_{\text{cryo}} = R + t_{\text{ins}} \quad (12.39) \qquad Q = \text{BOR} \cdot M_{\text{LH2}} \cdot \Delta H_{\text{vap}} \quad (12.40)$$

$$U = Q/(S_{\text{cryo}} \cdot \Delta T) \quad (12.41) \qquad \frac{1}{U} = \frac{t}{k_{\text{comp}}} + \frac{t_{\text{ins}}}{k_{\text{ins}}} + \frac{1}{h_{\text{out}}} \quad (12.42)$$

With the insulation thickness sorted, it is time to calculate the mass of the insulation, $M_{\text{insulation}}$. This is done by using Equation 12.43 [80, p.86]. This equation uses t_{ins} and S_{cryo} from the process above. Only the density of the insulation, ρ_{ins} , needs to be found.

$$M_{\text{insulation}} = \rho_{\text{ins}}\, t_{\text{ins}}\, S_{\text{cryo}} \quad (12.43)$$

[7] URL: `https://www.engineeringtoolbox.com/convective-heat-transfer-d_430.html` [Accessed on: 14-6-2021]

Liner materials

The sizing of the liner materials is faster than the sizing of the insulation as the thicknesses of the liner materials is already known. There are two different liners: a metal coating on the inside of the tank and a polymer layer on the outside of the tank. The thicknesses of these are respectively: $t_{\text{liner,inner}}$ and $t_{\text{liner,outer}}$. For the calculation of the mass of the liners, it is first needed to find the surface area of the liners. This is done by using the same calculation method for the fuel tank surface, but replacing the sphere radius, R, with $R_{\text{liner,inner}}$ or $R_{\text{liner,outer}}$. These radii can be found by following Equation 12.44 and Equation 12.45. The masses of the liners can then be found by following Equation 12.46. In this equation S_{liner} is the surface found from the new radius and ρ_{liner} is the density of the liner material used.

$$R_{\text{liner,inner}} = R - t_{\text{liner,inner}} \tag{12.44}$$

$$R_{\text{liner,outer}} = R + t_{\text{ins}} \tag{12.45}$$

$$M_{\text{liner}} = \rho_{\text{liner}}\, t_{\text{liner}}\, S_{\text{liner}} \tag{12.46}$$

Tank outer volume

The outer volume of the tank is determined by first considering the outer dimension of the spheres. This is done by subtracting the overlapping dimension of the spheres from the sphere dimension if there would not be overlapping. Then the thickness of the insulation and liner are added. In Equation 12.47 $dimension_{m,n,p}$ and $q_{m,n,p}$ are the dimension and number of spheres in m, n or p direction, respectively.

$$\text{dimension}_{m,n,p} = 2q_{m,n,p}R - (q_{m,n,p} - 1)(yR) + t_{\text{ins}} + t_{\text{liner}} \tag{12.47}$$

12.8. Limitations of the Sizing Method

The sizing of the tank comes with limitations that need to be remarked before advancing. The sizing of the surface area gets less accurate when R → 0 [mm] and the surface area S is negative for R < 130 [mm]. The largest contributors to S in Equation 12.23 are $S_{spheres}$ and S_{lenses}. In Equation 12.24 and Equation 12.34 it can be seen that $S_{spheres}$ is quadratically related to R and S_{lenses} is linearly related. This means that for small values of R S_{lenses} is larger than $S_{spheres}$ and S is negative as a result.

Furthermore, the insulation thickness iteration will diverge if the surface area is not in proportion with the hydrogen in the tank. This is explained by realising that the heat flow in the tank increases for larger S and that smaller amounts of hydrogen require more insulation to accomplish a 1.6% BOR. This means that for a set R and decreasing hydrogen mass the iteration will have more repetitions until it ultimately diverges. For this method with a 2 x 2 x 2 configuration and a sphere radius of 1 [m] a starting hydrogen mass of 11 [kg] is critical.

12.9. Recommendations

There are a few recommendations for future design phases of the tank. These parts have not been considered in detail, but need to be considered when implementing the tank in the H_2OPPER. A list of the recommendations is shown below.

- **Hydrogen Leakage**
  Hydrogen leakage is a possibility. This should be prevented as hydrogen mixed with air is a highly explosive gas. To make sure that the compartment of the LH2 tank is safe, the space should be continuously ventilated, as well as the areas that the pipelines run through. Sensors should be placed to be aware of where the hydrogen is leaking and the quantity of the spilled hydrogen. In addition, the walls of the compartment in which the tank is located should be made hydrogen tight to prevent hydrogen from permeating into other areas. In later phases, a more detailed analysis should be done on materials with a low hydrogen permeability to make the LH2 tank compartment hydrogen tight. Also, considerations should be made on the placement of ventilation and sensors, as hydrogen floats to the top of the compartments due to its low density.
- **Tank pressure control**

In order to control the mass flow of the withdrawn LH2 in the tank a pressure control system should be considered. This could be done by introducing heat in the tank in a controlled manner. This way the boil-off could be controlled so that a constant pressure is achieved in the tank. It could also be possible to design the tank to have an equal amount of boil-off volume to the mass flow volume of the LH2. However, this would make the tank specific to a set tank-fuel cell combination and thus decreasing the flexibility of the hydrogen system.

- **Tank cross-link**
  It is useful to have the tanks cross-linked with each other. In case of an engine-out situation, the LH2 intended for one engine can be used by the other engine. To implement this system, it is needed to determine the way the hydrogen is transferred between the tanks; either by using the pressure of the LH2 or another system. By cross-linking there is however more chance for hydrogen to leak out of the tank. Appropriate safety measures need to be established before this can be implemented
- **Belly Landing**
  As the tank is placed in the cargo hold of the aircraft, belly landings can become a critical situation. The cargo hold might get crushed and thereby putting loads on the fuel tanks it is not designed for. To make sure that the tank does not collapse, the structure around the tank should be made so that the tank will not get to carry additional loads during an impact. Another option is to analyze other locations of the hydrogen tank which can eliminate this problem.

13
Verification and Validation

This Chapter describes the verification and validation procedure during the design process. Verification and validation are independent procedures that make sure that the final design meets the requirements and fulfills its intended purpose. The Verification procedure for all the different subsystems is presented in Section 13.1 and the validation procedure in Section 13.2.

13.1. Verification

Multiple programs were written in Python to aid with calculations. To verify these programs, various unit and system tests were performed. For the unit testing, there are several approaches that are followed; first, the outputs of individual parts of the code were compared to hand calculations with the same inputs. Secondly, the behaviour of the units to certain inputs were compared to expectations. Thirdly, the sign and order of magnitude of outputs were compared to expectations.

13.1.1. Oswald Efficiency

The method to calculate the Oswald efficiency factor as described in Section 8.3, takes into account many different factors. However, simpler methods for Oswald factor estimation exist. For example, Raymer [34] presents a relation purely based on the aspect ratio of the aircraft, shown in Equation 13.1.

$$e = 1.78\left(1 - 0.045A^{0.68}\right) - 0.64 \tag{13.1}$$

This formula estimates the Oswald efficiency to be 0.775, which is only a 1.3% difference.

13.1.2. Fuel Tank

Several inputs were altered to check whether the outputs showed the correct behaviour. The first set of tests focused on the insulation. Several parameters such as the thermal conductivities and the allowable boil-off rate have an influence on the insulation thickness. The second set of tests put emphasis on the geometrics of the tank. Inputs such as the centroid distance and the number of spheres have an influence on the surface and volume of the tank. The correct behaviours were observed and therefore the sizing of the fuel tank has passed the performed system tests.

13.1.3. Structures

Unit tests were performed by testing individual functions with hand calculated results. In order to make hand calculations viable, a simplified load case was used. A taper ratio of 1 was used and one load was considered at a time. To ensure that the tool also works properly with different taper ratios, a system test was conducted for this.

The first conducted system test was doubling the skin thickness of the wingbox with no stringers present. The expected result for this test was that: all the stresses in the skin would be halved and the wingbox weight would be doubled. This is due to the linear relation between skin thickness and moment of inertia. The observed result matched the expected result

As a second system test, the taper ratio was changed from 1 to 0.5. This was done to ensure that the tool handled this correctly, as it was not part of the unit testing. The moment of inertia at the root was expected to decrease by a factor of 8 (2^3), as the moment of inertia of the skin is a function of the width/height to the third power. The bending stress is inversely related to the width/height to the power 2. This meant an increase of $1/(0.75^2)$ = 1.78 factor increase was expected at the middle of the wingbox. Both results were observed as expected.

The third system test was performed to verify the effect of the stringers. Five stringers were added to the top skin and two to the bottom skin. The expected result was a large decrease in stress on the top skin and a smaller decrease in the bottom skin. This is achieved by moving the centroid up through the addition of more stringers at the top skin. The bending stress in the top skin was observed to be reduced by a factor of 1.5 and in the bottom skin with a factor of 1.3.

Finally, as a larger system test, the weights of the individual components are compared to the values obtained with the class II weight estimation. The results can be found in Table 13.1. The weight of the wing was higher than expected, this could be contributed to the conservative assumptions that were made, one of them being the constantly distributed lift force. The same applied to the weight of the horizontal and vertical tail. The weight of the fuselage was also higher than that of the class II weight estimation. This was mainly due to the sizing of the fuselage with a constant cross-section.

Table 13.1: Comparison between the weights of the structural components and the weights obtained from the class II weight estimation

System	**Design weight [kg]**	**Class II weight [kg]**
Wing	795.2	725
Horizontal tail	107	98.3
Vertical tail	83.4	62.5
Fuselage	1064	1019.8

For the landing gear tool, several parameters regarding constraining angles were altered to see if expected values were computed. This showed that the tool was reliable for realistic values. An example: if the tip-over angle is increased, a more aft placed main landing gear would be required. This also means a higher nose wheel loading if a constraint is placed on the most forward location of the nose landing gear. A hand calculation including a sketch on scale showed that the tool computed the correct values to maintain the required separations.

13.1.4. Center of Gravity- & Weight -estimation

The weight estimation was tested by checking each of the individual weight estimation equations with hand calculations. After this, the weight of each subsystem/part with its corresponding center of gravity was manually inputted in an excel sheet that calculated the center of gravity of the OEW. The total center of gravity that resulted from the excel sheet was equal to that of the python script. As a second test, a system test is executed. In this test, several parameters such as c.g.s of parts and part-specific parameters such as the wing surface area were changed. All the inputs showed logical results and thus no unexpected behaviour was perceived.

13.1.5. Scissor Plot

For the scissor plot, the python program was verified using so-called sanity checks that originate from the source of the method. These sanity checks consisted of empirical formulas that verify the order of magnitude of the calculated coefficients and gradients. Additionally, all the values were re-calculated by hand. Lastly, units tests were performed, in which parameters such as the c.g. of the wing, the wing surface area and the airfoil dependent coefficients were altered. These alterations resulted in behaviour that was expected and thus verified the program.

13.1.6. Vertical Tail Sizing

The vertical sizing was verified by first hand calculating each separate equation and by order of magnitude sanity checks. As explained before in Subsection 7.3.1, a statistical method based on comparable aircraft was also applied to function as a reference value for a conventional configuration. To verify the vertical tail sizing tool at a system level, example values from [40] and [39] were used as an input to check the stability derivatives calculations. Since the tool used exactly the same method, the calculations were verified when the values matched exactly as well. The one engine inoperative sizing method presented by Torenbeek in

[22] was then used as a simplified model to verify the final result of the vertical tail area. As mentioned in Subsection 7.3.3, however, the disturbances were unknown and thus neglected, making the verification less reliable. An average difference of 10% was observed, where the method from Torenbeek consistently estimated a higher area. This discrepancy could be caused by different methods used for estimating $C_{L_{\alpha_v}}$ and τ, since Torenbeek's method for estimating both constants was not explicitly mentioned and the impact of these constants are highly determinant for the final result. More likely, however, is that the neglected disturbances caused this discrepancy. Nonetheless, this relative difference was considered accurate enough due to the highly sensitive nature of calculations with small constants in the denominator.

13.1.7. Estimation of C_{D_0}

The estimation of the C_{D_0} was verified by first verifying the individual wetted area calculations of the different parts of the aircraft. This was done with a combination of sanity checks and doing simple hand calculations. Also, the Reynolds number was verified individually by checking the order of magnitude. Finally, logic tests were performed where certain surface areas were increased to examine the behaviour of the C_{D_0}. The tool behaved as expected, meaning the tool was verified on a system level.

13.2. Validation

The validation procedure for all the different subsystems is described in this section. Validation is performed by comparing data to that of reference aircraft or by actual test which are post DSE activities.

13.2.1. High Lift Devices and Ailerons

In Table 13.2, the percentage of the span covered by high lift devices and ailerons is shown. As can be seen, the H_2OPPER has rather big high lift devices, especially considering they are fowler flaps, while most reference aircraft use plain or slotted flaps. This can be explained by the very large maximum lift coefficient required by the aircraft. Furthermore, the Twin Otter, which also has short take-off and landing capabilities, has an even larger HLD.

Table 13.2: Span percentage HLD and ailerons

Aircraft	High lift device [%]	Aileron [%]
L 410 NG	49	43
Beechcraft 1900D	44	44
Jetstream	49	33
Twin otter	95	18
Dornier	50	33
H_2OPPER	65	20

13.2.2. Oswald Efficiency

Validation of the estimation method for the Oswald efficiency factor is challenging at this stage, since little can be found for other reference aircraft Samoylovitch et al [88], found the factors for a number of reference aircraft. The only aircraft similar to the H_2OPPER is the Beechcraft, which is reported to have an Oswald efficiency of 0.76. This is enough to validate the calculation is in the right range. However, during future design phases, CFD and wind tunnel testing is necessary to better validate the Oswald efficiency factor, as it is an important parameter for estimating aircraft drag.

13.2.3. Power Output

To validate the power output that is required for take-off it was decided to compare the maximum engine power with similar propeller aircraft. The power that is required during take-off was estimated with the help of the take-off parameter that was used in the building of the W/P and W/S diagrams. This take-off parameter is based on all sorts of propeller engine aircraft. Therefore it was decided to validate if the power output that is calculated actually corresponds to other twin-engine propeller aircraft. In Table 13.3 the specification of reference propeller aircraft can be found. In Figure 13.1 the resulting plot from the data can be seen, with MTOW in [kg] on the x-axis and power output in [kW] of the engines on the y-axis. The red dot represents the H_2OPPER. What can be seen is that the power output is lower than what would be expected

for the aircraft. This can be easily explained by taking a closer look at two parameters that influence the power that is required for take-off. First of all, if the wing surface area of an aircraft is bigger less power will be needed for take-off since more lift is generated. The two lower outliers are the H_2OPPER with a surface area of 43 [m^2] and the CASA c212 with a surface area of 41 [m^2] which are both significantly higher than the other aircraft that are considered. Another important parameter that influences the take-off power is the lift coefficient during take-off. The average lift coefficient of twin-engine propeller aircraft during take-off is between 1.4 and 2 [89]. The lift coefficient of the H_2OPPER during take-off is 2.4. Both the reasons stated above justify why the output power that is necessary is lower than what would have been expected from looking at reference aircraft.

Table 13.3: Reference propeller aircraft specifications

Aircraft	**MTOW** [kg]	**Power [kW]**	**Wing surface area [m^2]**
L 410 NG [1]	7000	1340	34.86
DHC-6 Twin Otter [2]	5670	1118	39
Beechcraft 1900D[3]	7764	1908	28.8
Dornier Do 228[4]	6575	1158	32
L 410[5]	6600	1194	34.86
Harbin Y12[6]	5300	924	34.27
PZL M 28[7]	7500	1640	39.72
CASA c212[8]	8000	1342	41
Jetstream 31[9]	6954	1400	25.2
Metro III[10]	7257	1500	29
H_2OPPER	8618	1460	43

[1]URL: http://www.let.cz/documents/L410NG.pdfhttp://www.let.cz/documents/L410NG.pdf [Accessed on: 17-06-2021]
[2]URL: https://en.wikipedia.org/wiki/De_Havilland_Canada_DHC-6_Twin_Otter [Accessed on: 17-06-2021]
[3]URL: https://www.globalair.com/aircraft-for-sale/Specifications?specid=28 [Accessed on: 17-06-2021]
[4]URL: https://en.wikipedia.org/wiki/Dornier_228 [Accessed on: 17-06-2021]
[5]URL: https://en.wikipedia.org/wiki/Let_L-410_Turbolet [Accessed on: 17-06-2021]
[6]URL: https://en.wikipedia.org/wiki/Harbin_Y-12 [Accessed on: 17-06-2021]
[7]URL: https://m28aircraft.com/generalInformations/performance [Accessed on: 17-06-2021]
[8]URL: http://www.flugzeuginfo.net/acdata_php/acdata_c212_en.php [Accessed on: 17-06-2021]
[9]URL: https://en.wikipedia.org/wiki/British_Aerospace_Jetstream [Accessed on: 17-06-2021]
[10]URL: https://www.globalair.com/aircraft-for-sale/Specifications?specid=228 [Accessed on: 17-06-2021]

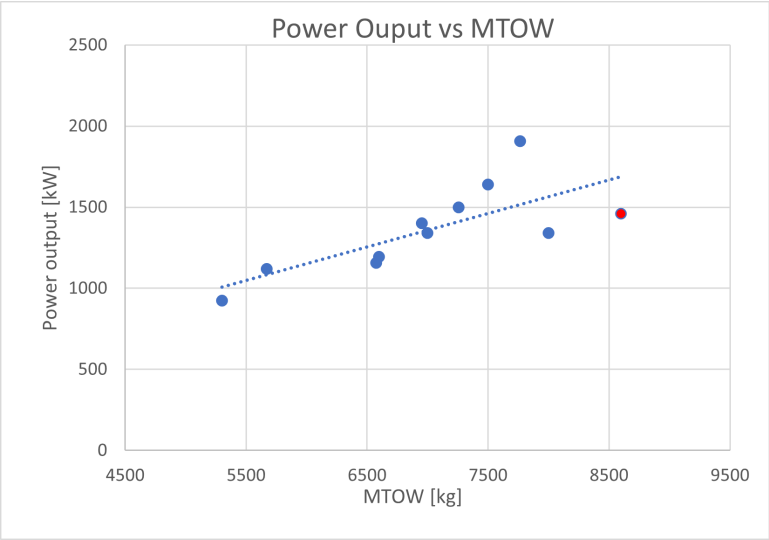

Figure 13.1: Power output of the engines versus the MTOW

13.2.4. Energy Consumption

To validate the total used energy during flight, as well as the division energy used during each flight phase, reference aircraft were consulted once again. In Figure 13.2, the range of different reference aircraft is plotted versus the total output energy they use. For all aircraft, the range for maximum payload was chosen, and the fuel mass belonging to that. It was chosen to compare output energies, since this is the most fair comparison, because the efficiency of turboprop aircraft differs from the designed hydrogen fuel cell. To determine the output energy for the reference aircraft, the fuel mass was multiplied by the specific energy of kerosene (43MJ/kg), and then multiplied by the efficiency. This was estimated to be 20%.[90][91]

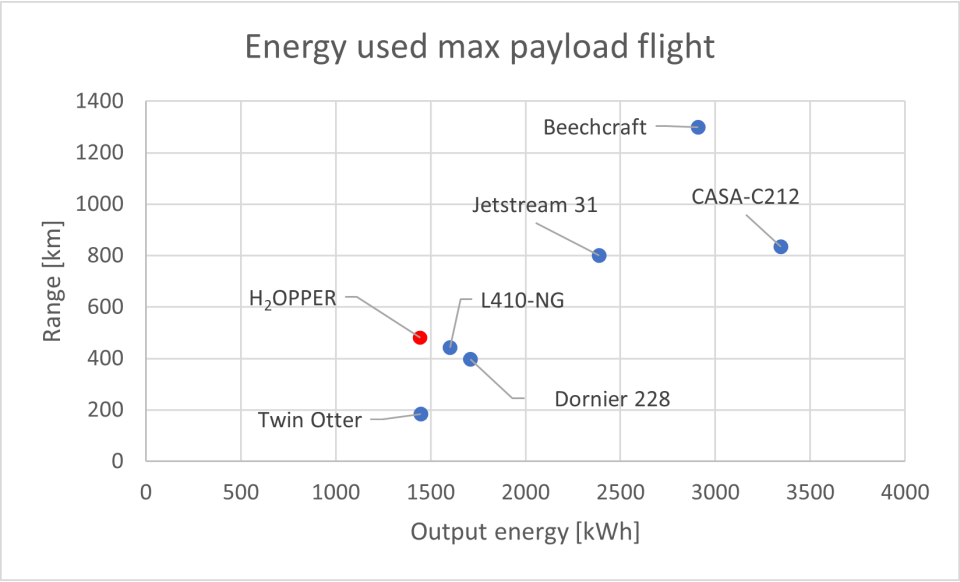

Figure 13.2: The output energy used for a max payload flight

As can be seen in the figure, the H_2OPPER does not differ much from the general trend of reference aircraft. It does have a large range compared to the used energy. The main reason for this is the energy savings that are done during startup, taxi and cruise. Since the aircraft is fully electric, during these phases only the batteries have to power subsystems of the aircraft, which is very efficient. A more detailed analysis on the different flight stages is shown in Table 13.4. The fuel fractions were taken from literature, for general turboprop engines. The fuel fraction for cruise was calculated with the Breguet range equation. They were used to calculate the burned fuel for each stage. This was then compared to the H_2OPPER. Clearly, startup and taxi require very little energy. Furthermore, descent utilized relatively more energy. This is because a

slow descent is chosen in order to recharge the batteries.

Table 13.4: Energy percentage for each flight phase

Stage	Fuel fraction [92]	Mass [%]	H_2OPPER[%]
Startup	0.99	10.9	1.3
Taxi	0.995	5.4	1.1
Take-off	0.995	5.3	6.3
Climb	0.985	16.0	15.3
Cruise	0.96	42.1	49.2
Descent	0.985	15.2	25.3
Shutdown	0.995	5.0	1.5

As a last validation check, the sensitivity to adding fuel was investigated. For this, the L 410 NG was consulted, by looking at the range that was added by removing 1kg of payload and replacing this with kerosene. The payload/range diagram was used for this. [93] For the L 410 NG, 1kg of fuel resulted in a range of 1.25 km extra. For the H_2OPPER, when adding 1kg of hydrogen and removing one kg of payload, an extra 10.3 km can be flown, which is 8.3 times as much. Since the energy density of hydrogen is 3 times as big as kerosene, and the efficiency is also more than twice as high, the actual ratio between the H_2OPPER and the L 410 NG range per energy used, is 1.25. This means that the H_2OPPER, when adding fuel, reaches a relatively larger range then the L 410 NG. This is again explainable, since the H_2OPPER uses less energy during the phases on the ground.

13.2.5. Fuel tank

There are several methods to validate the design of the fuel tank. Firstly, the sizing method could be compared to an existing fuel tank. From the paper of I. Tapeinos, a multi-sphere tank is obtained, which is sized using the same geometric equations [80, p.130]. There was, however, a difference in the composition of the tank; the tank in the paper does not contain an insulation layer. In addition, the tank liner on the inside is made from a polymer, Polyamide-12, whereas the designed tank uses an aluminium alloy liner and a polymer liner outside of the insulation layer. Therefore, only the tank masses without the liners and insulation were compared.

For the comparison, the tank dimensions from the paper were used as an input in the code written for the sizing of the fuel tank. The volume and tank mass are obtained as an output of the code and are compared with the data given in the paper. The inputs and outputs of the code and the values from the real tank are tabulated in Table 13.5. The two values that are compared are the volume and the mass of the tank. The volume has a good match; a difference of less than 3 %. This is a large discrepancy, considering that the intermediate values, such as the radius of the inner cylinder, correspond to the real tank within a 0.01 % error. The error of the volume can be explained by looking at the length of the internal cylinder of the real tank, for which an idealization was made for the shape. The length in the real tank is 0.110 [m], whereas the code calculates a length of 0.088 [m]. The real tank is sized with a slightly longer inner cylinder, which leads to an increase in volume of the real tank. This increase in volume is a fair addition, but it would mean that more insulation is needed for the tank. This however is expected to be minimal for such a small increase in surface and volume.

The mass of the tank has a larger error, a difference of 0.84 [kg] or 35 %. This is a large error that is not easily explained. The mass of the tank is calculated by multiplying the surface of the composite with the thickness and density of the composite. The surface formulas have been verified, the thickness used differs less than 1 % from the real tank, and the same composite density is taken in the code as in the report. This error could be explained by the addition of metallic openings to the tank. These were omitted in the designed tank. If this is the case, then the error will decrease with a larger tank, as only one inlet and one outlet is needed. This sizing of the tank can then be seen as validated.

Table 13.5: Output values from the tank sizing code and the given tank values [80, p.130].

Inputs	**-**	**Outputs**	**-**	**Real values**	**-**
Number of spheres [-]	2 x 2 x 1	Tank volume [L]	44.8	Tank volume [L]	46.1
Sphere radius [m]	0.145	Tank mass [kg]	1.54	Tank mass [kg]	2.38

The second method of validating will need to be performed on a physical tank. The physical tank shall be similar to the designed tank in order to be able to validate the components that were not covered by the first method of validating. The materials and their application that will have to be validated are the aluminium liner, the insulation material and the polymer liner. In this validation method, the performance of the material under cryogenic conditions will have to be tested as well as their performance after operational cycles. For aluminium, it is crucial it is minimally corroded by hydrogen and that it is resistant to large changes in temperature. The insulation should not crumble after operation cycles and retain its properties over time. The polymer should be tested for its ability to protect the insulation. In addition, it should be tested whether the composite tank wall is able to hold the pressure by means of bursts tests.

A decisive factor that will have to be tested is how the tank behaves with respect to large temperature changes. Due to the materials having different thermal expansion coefficients it is important to observe how the tank behaves after operational cycles. Peel off could be observed in case the coefficient are not similar enough.

Finally, the atmospheric conditions should also be considered. The change in atmospheric pressure at altitude could influence the isolation capabilities of the tank. Note that the isolation layer consists of PUR foam and gaps in the foam are filled with a non-condensable gas. This means that as the atmospheric pressure lowers the insulation gas will expand. The impact of this effect should be tested with regard to the insulation material and the polymer liner that keeps the gas in place.

13.2.6. Manoeuvre and Gust Loading Diagram

For the validation of the manoeuvre and gust loading diagram, firstly the calculated design speeds of the H_2OPPER were compared to the design speeds of reference aircraft, as shown in Table 13.6.

Table 13.6: Design speed comparison between reference aircraft and the H_2OPPER

Design speed [m/s]	**H_2OPPER**	**Beechcraft 1900D [94]**	**Twin Otter [95]**	**L 410 NG [93]**
VS0	33.9	43.2		
VS1	43.4	52.0		
VF	60.8	84.9		
VB	71.0			81.0
VA	74.3	91.6	67.9	

As can be seen in Table 13.6, the stall speed with flaps out (VS0) and the stall speed with no flaps (VS1) both are significantly lower than that of the Beechcraft 1900D. This mainly is because the H_2OPPER has a shorter take-off and landing distance than the Beechcraft (750 [m] against 1058 [m]). Furthermore, the wing surface area of the H_2OPPER is significantly larger, which also results in a lower stall speed. These two reasons also explain the lower flap speed (VF) of the H_2OPPER compared to the Beechcraft. Moreover, the design speed of maximum gust velocity (VB) is in the same order as that of the Aircraft Industries L 410 NG. Lastly, the maneuvering speed (VA) is in between that of the Beechcraft and the DHC-6 Twin Otter.

The maximum load factors of the H_2OPPER were compared to the maximum load factors of the Aircraft Industries L 410 NG, as shown in Table 13.7.

Table 13.7: Maximum load factor comparison between the H_2OPPER and Aircraft Industries L 410 NG

Maximum limit load factor	**H_2OPPER**	**L 410 NG [93]**
Positive	3.40	3.21
Negative	-1.40	-1.04

As can be seen in Table 13.7, both the positive and negative maximum limit load factors are a little bit higher for the H_2OPPER than for the L 410 NG. This difference mainly is because the H_2OPPER has a higher wing surface area than the L 410 NG (43 against 35 [m^2]). This makes it more sensitive to gusts, which results in higher load factors for the same gust speed.

Since there were no extreme differences in design speeds and maximum load factors that could not be explained, the manoeuvre and gust loading diagram of the H_2OPPER was considered validated.

13.2.7. Class-II Weight Estimation

The class-II weight estimation is aimed to compute an accurate result for the operating empty weight of an aircraft. As reasoned in Subsection 7.2.1, the weight estimation of individual components can have large fluctuations. Therefore, individual components/subsystems were not validated with one mass estimation of another aircraft, but rather validated by comparing the weights and fraction of MTOW of subsystems and parts of multiple aircraft. The data available to validate, originating from Torenbeek [38, p.266-288], consisted of a number of aircraft that listed the weights and fraction of MTOW for several subsystems and parts. All the weights of the individual components and subsystems of the H_2OPPER, as listed in Table 16.8, are converted to a fraction of the MTOW and then compared to the reference data. This resulted in no major inconsistencies and it was found that every weight was within the range of the minimum and maximum fraction of MTOW listed.

The OEW of the H_2OPPER, that flows out of the class-II is validated by comparison to the Aircraft Industries L 410 NG. It must be noted that the L 410 is not a hydrogen aircraft but rather powered by kerosene. As the H_2OPPER has hydrogen-specific systems, no direct comparison was possible between it and the L 410's OEW. To make a comparison of OEW's possible, it was decided to subtract the maximum payload from the maximum zero fuel weight (MZFW) for the L 410, which resulted in 4300 [kg] OEW. For the H_2OPPER, the mass of the hydrogen-specific systems is subtracted from the OEW (10% contingency included,) which resulted in 5167 [kg]. The results are shown in Table 13.8 [11].

Table 13.8: Weight comparison between the H_2OPPER and Aircraft Industries L 410 NG.

Parameter	**H_2OPPER**	**L 410 NG**
MTOW [kg]	8616.4	7000
OEW [kg] (w/o hydrogen systems)	5167	4300
OEW/MTOW	60.0%	61.4 %

As can be seen in the table above, the fraction of OEW over MTOW of the H_2OPPER is only 1.4% lower than that of the L 410. The small difference that does exist can be explained by the fact that the L 410 has a few kerosene specific systems, whereas for the H_2OPPER all fuel-specific systems are subtracted from the OEW (i.e. fuel-specific systems still exist for the L 410, but not for the H_2OPPER.) Kerosene specific systems are significantly lighter than hydrogen-specific systems, and can therefore account for the small difference of 1.4% between the two fractions. The H_2OPPER's operative empty weight, and with that the class-II weight estimation, is thus validated.

13.2.8. C.g. Loading Diagram

To validate the c.g. loading diagram, c.g. ranges of reference aircraft were compared with the c.g. range of the H_2OPPER, as shown in Table 13.9.

[11] URL:`https://www.airlines-inform.com/commercial-aircraft/l-410.html` [Accessed on: 17-06-2021]

Table 13.9: C.g. range comparison between reference aircraft and the H_2OPPER

Aircraft	C.g. range (as fraction of MAC)
L 410 NG [93]	0.19-0.30
Twin Otter [95]	0.20-0.36
H_2OPPER	0.50-0.64

As can be seen in Table 13.9, the c.g. range of the H_2OPPER is of the same order of magnitude as the reference aircraft (14% of the MAC against 11% and 16%). Furthermore, it can be seen that the c.g. range of the H_2OPPER is more to the trailing edge of the wing than those of the reference aircraft. This mainly is due to the wing of the aircraft being located further to the front than those of the reference aircraft, to be able to ensure small horizontal and vertical tail surfaces. Since the most important part of the c.g. range is the magnitude and the difference in location could be explained, the c.g. range of the H_2OPPER was considered validated.

13.2.9. Wingbox

Validation of the structural components has to be done by testing. This is out of the scope of the preliminary design but is vital in further design work. In order to do this in a cost-effective and reliable way, the test-pyramid can be used [96], as shown in Figure 13.3. Material coupons are tested extensively and, moving up the pyramid, elements and sub-assemblies are tested more briefly. The final test of the completed system is aimed to be tested only once, to show compliance with the requirements.

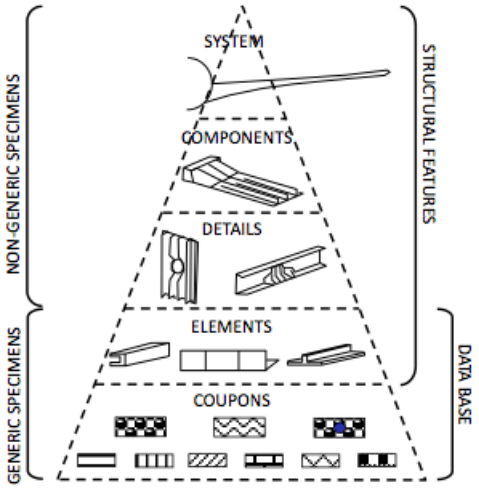

Figure 13.3: Test-pyramid for structural validation [96]

13.2.10. Landing Gear

Validation of the landing gear placement was performed by comparing the positioning of landing gear of reference aircraft.

Table 13.10: Landig gear placement comparison

	H_2OPPER	L 410	Twin-otter	Jetstream 31
Nose landing gear [m]	1.50	3.14	1.90	1.84
Main landing gear [m]	6.24	6.81	6.42	6.40
Lateral separation [m]	2.48	3.65	3.70	5.94

From Table 13.10 it can be seen that the main landing gear positioning is in line with that of reference aircraft. The nose landing gear is placed more forward to reduce the load on the nose landing gear. More research will have to be performed to see if the 1.5 [m] is a possible placement in terms of space for retractable landing gear. The lateral placement, however, does deviate significantly from that of reference aircraft. Even though no requirement dictates a higher separation than the three criteria described in Section 5.6, the current separation is just under 2.5 [m]. This higher separation can be explained by the available space for retracting the main landing gear sideways, or for the extra required lateral stability. It is expected that the main landing gear of the H_2OPPER is able to retract sideways due to the landing gear height of under 0.5 [m] and the extra height of the fuselage compared to reference aircraft. The landing gear of the Jetstream 31 is placed at the engine location which explains the lateral positioning of 5.94 [m].

13.2.11. Scissor Plot

To validate the scissor plot, the H_2OPPER's ratio of the horizontal tail area over wing surface area is compared to that of the Aircraft industries L 410 NG and the DHC-6 Twin Otter-400. This comparison is shown in Table 13.11 [12][13].

Table 13.11: Horizontal tail comparison between the H_2opper, L 410 NG and the Twin Otter 400.

Parameter	**H_2OPPER**	**L 410 NG**	**Twin Otter**
Horizontal tail surface area [m^2]	9.0	8.4	9.45
Wing surface area [m^2]	43	34.86	39.0
Tail over wing surface area ratio [-]	0.209	0.241	0.242

From the table above, it can be seen that the tail over wing surface area ratio of the H_2OPPER is slightly smaller than that of the other two aircraft. This difference can be explained by the fact that the H_2OPPER is optimized for a small horizontal tail by moving the wing to the front, and thereby creating a larger horizontal moment arm. Furthermore, the c.g. range fitted exactly in the scissor plot, resulting in the favorable scenario where the stability and controllability curves are simultaneously limiting. These two phenomena result in a smaller horizontal tail surface area, which is why the small difference between the H_2OPPER and the two other aircraft is deemed acceptable. Therefore, the scissor plot and thus the horizontal tail sizing is validated.

13.2.12. Vertical Tail Sizing

The vertical tail sizing tool was validated by comparison with the L 410 NG reference aircraft. Due to the L 410 also being a similar-sized two-propeller aircraft, the vertical tail was also likely to be sized for the one engine inoperative condition, making a relevant comparison possible. All necessary inputs were obtained from either inspection or the L 410 data-sheet from EASA [93]. The calculated tail size was then compared to the tail size that was obtained from inspection. The tool estimated a tail size that was 15% larger than the actual size. Considering that the tool included a 10% contingency margin for the tail-to-wing ratio, this discrepancy was deemed to be within a reasonable accuracy and was thus validated for the purpose of being an appropriate preliminary design estimator. However, it should again be noted that due to the highly sensitive nature of the calculations and the relatively high uncertainty of the stability derivatives and rudder effectiveness, the final design can still change quite significantly after a more in-depth CFD or wind-tunnel testing.

13.2.13. Estimation of C_{D_0}

The validation of the estimation tool for C_{D_0} was carried out by using reference values from similar aircraft [46]. Both the Reynolds number and the C_{D_0} were compared to reference values. It was observed that for comparable Reynolds numbers and characteristic lengths, the estimated C_{D_0} was usually within 10% larger than reference aircraft. This discrepancy is most likely caused by the larger taken contingency margin. Due to the high impact and still relative high uncertainty, the decision was made to keep this high contingency in place until wind tunnel tests indeed confirm a lower value. Although the estimated value is somewhat higher than reference aircraft, it was considered to be within reasonable margin and thus validated.

[12] `https://www.vikingair.com/sites/default/files/Viking-Twin-Otter-Series-400-Technical-Specifications-R-01-2018.pdf` [Accessed: 23-04-2021]

[13] `https://let.cz/documents/L410NG.pdf` [Accessed: 23-04-2021]

14
Ground Operations

For the ground operations analysis it was chosen to take a closer look at one of the possible markets that will be served by the electrical island hopper: The Maldives. The Maldives is an island region that is located south of India. The Maldives will be taken as a reference but the set-up of the ground operations can be generalised so that it can be used in different island regions as well, with minimal alterations. This chapter will show what is necessary as basis for the ground operations and logistics of the H_2OPPER. In Section 14.1 the machinery needed for hydrogen generations is discussed. After this in Section 14.2 the liquefaction of hydrogen is discussed. Then, the logistics concerning the hydrogen transport are discussed in Section 14.3. After this the storage facilities of the airport are presented in Section 14.4. In Section 14.5 the aircraft refuelling process is discussed. Finally, in Section 14.6 the central hubs for other island regions are presented.

14.1. Hydrogen Generation

One way to produce green hydrogen is with the help of an electrolyser. An electrolyser uses electricity to split water into hydrogen and oxygen. If this is done with green electricity, the hydrogen can also be considered green. One of the largest electrolysers that is in use today is the Atmospheric Alkaline Electrolyser (AAE) as it can produce 8000 [kg] of green hydrogen per day [1] . For a maximum range flight at max payload 120 [kg] of hydrogen is needed. This means that for each AAE more than 60 maximum range at maximum payload flights can be performed. Note that boil-off during transport and storage before the LH2 reaches the aircraft is not considered in this approximation. The chosen number of AAE's is thus dependent on the number of hydrogen powered flights performed per day in the island region.

The needed energy supply for the AAE is 129 [GWh] per year. Options for obtaining that energy in a green way is to make use of wind turbines or solar panels. In Table 14.1 an overview is made on the quantity of these energy production methods if all the required energy would have to be provided by this method. Depending on the geological and logistical characteristics of an island region a combination of those three methods could be reasoned in a trade-off.

A large constraint of electrolyser technology is that so far only fresh water is feasible for operation. This could be a complication for transportation logistics as around 72000 [kg] of water would be needed for the AAE each day. Currently, research is being done into electrolyser technology that can work with seawater [97]. However, no timescale is given as to when this technology might be available. This means that either seawater needs to be desalinated or fresh water needs to be delivered to the AAE.

The AAE A3880 is a system that takes up a total of 770 [m^2]. The island Funadhoo in the Maldives is a very small island and might not have enough space for the AAE to fit. However there are a lot of islands close by where the AAE can fit. It might even be the best solution to built a small platform for the AAE as it only requires to be about 30 by 25 [m]. Due to the limited available area for onshore wind turbines and solar panels the implementation of offshore wind turbines suggests to be advantageous.

[1] URL: https://nelhydrogen.com/product/atmospheric-alkaline-electrolyser-a-series/ [Accessed on: 24-06-2021]

Table 14.1: Overview of the power estimations per group

Process	**Energy required per year [GWh]**	**Onshore wind turbines** [2] [3]	**Offshore wind turbines** [4] [2]	**Solar panels [ha]** [5] [6] [7] [8].
Hydrogen generation	129	22	11	24.7
Hydrogen liquefaction	44	8	4	8.4
Total	173	30	15	33.1

14.2. Hydrogen Liquefaction

For the liquefaction of the hydrogen 15 [kWh/kg] is needed [98]. Considering that the AAE can produce up to 2,920,000 [kg] per year an extra of 44 [GWh] of energy per year is needed to liquefy the produced hydrogen. In Table 14.1 the quantity of green energy production methods is indicated to be able to power the liquefaction system.

The liquefaction system should be placed near the hydrogen generation system so that the produced hydrogen has to be transported in gaseous phase to a minimum extent. Further elaboration on this can be found in Section 14.3.

14.3. Hydrogen Transport

In the Maldives, almost all of the islands are dependent on the supply of fuel for the generation of electricity. Therefore there is already a logistic system in place to provide all the islands with their fuel needs. This is something which can be used to easily arrange the hydrogen transport in the Maldives as well. In the Maldives the island Funadhoo is used as central storage of all the fuel. On the island there are big tanks which contain Diesel, Petrol and Kerosene. To provide the hydrogen to all the airports a big liquid hydrogen tank could be placed to supply the islands without interruptions and shortages.

The fuel is distributed across all islands by making use of a fleet of boats. These boats storage capacities range from 20 to 2000 metric tonnes. To be able to transport the liquid hydrogen the boats should of course be equipped with special liquid hydrogen tanks. The H_2OPPER will use hydrogen to fly and therefore the amount of kerosene that will be needed in the island regions will go down. This drop in kerosene consumption will allow the boats to make room for liquid hydrogen tanks. It must be noted that some island may only have very small ports. However, since all the island are provided with fuel it is assumed that even the island with the smaller ports can be provided with hydrogen by the smaller boats of the fleet.

During transport boil-off losses will occur. These loses will have to be taken into consideration when the hydrogen distribution is implemented in the logistic operations of the concerned island region. In order to minimise losses the boiled off hydrogen could be used to generate electricity in combination with a fuel cell. However, a trade-off should be conducted to determine whether the added weight and expenses of such a system is profitable.

It was chosen to liquefy the hydrogen at the production site and thus only transport the hydrogen in liquid phase. This was due to two reasons. First of all, if the hydrogen is liquefied on the production site it means that not every island needs it own liquefaction system. Secondly, liquid hydrogen tanks can hold more

[2] The average onshore wind turbine rated at 2.5 – 3 [MW] can produce 6 [GWh] every year.
[3] URL: https://www.inspirecleanenergy.com/blog/clean-energy-101/how-much-energy-does-wind-turbine-produce [Accessed on: 15-06-2021]
[4] The average offshore wind turbine can produce 12 [GWh] every year (as output ratings of 7.5-10 MW are already used globally).
[5] The solar panel area is calculated by taking the average solar panel efficiency of 15%, the average intensity of solar intensity of 1360 [W/m^2] and the average sun time per day of 7 hours.
[6] URL: https://www.greenmatch.co.uk/blog/2014/11/how-efficient-are-solar-panels [Accessed on: 15-06-2021]
[7] URL: https://earthobservatory.nasa.gov/features/EnergyBalance/page2.php#:~:text=At%20Earth%27s%20average%20distance%20from,most%20recent%20NASA%20satellite%20missions. [Accessed on: 15-06-2021]
[8] URL: https://unboundsolar.com/solar-information/sun-hours-us-map [Accessed on: 15-06-2021]

hydrogen than similar sized gaseous tanks. This means that the hydrogen tanks will be able to transport more hydrogen per run.

14.4. Airport Storage

The liquid hydrogen has to be stored on the island so that the airport can utilize liquid hydrogen during the time between deliveries by boat. It was chosen to distinguish two situations.

The first situation is in case of a small island. In case of a small island it may be profitable to only have a liquid hydrogen tank stored at the port. From the port an insulated pipeline travels to the airport where an access point is situated. The pipeline may be buried to provide additional insulation as long as boiled-off hydrogen can escape. Furthermore, having a tank only at the port is easier to implement with respect to safety regulations since more space is assumed to be available than on the airport.

The second situation is in case of a larger island. In that case it may be more profitable to not only have a tank at the port but one as well on the airport. The liquid hydrogen can be carried to the airport by transport trucks or by pipeline. It is more expensive to built a long pipeline with enough insulation to prevent boil-off. However, over a longer time it can be more sustainable than transportation by trucks.

It has to be noted that having a tank on the port is essential as delivery boats need to be able to unload their payload quickly. In case of large quantities LH2 having a tank at the port provides flexibility to the delivery boat as it is not dependent on the island having enough transport trucks ready when docking.

Table 14.2: Overview of commercially available Linde hydrogen tanks [99]

Tank type	**Inner volume [m^3]**	**Storage capacity [kg]**	**Boil-off ratio [kg/-day]**
Spherical (Bulk storage)	1100-2300	70,200-145,000	<70-145 (<0.1%)
Cylindrical (Bulk storage)	300	19,300	<58 (<0.3%)
Cylindrical (high demand)	71	4600	<44 (<0.95%)
Cylindrical (low to medium demand)	11.5	900	<5.5 (<0.6%)
Cylindrical (low demand)	6	400	<2 (<0.5%)

In Table 14.2 an overview is provided of multiple LH2 tanks manufactured by Linde, a leading global industrial gases and engineering company. The overview is included to provide a sense of the possibilities of LH2 storage either where the hydrogen is generated and liquefied or on ports and airports. Depending on the quantity of hydrogen needed a choice can be made which type of tank or combination of tanks best suits the circumstances.

An important consideration is that for flights with 17 or 18 passengers the available mass for LH2 and thus the range increase considerably as seen in Chapter 16. For those flights it is thus not crucial to be able to refuel after each flight. It may be profitable to have these flights connect to smaller islands so that these do not need to have a tank at the airport. This would reduce the implementation cost to the infrastructure and logistic complication.

In order to make the most efficient use of the LH2 in the tanks the boil-off could be caught and used in combination with a fuel cell. The generated electricity could then be used to contribute to the power needed at either port, airport or other nearby infrastructure.

14.5. Refuelling Aircraft

The refuelling of the aircraft will be done with the help of a hydrogen refuelling truck. In essence it is the same as a kerosene refuelling truck but with a hydrogen tank instead. This truck will retrieve liquid hydrogen from the hydrogen storage tank or the pipeline. The truck will bring the liquid hydrogen to the aircraft where the refuelling will start. The refuelling process is more complicated than that of regular kerosene

refuelling. This is mainly due to the extra safety concerns that hydrogen brings along. Since hydrogen is very flammable and has a low ignition energy special gear and training is required for the ground staff.

Since hydrogen is a new sort of fuel that has not been used as commercial aircraft fuel yet, there are no regulations on the refuelling process. However, it needs to be noted that because of safety concerns it could mean that it is not possible to conduct parallel operations during the turn-around. This means that unloading of cargo and passengers can not happen at the same time as refuelling the aircraft [66].

This can cause problems for longer range aircraft since refuelling can take up a lot of time. However, for the shorter range aircraft this should be less of a problem. The refuelling time for the H_2OPPER was also analyzed. Currently a hydrogen refuel rate of 500 liters per minute can be achieved [66]. This means that for refuelling 234 [kg] of hydrogen only 6.7 minutes are needed. Since the maximum capacity of the tank is 234 [kg] the refuelling will at most take up 11.1% of the 1 hour turn-around time.

Another important consideration that has to be made is what to do with the hydrogen that is left after a flight. A consideration has to be made at what point in time it becomes more beneficial to collect the leftover LH2 or to accept boil-off losses and reduce logistic complication. Since sustainability is a key aspect of this design it was decided that if an aircraft does not have a following flight within 2 hours the LH2 should be returned to the airport tank. This way energy losses are kept to a minimum. However, an important consideration are the boil-off losses when opening tank valves. These can be obtained experimentally and should be taken into account when deciding if it is beneficial to return the LH2 to the airport tank.

In Section 9.3 it is discussed that when the aircraft descends from cruise altitude the battery recharges significantly. However, for shorter range missions aircraft usually fly with mission profiles that differ in altitude and descend angle due to being more efficient. This results in the necessity of battery recharging stations on the airport. Moreover, in case of an emergency and the aircraft has to return to the airport then a recharging station is necessary as well. In the worst case when the battery of 140.1 [kWh] has to be charged completely with a 280 [kW] charger then it would take 30 minutes which is 50% of the turn-around time. However, recharging is a process which can be performed parallel with other operations during turn-around. Since Tesla's superchargers can already reach power outputs of 250 [kW] it is assumed that a charging station of 280 [kW] is possible for the airports [9]. Note that this would mean that all airports where the aircraft lands should be provided with a recharge system.

14.6. Central Hubs for other Island Regions

The ground operations have so far been applied to the Maldives. However as has been stated in the introduction of this section, the ground operations should be easily generalised for other island regions as well. Therefore, a short closer look is taken on other island regions in the world. Almost in all island regions a distribution network of fossil fuels is in place. This is due to fact that the islands are very dependent on oil based fuels for their power generation. The big advantage of this is that complicated logistic operations for fuel supply already exist. With the help of some alterations these logistic operations can be adjusted to also fulfill the supply of liquid hydrogen. In Table 14.3 a list of possible markets can be seen with their corresponding possible central hub locations. The central hub locations given are possible central storage locations from which the hydrogen can be distributed over the entire island region. An example of a logistic plan other than that of the Maldives can be given for the Caribbean. SeaOne is a company that is currently launching a supply project of natural gas and natural gas liquid for the Caribbean[10]. This is another logistic operation that could be used as a base, this time for the liquid hydrogen supply to the Caribbean. The SeaOne infrastructure uses Colombia as central hub for the southern islands of the Caribbean and the Dominican Republic as central hub for the central islands of the Caribbean. This once again shows that the fuel supply to other island regions also already exists. Thus the steps that were taken to provide the Maldives with liquid hydrogen can generally also be taken for other island regions.

[9] URL: https://www.tesla.com/supercharger [Accessed on: 28-06-2021]

[10] URL: https://seaone.com/media/seaone-caribbeans-north-america-top-strategic-infrastructure-project [Accessed on: 15-06-2021]

Table 14.3: Island regions and central storage and distribution hub

Island region	**Central storage/distribution location**
French Polynesia	Tahiti
Bahama's	Florida USA
Central Caribbean	Dominican Republic
Southern Caribbean	Colombia
Solomon Islands & New Caledonia	Australia

15
Financial Evaluation

In this chapter an estimation is made regarding the financial feasibility of the aircraft. In order to do so the cost of the aircraft is broken into different parts in the cost breakdown structure discussed in Section 15.1. Then the operational cost of the aircraft is regarded in Section 15.2. Finally, the return on investment is treated in Section 15.3.

15.1. Cost Breakdown Structure

In order to produce the aircraft there are two principal costs. The first is the research, development, testing and evaluation cost. These are all the cost which need to be made before the aircraft can go in production. The second is the manufacturing cost and concerns all physical components of the aircraft. For each of these components a distinction can be made between material cost and labour cost. An overview can be seen in Figure 15.1. Note that the distinction between material cost and labour cost is only depicted for the fuel cell to avoid duplicity. In order to be able to estimate the manufacturing cost the cost of the reference aircraft, the L 410 NG, were taken as a point of reference.

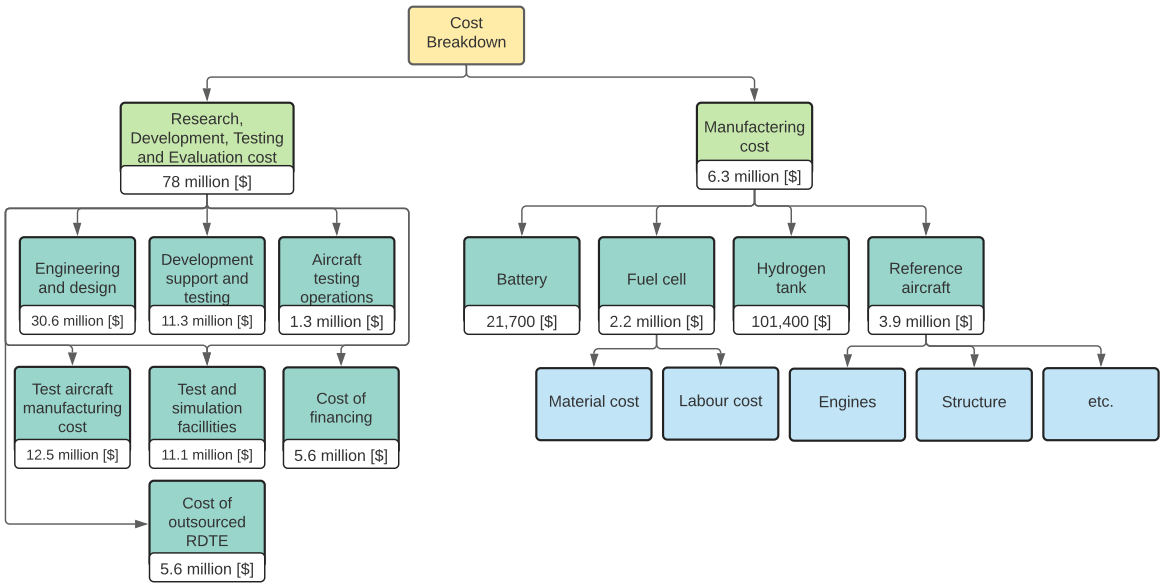

Figure 15.1: Cost breakdown structure of the aircraft

15.1.1. Research, Development, Testing and Evaluation

One of the inputs of the return of investment (RoI) is the research, development, testing and evaluation (RDTE) cost. These costs are made before any profit can be made on the aircraft. The RDTE costs of the aircraft is estimated using formulas based on empirical data, established by Roskam [89, VIII, p.28]. The estimation of the development cost is divided into six parts;

- Engineering and design cost, C_{ed}. This part is based on the number of man-hours needed to design and test the aircraft
- Development support and testing, C_{dst}. This part consists of various smaller tests needed for the development of the aircraft. Examples are wind tunnel and propulsion tests.

- Testing aircraft(s) , C_{ta}. This part is made up of the manufacturing and tooling costs for producing aircraft intended for testing.
- Aircraft testing operations, C_{to}. This part consists of the operational cost of testing the aircraft. For example, an aircraft needs to fly multiple hours before being able to be certified [1].
- Test and simulation facillities , C_{tsf}. This part consists of new testing facillities that need to be built up to test the aircraft. Examples for the H_2OPPER could be the testing of the fuel tank in cryogenic conditions.
- Cost of financing, C_{fin}. This part is made up of interest that needs to be paid on borrowed money.
- Profit of RDTE, C_{pro}. RDTE tasks that are being outsourced will come with profit margins for the involved company.

Of these parts, C_{ed}, C_{dst} and C_{to} will be estimated using the empirical formulas. Note that even though these formulas were devised in the 1980s, they are able to account for innovations and inflation. However, the estimates still need to be validated. The equations used are Equation 15.1,15.2 and 15.3 respectively. In these formulas, the following parameters are used:

- W_{ampr} is the aeronautical manufacturers planning report weight [lbs]. This weight excludes parts that will not be designed in-house. For example, the engines and the avionics, but it does include the weight of the fuel cell and the tanks. By using the values estimated from the class-II weight estimation, an W_{ampr} of 5393 [kg] or 11890 [lbs] is obtained.
- V_{max} is the maximum design speed [kts]. The aircraft is designed to fly at a speed of 175 [kts].
- N_{rdte} is the number of aircraft that will be built for the research, development, test and evaluation phase. It is decided to build two aircraft for this phase, where one will be used for static tests, and one is used for flight tests.
- N_{st} is the number of aircraft that will be used for static tests: one aircraft.
- CEF is the cost escalation factor [-]. This factor is based on the inflation measured from the year 1970. At the moment, one dollar from 1970 would have the same value as 6.94 dollars in 2021 [2]. By assuming that the aircraft development will continue on for at least 5 years, the CEF will be set to 8.5 to account for future inflations. This value is found by extrapolating the inflation between 1970 and 2021 to 2026.
- F_{diff} is a judgement factor, varying from 1 to 2 [-], which accounts for the difficulty (i.e. complexity) of a new airplane program. As the H_2OPPER uses radical new technologies, this factor will be set to 2 .
- F_{cad} is a judgement factor, varying from 0.8 to 1.2 [-], which accounts for the effect of computer aided design capability on airframe engineering and design cost. It is assumed that most engineers nowadays are more familiar with CAD programs and therefore this factor will be set to 0.8 .
  $h.c.$ is the hourly cost of the engineers working on the RDTE. From research it is obtained that the average hourly cost for an aerospace engineer is around 96 [$] [3].

$$C_{ed} = 0.0396\left(W_{ampr}\right)^{0.791}\left(V_{max}\right)^{1.526}\left(N_{rdte}\right)^{0.183}\left(F_{diff}\right)\left(F_{cad}\right)(h.c.) \tag{15.1}$$

$$C_{dst} = 0.008325\left(W_{ampr}\right)^{0.873}\left(V_{max}\right)^{1.890}\left(N_{rdte}\right)^{0.346}(CEF)\left(F_{diff}\right) \tag{15.2}$$

$$C_{fto} = 0.001244\left(W_{ampr}\right)^{1.160}\left(V_{max}\right)^{1.371}\left(N_{rdte} - N_{st}\right)^{1.281}(CEF)\left(F_{diff}\right) \tag{15.3}$$

The first equation yielded a cost of 30.6 million [$] for the engineering and design. From this it can be deduced that a total of 319,000 man-hours are needed for the design. By assuming full-time working weeks of forty hours and a team of a hundred people, the aircraft could be designed in less than 2 years. The second equation yielded a cost of 11.3 million [$] for the development support and testing. The third equation yielded a cost of 1.3 million [$] for the aircraft testing operations.

[1] URL: https://www.airbus.com/aircraft/how-is-an-aircraft-built/test-programme-and-certification.html [Accessed on: 17-6-2021]

[2] URL: https://www.usinflationcalculator.com/ [Accessed on: 17-06-2021]

[3] URL: http://www.salaryexplorer.com/salary-survey.php?loc=152&loctype=1&job=22&jobtype=1 [Accessed on: 17-06-2021]

For the manufacturing cost of the test aircraft, it is assumed that the manufacturing cost is higher as the production process is not established yet. However, the aircraft used for the static testing will be cheaper as not all the components need to be present for the static testing. It is assumed that both of these aircraft together will have an average cost the same as the final aircraft. In total this would be then 7.8 million [$].

The last three components of the RDTE cost are assumed based on fractions of the total cost. First, for the testing facilities, a factor of 0.2 is taken. This is a significant amount and can be justified as the H_2OPPER will contain various new systems that need to be tested; for example, the fuel cell and the fuel tank. Next, the financial cost is estimated to have a factor of 0.1 of the cost. This means that an interest rate of 10% is expected. This value is based on average long-term loans [4]. In addition, it is expected that organizations such as Climate Action from the European Union will aid the project by giving low-interest loans. At last, it is assumed that the outsourced RDTE will have a profit margin of 0.1 of the total cost. This value is obtained from average margins [89, VIII, p.35].

By combining all the costs, and adding up the factors above, a total RDTE cost of around 78 million [$] is obtained. Most companies are not willing to share these costs, therefore it is difficult to validate this number. However, the development costs for large companies, such as Boeing and Airbus, are known; the development costs per seat for the Airbus A320neo is 7.93 million [$], and for the Boeing 737 MAX it is 18.29 million [$] [100]. Scaling this to 19 passengers results in costs far above the estimated 65 million [$]: 151 and 348 million [$]. These reference aircraft however are also built for larger numbers of passengers and are certified differently than for commuter aircraft. It is therefore expected that the RDTE costs have some discrepancies. To make sure that the cost of 78 million [$] is reliable, a more detailed estimate will need to be made in the following phases of the design.

15.1.2. Manufacturing Cost

The cost of the reference aircraft L 410 NG was taken as a point of reference. The aircraft is listed at a price of 7.8 million [$][5]. It is assumed that the aircraft manufacturer handles a gross profit margin of 50%. Due to the scarcity of information on aircraft profit margins this assumption is based on discounts given by manufacturers of large aircraft[6]. This means that the manufacturing costs of the L 410 NG is estimated at 3.9 million [$]. It is assumed that this amount excludes RDTE cost.

To be able to make an estimate of the cost for manufacturing the H_2OPPER it is assumed that the manufacturing cost is the same as the reference aircraft together with the cost of the new power system. The new system includes the fuel cell, hydrogen tank and batteries. In this approximation the costs of kerosine engines and electrical engines are considered comparable.

LH2 Tank price

The hydrogen tanks price is estimated based on the total amount of energy that needs to be brought on board. The maximum amount of hydrogen that will be taken on board is 234 [kg]. The tank is estimated to cost 13 [$] per [kWh], bringing the total tank cost to 101,400 [$] [101]. For a 5.6 [kg] tank the cost is divided into 70% material cost and 30% manufacturing cost. For a 10.6 [kg] the ratio is 76% - 24%. This means that for larger tanks the material cost becomes more significant than the manufacturing cost. Since the tanks of the H_2OPPER will hold 33.4 [kg] each it is expected that the material costs will be more significant. However, in this approximation the geometrical and material configuration are not exactly replicated. Due to the more complicated shape and extra materials used in the tank it is expected that the true manufacturing costs are higher.

Batteries

The total number of batteries that is needed is 420 [kg]. For the cost estimation it is assumed that the cost for lithium metal batteries are equal to the cost of lithium ion batteries. Lithium ion batteries have an average

[4] URL: `https://www.fundera.com/business-loans/guides/business-loan-interest-rate` [Accessed on: 17-6-2021]
[5] Confirmed by the sales team of Let Kunovice in June 2021
[6] URL: `https://airinsight.com/aircraft-pricing-list-vs-market/` [Accessed on: 17-06-2021]

cost of around 140 [$] per [kWh] [7]. With an energy density of 369 [Wh/kg] this results in a total of 154,980 [kWh]. This brings the total battery cost to 21,697 [$].

Fuel cell system

In 'Manufacturing Cost Analysis of 100 and 250 kW Fuel Cell Systems for Primary Power and Combined Heat and Power Applications' [102] a cost analysis is made for 100 and 250 [kW] PEM fuel cell systems. As will be explained in Subsection 15.3.1 it is expected that approximately 23 aircraft will be sold per year. This means that less than 100 fuel cells are needed per year and less gain can be taken from the economies of scale. The cost analysis shows that economies of scale can play a big role in the cost reduction of fuel cells. A 22 % price drop may be realised if the units produced increases from < 100 units per year to 1000 units per year. However, for now it was decided to take the highest price (< 100 units/year) as reference for the fuel cell cost. It was found that a fuel cell with an output of 250 [kW] will cost a total of 714,952 [$]. For a 100 [kW] system the total cost is 411,670 [$]. What can be concluded from this is that a power increase of factor 2.5 only results in a price increase of factor 1.74. Therefore it was decided to linearize the price level between the 100 and 250 [kW] systems to calculate the price for the fuel cell systems needed for the H_2OPPER. For two 450 [kW] fuel cell systems a total price of 2,238,656 [$] is then calculated.

When adding the manufacturing cost of the L 410 NG together with the cost of the LH2 tank, the batteries and the fuel cell system the total manufacturing cost is found. For the H_2OPPER the total manufacturing cost equals around 6.3 million [$]

15.2. Operational Cost

The operational cost of a hydrogen aircraft will differ from a regular kerosene aircraft. For commuter aircraft an operational cost of 5% more is predicted compared to kerosene aircraft by the year 2040 in a study by McKinsey & Company [66]. The largest contributors to this change are the fuel costs and the maintenance costs.

In Chapter 14 the infrastructure for the liquid hydrogen was explained. From this it was clear that large investments in the island regions are needed to make it possible to produce green hydrogen. These large investments will cause the price of green hydrogen to be higher than kerosene. An important factor for the prices is the scale at which hydrogen is going to be used around the globe. If the transition to hydrogen aviation is progressed the prices for hydrogen can drop immensely. Predictions for liquid hydrogen prices in Europe by 2040 are ranging from 2.60 [$] to 3.50 [$] per [kg] [66]. This means LH2 will have a price of around 85 [$] per [MWh] compared to around 50 [$] per [MWh] for kerosene.

What must be noted is that this prediction is made for Europe. Island regions can be very isolated and the additional shipping costs of liquid hydrogen can be high. However, the price of LH2 per [kg] is determined for the largest part by the production costs and thus the European LH2 prices are deemed acceptable for this estimation.

During the first years of introducing liquid hydrogen aircraft the maintenance costs will also be higher. The new technology that is used for the tanks, fuel cells, and propulsion system will need extra check-ups. Furthermore since the various components of the aircraft are more expensive it will also be more expensive to replace the components or perform maintenance. However, the maintenance of electric motors is less expensive than that of combustion engines due to electric motors having less moving parts[8].

Two more categories of the operational costs that will see an increase when compared to regular kerosene aircraft are landing fees and depreciation & amortization. If two aircraft were to perform the same mission and one uses kerosene as fuel and the other uses hydrogen as fuel. The hydrogen aircraft will most likely have a higher MTOW. Since landing fees are determined based on the MTOW one could say that the landing fees for hydrogen aircraft will also be more expensive. Furthermore, for hydrogen aircraft larger capital expenditures are used to acquire, upgrade and maintain the aircraft. This means that the depreciation costs for hydrogen aircraft are also higher.

[7] URL: https://www.economist.com/graphic-detail/2021/03/31/lithium-battery-costs-have-fallen-by-98-in-three-decades [Accessed on: 17-06-2021]

[8] URL: electricmotorshavefewermovingparts [Accessed on: 17-06-2021]

Governments can play an important role in the relative cost of green hydrogen by subsidizing hydrogen or taxing CO_2 emissions. An example is seen in Australia where a plan for building three new green hydrogen plants was recently approved [9]. The hydrogen plants will be built with the help of $100 million dollars in government funding. The main goal of the investment is to bring the cost of green hydrogen down. Intervention from governments around the world can thus help reducing the relative cost gap between green hydrogen and kerosene.

The top level requirement of the operating cost not being higher than 10% compared to kerosene aircraft around 2030 is deemed feasible when observing that the operational cost is only 5% higher in 2040.

15.3. Return On Investment

Before being able to bring a new aircraft to the market the product has to be developed. In this preceding process the aircraft is designed, tested and evaluated to assure it complies with CS-23 regulations and it performs as expected. This phase requires a considerable investment and is discussed in Subsection 15.1.1. Together with the manufacturing cost discussed in Subsection 15.1.2 it forms the total cost of the process. The total revenue is dependent on the product price and the product sales. These are discussed in Subsection 15.3.1. Finally, the Break-Even Point is discussed in Subsection 15.3.2.

15.3.1. Revenue

The revenue of the aircraft sales will be dependent on the list price and the number of aircraft sold. The list price was set to 10 million [$] in the top-level requirements. In order to determine the expected sales of the aircraft an analysis was performed by observing the sales of aircraft with a similar passenger and range objectives.

Table 15.1: Similar aircraft sales

Name	Units sold	Time span	Units sold per year
Twin Otter DHC	844[10]	1965-1988	36
Twin Otter Viking	141[11]	2008-present	10
Beechcraft 1900D[12]	695	1982-2002	34
Jetstream 31[13]	386	1980-1993	29
L 410[14]	1200	1971-present	24
Dornier do 228[15]	245	1982-1997	16
CASA c-212[16]	583	1971-2012	14
Average	-	-	**23**

In Table 15.1 it can be seen that an average of 23 aircraft sold per year is a reasonable estimate. With a list price of 10 million [$] this results to a revenue of 230 million [$] per year.

15.3.2. Break-Even Point

In Figure 15.2 the total revenue is plotted alongside the total cost. The total cost consists of the variable cost and the fixed cost which are the manufacturing cost and RDTE cost, respectively. It can be seen that after 21

[9] URL: https://www.abc.net.au/news/2021-05-05/100-million-in-federal-grants-for-green-hydrogen/100117192 [Accessed on: 29-06-2021]
[10] URL: http://www.twinotterarchive.com/DHC-6_Index_new.html [Accessed on: 17-6-2021]
[11] URL: http://www.twinotterarchive.com/DHC-6_Index_new.html [Accessed on: 17-6-2021]
[12] URL: https://en.wikipedia.org/wiki/Beechcraft_1900 [Accessed on: 17-6-2021]
[13] URL: https://en.wikipedia.org/wiki/British_Aerospace_Jetstream [Accessed on: 17-6-2021]
[14] URL: http://www.let.cz/l410ng [Accessed on: 17-6-2021]
[15] URL: https://www.ainonline.com/aviation-news/aviation-international-news/2007-12-28/ruag-relaunch-do-228-production [Accessed on: 17-6-2021]
[16] URL: https://en.wikipedia.org/wiki/CASA_C-212_Aviocar [Accessed on: 17-6-2021]

units sold the Break-Even Point is attained. The time after which the Break-Even Point is reached is around one year.

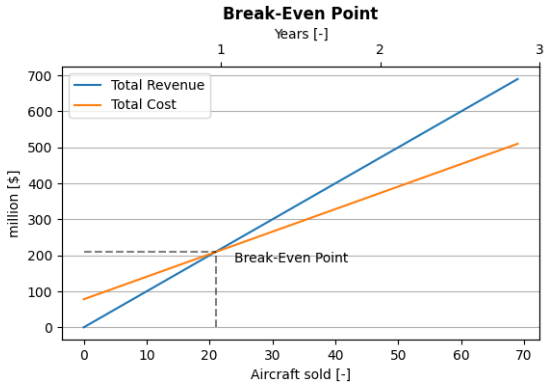

Figure 15.2: Break-Even Point

Once the Break-Even Point is passed the yearly result[17] of 86 million [$] is profit. This means that after three years and ten years a return on investment of 231% and 1002% is achieved, respectively.

Depending on the pace at which hydrogen power train systems develop in the coming 20 years it is unsure for how many years it is optimally profitable to produce the aircraft. If hydrogen power train systems do improve significantly it is advisable to partly reserve the made profit in the first years in order to be able to cover the RDTE cost for future generation systems.

15.3.3. Sensitivity Analysis

In this estimation the manufacturing price of the L 410 NG was estimated at 50% of the list price. However, due to the uncertainty of this margin another plot for the Break-Even Point can be seen in Figure 15.3. This time the profit margin is set to 30% meaning a manufacturing price of 70%. It can be seen that the Break-Even Point is reached at 36 sales. The yearly result is 50 million [$]. This means that after three years and ten years a return on investment of 93% and 542% is achieved, respectively.

Another consideration to make is the competitiveness of the list price of the aircraft. In the market analysis in Chapter 4 it can be seen that comparable aircraft prices range between 5.9-7.8 million [$]. This means that in order to be able to compete with these aircraft and make the predicted unit sales the list price of the aircraft should be lower. In Figure 15.4 a Break-Even Point plot can be seen for when the list price is set at 8 million [$]. In this case the Break-Even Point is reached at 45 unit sales and the yearly result is 40 million [$]. This means that after three years and ten years a return on investment of 54% and 413% is achieved, respectively.

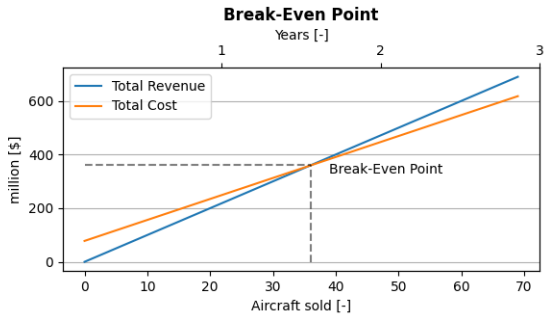

Figure 15.3: Break-Even Point with L 410 NG profit margin estimated at 30%

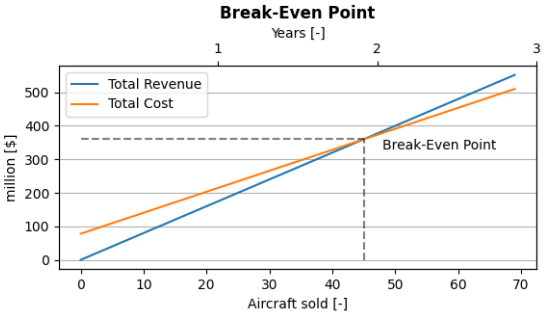

Figure 15.4: Break-Even Point with H_2OPPER list price set at 8 million [$]

[17] Yearly Revenue - Yearly Cost

16
Final Design Overview

In this chapter the final design will be presented including the main characteristics in Section 16.1, the green policy in Section 16.2 and the sensitivity analysis in Section 16.3. Afterwards, an overview of the requirement compliance is presented in Section 16.4. Finally, the mass budget breakdown is shown in Section 16.6.

16.1. Final Design

This section describes the overall characteristics of the H_2OPPER. The aircraft is a high-wing, sustainable and fully electrical aircraft designed to accommodate 19 passengers and to travel over 300 [NM] with maximum payload. It's main purpose is to facilitate climate-neutral travel in islands regions. Table 16.1 gives an overview of the technical specifications, Table 16.2 an overview of its dimensions and Table 16.3 shows the main performance characteristics. At last, Figure 16.2 gives a visual representation of the H_2OPPER and Figure 16.3 shows a three-view drawing of the H_2OPPER.

Table 16.1: Aircraft technical specifications

Weight	
Maximum take-off weight [kg]	8618
Maximum zero fuel weight [kg]	6804
Maximum payload weight [kg]	1814
Occupancy	
Crew members [-]	1 - 2
Passengers [-]	19
Powerplant	
Number of engines [-]	2
Take-off power per engine [kW]	730

Table 16.2: Aircraft dimensions

Exterior	
Exterior height [m]	7.9
Exterior length [m]	14.4
Wing span [m]	20.0
Interior	
Cabin height [m]	1.91
Cabin width [m]	1.95
Cabin length [m]	6.8
Seat pitch [m]	0.35

Table 16.3: Performance specifications

Performance	
Cruise speed [kts]	175
Service ceiling [FL]	150
Take-off distance [m]	750
Landing distance [m]	675
Maximum range [NM]	1177
Range at maximum payload [NM]	321
Rate of climb [m/s]	5.8

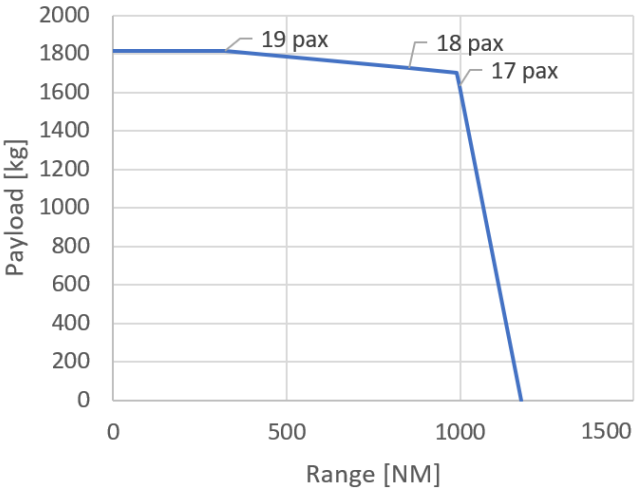

Figure 16.1: H_2OPPER payload-range diagram

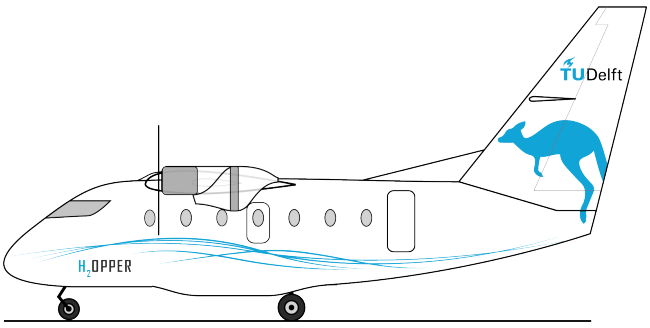

Figure 16.2: Visual representation of the H_2OPPER

Figure 16.1 shows the potential range for different payload configurations. The substitution of passengers with liquid hydrogen results in a substantial range increase. This range increase follows from the decision

that was made to add more liquid hydrogen tanks when there was a gap in the mass budget. The design decision was made to completely fill the weight that was left to get to the maximum allowable OEW (with 10% contingency) with hydrogen tanks in order to optimize for range at lower payload. Two other options that were considered were optimizing for range a maximum payload and adding 70 [kg] of payload to the maximum payload. However, the optimization at lower payload was chosen since the optimization for lower payload range resulted in an enormous range increase, compared to a moderate range increase and moderate payload increase for the other two options.

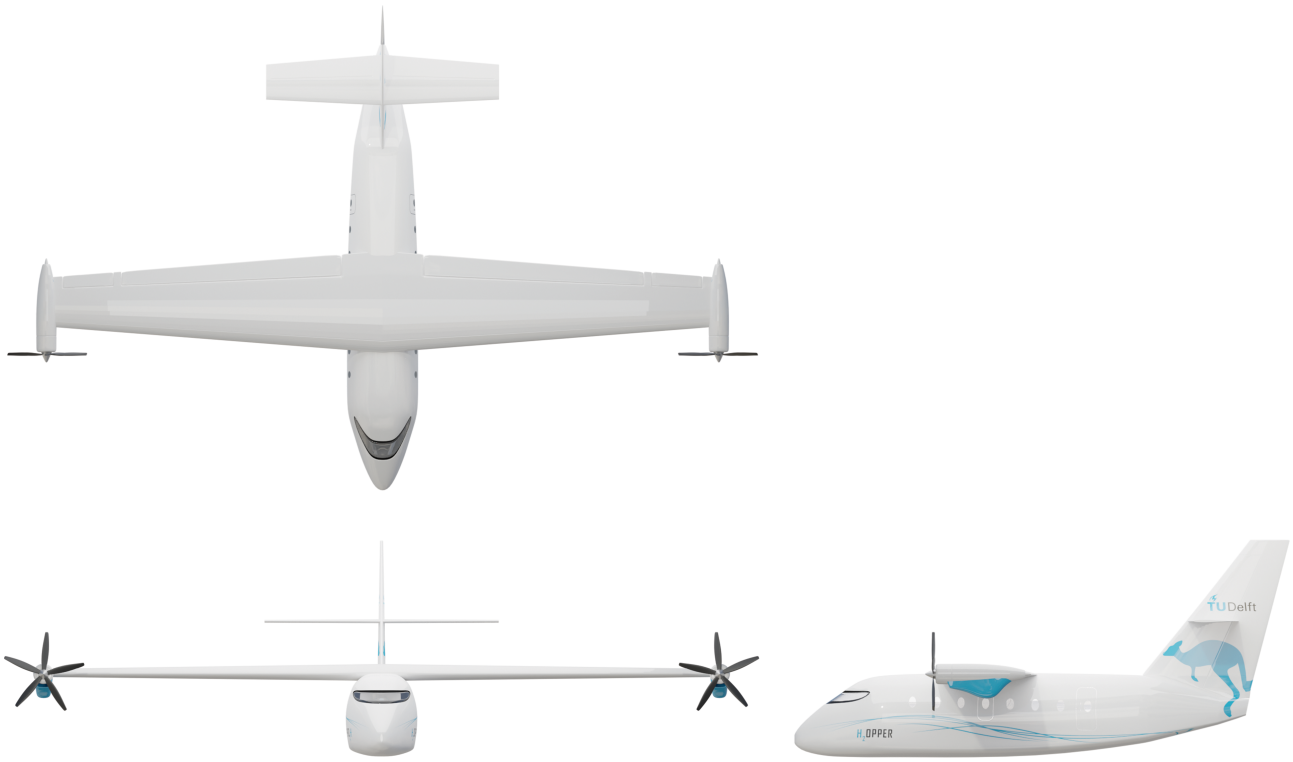

Figure 16.3: Three-view drawing of the H_2OPPER

16.2. Green Policy

The overall sustainability of the H_2OPPER is a key selling point. The aircraft is fully climate-neutral which means the aircraft has no impact on the environment when operating. Besides the operating sustainability, a recyclability percentage of 98% can be achieved for the main structural components.

The majority of the green indicators in the green policy were not directly used to asses sustainability in the final design. Rather, the indicators functioned to make the most sustainable choice for the design choices that led to the final design. The indicators were created to allow for a comparison between two design choices or options. The recyclability indicator was used to achieve the 98% recyclability and the energy efficiency indicator aided in assessing that the wing-tip mounted engines were advantageous for the H_2OPPER.

Two of the green indicators allowed to give final results regarding sustainability, rather than only allowing a comparison. The NO_x emission in landing and take-off equals zero for the final design and the noise level produced by the propellers equals 107.66 [dB].

16.3. Sensitivity Analysis

With all the different subsystems designed and the inputs and outputs of the design tools determined, the aircraft was iterated to have all subsystems working together. To identify the effects of altering parameters of the design, a sensitivity analysis was performed. This analysis served multiple purposes. First of all, it allowed to see if a change in variable results in a more efficient design after a set number of iterations. In Subsection 16.3.1 it is described how different parameters were optimized for an efficient design. Next to that, the effect of important assumptions and uncertainty ranges on the performance of the final design could be tested. In Subsection 16.3.2 this uncertainty analysis is described.

16.3.1. Aircraft Optimization

The aircraft was optimized for different input parameters. It should be noted that these designs were not fully iterated. All the design tools accounted for the final MTOW of 8618 [kg], while the actual weight of the aircraft ended up being lower than that for every design. The surface area is an input parameter that defines a large part of the other parameters of the aircraft. Therefore it was chosen to alter the surface area with the goal of optimizing for a low OEW.

Next to selecting a wing surface area, two other parameters that were altered were the amount of engines and the fuselage length. For both, the main goal again was to lower the OEW. Furthermore, because of the wing tip engines the vertical tail of the aircraft became extremely large. Therefore, these alterations had as a second goal to lower the vertical tail surface area. In Table 16.4, important parameters of the designed aircraft are displayed for different input parameters. The four leftmost designs all have 2 engines and a fuselage length of 12.24 [m]. The two rightmost designs both have a surface area of 43 [m^2]. The design with 4 engines has a fuselage length of 12.24 [m] and the rightmost design has 2 engines.

Table 16.4: Aircraft parameters of designs with different input parameters.

Parameter	**S = 40**	**S = 43**	**S = 45**	**S = 50**	**4 engines**	**l = 13.24**
OEW [kg]	6019	5962	5965	6017	6032	5958
C_{D_0} [-]	0.0282	0.0261	0.0252	0.0250	0.0261	0.0262
e [-]	0.752	0.781	0.794	0.814	0.850	0.779
Take-off power [kW]	1250	1170	1120	1070	1074	1070
Structural weight [kg]	2041	2058	2107	2239	2025	2057
Propulsion weight [kg]	1793	1697	1649	1567	1846	1696
Horizontal tail surface [m^2]	8.3	9.5	9.6	11.0	9.4	8.2
Vertical tail surface [m^2]	15.2	13.9	13.3	12.8	6.5	9.7

In Table 16.4, the structural weight consists of the structural weight of the wing, vertical tail, horizontal tail and fuselage. The propulsion weight consists of the weight of the engine, propeller, batteries, radiator and fuel cell and components. The hydrogen and hydrogen tank have not been included in the propulsion weight, as the weight did not differ significantly between designs. As can be seen in Table 16.4, the aircraft parameters Oswald efficiency, structural weight and horizontal wing surface have a positive correlation with the surface area. On the other hand, the parameters C_{D_0}, take-off power, propulsion weight and vertical tail surface all have a negative correlation with the surface area. Lastly, the OEW is the only parameter that does not only increase or decrease with the wing surface area. The design with a surface area of 43 [m^2] had the lowest OEW, since it had the optimal combination of structural and propulsion weight. Therefore it was decided to continue the design process with a surface area of 43 [m^2].

The two rightmost designs of Table 16.4 both have a surface area of 43 [m^2] and therefore were compared to the other design with a surface area of 43 [m^2]. It can be seen that for the design with 4 engines, the extra propulsion weight from the engines and propellers (+149 [kg]) is not compensated by the loss in structural weight (-33 [kg]), although the vertical tail surface size could be halved. For the design with a fuselage of 13.24 [m], the horizontal and vertical tail size could be reduced, which resulted in a structural weight loss (-48.57 [kg]). This weight loss was more than the weight gain of the extra meter of fuselage (+24 [kg]), mainly because the fuselage extension was part of the thinning tail cone.

Since the design with the wing surface area of 43 [m^2], 2 engines and fuselage length of 13.24 [m] was the design with the lowest OEW. This design was selected to start the iteration process.

16.3.2. Uncertainty Testing

Every aircraft design contains uncertainties until it has flown its first flight. Up until the current design point, assumptions were made which result in uncertainties in the design. An uncertainty analysis was performed

in order to check what the effect of the uncertainties is on the performance of the aircraft. This way, it can be tested how strong the design is at this design stage. The main uncertainties in the design of the aircraft are listed in Table 16.5. These uncertainties follow from the assumptions made during the design of the different subsystems.

Table 16.5: Uncertainties of aircraft subsystems

Subsystem	**Uncertainty**	**Origin**
Hydrogen tank	Insulation +5 [cm]	Thermal conductivity of polyurethane could be higher
Hydrogen tank	Wall density +50%	Ratio of carbon fibres and resin could be higher
Engine	Mass +-10 [kg]	Other extrapolating scale could be used
Fuel cell	Mass +25%	Cooling system could need fan for airflow
Fuel cell	Efficiency +10%	In 5 year, higher fuel cell efficiencies could be achieved
Propelller	Efficiency +- 5%	Efficiency could differ when doing actual simulations
Battery	Mass +35%	Use of lithium metal batteries could not be possible
Wingbox	Mass -10%	Lift distribution was assumed constant
Horizontal tail	Mass -10%	Lift distribution was assumed constant
Vertical tail	Mass -10%	Lift distribution was assumed constant
Fuselage	Mass -5%	Nose and tailcone could be optimized for actual loads
Control surfaces	Mass +20 [kg] or -85 [kg]	Mass could be in the range of the class II weight analysis
Avionics	Mass +85 [kg]	Avionics systems could not become lighter in 5 years
Landing gear	Mass +70 [kg]	Mass could be in the higher range of the class II weight analysis

In order to be able to make a comparison of the magnitude of the different uncertainties, the effect of the uncertainties was converted to a weight difference. For example, the uncertainty in propeller efficiency does not directly change the weight of a component. However, due to the lower propeller efficiency, the propeller, fuel cell and batteries need to be heavier in order to make the aircraft fly. The weight changes that result from the uncertainties of the different components are displayed in Figure 16.4. The red columns represent weight gains and the green columns weight losses.

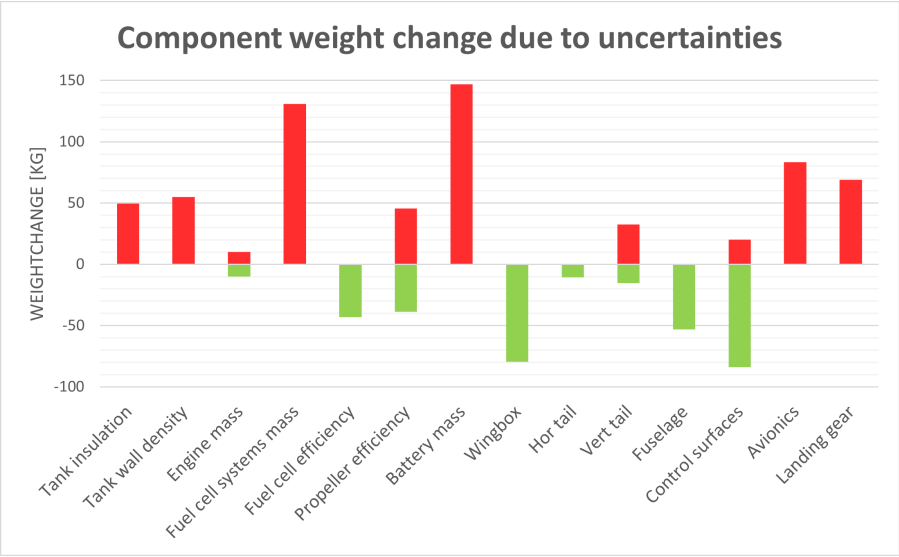

Figure 16.4: Aircraft component weight uncertainties

As can be seen in Figure 16.4, the largest uncertainties that cause a weight gain are the fuel cell systems and battery mass uncertainties. On the other hand, the wingbox and control surface uncertainties result in the largest weight losses.

To be able to quantify the effect of the uncertainties, the result of the uncertainties was expressed in range,

which is the most important parameter of the aircraft. For the baseline range, the hydrogen tank configuration was optimized for range at maximum payload weight, which means a tank with a capacity that can completely be used when flying at maximum payload, without going over the MTOW. This is different than the final aircraft configuration, which is optimized for range at a lower payload weight. The change was made to be able to equally compare the different uncertainty effects.

For every uncertainty, the weight change due to the uncertainty was taken into account and the hydrogen tank was made larger or smaller, while still being optimized for range at maximum payload weight. This means that every time the tank could be completely filled when flying at maximum payload, without going over the MTOW. The tank thus was the only component that changed, together with the uncertainty component. The MTOW of the aircraft was the same for all uncertainties. This resulted in a different range for every uncertainty, which is displayed in Figure 16.5. The green columns correspond to the green weight losses in Figure 16.4 and the red columns to the red weight gains. The blue column represents the range at the baseline configuration. Furthermore, the dashed line is the range at maximum payload as depicted by the top level requirement.

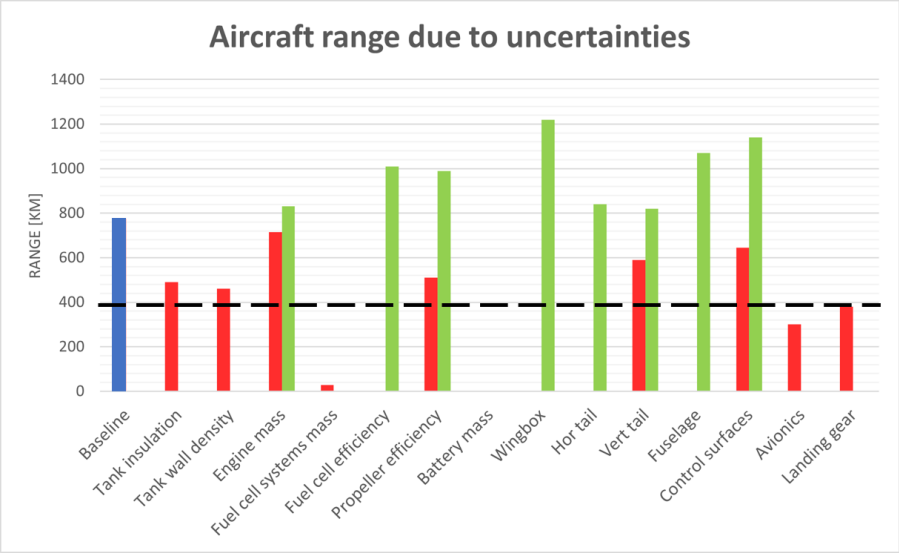

Figure 16.5: Aircraft range at maximum payload as a result of uncertainties in the design. The dashed line displays the top level range requirement.

As can be seen in Figure 16.5, the uncertainties have a considerable effect on the range of the aircraft. Four of the uncertainties lower the range below the requirement. Furthermore, the uncertainty in fuel cell systems mass lowers the range to 28 [km], while the uncertainty in battery mass even lower it to 0 [km]. This means there is no weight budget left for any hydrogen storage next to the amount necessary for loitering. On the other hand, five uncertainties increase the range with more than 200 [km], with the wingbox uncertainty even increasing it to 1220 [km].

What can be concluded from the uncertainty analysis firstly is that there are about as many uncertainties in performance increase as in performance decrease. Therefore, the uncertainty analysis does not show if the aircraft performs better or worse with all uncertainties included. Secondly, it can be concluded that the performance of the aircraft is really sensitive to uncertainties. Even when not considering multiple uncertainties combined, the range at maximum payload fluctuates between 0 and 1220 [km]. This is the result of the hydrogen tank being a relatively light component and the hydrogen having a extremely high energy density. Furthermore, it is the result of the design choice to completely fill the weight that is left over from the MTOW with hydrogen and hydrogen tank. Because of the sensitivity of the design it is recommended, when continuing the design process, to first focus extensively on the components with the largest uncertainties. This way, there will be more certainty on the aircraft's performance.

It should be noted that a contingency of 10% was applied on the OEW in order to account for uncertainties in further design stages. This is the expected weight increase when going from preliminary design to the

final detailed aircraft design [103]. As can be seen in Figure 16.4 and Figure 16.5 by looking at the landing gear, a weight increase due to uncertainties of at most 67 [kg] would still have the aircraft the aircraft be able to meet the top level range requirements. Therefore, there is a total contingency on the weight of 11% to still have the aircraft meet the top level requirements.

During the uncertainty analysis, the assumption was made that the different tank sizes and aircraft components did not significantly change the CG of the aircraft. Therefore the design was not completely iterated. The snowball effect of the component weight changes was partly taken into account by increasing or decreasing the hydrogen tank size, so the total weight of the aircraft always stayed the same. However, this did not cover the snowball effect completely. The only other thing the uncertainties changed was the CG, although minimally since the largest weight differences are located inside the aircraft wing (almost exactly on the CG).Therefore further iteration of the aircraft would have led to minimal design changes.

16.4. Compliance Matrix

The characteristics of the final design are compared to the requirements set by the top-level requirements in Table 16.6. One of the top-level requirements was that the design should comply with CS-23 regulations which are discussed in Table 16.7. In these tables compliance is indicated with N.D. if the requirement was out of the scope of analysis so far. Since no actual tests could be performed on the aircraft, a selection of CS-23 requirements was made that could be designed for in the current stage of the design. Since the aircraft meets all the current CS-23 requirements, it is expected that the aircraft shall meet all the CS-23 requirements in the future if testing will be performed.

Table 16.6: Compliance matrix of the H_2OPPER.

Performance	**Requirement**	**H_2OPPER**	**Margin**	**Section**	**Compliance**
HOPPER-T-F-TO-4	The aircraft shall be able to take-off and land within 750 [m]	750/675	0/75	Section 9.3	Yes
HOPPER-T-F-CR-1	The aircraft shall be able to maintain 175 kts during cruise	175	–	Section 9.3	Yes
HOPPER-T-F-CR-4	The aircraft shall have a maximum range of 300 [NM] with regulatory reserves	1177	+877	Section 16.1	Yes
HOPPER-T-F-CR-5	The aircraft shall have a range of 200 [NM] at maximum payload with regulatory reserves	321	+121	Section 16.1	Yes
Sizing	**Requirement**	**H_2OPPER**	**Margin**	**Section**	**Compliance**
HOPPER-T-F-TO-8	The MTOW of the aircraft shall be lower than 19000 [lbs]	18995	+5	Section 16.1	Yes
HOPPER-T-F-CR-6	The aircraft shall carry a maximum of 19 passengers	19	–	Section 7.2	Yes
HOPPER-T-F-CR-7	The aircraft shall carry a maximum payload of 1814 [kg]	1814	–	Section 7.2	Yes
HOPPER-C-CF-8	The aircraft shall provide the possibility to bring a minimum of 15 [kg] of cargo luggage	15	–	Section 7.2	Yes
HOPPER-T-F-AM-5	The aircraft shall be able to roll with 32 [deg/s]	43	+11	Section 6.5	Yes

HOPPER-C-R-SR-4	The aircraft shall be able to withstand loads up to the ultimate load of 5.1	5.1	–	Section 5.2	Yes
HOPPER-C-R-SR-5	The aircraft shall be able to withstand negative loads up to the ultimate load of -2.1	-2.1	–	Section 5.2	Yes
Regulation	**Requirement**	**H_2OPPER**	**Margin**	**Section**	**Compliance**
HOPPER-U-SR.1	The aircraft shall comply with EASA / FAR part 23 regulations	–	–	Table 16.7	Table 16.7
Operations	**Requirement**	**H_2OPPER**	**Margin**	**Section**	**Compliance**
HOPPER-U-EB.2	The aircraft shall be able to perform 3 maximum range flights a day at maximum payload	3	–	Section 14.5	Yes
HOPPER-C-R-LC-10	The aircraft shall be able to dock at a 1B Aerodrome	–	–	Section 6.2	Yes
HOPPER-C-S-1	The aircraft shall have a turn around time of less than 1 [hr]	–	–	Section 14.5	Yes
Cost	**Requirement**	**H_2OPPER**	**Margin**	**Section**	**Compliance**
HOPPER-C-C-1	The aircraft shall have a list price of at most 10 million [USD]	10 mln	–	Section 15.1	Yes
HOPPER-C-C-2	The aircraft operating cost shall not be more than 10 % of the average of comparable aircraft	5-10 %	<5 %	Section 15.2	Yes
Sustainability	**Requirement**	**H_2OPPER**	**Margin**	**Section**	**Compliance**
HOPPER-C-E-3	A minimum of 90 percent of the aircraft structure shall be recyclable	98	+8	Section 5.7	Yes
HOPPER-C-E-1	The aircraft shall be climate neutral	–	–	Section 16.2	Yes
HOPPER-C-R-NC-1	Noise levels shall be kept below 260 [EPNdB] for inhabitants within 75 [m] of the airport and the approach and departure routes [104]	–	–	Section 16.2	N.D
HOPPER-C-R-NC-2	NO_x emissions shall be 0 [g/kN] of thrust	0	–	Section 10.6	Yes

Table 16.7: Compliance matrix of the CS-23 regulations

Identifier	**Requirement**	**H_2OPPER**	**Margin**	**Section**	**Compliance**
HOPPER-C-R-CS-1	The aircraft shall be able to reach a climb gradient of 3 %	–	–	Section 9.3	Yes

HOPPER-C-R-CS-2	The aircraft shall be able to climb with a 1.2 % gradient with 1 engine operative	–	–	Section 9.3	Yes
HOPPER-C-R-CS-3	The center of gravity shall not shift more than +-7% during flight	1.25%	+5.75%	Section 7.2	Yes
HOPPER-C-R-CS-4	The aircraft shall have extra fuel for 45 minutes of maximum continuous power	–	–	Section 9.3	Yes
HOPPER-C-R-CS-5	The aircraft shall be able to withstand a gust speed of 20.12 [m/s] at VB for 0-4572 [m] altitude	–	–	Section 5.2	Yes
HOPPER-C-R-CS-6	The aircraft shall be able to withstand a gust speed of 15.24 [m/s] at VC for 0-4572 [m] altitude	–	–	Section 5.2	Yes
HOPPER-C-R-CS-7	The aircraft shall be able to withstand a gust speed of 7.62 [m/s] at VD for 0-4572 [m] altitude	–	–	Section 5.2	Yes
HOPPER-C-R-CS-8	It shall be possible to roll the aeroplane from a steady 30 [deg] banked turn through an angle of 60 [deg] within 10 [s]	–	–	Section 6.5	Yes
HOPPER-C-R-CS-9	No part of the pilot or the controls shall lie in the region of +-5 [deg] from the plane of rotation of any propeller	–	–	Section 5.3	Yes
HOPPER-C-R-CS-10	Each liquid-cooled engine shall have an independent cooling system, including coolant tank	–	–	Section 11.2	Yes
HOPPER-C-R-CS-11	Each propeller shall be able to be controlled separately	–	–	Section 11.2	Yes
HOPPER-C-R-CS-12	The clearance between each propeller and the ground shall be at least 18 [cm]	148	+130	Section 5.6	Yes
HOPPER-C-R-CS-13	There shall be at least 12.7 [mm] longitudinal clearance between the propeller blades or cuffs and stationary parts of the aircraft	1173.8	+1161.1	Section 11.2	Yes
HOPPER-C-R-CS-14	There shall be at least 25 [mm] radial clearance between the blade tips and the aeroplane structure	7470	+7445	Section 5.6	Yes

16.5. Feasibility Analysis

In Table 16.6 it can be seen that the operations requirement HOPPER-U-EB.2 is met at maximum payload. However, this is not the case for maximum range with no payload. This is due to the large range the aircraft can cover which takes too long in-flight to be able to perform three mission in one day.

In Table 16.6 it can be seen that the noise requirement of is not determined. In order to design an aircraft with minimal noise levels research has to be performed with help of experimental data, which was out of the scope of this conceptual research.

16.6. Mass Budget Breakdown

Table 16.8 shows the mass budget breakdown of the H_2OPPER and displays the center of gravity of each subsystem/part. The mass of each subsystem/part is calculated using tools or taken from sizing procedures, which is documented in Subsection 7.2.1. When no accurate estimate could be calculated with the available parameters, the mass of the subsystem or part was determined using the class-II weight estimation method (Subsection 7.2.1.) As can be seen from the table, the operational empty weight (OEW) is 6684.4 [kg]. The maximum take-off weight is 8616.4 [kg], the MTOW's mass breakdown is showcased in Figure 16.6. The mass breakdown of the airframe and systems parts of the H_2OPPER are shown in Figure 16.7 and Figure 16.8, respectively.

Table 16.8: H_2OPPER mass breakdown with corresponding center of gravity

Subsystem/Part	**Mass [kg]**	**% of MTOW**	$x_{c.g.}$ **[m]**
Fuselage	1064.10	12.34%	5.96
Wing	795.2	9.22%	5.57
Landing gear	379.01	4.39%	5.83
Vertical tail	83.40	0.97%	12.74
Horizontal tail	107.0	1.24%	11.49
Flight controls	170.03	1.97%	9.15
Fuel cells	517.32	5.97%	5.57
Hydrogen tank	156	1.81%	4.70
Batteries	420	4.87%	5.57
Cooling system	290	3.36%	5.57
Engines	458	5.31%	5.07
Propeller	158	2.15%	4.62
Avionics	482.31	5.60%	5.96
Engine control	15.72	0.18%	5.07
Instruments	62.15	0.72%	1.50
Electrical	253.10	2.94%	3.96
Hydraulics	49.19	0.57%	8.85
Furnishing	303.58	3.52%	5.14
Handling gear	2.58	0.03%	2.00
Air-conditioning	87.01	1.01%	5.96
Lavatory	17.78	0.21%	8.78
Flight crew	144	1.67%	2.00
OEW +10%	**6684.4**	**77.57%**	**5.71**
Hydrogen	118	1.37%	4.70
Payload	1814	21.05%	-
MTOW	**8616.4**	**100%**	5.64

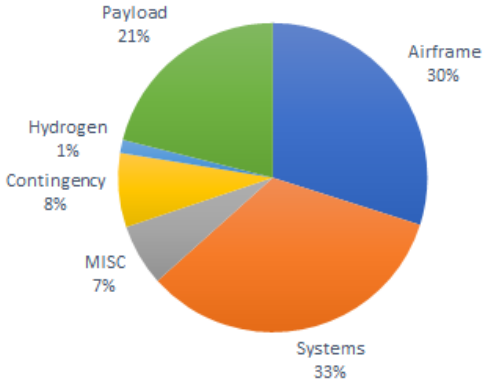

Figure 16.6: Max take-off weight breakdown

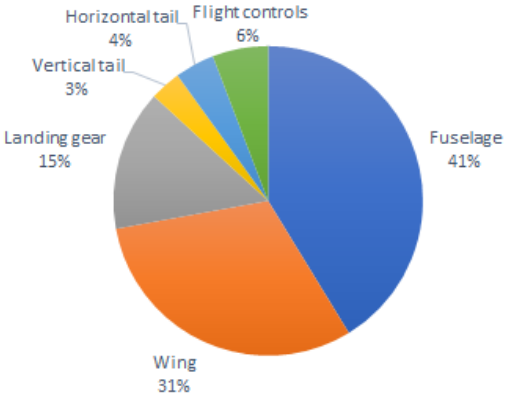

Figure 16.7: Airframe mass breakdown

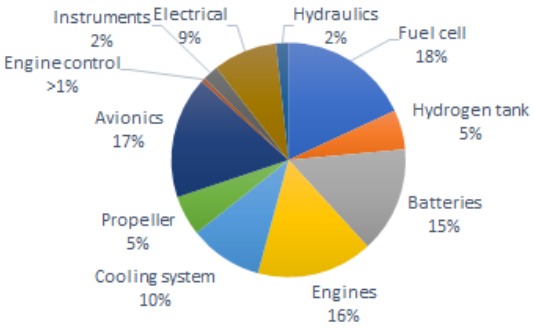

Figure 16.8: Systems mass breakdown

17
Risks

During this design phase, some plausible technical risks were identified that could have a consequence on the technical performance, schedule and cost requirements. The risks have been divided into multiple categories, related to energy systems, structure and flight dynamics. For each risk, a pre- and post-mitigation risk level is given. These are presented in a heat map in Section 17.4.

17.1. Energy Systems

E1 - High (9) to Medium (6):
Hydrogen production capacity is not enough at launch.

- **Description:** The infrastructure needed to support the aircraft is not yet available, and needs to be built up concurrently with the aircraft.
- **Mitigation:** Focus on gradual introduction to different markets to make sure that the infrastructure is ready.

E2 - Medium (6) to Low (2):
The LH2 tank production cannot be automized.

- **Description:** The LH2 tank has a non-conventional shape and consists of different material layers. Automization of the production might require new techniques that are not readily available on large scale.
- **Mitigation:** Before initial production, it is needed to research possible methods of production and invest in new techniques, such as the use of robotic arms.

E3 - Medium (6) to Low (3):
The reliability of the energy system is lower than the propulsion system of conventional aircraft.

- **Description:** The use of new technology comes with uncertainty of reliability. If the reliability is lower compared to conventional aircraft, the H_2OPPER may need to conform to tighter regulations.
- **Mitigation:** Take into account that long-term testing is needed to get a complete overview of the failure modes of the energy system. In addition, allow for redundancy, such as the use of batteries, next to the fuel cells.

E4 - Low (4) to Low (2):
A lightning strike is able to interfere with the energy system.

- **Description:** Interference might occur with the electronic components, causing component failure. This is more relevant for the H_2OPPER, as it completely relies on electricity.
- **Mitigation:** Evaluate the effects of lightning on the components of the aircraft and design appropriate shielding such as wire meshes and diverter strips.

E5 - High (9) to Medium (6):
Battery energy and power density will be lower than expected

- **Description:** A lot of research is currently being done on lithium-metal batteries, however it might be possible that the technology will not be available yet within 5 years
- **Mitigation:** Using a combination of batteries that are already available. This would include batteries with a very high power density for take-off and climb-out and batteries with high energy density for start-up, taxi and climb.

E6 - Medium (6) to Low (4):
Leaked hydrogen is not able to be contained within the belly of the aircraft.

- **Description:** Due to the small molecular size of hydrogen, it easily permeates through materials. When it enters the cabin, it can cause a dangerous situation as hydrogen mixed with oxygen can be an highly explosive gas.
- **Mitigation:** To prevent the hydrogen from entering the cabin, the belly should be ventilated enough to keep the mixtures level below a critical point. In addition, liners should be used to slow down the permeation of hydrogen.

E7 - Medium (6) to Low (4):
Fuel cell overheats during take-off

- **Description:** During take-off, the radiator is less effective then during cruise, since the flight speed is lower.
- **Mitigation:** The radiator is placed behind the propeller, which speeds up the flow, especially when not travelling fast. Furthermore, the fuel cell is cold when starting, so it is allowed to increase in temperature.

E8 - Medium (6) to Low (4):
The batteries may encounter thermal runaway.

- **Description:** The high energy density of Li-S batteries come with added risks due to the use of flammable materials. Combined with the densely packed configuration, heat can propagate quickly.
- **Mitigation:** Use of battery management systems and safety electronics to monitor and shut down batteries when temperatures are too high or voltages too low. Furthermore, the use of cooling systems can also greatly reduce the probability of a thermal runaway.

E9 - High (8) to Low (2):
The boil-off valve of the LH2 tank does not function.

- **Description:** If the boil-off in the LH2 tank can not escape, the tank will fail due to overpressure.
- **Mitigation:** Place a secondary boil-off valve on the tank.

E10 - High (9) to Low (4):
One fuel cell fails.

- **Description:** If one fuel cell fails, the engine on the shared wing does not get enough power from the battery only.
- **Mitigation:** Each fuel cell is able to provide electricity to the other wing by connecting them with cables.

E11 - High (8) to Low (4):
A fuel pipe fails and hydrogen starts leaking in the aircraft.

- **Description:** Due to the high permeability of hydrogen it might leak at critical points as connections. Due to the leak, the hydrogen concentration in the air might raise above critical levels.
- **Mitigation:** Place sensors above the critical points to detect evaporated LH2.

17.2. Structure

S1 - Very High (12) to Medium (6):
Corrosion damages the aircraft structure.

- **Description:** The humid climate of the island regions increases the probability of corrosion damage. Propellers are especially susceptible to corrosion [1].
- **Mitigation:** Regular inspections and application of fresh paint.

S2 - High (9) to Low (3):
Propeller vibrations reduce the fatigue free life of the wing.

- **Description:** Due to the wing tip engines, the engines are attached to the more slender part of the wing. This part is less resistant to vibrations and the vibrations also act over a larger part of the wing.
- **Mitigation:** Install state of the art vibration dampers and perform extra fatigue inspection around the engines. This will add weight to the engine, but might save enough weight on the wingbox to make up for this.

S3 - Medium (6) to Low (4):
System maintenance takes longer due to limited space in the wingbox.

- **Description:** Many of fuel system components are located in the wingbox structure. Inspections and replacement of these systems might take longer due to the tight space.
- **Mitigation:** Add inspection holes and removable panels to the bottom side of the wing and schedule extra time for maintenance.

[1] URL: https://www.aopa.org/go-fly/aircraft-and-ownership/maintenance-and-inspections/aircraft-corrosion [Accessed on: 18-6-2021]

17.3. Flight Dynamics

F1 High (9) to low (2):
The wing tip mounted engines show worse performance than expected.

- **Description:** The effect due to wing tip mounted engines is less beneficial in practice than expected. This would increase the zero-lift drag coefficient and decrease the oswald efficiency, both decreasing aircraft performance.
- **Mitigation:** The benefits of wing tip mounted engines on the drag coefficient and oswald efficiency are underestimated. Thereby, decreasing the possibility and severity of overestimating the beneficial effects.

F2 - Medium (6) to Low (4):
The large vertical tail area causes steerability issues due to cross winds.

- **Description:** The large vertical tail may cause the aircraft to be disturbed a lot by cross winds during take-off and landing, causing the aircraft to drift.
- **Mitigation:** Training pilots to be able to cope with the extra perturbations caused by the cross winds.

F3 - High (9) to Medium (6):
A deep stall can happen at the horizontal tail.

- **Description:** The aircraft has a high wing and a horizontal tail that is on the lower end of the vertical tail. At high angles of attack this may cause a deep stall to happen at the horizontal tail.
- **Mitigation:** The horizontal tail is located higher than what would give the lightest option regarding vertical tail structure. Therefore, the tail opted for is a crucifix tail and not a low tail, decreasing deep stall probability.

17.4. Heat Map

The risks of the Island Hopper are displayed in a heat map shown in Figure 17.1. The risk severities and probabilities shift after mitigation and a new heat map is made, which is shown in Figure 17.2.

Figure 17.1: Heat map showing the total pre-mitigation levels of risk for each event

Catastrophic (4)		E9, E11,		
Critical (3)		E2, E3, E6, E7, E8,	E1, E5, E10, S2 F1 , F3	S1
Marginal (2)		E4,	S3 F2	
Negligible (1)				
Severity / Probability	**Negligible (1)**	**Improbable (2)**	**Probable (3)**	**Highly Probable (4)**

Figure 17.2: Heat map showing the total post-mitigation levels of risk for each event

Catastrophic (4)				
Critical (3)	E3, S2	E1, E5, S1		
Marginal (2)	E2, E4, E9,	E6, E7, E8, E10, E11, S3 F2, F3		
Negligible (1)		F1		
Severity / Probability	**Negligible (1)**	**Improbable (2)**	**Probable (3)**	**Highly Probable (4)**

18
RAMS

In this chapter the RAMS characteristics of the aircraft will be described which stand for reliability, availability, maintainability and safety. The general implementation and philosophy will be reported. These characteristics will be mainly qualitatively described.

18.1. Reliability

For the operator of the aircraft reliability of the aircraft is very important for the cost effectiveness. Especially in island operations were airports are small and the inhabitants rely on air travel for emergency situations. Due to the smaller airports maintenance can not be performed on every airport, this means maintenance has to be monitored closely. Monitoring software can be used to forecast system failures and schedule maintenance ahead of time [1]. For conventional aircraft systems there is already a lot of data available. However, for more unconventional systems, such as the hydrogen tank and fuel cell, more data needs to be collected. The limited available data means that a causal reliability forecasting model would be preferred. This model uses measurements of certain factors to predict the potential failure of a system. An example for such a factor is the power output of the hydrogen fuel cell.

18.2. Availability

Another important factor for the cost effectiveness of the aircraft is the availability. The availability of the aircraft is mainly dependent on the turn-around time and the maintenance schedule. With a turn-around time of one hour, the aircraft meets the requirement set by the customer. The maintainability of the aircraft will discussed in more depth in the next section.

18.3. Maintainability

In order to ensure a good reliability and availability a proper maintenance procedure has to be in place. The main differences to conventional aircraft are the operative environment and the new technology of hydrogen as energy storage. The environment introduces a lot of humidity and corrosive wear due to the island region. This would require a proper corrosion prevention program to maintain a good surface coating and apply protective treatments. Using hydrogen as energy storage requires the use of a fuel cell and batteries for the current design. These have to be replaced multiple times over the life span of the aircraft.

18.4. Safety

The aircraft contains multiple safety critical functions to maintain a certain safety standard for the passengers. One of the noticeable differences the designed aircraft has to conventional aircraft is the addition of liquid hydrogen fuel tanks. The tanks are placed in the bottom side of the fuselage which in conventional aircraft act as a crumple zone when a belly landing is performed. Therefore, the recommendation is made to strengthen this under side. Multiple control systems keep track of the status of the entire energy flow and will warn the pilot in case values are out of bound. In terms of structural integrity under heavy loads, a safety factor of 1.5 is used which is common in the aerospace industry.

Redundancy is an import aspect of safety. Therefore, in the design multiple systems are set in place to ensure a certain redundancy. The entire energy flow system, from liquid hydrogen tank to engine, is copied for both wings. Both of the systems can work independent but can also complement each other in case an engine is inoperative.

[1] URL: https://www.exsyn.com/blog/nextgen-aircraft-reliability-monitoring [Accessed on: 16-6-2021]

19
Future Endeavours

With the conceptual phase finished, it is interesting to see what the future planning of the project will look like. A work flow diagram is made showing the activities that are planned from the current phase up to the post-launch phase. In addition, a Gantt chart is made to indicate the estimated time needed to complete each activity.

19.1. Work Flow Diagram

The Work Flow Diagram (WFD) is divided into five phases: Research and Development, Prototype, Production, Operational, and End of Life. Each phase contains a green block showing the testing stages of the design. These stages are dependent on the CS-23 regulations and need to be monitored through the whole design of the aircraft.

The first phase concerns finding an optimized design for the aircraft, as well as obtaining funding to enable the development phase. The funding is used for the RDTE phase, but also to set-up the infrastructure needed for the aircraft. The funding is obtained by looking for investors and by applying for government funds. The details of the design, such as joint types, will then be worked out and are put in a CAD object. In addition, initial buyers should be identified before continuing on with the project. With an optimized design, the design is used in simulations to find the aerodynamic characteristics of the aircraft and to find the eigenmodes of the aircraft. These can be used to find the gains of the control systems of the aircraft.

With a design ready, two prototypes can be built; one for static testing, such as wing bend tests, and one for flight tests, such as handling and performance. These qualification tests are performed under ultimate loads and the aircraft are discarded after the testing phase. The data is obtained to prove compliance to CS-23.

The third phase concerns the production of the aircraft. Contractors are hired and the production of the aircraft is started. Personnel will be educated to operate the aircraft and the acceptance testing phase will start. These aircraft are tested under normal operational conditions and are not discarded after testing. If the certification procedure is finished , it is possible to launch the aircraft. With the launch, it is time to relocate certain engineers that are not needed anymore for the project. In addition, pilot training should be provided for the launch of the aircraft.

After launch, the aircraft shall be tested to obtain data on long-term use. The sold aircraft will also need to be inspected and maintenance needs to be provided when needed. In addition to standard maintenance, the battery and fuel cell need to be replaced after a certain amount of cycles: the battery needs to be replaced every 1000 charging cycles, and the fuel cell after 40,000 [hr] of operating hours.

At the end of the operations, the aircraft needs to be recycled. Parts of the structure, such as the skin, are removed and melted down to be reused. Some parts of the aircraft, such as the seats and engines, can be sold as is to make up for the cost of recycling. If there are no more aircraft in operation, it is time to end the support of the aircraft.

19.2. Gantt Chart

In the Gantt chart on page 132 the different phases after the conceptual phase can be seen. Furthermore, an estimate is given on the duration of these phases. Note that once the aircraft goes in production the operational phase begins. The Operational phase will continue as long as the aircraft is in operation.

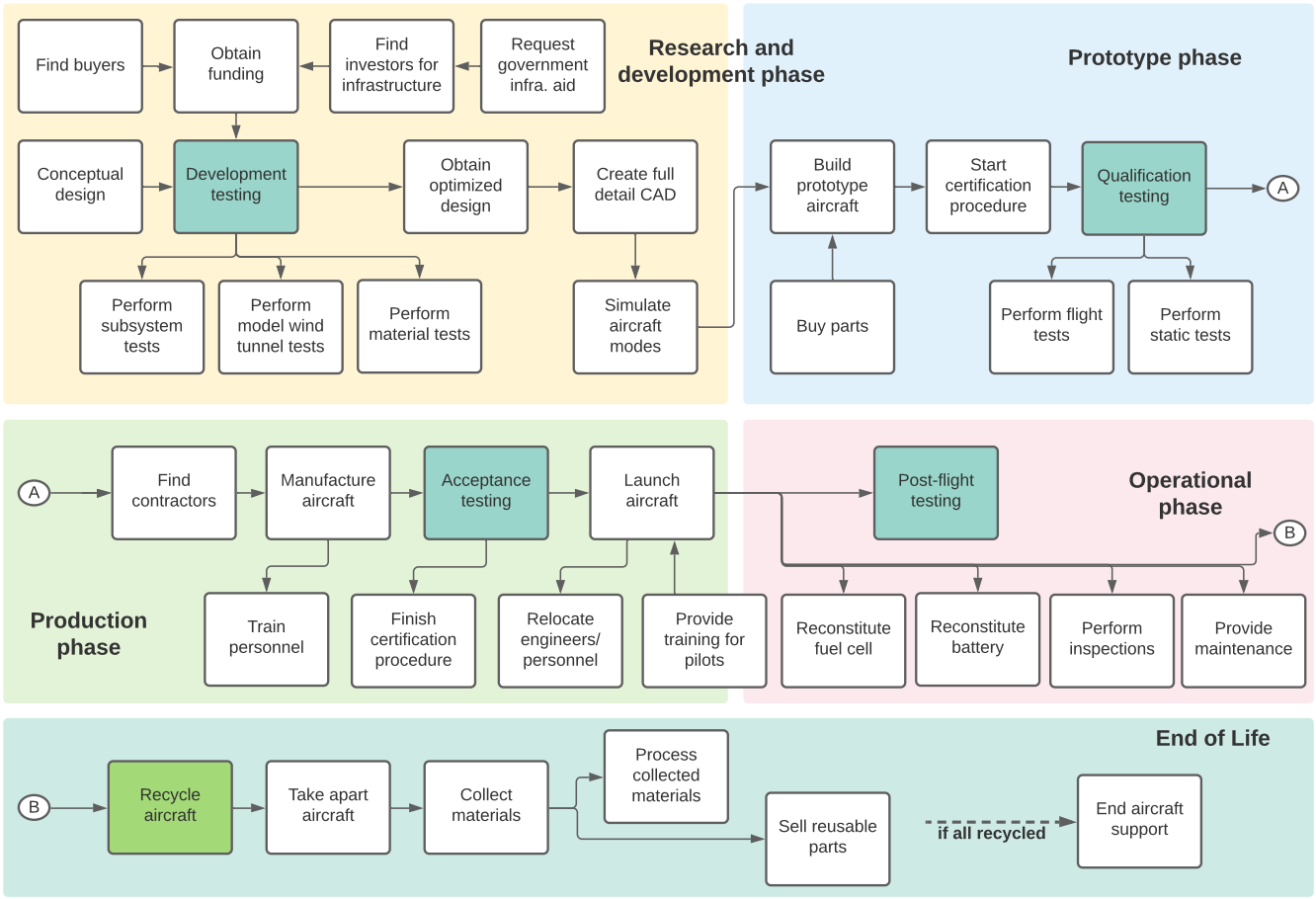

Figure 19.1: Post DSE activities flow diagram

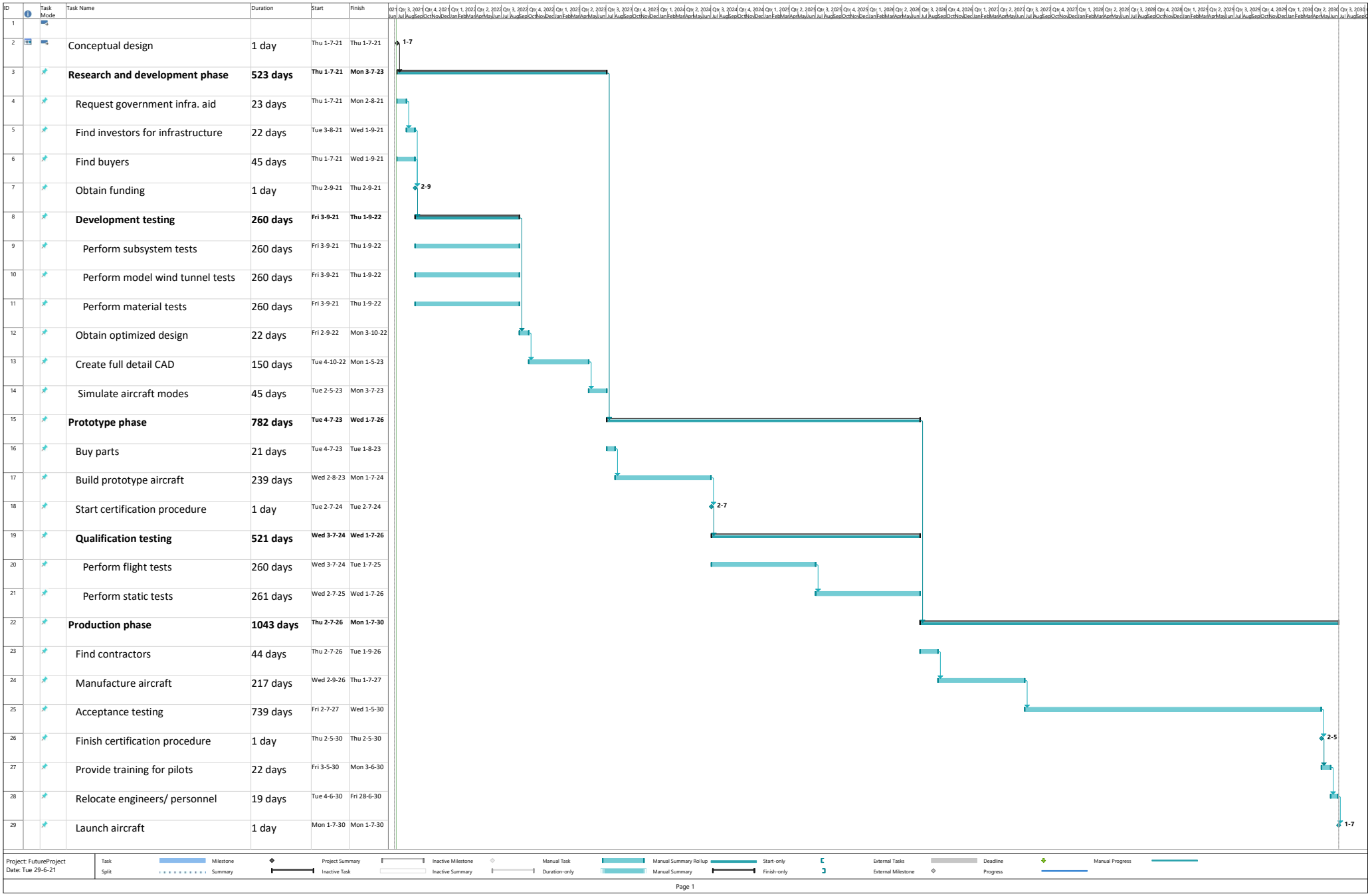

ID	Task Mode	Task Name	Duration	Start	Finish
1					
2		Conceptual design	1 day	Thu 1-7-21	Thu 1-7-21
3		**Research and development phase**	**523 days**	**Thu 1-7-21**	**Mon 3-7-23**
4		Request government infra. aid	23 days	Thu 1-7-21	Mon 2-8-21
5		Find investors for infrastructure	22 days	Tue 3-8-21	Wed 1-9-21
6		Find buyers	45 days	Thu 1-7-21	Wed 1-9-21
7		Obtain funding	1 day	Thu 2-9-21	Thu 2-9-21
8		**Development testing**	**260 days**	**Fri 3-9-21**	**Thu 1-9-22**
9		Perform subsystem tests	260 days	Fri 3-9-21	Thu 1-9-22
10		Perform model wind tunnel tests	260 days	Fri 3-9-21	Thu 1-9-22
11		Perform material tests	260 days	Fri 3-9-21	Thu 1-9-22
12		Obtain optimized design	22 days	Fri 2-9-22	Mon 3-10-22
13		Create full detail CAD	150 days	Tue 4-10-22	Mon 1-5-23
14		Simulate aircraft modes	45 days	Tue 2-5-23	Mon 3-7-23
15		**Prototype phase**	**782 days**	**Tue 4-7-23**	**Wed 1-7-26**
16		Buy parts	21 days	Tue 4-7-23	Tue 1-8-23
17		Build prototype aircraft	239 days	Wed 2-8-23	Mon 1-7-24
18		Start certification procedure	1 day	Tue 2-7-24	Tue 2-7-24
19		**Qualification testing**	**521 days**	**Wed 3-7-24**	**Wed 1-7-26**
20		Perform flight tests	260 days	Wed 3-7-24	Tue 1-7-25
21		Perform static tests	261 days	Wed 2-7-25	Wed 1-7-26
22		**Production phase**	**1043 days**	**Thu 2-7-26**	**Mon 1-7-30**
23		Find contractors	44 days	Thu 2-7-26	Tue 1-9-26
24		Manufacture aircraft	217 days	Wed 2-9-26	Thu 1-7-27
25		Acceptance testing	739 days	Fri 2-7-27	Wed 1-5-30
26		Finish certification procedure	1 day	Thu 2-5-30	Thu 2-5-30
27		Provide training for pilots	22 days	Fri 3-5-30	Mon 3-6-30
28		Relocate engineers/ personnel	19 days	Tue 4-6-30	Fri 28-6-30
29		Launch aircraft	1 day	Mon 1-7-30	Mon 1-7-30

20
Conclusion

The aim of the project was to design a fully electrically propelled net-zero emissions aircraft suitable for island-hopping operations. The result is the H_2OPPER. The design combines various innovations with as a result an aircraft that is leading in terms of sustainability, while still being commercially attractive.

The aircraft is powered by hydrogen, stored in a liquid state at 20 Kelvin. The hydrogen is stored in an unusual but efficient container: a multi-spherical composite tank, which allows for weight savings and flexibility in placement. To maximize the efficiency of the aircraft during cruise, batteries are incorporated for the high-demanding flight phases, such as take-off. After the climb, these batteries are recharged for the next take-off. To dissipate the heat released from the energy system, radiators placed behind the propellers are used. These radiators are able to make use of the accelerated air from the propeller. Part of the heat is also used to boil the liquid hydrogen to an acceptable temperature for energy conversion. To reduce the power needs of the aircraft, the two propeller engines are placed on the wing tips. By counter-rotating the propellers compared to the wingtip vortices, the amount of induced drag is reduced significantly.

When airlines fly with the H_2OPPER, they can expect to have net-zero emissions. The aircraft will be able to reach a distance of 321 nautical miles at a maximum payload of nineteen passengers. A distance of 1000 nautical miles can already be flown with just two passengers less. The aircraft is able to operate from runways as short as 750 meters long and cruises at a speed of 175 knots. The structure of the aircraft is 98 % recyclable. The aircraft achieves all this while maintaining an operating cost less than 10 % above comparable kerosene aircraft. In addition, aircraft shows preliminary compliance with the CS-23 regulations. At last, the aircraft meets all the requirements set by the customer.

The structural design of the H_2OPPER is optimized to withstand all the ultimate loading conditions with the minimum weight. Due to its favourable specific properties, Al-Li 2099-T83 was found to be optimal for the wingbox skin and lower stringers, and the lower fuselage skins. For the upper fuselage skin and front wing skin GLARE was selected, due to its high impact resistance and tensile strength. For the landing gear Ti-5Al-5Mo-5V-3C was selected, due to its high yield stress.

The production of the liquid hydrogen and the distribution to the island regions is found to be feasible using the existing transportation network. From a market analysis, it was found that the operational costs are only 5 to 10% higher than conventional aircraft. Together with its sustainable performance and superior range to other sustainable aircraft, the H_2OPPER should have a strong position in the market. From the financial evaluation it was concluded that only 18 aircraft have to be sold to break even. This makes the H_2OPPER project very attractive for investors.

For the next phase of the design it is recommended to perform a low speed wind tunnel test, in order to quantify the effect of the wing tip engines on the aerodynamic properties of the wing. Also the contribution of the Meredith effect on the drag performance of the radiator should be further investigated, focusing on the acceleration of the air by propeller and the thrust generation at lower velocities.

After the conceptual phase it is estimated that 9 years are needed to reach the launch of the H_2OPPER. With proper funding, it is possible to get a detailed design from which prototypes can be made. One will be made for static tests and one for flight tests. After confirming reliable and safe flight under ultimate conditions, it will be possible to enter the production phase, in which acceptance testing is performed to reach certification conform CS-23.

Bibliography

[1] D. S. Lee, D. W. Fahey, P. M. Forster, P. J. Newton, R. C. Wit, L. L. Lim, B. Owen, and R. Sausen, "Aviation and global climate change in the 21st century," *Atmospheric Environment*, vol. 43, no. 22-23, pp. 3520–3537, 2009.

[2] S. Salem, "Climate Change and the Sinking Island States in the Pacific," *E-International Relations*, 2020. Accessed: 30-04-2021.

[3] G. Carter, "Establishing a pacific voice in the climate change negotiations," *The new Pacific diplomacy*, vol. 1, pp. 205–218, 2015.

[4] A. I. G. Cummins, C. D. Dolman, T. A. Gehlen, T. J. W. Koning, W. A. Mathoera, H. R. A. M. Spaan, D. I. Timmermans, D. D. P. Vlot, O. van Voorst, and S. G. Wulffraat, "Baseline Report Electric Island Hopper," tech. rep., University of Technology, Delft, NL, Baseline Report, 2021.

[5] K. Franz, M. Fromhold-Eisebith, J. Feldhusen, A. Ewert, J. Heller, J. Pollmanns, and E. Stumpf, "Interdisziplinäre bewertungsplattform zur lebenszyklusanalyse im flugzeugvorentwurf," in *Deutscher Luft- und Raumfahrtkongress 2013*, 2013.

[6] K. Franz, K. Risse, and E. Stumpf, "Framework for sustainability-driven aircraft design," in *2013 Aviation Technology, Integration, and Operations Conference*, p. 4393, 2013.

[7] B. Albert, "What is the meaning of carbon-neutral, net-zero and climate-neutral?." `https://100percentrenewables.com.au/meaning-carbon-neutral-net-zero-climate-neutral/`, 2020. Accessed: 29-04-2021.

[8] J. Madigan, "The Contrail Education Project." `https://web.archive.org/web/20160408184845/http://science-edu.larc.nasa.gov/contrail-edu/faq.php`, 2015. Accessed: 29-04-2021.

[9] J. S. Cheema, "The mass growth factor–snowball effects in aircraft design," 2020.

[10] F. Nicolosi, P. Della Vecchia, D. Ciliberti, and V. Cusati, "Fuselage aerodynamic prediction methods," *Aerospace Science and Technology*, vol. 55, pp. 332–343, 2016.

[11] L. Hedges, A. Travin, and P. Spalart, "Detached-eddy simulations over a simplified landing gear," *J. Fluids Eng.*, vol. 124, no. 2, pp. 413–423, 2002.

[12] R. Kothari, D. Buddhi, and R. Sawhney, "Comparison of environmental and economic aspects of various hydrogen production methods," *Renewable and Sustainable Energy Reviews*, vol. 12, no. 2, pp. 553–563, 2008.

[13] G. P. Brasseur, J.-F. Müller, and C. Granier, "Atmospheric impact of nox emissions by subsonic aircraft: A three-dimensional model study," *Journal of Geophysical Research: Atmospheres*, vol. 101, no. D1, pp. 1423–1428, 1996.

[14] M. F. Ashby, *Materials and the environment: eco-informed material choice*. Elsevier, 2012.

[15] R. Sordello, O. Ratel, F. F. De Lachapelle, C. Leger, A. Dambry, and S. Vanpeene, "Evidence of the impact of noise pollution on biodiversity: a systematic map," *Environmental Evidence*, vol. 9, no. 1, pp. 1–27, 2020.

[16] G.J.J. Ruijgrok, *Elements of Aviation Acoustics*. VSSD, 2007.

[17] C. Rice, N. K. Ragbir, S. Rice, and G. Barcia, "Willingness to pay for sustainable aviation depends on ticket price, greenhouse gas reductions and gender," *Technology in Society*, vol. 60, p. 101224, 2020.

[18] European Aviation Safety Agency, "Certification specifications for normal-category aeroplanes - amendment 2." `https://www.easa.europa.eu/sites/default/files/dfu/CS-23%20Amendment%202%20(corrigendum).pdf`, 2010.

[19] P. Y. James Ainsworth, Craig Collier, "Airframe wingbox preliminary design and weight prediction," *Society of Allied Weight Engineers*, 2010.

[20] T.H.G. Megson, *Aircraft Structures for Engineering Students*. Elsevier, 2017.

[21] Micheal C.Y. Niu, *Airframe Stress Analysis and Sizing*. HONG KONG CONMILIT PRESS LTD., 1997.

[22] Torenbeek, E., *Synthesis of subsonic airplane design*. Delft University Press, 1982.

[23] N. S. Currey, *Aircraft landing gear design: principles and practices*. American Institute of Aeronautics and Astronautics, 1988.

[24] N. Heerens, "Landing gear design in an automated design environment," *Thesis TU Delft*, 2014.

[25] G. Zhu, "Recycling of glass fibre reinforced aluminium laminates and silicon removal from aerospace al alloy," *"Delft University of Technology"*, 2012.

[26] R. Wanhill, "Glare®: A versatile fibre metal laminate (fml) concept," *Aerospace materials and material technologies*, pp. 291–307, 2017.

[27] P. Singh, H. Pungotra, and N. S. Kalsi, "On the characteristics of titanium alloys for the aircraft applications," *Materials today: proceedings*, vol. 4, no. 8, pp. 8971–8982, 2017.

[28] A. Vlot, *Glare: history of the development of a new aircraft material*. Springer Science & Business Media, 2007.

[29] C. Jawalkar, S. Kant, *et al.*, "A review on use of aluminium alloys in aircraft components," *i-Manager's Journal on Material Science*, vol. 3, no. 3, p. 33, 2015.

[30] T. Dursun and C. Soutis, "Recent developments in advanced aircraft aluminium alloys," *Materials & Design (1980-2015)*, vol. 56, pp. 862–871, 2014.

[31] P. Manda, A. Pathak, A. Mukhopadhyay, U. Chakkingal, and A. Singh, "Ti-5al-5mo-5v-3cr and similar mo equivalent alloys: First principles calculations and experimental investigations," *Journal of applied research and technology*, vol. 15, no. 1, pp. 21–26, 2017.

[32] R. Rahman Rashid, S. Sun, G. Wang, and M. Dargusch, "Machinability of a near beta titanium alloy," *Proceedings of the Institution of Mechanical Engineers, Part B: Journal of Engineering Manufacture*, vol. 225, no. 12, pp. 2151–2162, 2011.

[33] S. Chai and W. Mason, "Landing gear integration in aircraft conceptual design," in *6th Symposium on Multidisciplinary Analysis and Optimization*, p. 4038, 1996.

[34] D. P. Raymer, "Aircraft design: A conceptual approach, aiaa education series, american institute of aeronautics and astronautics," *Inc, Washington, DC*, 1989.

[35] D. Raymer, *Aircraft design: a conceptual approach*. American Institute of Aeronautics and Astronautics, Inc., 2012.

[36] A. I. G. Cummins, C. D. Dolman, T. A. Gehlen, T. J. W. Koning, W. A. Mathoera, H. R. A. M. Spaan, D. I. Timmermans, D. D. P. Vlot, O. van Voorst, and S. G. Wulffraat, "Midterm Report Eletric Island Hopper," tech. rep., University of Technology, Delft, NL, Midterm Report, 2021.

[37] F. T. Jane, *Jane's All the World's Aircraft 2021*. Jane's Group UK Limited., 2021.

[38] E. Torenbeek, "Synthesis of subsonic aircraft design," *Student edition, Delft University of Technology/-Martinus Nijhoff*, 1982.

[39] D. Ciliberti, "An improved preliminary design methodology for aircraft directional stability prediction and vertical tailplane sizing," *University of Naples "Federico II*, 2016.

[40] P. Della Vecchia, "Development of methodologies for the aerodynamic design and optimization of new regional turboprop aircraft," *unina*, 2013.

[41] F. Diederich *et al.*, "A plan-form parameter for correlating certain aerodynamic characteristics of swept wings," 1951.

[42] W. Camilleri, K. Chircop, D. Zammit-Mangion, R. Sabatini, and V. Sethi, "Design and validation of a detailed aircraft performance model for trajectory optimisation," in *AIAA Modeling and Simulation Technologies Conference*, p. 4566, 2012.

[43] O. Al-Shamma, R. Ali, and H. S. Hasan, "An educational rudder sizing algorithm for utilization in aircraft design software," *International Journal of Applied Engineering Research*, vol. 13, no. 10, pp. 7889–7894, 2018.

[44] F. Nicolosi, D. Ciliberti, P. Della Vecchia, S. Corcione, and V. Cusati, "A comprehensive review of vertical tail design," *Aircraft Engineering and Aerospace Technology*, 2017.

[45] J. Mulder, W. van Staveren, J. van der Vaart, E. de Weerdt, C. de Visser, A. in 't Veld, and E. Mooij, "Flight dynamics lecture notes," March 2013.

[46] P. M. Sforza, "Estimating zero-lift drag coefficients and maximum l/d in subsonic flight," in *2018 AIAA Aerospace Sciences Meeting*, p. 0273, 2018.

[47] M. Niţă and D. Scholz, *Estimating the Oswald factor from basic aircraft geometrical parameters*. Deutsche Gesellschaft für Luft-und Raumfahrt-Lilienthal-Oberth eV, 2012.

[48] S. Hoerner, "Fluid-dynamic drag," in *Library of Congress Catalog Card*, 1958.

[49] I. Kroo and R. Shevell, "Aircraft design: Synthesis and analysis," *Desktop Aeronautics Inc., Textbook Version 0.99*, 2001.

[50] D. P. Witkowski, A. K. Lee, and J. P. Sullivan, "Aerodynamic interaction between propellers and wings," *Journal of Aircraft*, vol. 26, no. 9, pp. 829–836, 1989.

[51] L. L. M. Veldhuis, "Propeller wing aerodynamic interference," 2005.

[52] M. H. SNYDER JR and G. W. ZUMWALT, "Effects of wingtip-mounted propellers on wing lift and induced drag.," *Journal of Aircraft*, vol. 6, no. 5, pp. 392–397, 1969.

[53] T. Sinnige, N. van Arnhem, T. C. Stokkermans, G. Eitelberg, and L. L. Veldhuis, "Wingtip-mounted propellers: Aerodynamic analysis of interaction effects and comparison with conventional layout," *Journal of Aircraft*, vol. 56, no. 1, pp. 295–312, 2019.

[54] J. R. Hooker, A. Wick, S. R. Ginn, J. Walker, and B. T. Schiltgen, "Overview of low speed wind tunnel testing conducted on a wingtip mounted propeller for the workshop for integrated propeller prediction," in *AIAA AVIATION 2020 FORUM*, p. 2673, 2020.

[55] Y. S. Chati and H. Balakrishnan, "Analysis of aircraft fuel burn and emissions in the landing and take off cycle using operational data," in *International Conference on Research in Air Transportation*, 2014.

[56] B. Garrett-Glaser, "The batteries behind the electric aircraft revolution." https://www.aviationtoday.com/2020/09/08/batteries-behind-electric-aircraft-revolution/, 2020. Accessed: 12-05-2021.

[57] R.M. Dell, P.T Mosely, D.A.J Rand, *Towards Sustainable Road Transport*. Elsevier, 2014.

[58] G. Litster, S. McLean, "Pem fuel cell electrodes," *Journal of Power Sources*, vol. 130, pp. 61–76, 2004.

[59] S. K. G. Zhang, "A critical review of cooling techniques in proton exchange membrane fuel cell stacks," *International Journal of Hydrogen Energy*, vol. 37, no. 3, pp. 2412–2429, 2012.

[60] Y. S. S. Y. Qinghe Li, Zhiqiang Liu and C. Deng, "A review on temperature control of proton exchange membrane fuel cells," *Processes*, 2021.

[61] J. S. D.G. Charyulu, G. Singh, "Performance evaluation of a radiator in a diesel engine-a case study," *Applied Thermal Engineering*, vol. 19, no. 6, pp. 625–639, 1999.

[62] S. S. W.Wiebe, T.V. Unwerth, "Using of an electrochemical compressor for hydrogen recirculation in fuel cell vehicles," tech. rep., WILEY-VCH Verlag GmbH & Co., 2020. Accessed: 9-06-2021.

[63] Y. Teeuwen, "Propeller design for conceptual turboprop aircraft," 2017.

[64] M. Hwang, S.H. Kim, "An experimental study on the cathode humidification and evaporative cooling of polymer electrolyte membrane fuel cells using direct water injection method at high current densities," *Applied Thermal Engineering*, vol. 99, pp. 635–644, 2016.

[65] W. Zittel, R. Wurster, and L. Bolkow, "Advantages and disadvantages of hydrogen. hydrogen in the energy sector," 1996.

[66] C. Sky, "Hydrogen-powered aviation," tech. rep., EU, 2020. Accessed: 8-06-2021.

[67] A. Baroutaji, T. Wilberforce, M. Ramadan, and A. G. Olabi, "Comprehensive investigation on hydrogen and fuel cell technology in the aviation and aerospace sectors," *Renewable and sustainable energy reviews*, vol. 106, pp. 31–40, 2019.

[68] X. Wang, E. Bibeau, and G. Naterer, "Experimental correlation of forced convection heat transfer from

a naca airfoil," *Experimental Thermal and Fluid Science*, vol. 31, no. 8, pp. 1073–1082, 2007.

[69] M. Hassanalian, V. Pellerito, A. Sedaghat, F. Sabri, L. Borvayeh, and S. Sadeghi, "Aerodynamics loads variations of wings with novel heating of top surface: Bioinspiration and experimental study," *Experimental Thermal and Fluid Science*, vol. 109, p. 109884, 2019.

[70] H. Kallath, F. K. Kholi, M. Y. Ha, J. K. Min, and J. Chetwynd-Chatwin, "Computational study on the aerodynamics of a surface-heated wing for thermal management," *AIAA Journal*, vol. 58, no. 10, pp. 4339–4356, 2020.

[71] P. Luca and P. Marco, "The bonus of aircraft piston engines, an update of the meredith effect," *International Journal of Heat and Technology*, 2007.

[72] S. M. SHULI WANG, SHUO ZHANG, "An energy efficiency optimization method for fixed pitch propeller electric aircraft propulsion systems," tech. rep., IEEE Access, 2019.

[73] S. Swedenborg, "Modeling and simulation of cooling system for fuel cell vehicle," tech. rep., Uppsala Universitet, 2017. Accessed: 21-06-2021.

[74] N. F. P. Association *et al.*, *NFPA 70: National Electrical Code*. NationalFireProtectionAssoc, 2011.

[75] Advanced Energy, "Application note – an1701; how to select power supplies for high-altitude applications." `https://www.advancedenergy.com/globalassets/resources-root/application-notes/en-lv-power-supplies-for-high-altitude-applications-application-note.pdf`, n.d. Accessed: 10-06-2021.

[76] INTERNATIONAL COMMISSION ON NON-IONIZING RADIATION PROTECTION, "Health physics 99(6):818-836; 2010." `https://www.icnirp.org/cms/upload/publications/ICNIRPLFgdl.pdf`, 2010. Accessed: 10-06-2021.

[77] W. Daud, R. Rosli, E. Majlan, S. Hamid, R. Mohamed, and T. Husaini, "Pem fuel cell system control: A review," *Renewable Energy*, vol. 113, pp. 620–638, 2017.

[78] H. Hellendoorn and C. Thomas, "Defuzzification in fuzzy controllers," *Journal of Intelligent & Fuzzy Systems*, vol. 1, no. 2, pp. 109–123, 1993.

[79] G. L. M. Vonhoff, "Conceptual design of hydrogen fuel cell aircraft," tech. rep., TU Delft, 2021.

[80] I. Tapeinos, "Multi-spherical composite-overwrapped cryogenic fuel tanks for hypersonic aircrafts," tech. rep., TU Delft, 2019.

[81] S. K. Mital, J. Z. Gyekenyesi, S. M. Arnold, R. M. Sullivan, J. M. Manderscheid, and P. L. Murthy, "Review of current state of the art and key design issues with potential solutions for liquid hydrogen cryogenic storage tank structures for aircraft applications," *Aerospace Engineering Papers, NASA*, 2006.

[82] C. Winnefeld, T. Kadyk, B. Bensmann, U. Krewer, and R. Hanke-Rauschenbach, "Modelling and designing cryogenic hydrogen tanks for future aircraft applications," *Energies*, vol. 11, no. 1, p. 105, 2018.

[83] I. G. Tapeinos, S. Koussios, and R. M. Groves, "Design and analysis of a multi-cell subscale tank for liquid hydrogen storage," *International Journal of Hydrogen Energy*, vol. 41, no. 5, pp. 3676–3688, 2016.

[84] N. Semaltianos, "Thermally evaporated aluminium thin films," *Applied surface science*, vol. 183, no. 3-4, pp. 223–229, 2001.

[85] M. Verkerk and W. Brankaert, "Effects of water on the growth of aluminium films deposited by vacuum evaporation," *Thin Solid Films*, vol. 139, no. 1, pp. 77–88, 1986.

[86] C. San Marchi and B. P. Somerday, "Technical reference on hydrogen compatibility of materials," *Sandia National Laboratories, SANDIA REPORT SAND2008-1163*, pp. 1211–1, 2008.

[87] A. Demharter, "Polyurethane rigid foam, a proven thermal insulating material for applications between+ 130 c and- 196 c," *Cryogenics*, vol. 38, no. 1, pp. 113–117, 1998.

[88] O. Samoylovitch and D. Strelets, "Determination of the oswald efficiency factor at the aeroplane design preliminary stage," *Aircraft Design*, vol. 3, no. 3, pp. 167–174, 2000.

[89] J. Roskam, *Airplane design*. DARcorporation, 1985.

[90] L. B. Braga, J. L. Silveira, M. E. da Silva, E. B. Machin, D. T. Pedroso, and C. E. Tuna, "Comparative analysis between a pem fuel cell and an internal combustion engine driving an electricity generator: Technical, economical and ecological aspects," *Applied thermal engineering*, vol. 63, no. 1, pp. 354–

361, 2014.

[91] O. Balli and A. Hepbasli, "Energetic and exergetic analyses of t56 turboprop engine," *Energy conversion and management*, vol. 73, pp. 106–120, 2013.

[92] I. Lappas and A. Ikenaga, "Conceptual design and performance optimization of a tip device for a regional turboprop aircraft," *Aerospace*, vol. 6, no. 10, p. 107, 2019.

[93] EASA, *Type-certificate data sheet No. EASA.A.026 for L-410.* 2020.

[94] FAS, *Type-certificate data sheet No. A24CE for for Beechcraft 1900D.* 1998.

[95] EASA, *Type-certificate data sheet No. EASA.IM.A.575 for DHC-6 - Series.* 2017.

[96] T. K. Richard Butler, Timothy J. Dodwell, "Uncertainty quantification of composite structureswith defects using multilevel monte carlo simulations," *American Institute of Aeronautics and Astronautics*, 2015.

[97] M. K. S. Dresp, F. Dionigi and P. Strasser, "Direct electrolytic splitting of seawater: Oppurtunities and challenges," tech. rep., Technical University Berlin, 2019.

[98] Sheffield, J. W. and Folkson, R., "Alternative Fuels and Advanced Vehicle Technologies for Improved Environmental Performance." `https://www.sciencedirect.com/topics/engineering/cryogenic-hydrogen`, 2014. Accessed: 29-04-2021.

[99] L. Decker, "Liquid hydrogen distribution technology. hyper closing seminar," 2019.

[100] P. Nolte, A. Apffelstaedt, V. Gollnick, and T. Rötger, "Quantitative assessment of technology impact on aviation fuel efficiency," *Air Transport and Operations*, 06 2012.

[101] V. H. Karen Law, Jeffrey Rosenfeld and J. Leonard, "U.s. department of energy hydrogen storage cost analysis," tech. rep., U.S. Department of Energy, 2013. Accessed: 16-06-2021.

[102] B. M. Institute, "Manufacturing cost analysis of 100 and 250 kw fuel cell systems for primary power and combined heat and power applications," tech. rep., U.S. Department of Energy, 2016. Accessed: 16-06-2021.

[103] O. D. Weck, "A systems approach to mass budget management," *11th AIAA/ISSMO Multidisciplinary Analysis and Optimization Conference*, 2006.

[104] International Civil Aviation Organization, "Annex 16 - volume 1." `https://www.icao.int/environmental-protection/pages/reduction-of-noise-at-source.aspx`, 2013. Accessed: 28-06-2021.